

ABSTRACT

Title of Dissertation: DEVELOPMENT OF MACH SCALE ROTORS
WITH COMPOSITE TAILORED COUPLINGS
FOR VIBRATION REDUCTION

Jinsong Bao, Doctor of Philosophy, 2004

Dissertation directed by: Professor Inderjit Chopra
Department of Aerospace Engineering

The use of composite tailored couplings in rotor blades to reduce vibratory hub loads was studied through design, structural and aeroelastic analysis, fabrication, and wind tunnel test of Mach scale articulated composite rotors with tailored flap-bending/torsion couplings. The rotor design was nominally based on the UH-60 BLACK HAWK rotor. The 6-foot diameter blades have a SC1095 profile and feature a linear twist of -12 deg. The analysis of composite rotor was carried out using a mixed cross-section structural model, and UMARC.

Five sets of composite rotor were fabricated, including a baseline rotor without coupling, rotors with spanwise uniform positive coupling and negative coupling, and rotors with spanwise dual-segmented coupling (FBT-P/N) and triple-segmented coupling. The blade composite D-spar is the primary structural element supporting the blade loads and providing the desired elastic couplings.

Non-rotating tests were performed to examine blade structural properties. The measurements showed good correlation with predictions, and good repeatability for the four blades of each rotor set.

All rotors were tested at a rotor speed of 2300 rpm (tip Mach number 0.65) at different advance ratios and thrust levels, in the Glenn L. Martin Wind Tunnel at the University of Maryland. The test results showed that flap-bending/torsion couplings have a significant effect on the rotor vibratory hub loads. All coupled rotors reduced the 4/rev vertical force for advance ratios up to 0.3, with reductions ranging from 1 to 34%. The mixed coupling rotor FBT-P/N reduced overall 4/rev hub loads at advance ratios of 0.1, 0.2 and 0.3. At a rotor speed of 2300 rpm and an advance ratio of 0.3, the FBT-P/N rotor achieved 15% reduction for 4/rev vertical force, 3% for 4/rev in-plane force and 14% for 4/rev head moment. The reductions in the 4/rev hub loads are related to the experimentally observed reductions in 3/rev and 5/rev blade flap bending moments.

Through the present research, it has been experimentally demonstrated that structural couplings can significantly impact rotor vibration characteristics, and with suitable design optimization (coupling strength and spanwise distribution) they can be used to reduce vibratory hub loads without penalties.

DEVELOPMENT OF MACH SCALE ROTORS
WITH COMPOSITE TAILORED COUPLINGS
FOR VIBRATION REDUCTION

by

Jinsong Bao

Dissertation submitted to the Faculty of the Graduate School of the
University of Maryland, College Park in partial fulfillment
of the requirements for the degree of
Doctor of Philosophy
2004

Advisory Committee:

Professor Inderjit Chopra, Chair/Advisor
Associate Professor James Baeder
Professor Jian-Guo Liu, Dean's Representative
Professor Darryll Pines
Professor Norman Wereley

© Copyright by

Jinsong Bao

2004

DEDICATION

to my parents, my wife, and my daughter

ACKNOWLEDGEMENTS

I would like to express my deepest gratitude and appreciation to my advisor, Dr. Inderjit Chopra. Without his invaluable guidance, constant encouragement and support, this work would not be completed. I am also thankful to all members of my dissertation committee: Dr. James Baeder, Dr. Jian-Guo Liu, Dr. Darryll Pines and Dr. Norman Wereley. Their comments, suggestions and constructive criticisms have enriched my research. Also, I thank Dr. Anthony Vizzini (current at Mississippi State University) for his suggestions in the fabrication of composite models.

I would like to thank Dr. Andreas Bernhard (he is the program manager of this project at Sikorsky Aircraft Corporation) for his invaluable technical support, countless feedbacks, and constructive comments and suggestions for the years of this research. I would also like to thank Dr. V. T. Nagaraj, not only for his generous technical supports over the course of this work, but for his sincere advice through the sharing of his experience and technical expertise.

I would like to acknowledge the support provided by shared funding from the U.S. rotorcraft industry and government under the

RITA/NASA Cooperative Agreement No.NCC2-9019, Advanced Rotorcraft Technology, 01 January 2001, with Technical Monitor Mr. William Welsh from Sikorsky Aircraft Corporation.

I thank all my friends at the Alfred Gessow Rotorcraft Center for their kind assistance and technical support. I have been benefited from studying and working together, and sharing stories with my colleagues. Especially, I would like to thank for the technical supports from Anubhav Datta, Jayant Sirohi, Mao Yang, Joshua Ellison, Beatrice Roget, Jinwei Shen, Ben Berry and Mark Kimball. Thanks as well to Bernie LaFrance at the Engineering Machine Shop, Matt Fox at the Manufacturing Building and Les Yeh at the Wind Tunnel for their technical supports.

I want to express my appreciations here for the moral support of my many teachers and friends, especially from Prof. Shoushen Liu and Prof. Xiaogu Zhang; Qiang Liu, Huaming Wang, and Hao Kang.

Above all, I would like to profoundly acknowledge my wife, Hong, for her love, patience, and encouragement at all times. I would like to express my deep gratitude for the love and support of my parents. I thank my daughter, Yiwen, for her love and smile, and the joys she gives us every day. Without their support and understanding, I could not have completed this work.

TABLE OF CONTENTS

List of Tables	ix
List of Figures	xi
1 Introduction	1
1.1 Problem Statement	1
1.2 Background and Motivation	2
1.3 Summary of Previous Work	7
1.3.1 Structural Modeling of Composite Blade	7
1.3.2 Aeroelastic Analysis of Composite Rotor	8
1.3.3 Experimental Investigation of Composite Coupled Blade	12
1.4 Scope of Present Research	16
1.5 Contributions of Present Research	20
1.6 Overview of Dissertation	22
2 Composite Rotor Analytic Model	24
2.1 Composite Blade Cross-Section Structural Model	25
2.1.1 Coordinate System and Basic Assumptions	26
2.1.2 Laminate Analysis	26

2.1.3	Displacement Model	29
2.1.4	Mixed Force and Displacement Model	33
2.2	Composite Rotor Analysis	36
2.2.1	Equations of Motion	36
2.2.2	Coupled Trim Analysis	39
3	Design of Mach Scale Composite Tailored Rotor	53
3.1	General Design Issues	53
3.2	Full Scale Rotor Analysis	55
3.2.1	Full Scale Rotors	56
3.2.2	Effect of Couplings on Blade Frequency and Mode Shape .	57
3.2.3	Effect of Couplings on Vibratory Hub Loads	58
3.3	Parameters of Mach Scale Composite Tailored Rotor	59
3.4	Structural Design of Mach Scale Composite Tailored Blade	61
3.4.1	Composite Material Selection	61
3.4.2	Measurement of Composite Mechanical Properties	63
3.4.3	Structural Design of Composite Spar	65
3.4.4	Design of Composite Blade Root Insert	67
3.4.5	Design of Leading-Edge Weight	68
3.5	Layup Design of Composite D-spar	69
4	Fabrication of Mach Scale Composite Tailored Rotor	104
4.1	Design of New Twisted Blade Mold	104
4.2	Fabrication Process	106
4.2.1	Preparation of Foam Core	106
4.2.2	Preparation of Blade Layup	108

4.2.3	Layup of Composite D-spar	109
4.2.4	Blade Curing and Finishing	111
5	Experimental Examination of Blade Structural Properties	125
5.1	Bench-top Static Test	125
5.1.1	Test Setup	125
5.1.2	Test Results	127
5.2	Bench-top Shaker Test	129
5.3	Non-rotating Dynamic Test	131
6	Wind Tunnel Test Results and Discussion	151
6.1	Test Facilities	151
6.1.1	Rotor Test Stand	151
6.1.2	Wind Tunnel	153
6.2	Test Procedure	153
6.3	Results and Discussion	155
6.3.1	Overview of Test Data Quality	155
6.3.2	Rotor Vibratory Hub Loads	156
6.3.3	Blade Oscillatory Flap Bending Moment	162
6.4	Feasibility Study of Full Scale Composite Tailored Rotor	164
7	Summaries and Conclusions	192
7.1	Composite Rotor Analysis	192
7.2	Mach Scale Composite Tailored Blade Design	193
7.3	Mach Scale Composite Tailored Blade Fabrication	195
7.4	Bench-top Tests	195
7.5	Wind Tunnel Tests	196

7.6 Recommendations for Future Work	198
A Composite Blade Section Properties (Displacement Method)	200
B Composite Blade Section Properties (Mixed Method)	203
C Process of Blade Composite D-Spar Wrapping	205
C.1 Tailoring Unidirectional Prepreg	205
C.2 Making Foam Core Mandrel	206
C.3 Wrapping Composite D-Spar	206
D Additional Wind Tunnel Test Data	208
Bibliography	219

LIST OF TABLES

3.1	Scaling parameters of small scale rotor	74
3.2	Three previous model tests in the Glenn L. Martin Wind Tunnel .	74
3.3	Basic parameters of the UH-60 BLACK HAWK rotor	75
3.4	Non-dimensional blade natural frequencies of a full scale baseline articulated rotor and its simulated composite coupled derivatives (FBT: flap-bending/torsion coupling, CBT: chordwise-bending/torsion coupling, P: positive, N: negative, P/N: positive/negative)	75
3.5	Parameters of Mach scale composite rotor	76
3.6	Mechanical properties of IM7/8552 graphite/epoxy unidirectional prepreg tape	76
3.7	Layup of composite blade with two-cell D-spar	77
3.8	Skin, spar and web layups of Mach scale composite blades	77
3.9	Normalized cross-section stiffness of Mach scale composite tailored blade, with respect to baseline flap stiffness	77
3.10	Non-dimensional natural frequencies of Mach scale composite tailored at 2300 rpm	78

3.11	Predicted reduction (percentage) of 4/rev vibratory hub loads of composite rotor with mixed flap-bending/torsion couplings ($C_T/\sigma = 0.08$; μ : advance ratio; F_{xH}^{4P} : 4/rev drag force, F_{yH}^{4P} : 4/rev side force, F_{zH}^{4P} : 4/rev vertical force, M_{xH}^{4P} : 4/rev rolling moment, M_{yH}^{4P} : 4/rev pitching moment, M_{zH}^{4P} : 4/rev torque, F_{iH}^{4P} : $(F_{xH}^{4P^2} + F_{yH}^{4P^2})^{0.5}$, M_{hH}^{4P} : $(M_{xH}^{4P^2} + M_{yH}^{4P^2})^{0.5}$)	78
6.1	Test matrix for wind tunnel test of Mach scale composite rotors	167
6.2	Skin, spar and web layups of full scale composite tailored rotors	168
6.3	Normalized stiffness of the UH-60 blade and the full scale composite coupled blade, with respect to the UH-60 flapwise stiffness (EI_y : flapwise stiffness, EI_z : chordwise stiffness, GJ : torsion stiffness, EFT : flap-bending/torsion coupled stiffness)	169
6.4	Natural frequency comparison of the UH-60 blade and the full scale composite coupled blade	169

LIST OF FIGURES

2.1	Coordinate systems of a composite blade	47
2.2	Fiber axis and lamina axis of a composite lamina	48
2.3	Force and moment resultants on a general plate segment	49
2.4	Generalized beam forces and moments	50
2.5	Tip bending slope of composite beams with flap-bending/torsion coupling under a unit tip flapwise bending force	51
2.6	Tip twist of composite beams with flap-bending/torsion coupling under a unit tip torque	52
3.1	The second flap mode shape of full scale articulated rotors (FBT: flap-bending/torsion coupling, P: positive, N: negative, P/N: pos- itive/negative)	79
3.2	4/rev vibratory hub loads of a full scale baseline rotor and its simulated derivatives with flap-bending/torsion coupling ($\mu =$ $0.12, C_T/\sigma = 0.08; F_{yH}^{4P}$: 4/rev side force, F_{zH}^{4P} : 4/rev vertical force, M_{xH}^{4P} : 4/rev rolling moment, M_{yH}^{4P} : 4/rev pitching moment, M_{zH}^{4P} : 4/rev torque)	80

3.3	4/rev vibratory hub loads of a full scale baseline rotor and its simulated derivatives with flap-bending/torsion coupling ($\mu = 0.3, C_T/\sigma = 0.08$)	81
3.4	4/rev vibratory hub loads of a full scale baseline rotor and its simulated derivatives with chordwise-bending/torsion coupling ($\mu = 0.12, C_T/\sigma = 0.08$)	82
3.5	4/rev vibratory hub loads of a full scale baseline rotor and its simulated derivatives with chordwise-bending/torsion coupling ($\mu = 0.3, C_T/\sigma = 0.08$)	83
3.6	Articulated rotor hub	84
3.7	Design drawing of an articulated hub arm	85
3.8	Structure of Mach scale composite tailored blade	86
3.9	Material test of IM7/8552 prepreg	87
3.10	IM7/8552 test coupon with the layup of $[\pm 45]_{2s}$	88
3.11	Composite blade cross-sections with one-cell box spar and two-cell D-spar	88
3.12	Blade root insert details	89
3.13	Composite root insert	90
3.14	Tensile test results of blade root inserts	91
3.15	Failure of a composite blade with aluminum root insert	92
3.16	Tungsten rod with composite cage	93
3.17	Tungsten leading edge weight with airfoil profile	93
3.18	Design flow chart of composite D-spar	94
3.19	Flapwise stiffness (EI_y) of composite tailored blade versus fiber orientation angle of the D-spar	95

3.20	Torsion stiffness (GJ) of composite tailored blade versus fiber orientation angle of the D-spar	96
3.21	Flap-bending/torsion coupling stiffness (EFT) of composite tailored blade versus fiber orientation angle of the D-spar	97
3.22	Definition of fiber orientation angle	98
3.23	Lay-up of different composite tailored blade configurations (top view of D-spar). FBT:flap-bending/torsion coupling; P: positive coupling; N: negative coupling; 0: no coupling; (a) baseline uncoupled blade; (b) FBT-P uniform positive coupling; (c) FBT-N uniform negative coupling; (d) FBT-P/N spanwise segmented coupling (positive outboard and negative inboard; (e) FBT-P/0/N spanwise segmented coupling (positive outboard, uncoupled midspan, negative inboard)	99
3.24	Fan plots of Mach scale composite tailored rotors	100
3.25	The second flap mode shape of composite tailored blades	101
3.26	Predicted 4/rev vibratory hub loads of Mach scale composite tailored rotors ($\mu = 0.12, C_T/\sigma = 0.08$)	102
3.27	Predicted 4/rev vibratory hub loads of Mach scale composite tailored rotors ($\mu = 0.33, C_T/\sigma = 0.08$)	103
4.1	Internal cross-section profile of the blade mold	113
4.2	Dimensions of the blade mold	114
4.3	New twisted blade mold	115
4.4	Blade-hub connecting grip	115
4.5	Fastening the mold	116
4.6	Components of Mach scale composite tailored blade	117

4.7	Foam sanding machine	118
4.8	Cutting the foam core	118
4.9	Milling leading edge slots in the fore foam core	119
4.10	Tailoring composite lamina	120
4.11	Foam mandrel of composite D-spar	121
4.12	Layup of mixed coupling blade (FBT-P/N)	121
4.13	Composite tailored D-spar	122
4.14	Final assembly of composite blade in the mold	122
4.15	Trimming of the blade tip using CNC machine	123
4.16	Trimming of the blade trailing edge using CNC machine	124
4.17	Mach scale composite tailored blade with linear pretwist	124
5.1	Bench-top static test stand	133
5.2	Measurement system for blade static deflection	134
5.3	Optical geometry to measure blade slope	135
5.4	Tip response of baseline composite blades under tip flapwise bending force	136
5.5	Tip response of composite blades with mixed flap-bending/torsion coupling (FBT-P/N) under tip flapwise bending force	137
5.6	Tip response of composite blades with negative flap-bending/torsion coupling (FBT-N) under tip flapwise bending force	138
5.7	Tip response of composite blades with positive flap-bending/torsion coupling (FBT-P) under tip flapwise bending force	139
5.8	Tip response of composite blades with mixed flap-bending/torsion coupling (FBT-P/0/N) under tip flapwise bending force	140
5.9	Tip response of baseline composite blades under tip torque	141

5.10	Tip response of composite blades with mixed flap-bending/torsion coupling (FBT-P/N) under tip torque	142
5.11	Tip response of composite blades with negative flap-bending/torsion coupling (FBT-N) under tip torque	143
5.12	Tip response of composite blades with positive flap-bending/torsion coupling (FBT-P) under tip torque	144
5.13	Tip response of composite blades with mixed flap-bending/torsion coupling (FBT-P/0/N) under tip torque	145
5.14	Bench-top shaker test of a cantilevered composite tailored blade .	146
5.15	Flapwise natural frequencies of a cantilevered composite tailored blade: NACA0012 profile; spar layup: [35] ₄ ; skin layup: ±45; web: ±35 _s (35%chord)	147
5.16	Flapwise natural frequencies of a cantilevered composite tailored blade: SC1095 profile; spar layup: [33] ₄ ; skin layup: ±45; web: ±33 (35%chord)	148
5.17	Non-rotating dynamic test of composite tailored blade using piezo-electric actuator	149
5.18	Frequency response of non-rotating composite tailored blades . . .	150
6.1	Rotor test stand in the Glenn L. Martin Wind Tunnel	170
6.2	Rotor torque disk	171
6.3	Lissajous figure of two flap angle signals	171
6.4	Accumulator connected to the hydraulic motor	172
6.5	The average, minimum and maximum values of the measured 4/rev vibration at $\mu = 0.1$, $C_T/\sigma = 0.094$, 2300 rpm	173

6.6	The average, minimum and maximum values of the measured 4/rev vibration at $\mu = 0.2, C_T/\sigma = 0.093, 2300$ rpm	174
6.7	The average, minimum and maximum values of the measured 4/rev vibration at $\mu = 0.3, C_T/\sigma = 0.078, 2300$ rpm	175
6.8	The average, minimum and maximum values of the measured 4/rev vibration at $\mu = 0.35, C_T/\sigma = 0.052, 2300$ rpm	176
6.9	The average, minimum and maximum values of the measured 4/rev vibration at $\mu = 0.38, C_T/\sigma = 0.042, 2300$ rpm	177
6.10	Non-dimensional measured 4/rev vibratory hub loads at $\mu =$ 0.1, $C_T/\sigma = 0.094, 2300$ rpm (F_{xH}^{4P} : 4/rev drag force, F_{yH}^{4P} : 4/rev side force, F_{zH}^{4P} : 4/rev vertical force, M_{xH}^{4P} : 4/rev rolling moment, M_{yH}^{4P} : 4/rev pitching moment, M_{zH}^{4P} : 4/rev torque)	178
6.11	Non-dimensional measured 4/rev vibratory hub loads at $\mu =$ 0.2, $C_T/\sigma = 0.093, 2300$ rpm	179
6.12	Non-dimensional measured 4/rev vibratory hub loads at $\mu =$ 0.3, $C_T/\sigma = 0.078, 2300$ rpm	180
6.13	Predicted 4/rev vibratory hub loads at $\mu = 0.3, C_T/\sigma = 0.078,$ 2300 rpm	181
6.14	Non-dimensional measured 4/rev vibratory hub loads at $\mu =$ 0.1, $C_T/\sigma = 0.094, 2000$ rpm	182
6.15	Non-dimensional measured 4/rev vibratory hub loads at $\mu =$ 0.2, $C_T/\sigma = 0.090, 2000$ rpm	183
6.16	Non-dimensional measured 4/rev vibratory hub loads at $\mu =$ 0.3, $C_T/\sigma = 0.071, 2000$ rpm	184

6.17	Non-dimensional measured 4/rev vibratory hub loads at $\mu =$ 0.1, $C_T/\sigma = 0.077$, 2300 rpm	185
6.18	Non-dimensional measured 4/rev vibratory hub loads at $\mu =$ 0.2, $C_T/\sigma = 0.075$, 2300 rpm	186
6.19	Non-dimensional measured 4/rev vibratory hub loads at $\mu =$ 0.3, $C_T/\sigma = 0.061$, 2300 rpm	187
6.20	Blade oscillatory flap bending moment at $\mu = 0.3$, 2000 rpm . . .	188
6.21	Blade oscillatory flap bending moment at $\mu = 0.1$, 2300 rpm . . .	189
6.22	Blade oscillatory flap bending moment at $\mu = 0.2$, 2300 rpm . . .	190
6.23	Blade oscillatory flap bending moment at $\mu = 0.3$, 2300 rpm . . .	191
D.1	The average, minimum and maximum values of the measured 4/rev vibration at $\mu = 0.1$, $C_T/\sigma = 0.094$, 2000 rpm	209
D.2	The average, minimum and maximum values of the measured 4/rev vibration at $\mu = 0.2$, $C_T/\sigma = 0.090$, 2000 rpm	210
D.3	The average, minimum and maximum values of the measured 4/rev vibration at $\mu = 0.3$, $C_T/\sigma = 0.071$, 2000 rpm	211
D.4	Non-dimensional measured 4/rev vibratory hub loads at $\mu =$ 0.1, $C_T/\sigma = 0.077$, 2000 rpm	212
D.5	Non-dimensional measured 4/rev vibratory hub loads at $\mu =$ 0.2, $C_T/\sigma = 0.072$, 2000 rpm	213
D.6	Non-dimensional measured 4/rev vibratory hub loads at $\mu =$ 0.3, $C_T/\sigma = 0.060$, 2000 rpm	214
D.7	Non-dimensional measured 4/rev vibratory hub loads at $\mu =$ 0.35, $C_T/\sigma = 0.052$, 2300 rpm	215

D.8	Non-dimensional measured 4/rev vibratory hub loads at $\mu =$ 0.38, $C_T/\sigma = 0.042$, 2300 rpm	216
D.9	Non-dimensional measured 4/rev vibratory hub loads at $\mu =$ 0.35, $C_T/\sigma = 0.033$, 2300 rpm	217
D.10	Non-dimensional measured 4/rev vibratory hub loads at $\mu =$ 0.38, $C_T/\sigma = 0.024$, 2300 rpm	218

Chapter 1

Introduction

1.1 Problem Statement

Since the early 1960's, composite materials have been widely used in the primary rotor blade structure, because of their higher specific strength and stiffness, better corrosion resistance, better damage tolerance and superior fatigue characteristics compared to metals [1, 2, 3]. The use of composite materials also allows easy incorporation of advanced blade geometry. Another advantage of composite structures is the design flexibility to introduce specific elastic couplings. During the past two decades, a wealth of analytic research on rotors with composite coupled blades has indicated that composite tailored elastic couplings can beneficially influence aeroelastic characteristics of a rotor, such as reducing rotor vibratory hub loads and increasing aeromechanical stability. However, to date, none of the production helicopter composite rotors incorporates elastic couplings.

Even though the potential benefits of composite tailored couplings have been demonstrated by analyses, it is important to validate the analyses and conclu-

sively demonstrate the benefits experimentally, prior to the introduction of such a technology in the next generation full scale rotor system. The primary purpose of this dissertation is the development and experimental evaluation of Mach scale rotors with composite tailored couplings for vibration reduction.

1.2 Background and Motivation

Compared to fixed-wing aircraft, helicopters incorporate slender and flexible rotor blades. These elastic blades have to operate in non-steady and asymmetric aerodynamic environment. The complex aerodynamic environment and the dynamic response of the elastic blades, which also have interaction with fuselage structure and mechanical control systems, result in large blade vibratory loads [4, 5]. For a helicopter with N_b identical blades, the $(kN_b \pm 1)/\text{rev}$ and kN_b/rev (where k is an arbitrary integer) blade vibratory loads in the rotating frame are filtered through the hub to the fuselage at the frequency of kN_b/rev in the fixed frame. This becomes a primary source of vibration of helicopters. The high vibration levels limit helicopter performance, reduce the structural life of components, lead to pilot fatigue and poor ride qualities, and increase operating cost.

There have been many passive and active concepts used or proposed to reduce the helicopter vibration [6, 7, 8]. These approaches may be classified into four categories:

1. Modification of hub or pylon dynamics: This category involves installation of rotor hub vibration absorbers [9, 10, 11], or vibration isolation [12, 13]. These passive devices have been, and still widely used for the vibration reduction of

production helicopters. However, they cause considerable weight and drag penalties, increase maintenance costs and rapidly degrade performance away from the tuned flight condition.

2. Modification of fuselage dynamics: Absorbers or actuators are mounted in the fuselage structure to apply vibration suppression at several key locations. These devices can be typically passive spring-mass absorbers, or actively-controlled actuators. Examples for the active system are: Active Control of Structural Response (ACSR), which has been tested in the Westland W-3 [14] and the Sikorsky S-76 [15]; Active Vibration Control (AVC) [16] which is standard equipment on the Sikorsky S-92 and the UH-60M; and Dynamically Tailored Airframe Structures (DTAS) recently proposed for the Bell quad-tiltrotor concept [17]. The disadvantages of this type of devices are large weight penalty and mechanical complexity of the system.

3. Modification of blade dynamics: The dynamic response of a rotor blade is governed by fundamental blade dynamic characteristics, like blade natural frequencies and blade mode shapes. When these characteristics are modified, the aeroelastic response of the blade may get adjusted to reduce blade vibratory loads [18, 19]. A wind tunnel test was performed to demonstrate this concept [20] on a model scale. This approach is associated with the design optimization of blade [20, 21]. The “aeroelastically conformable rotor” [22, 23] may be also included in this category. By aeroelastically shaping blade dynamic twist, it may reduce rotor loads and improve aerodynamic efficiency. However, a major drawback of these concepts is the poor off-design performance. Also, they are not robust to changes in flight conditions.

4. Modification of blade aerodynamics: This is a direct way to eliminate

or reduce vibration at its source by modifying aerodynamic loads of the rotor blade. Higher Harmonic Control (HHC) and Individual Blade Control (IBC) are two typical examples of these active concepts. HHC systems employ higher harmonic excitation of the swashplate at N_b/rev with servo actuators. It has been widely studied both theoretically [24, 25, 26] and experimentally [27, 28]. Even though this technique shows potential for vibration reduction, it is restricted to N_b/rev excitation in fixed frame and promotes dynamic stall in extreme flight conditions. The IBC systems control the pitch of each blade independently with the excitation in the rotating frame [29, 30, 31, 32]. The early versions of IBC are based on employing additional hydraulic actuators between the swashplate rotating ring and pitch horn. The major drawback is the mechanical complexity of hydraulic slipping to transfer hydraulic power from rotating to fixed frame. With the development of smart structures [8, 33], several more concepts with active vibration reduction control have been investigated. Recently, innovative concepts of smart rotor with each blade actuated by smart-material actuators, such as trailing-edge flap concept [34]-[39] and active twist rotor [40]-[46], have received considerable attention. Although these active approaches have shown the potential for a significant vibration reduction, there are still many challenges to overcome before these concepts can be applied to production helicopters. A major drawback is the limited authority in terms of stroke of current smart material actuators. It is extremely challenging to design an actuator that can produce the desired actuation force and stroke, fit in a limited space (inside a blade profile) and endure a high centrifugal force environment. Second is the issue of its power and weight. An active actuator needs an additional power supply system, which also causes a weight penalty. Another concern is safety

issue. An active vibration control system consists of more subsystems than a passive device, which may have a detrimental effect on the blade integrity and the reliability of the system. Thus, the designer must pay more attention to the failure of the active system.

The designer is thus faced with difficult choices for vibration reduction: ranging from fixed frame to rotating frame devices and spanning passive and active systems. Each of these incurs cost in terms of weight, power consumption, complexity, reliability and maintainability. Given the fact that many modern rotor blades embrace composite technology for the primary structural-dynamic function of the blade, it is worthwhile to consider the benefit of inherent vibration reduction that may be achieved by combining the primary structural-dynamic function with elastically tailored vibration reduction function. This vibration reduction will at least reduce, if not eliminate, the requirements for dedicated helicopter vibration reduction systems.

The introduction of advanced composite materials in the 1960s opened a new field of aircraft construction, because composite materials not only can be strong and lightweight, but also can permit aeroelastic tailoring. Composite tailoring can be generally defined as the intentional distribution of fiber orientation and layup to meet specific structural requirements or achieve desired elastic couplings. The composite tailoring technology has been applied to the fixed-wing aircraft. The Grumman X-29 experimental plane was successfully flown with a composite bending/torsion coupled forward swept wing to overcome its divergence instability at high speeds [47]. However, composite elastic couplings have not been used on any current production helicopter blades, even though the potential benefits of composite couplings on helicopter rotors have been demon-

strated by many analyses for rotor vibration reduction [48] - [53]. One most likely factor can be the lack of experimental verification of these composite coupling benefits in a rotor system.

Despite the fact that substantial progress has been made towards the development of aeroelastic and structural analyses for full scale composite tailored rotors, there has been limited work on the design, fabrication and testing of small scale dynamically-scaled composite model rotors with composite tailored couplings for experimental verification. Compared to the design of full scale composite blade, at model scale the smaller number of composite plies and the space constraints make it more challenging to achieve the desired composite blade properties and couplings. Also, at Mach scale, the high rotor speed results in a centrifugal field that is higher than at full scale (by the inverse of the scale factor) and thus places extremely strict demands on the rotor blade structural design.

The present work will experimentally evaluate the effect of composite tailored coupling and explore the possibility of using composite tailored couplings to passively reduce rotor vibratory loads. The objective is to develop a set of articulated Mach scale composite tailored rotors with minimum vibration, to demonstrate the effect of different composite couplings through wind tunnel testing, and to generate test data for the validation of composite rotor analyses.

1.3 Summary of Previous Work

1.3.1 Structural Modeling of Composite Blade

Typically, the aeroelastic analysis of composite rotor includes two steps: the calculation of composite blade cross-section structural properties and the analysis of composite rotor aeroelastic behavior. Using a separate detailed structural analysis, the composite blade cross-section stiffnesses and couplings are calculated at different spanwise locations of the blade. Then, these stiffnesses are used as input for the comprehensive rotor aeroelastic analysis code to study rotor dynamic characteristics.

Jung, Nagaraj and Chopra [54], Hodges [55], and Friedmann and Hodges [56] have presented reviews on the status of structural modeling of composite blades. Their reviews encompassed modeling of thin- and thick-walled composite blades, and structural analysis of single cell box beams and multi-cell generalized sections. For example, Ref. [54] reviewed the influence of non-uniformities in blade properties, non-classical structural effects, large deformations, aeroelastic stability in hover and in forward flight, aeromechanical stability, and design optimization. The need for a high quality reliable test data on a dynamically scaled composite tailored rotor was emphasized for validation studies [54].

Generally, the structural modeling of the composite blade section can be separated into two groups: direct analytical method [57] -[66] and finite element analysis [67]-[72]. The direct analytical methods are typically based on combination of beam theory, plate theory and classical lamination theory. They are simple and can provide a physical understanding of the structural behavior in terms of relationship between the various effects. They are very useful for de-

sign and optimization studies. The finite element analyses can model complex geometry and non-uniformity of a cross-section. They are especially useful for detailed stress analysis of blades.

1.3.2 Aeroelastic Analysis of Composite Rotor

A great deal of aeroelastic analyses of composite rotors (including hingeless rotor, bearingless rotor, tilt rotor, and articulated rotor) have been carried out during the past two decades.

Pioneering work by Hong and Chopra [61] modeled the composite blade as a laminated thin-walled beam. The effects of elastic couplings (extension-torsion coupling, flap-bending/torsion coupling and chordwise-bending/torsion coupling) on aeroelastic stability in hover was studied. Analysis results showed that lag mode damping was strongly affected by the chordwise-bending/torsion couplings. Based on the structural model of Ref. [61], Panda and Chopra [73] extended the analysis to include dynamics of the composite rotor in forward flight. Their work showed the effects of elastic couplings on vibratory loads and isolated rotor stability of hingeless rotors in forward flight.

Smith and Chopra [62] extended the earlier composite analysis [61] by modeling precisely the nonclassical phenomena (such as transverse shear and section warping) and integrated the composite structural analysis into the early version of the University of Maryland Advanced Rotorcraft Code (UMARC) [74, 75]. They studied the potential of tailored composite couplings to improve aeromechanical stability and reduce vibratory blade loads of a soft in-plane hingeless rotor in forward flight. Their analysis showed that negative composite chordwise-bending/torsion coupling had a significant improvement on blade stability and

resulted in a small increase in 4/rev vibratory hub loads. For example, lag mode damping can be increased by 300% over a range of thrust levels and forward speeds. On the other hand, flap-bending/torsion and extension/torsion couplings slightly changed 4/rev vibratory hub forces and moments, and had a negligible influence on aeroelastic stability.

Yuan, Friedmann and Venkatesan [76, 77] developed a twenty three degree of freedom element blade model to analyze the aeroelastic response and stability of a composite hingeless blade, based on a moderate deflection theory. It included the effect of transverse shear and warping restraint. Composite couplings were shown to have substantial influence on aeroelastic stability in both hover and forward flight conditions. Their study showed that the flap-bending/torsion coupling associated with tip sweep could induce aeroelastic instability.

Fulton and Hodges [78, 79] also investigated the aeroelastic stability of composite hingeless rotor in hover. The analysis placed no restrictions on the magnitudes of blade displacement and rotations for the small strain. The analysis model included the transverse shear effects. The study covered both extension/torsion and bending/torsion coupled composite blades. In some cases, the bending/torsion coupling was shown to increase blade stability.

Nixon [80] studied the potential for improving the performance and aeroelastic stability of tiltrotors through the use of composite coupled blades. It was shown that passive blade twist control via elastic extension/torsion coupling of the rotor blade has the capability of significantly improving tiltrotor aerodynamic performance. His investigation also showed that the bending/torsion coupling of the composite blade was a very effective means for increasing the flutter velocity of a tiltrotor, and the magnitude of desired coupling did not bring an adverse

effect on performance or blade loads. Nixon, Piatak, Corso and Popelka [81] reviewed the unique composite aeroelastic tailoring of wings for stability augmentation and performance enhancements of tiltrotor. With the incorporation of bending/torsion coupling and extension/torsion coupling, they drew the same conclusions as of Ref. [80].

Tracy and Chopra [82] investigated the aeromechanical stability of a composite bearingless rotor in forward flight. In this analysis, the flexbeam was modeled as a composite thin-walled H-section beam. The structural analysis included the effects of torsion related out-of-plane warping and edge-restrained warping. The out-of-plane warping model was developed using a fourth order polynomial over the cross section area. The effects of warping restraint were incorporated by modifying the torsional stiffness distribution along the blade. Again, the negative chordwise-bending/torsion couplings were predicted to have a stabilizing effect on the regressive lag mode in hover and forward flight. The stability margin was increased by as much as 250%. It was shown that several vibratory hub loads were measurably influenced by the introduction of chordwise-bending/torsion couplings in the flexbeam.

Recently, the analysis of Floros and Smith [52, 53] showed that proper shaping of the aeroelastically induced rotor twist distribution using different spar layup configurations can reduce blade stall and alleviate vibratory loads for both hingeless and articulated rotors. The blade cross-section structural model was based on Vlasov theory for multi-cell closed sections, including the non-classical effects. The blade was structurally modeled as two-cell NACA0015 airfoil with a D-spar and skin. Their investigations showed that the angle of attack on the retreating blade can be reduced up to two degrees by introducing coupled elastic

twist, resulting in a significant reduction in blade stall. The composite couplings were shown not to produce significant improvements in all of the vibratory hub loads simultaneously.

Ganguli and Chopra [49] presented an aeroelastic optimization study of a soft in-plane hingeless rotor blade consisting of a two-cell rectangular composite box-beam spar, based on the composite blade model of Chandra and Chopra [65]. The design variables were the fiber angles of the box-beam walls for five equally spaced spanwise blade elements. The constraints were placed on blade inertia and frequency placement. The objective function was defined as the sum of the scalar norms of six non-dimensional 4/rev hub loads. It was shown that an optimized flap-bending/torsion coupled design could reduce 4/rev vibratory hub forces and moments by 5% to 28% at a forward speed of $\mu = 0.3$, compared with the uncoupled case. In contrast, it was shown that chordwise-bending/torsion coupling had a negligible influence on the reduction of vibratory hub loads. But, the negative chordwise-bending/torsion coupling showed a significant increase in lag mode damping. The optimized configuration showed comparable benefits with the incorporation of free wake and unsteady aerodynamics in Ref. [49]. They also performed an aeroelastic optimization of an advanced geometry composite hingeless rotor with expanded design variables that include tip sweep and anhedral angles, planform taper, and ply lay-up of composite walls [48, 50]. The objective function was a combination of the vibratory hub loads and vibratory blade bending moments. Their study showed that the optimized flap-bending/torsion couplings (optimization in both coupling value and spanwise coupling distribution) can significantly reduce rotor vibratory hub loads.

Yuan and Friedmann [51] also applied structural optimization to two-cell

composite hingeless rotor blades with swept tips, using composite blade model developed in Refs. [76, 77]. The aeroelastic analysis was based on a moderate deflection finite element model. The aerodynamic loads were obtained using Greenberg's theory with a quasi-steady assumption. Reverse flow effect was included, but stall and compressibility effects were neglected. The induced flow was assumed to be uniform and steady. Ply orientation of the blade cross section and tip sweep and anhedral angles were selected as design variables. It was shown that selecting 4/rev vertical shear as the objective function could result in a notable reduction in vertical hub load component, however other hub load components could increase. Depending on the configuration considered and objective function used, the reduction in vertical hub force ranged from 30 to 50% from the baseline values.

These aeroelastic optimization analyses of composite tailored rotor [48]- [51] indicate a promising passive approach to reduce the rotor vibration without weight penalty and at no addition power requirement.

A limitation of the preceding analyses (with the exception of Ganguli and Chopra [49]) is the use of linear inflow distributions, which appears inadequate to predict forward flight vibratory loads. Recently, more sophisticated analyses have included free wake modeling to improve vibration prediction capability, such as by Datta and Chopra [83].

1.3.3 Experimental Investigation of Composite Coupled Blade

Despite substantial progress in the development of structural and aeroelastic analyses for composite coupled rotor blades, there has been limited work on the

design, development and testing of composite rotors incorporating composite couplings.

Chandra and Chopra [63, 64, 65] fabricated composite beams out of AS4/3501-6 graphite/epoxy as well as Kevlar/epoxy prepregs. The beams had various cross-sections, including rectangular solid sections, I-sections, box-sections, and two-cell airfoil sections. These beams displayed extension/torsion, or bending/torsion couplings. Composite beams were built using an autoclave molding technique, except for the two-cell blades that were built using a matched-die molding technique. For composite blades, first the D-spar was fabricated, and second the cured spar and trailing edge section were wrapped in composite skin plies and cured. These blades were not “flight-worthy” and were used for static testing to experimentally evaluate blade structural properties. Cantilevered beams were tested under static bending, torsional, and extensional loads to obtain the structural response. The beam bending slope and twist were measured using a simple laser optical system. The high quality experimental data generated from these tests were used extensively by them as well as other researchers to validate the analyses. Later, they also conducted the experimental and analytical studies of the rotating and non-rotating frequencies and mode shapes of composite box beams [84] and I-section beams [85]. For the rotating environment, the beams were tested in a vacuum chamber and the excitation was provided by piezoelectric actuators.

Nixon [81, 86] conducted static torsion and axial tension tests on composite (IM6/R6376 and T300/5208 graphite/epoxy) closed-section beams with extension/torsion coupling. The beam cross-sections included circular shape and noncircular shapes. The beams were loaded by pure torsion and axial force re-

spectively, and the resulting twist and extension were measured. With the non-circular shapes, the effects associated with warping and shear deformation on the extension/torsion coupling was also experimental examined. The measured data were compared to the analytical predictions obtained using Rehfield analysis [58] and MSC/NASTRAN analysis. Lake, Izadpanah and Baucom [87, 88] also carried out free vibration tests of similar composite beams with noncircular shapes, and compared the measured natural frequencies with the analysis of MSC/NASTRAN. The thin-walled composite beams were fabricated by utilizing an expandable silicon rubber mandrel and a segmented aluminum female mold with the desired external beam geometry. Ref. [89] provided a modified silicone rubber tooling for this fabrication process.

Minguet and Dugundji [90, 91] performed static and dynamic tests to verify their analysis of solid-section composite (AS4/3501-6 graphite/epoxy) extension/torsion and bending/torsion coupled beams. The cantilevered composite beams were subjected to static tip loads with different root twist angles, and the resulting root strains and spanwise deflections were measured. High static loadings were applied at the beam tip, which caused large deflections. For the vibration tests, beam natural frequencies and mode shapes were measured using an electromagnetic shaker (placed underneath and connected to the beam with soft spring) to excite the beam.

Bauchau, Coffenberry, and Rehfield [92] built and tested a thin-walled composite box beam. The extension/torsion coupled beam consisted of two composite (T-300/948A1 graphite/epoxy) laminated plates, aluminum C-channel webs and an aluminum honeycomb core. The simply supported beam was subjected to a center torque. The deflections and strains were respectively measured by

dial gages and strain gage rosettes. The experimental data were compared with the analysis of Bauchau [60].

An experimental investigation of the structural dynamics characteristics of rotating composite (P109/glass) blades was conducted by Rand [93]. The blades were built as thin-walled beams with rectangular cross-section, and were tested in a vacuum chamber with rotating periodic excitation. The composite layup configurations included uncoupled, extension/torsion coupling and bending/shear coupling. The rotating natural frequencies and beam strains were measured and compared with theoretical predictions.

Epps and Chandra [94] also tested composite solid-section beams in a vacuum chamber with piezoceramic excitation. These flap-bending/torsion coupled beams were made of graphite/epoxy materials with different tip sweep angles and ply angles. The test data were used to validate the predictions of blade frequencies.

All these experiments were focused on the structural properties of composite blades. There are a very few experimental investigations to investigate the effect of composite tailored couplings on rotor aeroelastic behaviors.

Done [95] mentioned that Westland Helicopter conducted experimental research of composite coupled blades. However, no information of this research is available in the open literature.

Tracy and Chopra [96] built composite (AS4/3501-6 graphite/epoxy) coupled flexbeams using an autoclave molding technique, and tested a four-bladed, six-foot diameter, Froude scale soft in-plane hingeless model rotor on a hover stand to experimentally examine the effect of elastic couplings on lag mode stability. The rotor blade itself was uncoupled. Two sets of flexbeams were fabricated:

rectangular cross-section flexures with flap-bending/torsion coupling, and H-section flexures with chordwise-bending/torsion coupling. From the test data, negative chordwise-bending/torsion coupling was shown to significantly increase the lag mode stability for positive collective pitch, while flap-bending/torsion coupling had only a small effect on the lag damping. The lag damping was destabilized with the introduction of positive chordwise-bending/torsion coupling. The experimental damping data were satisfactorily compared with the UMARC predictions.

1.4 Scope of Present Research

The primary objective of the current research is to develop and experimentally evaluate Mach scale rotor blades with composite tailored flap-bending/torsion couplings for vibration reduction. The research work is carried out in three phases: analysis and design, fabrication, and experimental studies.

The aeroelastic analysis of composite rotor includes two steps: the calculation of composite blade section properties and the analysis of composite rotor aeroelastic behavior. Using a stand-alone code, the composite blade cross-section stiffnesses and couplings are calculated for different spanwise elements of the blade. Then, these stiffnesses are used as input for the comprehensive rotor aeroelastic analysis to obtain vibratory hub loads. The structural model used in the present work is derived from the mixed force and displacement analysis [66]. In this model, the composite laminate analysis is based on classical lamination theory. The displacement formulation is used to obtain direct strain components, whereas the shear related terms are obtained from the equations

of equilibrium of the blade general shell segment. The formulation for the blade extensional stiffness, bending stiffness, torsion stiffness, and coupling stiffnesses between flap, lag, torsion and axial motions are derived from the strain energy formulation of the blade.

Rotor aeroelastic analysis is carried out using University of Maryland Advanced Rotorcraft Code (UMARC) [97]. In UMARC, the rotor-fuselage equations are formulated using Hamilton's principle and are discretized using finite elements in space and time. The effect of composite materials is introduced through the strain energy variation. The rotor blade is discretized in the spatial domain using 15 degree of freedom beam finite elements having axial, flap, lag and torsion degrees of freedom. The aerodynamic analysis includes a free wake model. Rotor hub loads are calculated using the force summation method. The blade loads in the rotating system are then transformed to the fixed frame, and summed over the total number of blades to obtain the rotor hub loads. The vehicle trim and blade response solutions are calculated as one coupled solution. The blade response is calculated using finite elements in time after the nonlinear equations in space are transformed into normal mode equations.

Before the design of Mach scale composite tailored rotor, a comparison study is performed for a full scale baseline articulated rotor and its simulated composite coupled derivatives, in which blade elastic couplings are introduced. This study explores the impact of elastic couplings on full scale rotor aeroelastic behavior and provide guidelines for the design of Mach scale composite tailored rotors. The basic properties of the baseline full scale rotor are similar as those of the UH-60 BLACK HAWK rotor. The coupled versions of the baseline rotor include flap-bending/torsion composite couplings and chordwise-bending/torsion com-

posite couplings. For each category, different spanwise coupling distributions are examined.

The Mach scale rotors are designed for testing in the Glenn L. Martin Wind Tunnel at the University of Maryland, and are nominally based on the articulated UH-60 BLACK HAWK rotor. Parameters of the Mach scale rotor are constrained by an existing articulated rotor hub and the test section dimensions of the wind tunnel. A nominal speed of 2300 rpm is set for the composite tailored rotor to achieve the tip Mach number of 0.65. The key structural element of rotor blade is its composite D-spar, which not only withstands blade loads, but also permits composite tailoring to obtain desired coupling for the blade. A novel composite root insert is designed to transfer the blade loads from the blade D-spar to the hub. The blade structure also includes a composite weave skin, leading-edge weights with airfoil profile, and an aft foam core.

The optimized design of composite D-spar including composite layup and spanwise coupling distributions is determined using an iterative process combining composite blade cross-section structural analysis and comprehensive rotor aeroelastic analysis. The objective of this iterative process is to obtain minimum frequency variation between the baseline rotor and coupled rotors, as well as an optimum design of Mach scale composite tailored rotor for minimum 4/rev rotor vibratory hub loads. Prior to the design of the composite D-spar, a material test of IM7/8552 graphite/epoxy composite prepreg is carried out to provide the mechanical properties of the material for the blade design. To perform comparison studies, five sets of Mach scale composite tailored rotors are designed with different coupling configurations, including an uncoupled baseline blade with balanced D-spar layup, two rotors with spanwise uniform flap-bending/torsion couplings,

and two rotors with spanwise segmented flap-bending/torsion couplings.

The Mach scale composite tailored blades are fabricated using a matched-die molding technique. For the blade fabrication, a new twisted mold is designed using I-deas CAD package, and is manufactured by a three-axis CNC machine. Each composite D-spar is fabricated with IM7/8552 graphite/epoxy prepreg layup wrapping around the cured foam core mandrel, in which leading-edge weights and the root insert are embedded. The wrapped D-spar, the aft foam core and the weave skin are co-cured in one curing cycle. In the fabrication process, specially designed tools, and CNC machines are used to minimize fabrication error. Before the fabrication of final versions of Mach scale composite tailored rotors, several proof-of-concept composite tailored blades were fabricated. Bench-top and hover testing were performed to experimentally evaluate the design of these blades, including the stiffness properties and structural integrity. After these examinations, five sets of Mach scale composite rotors are fabricated. For each rotor configuration, six or seven blades are built.

Prior to hover testing of Mach scale composite tailored rotors, a series of bench-top static tests, bench-top shaker tests, and non-rotating dynamic tests (a piezoelectric actuator replaces hub pitch-link to provide the excitation) on the hover stand are performed to examine the blade structural properties. The bench-top static tests are also used to select four blades with closest structural properties for each rotor set.

For the wind tunnel tests, two adjacent flap hinges of the articulated hub are instrumented with Hall effect sensors to measure blade flap angles. The measurements are used to trim the rotor during the testing. Other test parameters include forward speed (advance ratio), shaft angle, rotor speed, and collective

pitch. A six-component fixed frame balance is used to measure rotor hub loads. Rotor torque is measured by a rotor torque disk. To evaluate the test quality, the average, the minimum and the maximum values of measured 4/rev balance data are examined. The measured 4/rev vibratory hub loads of composite coupled rotors are compared with those of baseline uncoupled composite rotor to demonstrate the effect of flap-bending/torsion couplings on the vibratory hub loads.

1.5 Contributions of Present Research

The review of previous work has indicated that no experimental research has been performed, to date, to evaluate the effect of composite couplings on rotor vibration reduction, despite the fact that analytic research has been conducted for about twenty years. The present research addresses this serious deficiency and will present a systemic experimental evaluation and understanding of the effect of composite couplings on vibratory hub loads. Specific contributions of this dissertation are:

1. Formulation of composite blade cross-section structural analysis of a realistic blade using mixed formulation. Modification of comprehensive aeroelastic analysis UMARC to include refined composite blade analysis.
2. Analysis of the effect of elastic couplings on the vibratory hub loads of a full scale articulated rotor, and special parametric studies to identify key design parameters that can impact vibratory loads.
3. Design of a series of Mach scale composite tailored rotors, including a

baseline rotor without couplings, two rotors with spanwise uniform flap-bending/torsion couplings (positive and negative), and two rotors with spanwise segmented flap-bending/torsion couplings (dual-segmented and triple-segmented).

4. Design of a new twisted blade mold. This mold has already been used by other researchers to build pretwisted blades.
5. Material test of IM7/8552 graphite/epoxy prepreg tape. It provides the basic mechanical properties of this material.
6. Design of a novel composite blade root insert to transfer the blade loads to the hub.
7. Development of a new fabrication process to manufacture Mach scale composite tailored rotor blades. Using this process, five sets of high quality composite tailored rotors (each rotor set has four blades plus a spare blade) were successfully fabricated with identical structural properties, good blade structural integrity, and good correlation between measured and predicted blade structural properties.
8. Development of a novel non-rotating blade dynamic test method, using a piezoelectric actuator.
9. Successful testing of all five sets of Mach scale composite tailored rotor in the wind tunnel, up to a maximum rotor speed of 2300 rpm (with corresponding tip Mach number 0.65) and maximum advance ratio of 0.38.
10. Development of a composite tailored rotor with mixed coupling blades (spanwise dual-segmented flap-bending/torsion coupling). Experimental

demonstration of an overall reduction of 4/rev vibratory hub loads for a variety of flight conditions and thrust levels, demonstrating the feasibility of the concept.

11. This is the first time that vibration reduction by means of composite structural coupling within rotor blade has been experimentally demonstrated. This is also the first time that the effect of structural couplings has been systematically evaluated, both experimentally and analytically.

The current research will help in the development of a next generation full scale composite tailored rotor with low vibration, without causing major modifications to an existing rotor hub system, retaining the existing blade profile and planform, and without any weight penalty and additional power requirement.

1.6 Overview of Dissertation

The remaining chapters of this dissertation present the details of analytical models, blade design and fabrication, bench-top tests, wind tunnel tests, and conclusions of the present work.

- Chapter 2. The formulations of two composite cross-section structural models are derived, one based on a displacement method, and another based on a mixed force and displacement method. The important features and modification of a comprehensive aeroelastic analysis code (UMARC) are also described.
- Chapter 3. The design approach for Mach scale rotor with composite tailored blades is presented. The effect of elastic couplings on a full scale rotor

and its simulated coupled configurations are investigated. The important design parameters of Mach scale composite rotor are determined. Material testing of graphite/epoxy composite prepreg is conducted. The design of the Mach scale composite tailored blade structure is presented in detail. The blade composite D-spar layup and ply orientation are determined.

- Chapter 4. A new twisted blade mold is designed and manufactured. The detailed fabrication processes of blade parts are presented. Five sets of Mach scale composite tailored rotor with different flap-bending/torsion coupling configurations are manufactured.
- Chapter 5. The experimental setup and procedures of the bench-top static test, bench-top shaker test and non-rotating dynamic test are discussed. Measured data are presented and correlated with the blade structural predictions.
- Chapter 6. Rotor test stand and wind tunnel facilities are described. The detailed wind tunnel testing procedures of Mach scale composite tailored rotors are presented. The quality of measured data is evaluated. The test results are presented and discussed. A full scale feasibility study is also included.
- Chapter 7. The conclusions of the present work are summarized and some recommendations for future work are included.

Chapter 2

Composite Rotor Analytic Model

Typically, an aeroelastic analysis of a composite rotor includes two steps: the calculation of blade cross-section properties and the analysis of rotor aeroelastic behavior. Using a separate structural analytic model, the composite blade stiffnesses and couplings are calculated, and then used as input for the comprehensive rotor aeroelastic analysis.

In this chapter, two structural models are presented for the analysis of composite blade. The first model uses displacement method, based on an extended Vlasov theory. The second model, which is used in the present research, is based on a mixed force and displacement method. The formulations for the blade cross-section extensional stiffness, bending stiffnesses, torsion stiffness, and coupling stiffnesses between flap, lag, torsion and axial motions are derived.

Rotor aeroelastic analysis is performed using a version of the University of Maryland Advanced Rotorcraft Code (UMARC). This version can be used to perform the analysis of composite rotor. The finite element analysis for the rotor blade is based on Hamilton's principle. The effect of composite material structural coupling is intrinsically included in the strain energy variation in the

derivation of the governing equations. The blade equations of motion and rotor trim analysis of UMARC are briefly described in this chapter.

2.1 Composite Blade Cross-Section Structural Model

In this section, two composite structural models (displacement model, and mixed force and displacement model) are presented to calculate the cross-section structural properties for generic cross-sections. These properties include blade axial stiffness, chordwise stiffness, flapwise stiffness, torsion stiffness and coupling stiffnesses. The displacement model developed by Chandra and Chopra [64, 65], is based on Vlasov theory [98, 99] combined with classical lamination theory. Development of the model involves reducing the two-dimensional stress and displacement field associated with a local plate element to the one-dimensional generalized force and displacement field identified with a beam. In this model, the assumed displacement field is used to compute the strain energy and the beam cross-section stiffness relations; and the equations of motion are obtained through energy principles. This model is re-derived in Section 2.1.3. The other model that is considered and re-derived in Section 2.1.4 is based on the mixed force and displacement method developed by Jung, Nagaraj and Chopra [54, 66, 100]. It is a combination of the displacement and the force formulations in which the displacement formulation is used to obtain direct strains, whereas the shear related terms are obtained from the equations of equilibrium of the plate.

2.1.1 Coordinate System and Basic Assumptions

Some notations for coordinate system are different between references [64, 66, 101, 53], which may be confusing in deriving formulations. In present work, a Cartesian coordinate system (x, y, z) is used for a composite blade (as shown in Figure 2.1), where x is the longitudinal axis of the blade, and y and z are cross-section coordinates. An orthogonal coordinate system (ξ, s, n) is used for a plate segment of the blade, where s is the contour coordinate tangent to the mid-surface of the plate, n is the normal to the plate mid-surface and ξ is along the longitudinal axis of the blade. The angle between the contour and the horizontal plane is θ . An additional contour coordinate system is used, parallel to (ξ, s, n) , with origin at the pole, P (see Figure 2.1 b).

The fundamental assumptions made for the composite structural analysis are: a) the contour does not deform in its own plane, meaning that the in-plane warping of the cross-section is neglected; b) the normal stress in the contour direction is neglected relative to the normal axial stress; c) each general plate segment behaves as a thin plate, and d) the laminate analysis of a general plate segment is governed by linear classical lamination theory.

2.1.2 Laminate Analysis

A composite laminate consists of multiple layers of fiber-reinforced materials. Each layer is thin and may have a different fiber orientation. The behavior of laminate depends on the material properties of each layer, fiber orientation angle, stacking arrangement of the layers, and ply thickness and location.

For the individual layer, there are four basic mechanical properties. They are E_1 : the longitudinal tensile modulus in the direction of the fiber orientation

(axis 1 in Figure 2.2); E_2 : the tensile modulus transverse to the fiber direction (axis 2 in Figure 2.2); G_{12} : in plane shear modulus, and ν_{12} : major Poisson ratio. The constitutive relations between stress and strain along the principal directions of the fiber are

$$\begin{Bmatrix} \sigma_1 \\ \sigma_2 \\ \tau_{12} \end{Bmatrix} = \begin{bmatrix} Q_{11} & Q_{12} & 0 \\ Q_{12} & Q_{22} & 0 \\ 0 & 0 & Q_{66} \end{bmatrix} \begin{Bmatrix} \epsilon_1 \\ \epsilon_2 \\ \gamma_{12} \end{Bmatrix} \quad (2.1)$$

where stiffness coefficients Q_{11} , Q_{12} , Q_{22} and Q_{66} are defined in terms of the basic main mechanical constants

$$Q_{11} = \frac{E_1}{1 - \nu_{12}\nu_{21}} \quad (2.2)$$

$$Q_{12} = \frac{\nu_{12}E_2}{1 - \nu_{12}\nu_{21}} \quad (2.3)$$

$$Q_{22} = \frac{E_2}{1 - \nu_{12}\nu_{21}} \quad (2.4)$$

$$Q_{66} = G_{12} \quad (2.5)$$

where the minor Poisson's ration is given by

$$\nu_{21} = \frac{E_2\nu_{12}}{E_1} \quad (2.6)$$

From these constants, the strain-stress relations along an arbitrary lamina axis (axes x and y in Figure 2.2) can be built:

$$\begin{pmatrix} \sigma_x \\ \sigma_y \\ \tau_{xy} \end{pmatrix} = \begin{bmatrix} \bar{Q}_{11} & \bar{Q}_{12} & \bar{Q}_{16} \\ \bar{Q}_{12} & \bar{Q}_{22} & \bar{Q}_{26} \\ \bar{Q}_{16} & \bar{Q}_{26} & \bar{Q}_{66} \end{bmatrix} \begin{pmatrix} \epsilon_x \\ \epsilon_y \\ \gamma_{xy} \end{pmatrix} \quad (2.7)$$

where

$$\begin{aligned} \bar{Q}_{11} &= Q_{11}\cos^4\theta + 2(Q_{12} + 2Q_{66})\sin^2\theta\cos^2\theta + Q_{22}\sin^4\theta \\ \bar{Q}_{12} &= (Q_{11} + Q_{22} - 4Q_{66})\sin^2\theta\cos^2\theta + Q_{12}(\sin^4\theta + \cos^4\theta) \\ \bar{Q}_{22} &= Q_{11}\sin^4\theta + 2(Q_{12} + 2Q_{66})\sin^2\theta\cos^2\theta + Q_{22}\cos^4\theta \\ \bar{Q}_{16} &= (Q_{11} - Q_{12} - 2Q_{66})\sin\theta\cos^3\theta + (Q_{12} - Q_{22} + 2Q_{66})\sin^3\theta\cos\theta \\ \bar{Q}_{26} &= (Q_{11} - Q_{12} - 2Q_{66})\sin^3\theta\cos\theta + (Q_{12} - Q_{22} + 2Q_{66})\sin\theta\cos^3\theta \\ \bar{Q}_{66} &= (Q_{11} + Q_{22} - 2Q_{12} - 2Q_{66})\sin^2\theta\cos^2\theta + Q_{66}(\sin^4\theta + \cos^4\theta) \end{aligned} \quad (2.8)$$

The properties of composite laminate are calculated by integrating through the thickness of the plate. The classical relationship between the force and moment resultants and the linear laminate strains is defined in several text books discussing macromechanical behavior of composite laminates [102, 103]. Taking the Kirchhoff hypothesis and the plane-stress assumption into account, this relation for a general plate segment (see Figure 2.3) is given as

$$\begin{pmatrix} N_\xi \\ N_s \\ N_{\xi s} \\ M_\xi \\ M_s \\ M_{\xi s} \end{pmatrix} = \begin{bmatrix} A_{11} & A_{12} & A_{16} & B_{11} & B_{12} & B_{16} \\ A_{12} & A_{22} & A_{26} & B_{12} & B_{22} & B_{16} \\ A_{16} & A_{26} & A_{66} & B_{16} & B_{26} & B_{66} \\ B_{11} & B_{12} & B_{16} & D_{11} & D_{12} & D_{16} \\ B_{12} & B_{22} & B_{26} & D_{12} & D_{22} & D_{16} \\ B_{16} & B_{26} & B_{66} & D_{16} & D_{26} & D_{66} \end{bmatrix} \begin{pmatrix} \epsilon_\xi \\ \epsilon_s \\ \gamma_{\xi s} \\ \kappa_\xi \\ \kappa_s \\ \kappa_{\xi s} \end{pmatrix} \quad (2.9)$$

where

$$A_{ij} = \sum_{k=1}^{N_l} Q_{ij}^k (h_{k+1} - h_k) \quad (2.10)$$

$$B_{ij} = \frac{1}{2} \sum_{k=1}^{N_l} Q_{ij}^k (h_{k+1}^2 - h_k^2) \quad (2.11)$$

$$D_{ij} = \frac{1}{3} \sum_{k=1}^{N_l} Q_{ij}^k (h_{k+1}^3 - h_k^3) \quad (2.12)$$

Q_{ij}^k refers to the stiffness matrix of the k th layer and h_{k+1} and h_k are coordinates of the k th layer with respect to the laminate mid-plane.

A , B and D are called extensional stiffness, coupling stiffness and bending stiffness respectively. These laminate stiffness matrices define a relationship between the loads applied to a laminate and the laminate deformation, which is important in the analysis for a composite laminate.

2.1.3 Displacement Model

In this model, the strain-displacement relations for a composite plate is derived from the beam displacement by Chandra and Chopra[64, 65]. In those references the plate strains and curvatures are derived by means of geometric considerations and are given by

$$\epsilon_\xi = u' + z\phi'_y + y\phi'_z - \psi(s)\phi''_x \quad (2.13)$$

$$\gamma_{\xi s} = \gamma_{xy}\cos\theta + \gamma_{xz}\sin\theta + r\phi'_x \quad (2.14)$$

$$\kappa_\xi = \phi'_y\cos\theta - \phi'_z\sin\theta - \gamma'_{xz}\cos\theta + \gamma'_{xy}\sin\theta - q\phi''_x \quad (2.15)$$

$$\kappa_{\xi s} = -2\phi'_x \quad (2.16)$$

where ψ is the warping function in terms of the contour coordinate s (Figure 2.1 b). The blade displacements are u , ϕ_x , ϕ_y and ϕ_z for longitudinal deformation, torsion, flap and lag rotations respectively.

Adequate treatment of the transverse in-plane stresses and strains is important in composite blade analysis [62]. Applying the fundamental assumptions from Vlasov theory, the normal stress in the contour direction, σ_s , is neglected relative to the normal axial stress, σ_ξ . However, the influence of ϵ_s on the transverse in-plane behavior can not be neglected, because the Poisson's effect can be significant. There are two methods to account for in-plane elastic behavior. One is to assume that for each lamina of the plate segment $\sigma_s = 0$ and ϵ_s is eliminated from the constitutive relations by substitution. This assumption is similar in nature to plane stress. This results in modified constitutive relations, used by Ganguli [49] and Tracy [82].

$$\begin{Bmatrix} \sigma_\xi \\ \tau_{\xi s} \end{Bmatrix} = Q' \begin{Bmatrix} \epsilon_\xi \\ \gamma_{\xi s} \end{Bmatrix} \quad (2.17)$$

where the modified stiffness matrix Q' (lamina plane stress) is defined as

$$Q' = \begin{bmatrix} \bar{Q}_{11} - \frac{\bar{Q}_{12}^2}{\bar{Q}_{22}} & \bar{Q}_{16} - \frac{\bar{Q}_{12}\bar{Q}_{26}}{\bar{Q}_{22}} \\ \bar{Q}_{16} - \frac{\bar{Q}_{12}\bar{Q}_{26}}{\bar{Q}_{22}} & \bar{Q}_{66} - \frac{\bar{Q}_{26}^2}{\bar{Q}_{22}} \end{bmatrix} \quad (2.18)$$

In another method, the assumption is made that laminate transverse in-plane stress resultant N_s is zero, and ϵ_s is eliminated from the classical relationship between the force and moment resultants in Equation 2.9. Therefore, the stiffness matrix A simplifies to A' (laminate plane stress),

$$A' = \begin{bmatrix} A_{11} - \frac{A_{12}^2}{A_{22}} & A_{16} - \frac{A_{12}A_{26}}{A_{22}} \\ A_{16} - \frac{A_{12}A_{26}}{A_{22}} & A_{66} - \frac{A_{26}^2}{A_{22}} \end{bmatrix} \quad (2.19)$$

The stiffness matrix A' is used in the present work.

The stress resultants (N_ξ , $N_{\xi s}$, M_ξ and $M_{\xi s}$) are related to the blade force and moment through the principle of virtual work.

$$U_s = \frac{1}{2} \int_s (N_\xi \epsilon_\xi + N_{\xi s} \gamma_{\xi s} + M_\xi \kappa_\xi + M_{\xi s} \kappa_{\xi s}) ds \quad (2.20)$$

Substituting the strains and curvatures (Equations 2.13-2.16) into the variation of the strain energy, Equation 2.20 can be re-written in terms of the blade displacements.

$$\begin{aligned} \delta U = & N_x \delta u' + M_y \delta \phi'_y + M_z \delta \phi'_z + T_s \delta \phi'_x + M_\omega \delta \phi''_x \\ & + G_y \delta \gamma_{xy} + G_z \delta \gamma_{xz} + F_y \delta \gamma'_{xy} + F_z \delta \gamma'_{xz} \end{aligned} \quad (2.21)$$

where the generalized blade forces and moments (see Figure 2.4) are obtained by integrating the plate force and moment resultants around the blade cross section,

$$N_x = \int_s N_\xi ds \quad (2.22)$$

$$M_y = \int_s (N_\xi z + M_\xi \cos \theta) ds \quad (2.23)$$

$$M_z = \int_s (N_\xi y - M_\xi \sin \theta) ds \quad (2.24)$$

$$M_\omega = - \int_s (N_\xi \psi - M_\xi q) ds \quad (2.25)$$

$$T_s = \int_s (rN_{\xi s} - 2M_{\xi s}) ds \quad (2.26)$$

$$G_y = \int_s N_{\xi s} \cos \theta ds \quad (2.27)$$

$$G_z = \int_s N_{\xi s} \sin \theta ds \quad (2.28)$$

$$F_y = \int_s M_{\xi} \sin \theta ds \quad (2.29)$$

$$F_z = - \int_s M_{\xi} \cos \theta ds \quad (2.30)$$

These equations build the relation between the generalized blade forces and the generalized beam displacements. Combining these equations with the strain-displacement relations and the stress-resultant equations, results in the one-dimensional beam element equations:

$$\begin{pmatrix} Q_x \\ M_y \\ -M_z \\ M_\omega \\ T_s \\ G_y \\ G_z \\ F_y \\ F_z \end{pmatrix} = \mathbf{K} \begin{pmatrix} u' \\ \phi'_y \\ \phi'_z \\ \phi''_x \\ \phi'_x \\ \gamma_{xy} \\ \gamma_{xz} \\ \gamma'_{xy} \\ \gamma'_{xz} \end{pmatrix} \quad (2.31)$$

The coefficients of stiffness matrix \mathbf{K} are derived from the above equation and are given in Appendix A. They are similar to those in References [64, 53], with a slightly different notation and numbering convention. The generalized force and

moments, on the left hand side of the equation, N_x , M_y , M_z and T_s are related with the axial, flap, lag and torsion deformations. Thus, the coefficients k_{11} , k_{22} , k_{33} , and k_{55} are blade cross-section axial stiffness, flapwise stiffness, lag stiffness, and torsion stiffness, respectively. For an isotropic blade, the off-diagonal terms in the stiffness matrix \mathbf{K} are zero. Composite coupled blades have non-zero off-diagonal terms. The coefficients k_{25} and k_{35} are blade flap-bending/torsion coupling stiffness and chordwise-bending/torsion coupling stiffness.

2.1.4 Mixed Force and Displacement Model

Another structural model that is considered in the present work is based on the mixed force and displacement formulation present by Jung, Nagaraj and Chopra [54, 66, 100]. In this model, it is assumed that transverse in-plane stress resultant N_s is zero, and ϵ_s is eliminated from the constitutive relations. For a thin-walled composite blade with closed cross-section, the influence of thickness on the cross-section stiffness is small. In the present research, the membrane stiffness terms are used to generate the cross-section stiffness. Therefore,

$$\begin{Bmatrix} N_\xi \\ N_{\xi s} \end{Bmatrix} = A' \begin{Bmatrix} \epsilon_\xi \\ \gamma_{\xi s} \end{Bmatrix} \quad (2.32)$$

where the modified stiffness matrix A' was defined in Equation 2.19. Then Equation 2.32 is written in a semi-inverted form [54, 66, 100] as

$$\begin{Bmatrix} N_\xi \\ \gamma_{\xi s} \end{Bmatrix} = \begin{bmatrix} A'_{11} - \frac{A'^2_{16}}{A'_{66}} & \frac{A'_{16}}{A'_{66}} \\ -\frac{A'_{16}}{A'_{66}} & \frac{1}{A'_{66}} \end{bmatrix} \begin{Bmatrix} \epsilon_\xi \\ N_{\xi s} \end{Bmatrix} \quad (2.33)$$

The axial strain ϵ_ξ is assumed as

$$\epsilon_\xi = u' + z\phi'_y + y\phi'_z \quad (2.34)$$

Here, the ϕ''_x term is neglected from Equation 2.13 for a closed cross section.

From the Equation 2.33, the shear strain is given by

$$\gamma_{\xi s} = -\frac{A'_{16}}{A'_{66}}\epsilon_\xi + \frac{1}{A'_{66}}N_{\xi s} \quad (2.35)$$

Combining this equation with Equation 2.15 and using the conditions of continuity of the shell wall displacements [66] for a closed cross section,

$$\int_s \gamma_{xy} ds = 0 \quad (2.36)$$

$$\int_s \gamma_{xz} ds = 0 \quad (2.37)$$

the following equation is obtained for shear flow $N_{\xi s}$:

$$\begin{aligned} \int_s \frac{1}{A'_{66}} N_{\xi s} ds &= \int_s r\phi'_x ds + \int_s \frac{A'_{16}}{A'_{66}} \epsilon_\xi ds \\ &= \int_s r\phi'_x ds + \int_s \frac{A'_{16}}{A'_{66}} u' ds + \int_s \frac{A'_{16}}{A'_{66}} z\phi'_y ds + \int_s \frac{A'_{16}}{A'_{66}} y\phi'_z ds \end{aligned} \quad (2.38)$$

Because $N_{\xi s}$ is constant for each cell of cross-section, the above equation is simplified as

$$N_{\xi s} = C_u u' + C_{\phi_y} \phi'_y + C_{\phi_z} \phi'_z + C_{\phi_x} \phi'_x \quad (2.39)$$

where

$$C_u = \frac{\int_s \frac{A'_{16}}{A'_{66}} ds}{\int_s \frac{1}{A'_{66}} ds} \quad (2.40)$$

$$C_{\phi_y} = \frac{\int_s \frac{A'_{16}}{A'_{66}} z ds}{\int_s \frac{1}{A'_{66}} ds} \quad (2.41)$$

$$C_{\phi_z} = \frac{\int_s \frac{A'_{16}}{A'_{66}} y ds}{\int_s \frac{1}{A'_{66}} ds} \quad (2.42)$$

$$C_{\phi_x} = \frac{\int_s r ds}{\int_s \frac{1}{A'_{66}} ds} \quad (2.43)$$

The stress resultants N_ξ and N_{ξ_s} are related to the strain energy of the blade via

$$\begin{aligned} U_s &= \frac{1}{2} \int_s (N_\xi \epsilon_\xi + N_{\xi_s} \gamma_{\xi_s}) ds \\ &= \frac{1}{2} \int_s [(A'_{11} - \frac{A'^2_{16}}{A'_{66}}) \epsilon_\xi^2 + \frac{1}{A'_{66}} N_{\xi_s}^2] ds \end{aligned} \quad (2.44)$$

Substituting Equations 2.34 and 2.39 into the above equation, the strain energy becomes

$$\begin{aligned} U_s &= \frac{1}{2} \int_s [(A'_{11} - \frac{A'^2_{16}}{A'_{66}})(u' + z\phi'_y + y\phi'_z)^2 + \frac{1}{A'_{66}}(C_u u' + C_{\phi_y} \phi'_y + C_{\phi_z} \phi'_z + C_{\phi_x} \phi'_x)^2] ds \\ &= \frac{1}{2} [u' \ \phi'_y \ \phi'_z \ \phi'_x] \mathbf{K} [u' \ \phi'_y \ \phi'_z \ \phi'_x]^T \end{aligned} \quad (2.45)$$

The elements of stiffness matrix \mathbf{K} are contour integrals over the cross section and are given in Appendix B. The coefficients k_{11} , k_{22} , k_{33} , k_{44} and k_{24} are blade cross-section axial stiffness, flapwise stiffness, lag stiffness, torsion stiffness and flap-bending/torsion coupling stiffness, respectively.

Validation studies for the displacement and the mixed methods are performed by comparing the predicted results with available experimental data. Figures 2.5 and 2.6 show the comparison results of the tip response as a function of ply orientation angle under tip loads for a flap-bending/torsion coupled composite beam. The measurement was carried out by Chandra and Chopra [65]. It is noted that although both predictions yield similar results, the mixed method is more accurate, compared to the experimental data. Jung, Nagaraj and Chopra [66] also performed validation studies for different cases, and drew the same conclusion. Thus, the mixed method is used for the structural analysis of composite tailored blade in the present work.

2.2 Composite Rotor Analysis

The University of Maryland Advanced Rotorcraft Code (UMARC) [97, 104, 101] is a comprehensive rotor code to perform rotor aeroelastic analysis for a wide range of rotor configurations. A modified version is used to perform the aeroelastic analysis of composite coupled rotor in the present work. In UMARC, the rotor-fuselage equations are formulated using Hamilton's principle and are discretized using finite elements in space and time. Composite materials influence only the variation in the strain energy. In this section, the rotor equations of motion and rotor trim analysis of the UMARC are briefly described.

2.2.1 Equations of Motion

A finite element method based upon Hamilton's principle is used to derive the equations of motion for the rotor blade [97]. The generalized Hamilton's

principle is expressed as

$$\delta\Pi = \int_{t_1}^{t_2} (\delta U - \delta T - \delta W) dt = 0 \quad (2.46)$$

where δU , δT are the variations of strain energy and kinetic energy, respectively, and δW is the virtual work done by external forces. These variations have contributions from both the rotor and the fuselage. The contributions from the rotor can be expressed as the sum of contributions from each blade.

The rotor blade is discretized in the spatial domain using a fifteen degree of freedom beam finite elements having axial, flap, lag and torsion degrees of freedom. These degrees of freedom are distributed over five element nodes (two boundary nodes and three interior nodes). There are six degrees of freedom at each element boundary node. There are two internal nodes for elastic axial deflection u and one internal node for elastic twist $\hat{\phi}$. Between elements, there is continuity of displacement and slope for flap and lag bending deflections, and continuity of displacement for elastic twist and axial deflection. Gaussian quadrature is used for the integration over each blade element. The blade element mass (\mathbf{M}), damping (\mathbf{C}) and stiffness (\mathbf{K}) matrices, as well as the element load vector \mathbf{F} are assembled into global matrices which in turn result in the blade equations of motion. The finite element equations for the b th blade can be expressed as:

$$\mathbf{M} \ddot{\mathbf{q}}_b + \mathbf{C} \dot{\mathbf{q}}_b + \mathbf{K} \mathbf{q}_b - \mathbf{F} = \mathbf{0} \quad (2.47)$$

where \mathbf{q}_b is the blade global displacement vector.

Blade strain energy is stored when the blade undergoes elastic deformation. Kinetic energy is stored when the blade moves with some velocity. External

aerodynamic loads distributed along the length of the blade contribute to the virtual work of the blade. For a composite rotor blade, the effect of composite elastic couplings is implicitly included in the strain energy. Strain energy expressions were derived for a generic composite beam by Smith [105] and Ganguli [104]. These expressions not only consist of axial deformation, flap bending, lag bending and elastic twist, but also include coupled axial/flap/lag/torsion deformations. Expressions for kinetic energy and virtual work of composite blade are identical for composite and isotropic blades [97].

The aerodynamic analysis includes a free wake model. Noncirculatory airloads and compressibility effects are also incorporated. Rotor hub loads are calculated using the force summation method. For this, the blade aerodynamic and inertial loads are integrated along the blade span to obtain blade loads at the root. The blade loads in rotating system are then transformed to the fixed frame, and summed over the total number of blades to obtain the rotor hub loads. The calculation of steady hub loads ($0/rev$) is needed to trim the helicopter. The harmonics of the hub loads (N_b/rev) are responsible for vibration. In present research, $4/rev$ hub loads are source of rotor vibration. The details of blade motion's derivation and aerodynamic modeling are described in Ref. [97, 104].

Blade Strain Energy

Each rotor blade is considered to be a long slender anisotropic beam. The strain energy for the system can be written as

$$U = \frac{1}{2} \int_0^R \int \int_A (\sigma_{xx}\epsilon_{xx} + \sigma_{x\eta}\epsilon_{x\eta} + \sigma_{x\zeta}\epsilon_{x\zeta}) d\eta d\zeta dx \quad (2.48)$$

where ϵ_{xx} is the axial strain and $\epsilon_{x\eta}$ and $\epsilon_{x\zeta}$ are the shear strains. Similarly, σ_{xx}

is the axial stress and $\sigma_{x\eta}$ and $\sigma_{x\zeta}$ are the shear stresses. Taking the variation of the strain energy in the above equation yields

$$\delta U = \int_0^R \int \int_A (\sigma_{xx} \delta \epsilon_{xx} + \sigma_{x\eta} \delta \epsilon_{x\eta} + \sigma_{x\zeta} \delta \epsilon_{x\zeta}) d\eta d\zeta dx \quad (2.49)$$

By substituting the strain-displacement relations and the stress-strain relations of composite materials into the strain variation yields the strain energy equation for the composite blade

$$\delta U = \int_0^R (U_{u'_e} \delta u' + U_{v''} \delta v'' + U_{w'} \delta w' + U_{w''} \delta w'' + U_{\hat{\phi}} \delta \hat{\phi} + U_{\hat{\phi}'} \delta \hat{\phi}' + U_{\hat{\phi}''} \delta \hat{\phi}'') dx \quad (2.50)$$

where strain energy terms $U_{u'_e}$, $U_{v''}$, $U_{w'}$, $U_{w''}$, $U_{\hat{\phi}}$, $U_{\hat{\phi}'}$ and $U_{\hat{\phi}''}$ in Equation 2.50 were derived by Ganguli [104].

2.2.2 Coupled Trim Analysis

Vehicle trim involves the calculation of the rotor control settings, disk orientation and vehicle orientation for the prescribed flight conditions. A primary assumption in the trim analysis is that the helicopter is operating in a steady level flight condition. Normally, the trim solutions can be categorized into: propulsive trim and wind tunnel trim. Both trim solutions are used in the present work. In UMARC, vehicle trim and rotor steady response are solved as one coupled solution iteratively until the convergence criteria is satisfied. The vehicle equations are independent of the structural nature of the rotor blades and thus are identical for both conventional and composite coupled blades.

Free Flight Propulsive Trim

The solution of propulsive trim simulates the free-flight condition of helicopter. It is obtained from a set of vehicle equilibrium equations for three forces

(longitudinal, lateral and vertical) and three moments (pitch, roll and yaw) [97]:

$$\begin{aligned}
F_1 &= D_F \cos \theta_{FP} + H \cos \alpha_s - T \sin \alpha_s \\
F_2 &= Y_F + Y \cos \phi_s + T \sin \phi_s + T_{tr} \\
F_3 &= T \cos \alpha_s \cos \phi_s - D_F \sin \theta_{FP} + H \sin \alpha_s - Y \sin \phi_s - W - L_{ht} \\
F_4 &= M_{x_R} + M_{x_F} + Y_F(\bar{h} \cos \phi_s + y_{cg} \sin \phi_s) \\
&\quad + W(\bar{h} \sin \phi_s - y_{cg} \cos \phi_s) + T_{tr}(\bar{h} - z_{tr}) \\
F_5 &= M_{y_R} + M_{y_F} + W(\bar{h} \sin \alpha_s - x_{cg} \cos \alpha_s) \\
&\quad - D_F(\bar{h} \cos(\alpha_s + \theta_{FP}) + x_{cg} \sin(\alpha_s + \theta_{FP})) + L_{ht}(x_{ht} - x_{cg}) \\
F_6 &= M_{z_R} + M_{z_F} + T_{tr}(x_{tr} - x_{cg}) - D_F y_{cg} \cos \alpha_s - Y x_{cg} \cos \phi_s \quad (2.51)
\end{aligned}$$

where F_1, F_2 , and F_3 are three force equilibrium residuals, and F_4, F_5 and F_6 are three moment equilibrium residuals, respectively.

The parameters H , Y , and T are rotor drag, side force and thrust, respectively; and D_F , Y_F , and W are fuselage drag, side force and gross weight, respectively. The terms T_{tr} , x_{tr} , and z_{tr} , represent the tail rotor thrust, the distance of the tail rotor hub behind the vehicle center of gravity, and the distance of the tail rotor hub above the vehicle center of gravity. x_{ht} is the distance of the horizontal tail behind the vehicle center of gravity. The terms, M_{x_R} and M_{x_F} , are the rotor and fuselage moments, respectively. x_{cg} and y_{cg} and h are, respectively, the relative location of the rotor hub center with respect to the vehicle center of gravity in the X_F, Y_F , and Z_F directions.

The unknown quantities for this trim analysis are

$$\theta^T = [\theta_{75} \ \theta_{1c} \ \theta_{1s} \ \theta_{tr} \ \alpha_s \ \phi_s] \quad (2.52)$$

where the three rotor control settings are θ_{75} (the collective pitch angle at 75% radius), θ_{1c} (lateral cyclic pitch), θ_{1s} (longitudinal cyclic pitch); the tail rotor collective pitch is θ_{tr} ; and the vehicle orientations are the longitudinal and lateral shaft tilts: α_s and ϕ_s .

Wind Tunnel Trim

The wind tunnel trim simulates the test condition of model rotors in a wind tunnel. During the trim procedure, the cyclic pitch controls (θ_{1c} and θ_{1s}) are adjusted to trim the blade flap angles (β_{1c} and β_{1s}) to zero, for a prescribed thrust level (C_T/σ), shaft tilt angles (α_s , ϕ_s) and advance ratio (μ). For this trim, the fuselage loads and tail rotor are neglected, therefore the resulting force vector is

$$\begin{aligned} F_1 &= T \\ F_2 &= M_y \\ F_3 &= M_x \end{aligned} \tag{2.53}$$

where F_1 is the thrust residual, F_2 and F_3 are the pitch and roll moment residuals at the rotor hub. The trim unknown terms are reduced to

$$\theta^T = [\theta_{75} \ \theta_{1c} \ \theta_{1s}] \tag{2.54}$$

Blade Response Equations

The blade response equations are solved using a normal mode approach to reduce computational time. The blade finite element equations are transformed into normal mode equations using coupled natural rotating blade modes about

a steady mean position. The blade global displacement vector \mathbf{q}_b is represented in terms of m modes,

$$\mathbf{q}_b = \Phi \mathbf{p}_b \quad (2.55)$$

where \mathbf{p}_b is the vector of normal mode coordinates. Substituting Equation 2.55 into Equation 2.47 results in

$$\bar{\mathbf{M}} \mathbf{p}_b^{**} + \bar{\mathbf{C}} \mathbf{p}_b^* + \bar{\mathbf{K}} \mathbf{p}_b - \bar{\mathbf{F}} = \mathbf{0} \quad (2.56)$$

where

$$\bar{\mathbf{M}} = \Phi^T \mathbf{M} \Phi \quad (2.57)$$

$$\bar{\mathbf{C}} = \Phi^T \mathbf{C} \Phi \quad (2.58)$$

$$\bar{\mathbf{K}} = \Phi^T \mathbf{K} \Phi \quad (2.59)$$

$$\bar{\mathbf{F}} = \Phi^T \mathbf{F} \quad (2.60)$$

In the above equations $\bar{\mathbf{M}}$, $\bar{\mathbf{C}}$, $\bar{\mathbf{K}}$ and $\bar{\mathbf{F}}$ are the modal matrices. When the external loads and the damping are neglected, the rotor natural vibration characteristics can be determined.

Finite Element in Time

The blade response equations given in Equation 2.56 are nonlinear and period. The blade response is solved separately in the spanwise and azimuthal coordinates. The spanwise response is obtained as a global vector in terms of normal modes from the finite element discretization. A temporal finite element method based on the Hamilton's principle in weak form is used to determine the azimuthal response of Equation 2.56. For this, the blade azimuthal response is assumed periodic with respect to rotor revolution.

Using Hamilton's principle, the blade normal mode equations (Equation 2.56) are rewritten in first order form and integrated by parts to yield,

$$\int_0^{2\pi} \begin{Bmatrix} \delta \mathbf{p}_b \\ \delta \dot{\mathbf{p}}_b \end{Bmatrix}^T \begin{Bmatrix} \bar{\mathbf{F}} - \bar{\mathbf{C}} \dot{\mathbf{p}}_b^* - \bar{\mathbf{K}} \mathbf{p}_b \\ \bar{\mathbf{M}} \dot{\mathbf{p}}_b^* \end{Bmatrix} d\psi = \begin{Bmatrix} \delta \mathbf{p}_b \\ \delta \dot{\mathbf{p}}_b^* \end{Bmatrix}^T \begin{Bmatrix} \bar{\mathbf{M}} \dot{\mathbf{p}}_b^* \\ 0 \end{Bmatrix} \Big|_0^{2\pi} \quad (2.61)$$

The damping and stiffness matrices of the response equations contain periodic coefficients, while the load vector is both nonlinear and periodic. The mass matrix is independent of periodic terms. The right hand side of the Equation 2.61 is zero due to the periodicity condition of the response $\dot{\mathbf{p}}_b^*(2\pi) = \dot{\mathbf{p}}_b^*(0)$. The above equation can be rewritten as

$$\int_0^{2\pi} \delta \mathbf{y}^T \mathbf{Q} d\psi = 0 \quad (2.62)$$

where

$$\mathbf{y} = \begin{Bmatrix} \mathbf{p}_b \\ \dot{\mathbf{p}}_b \end{Bmatrix} \quad (2.63)$$

and

$$\mathbf{Q} = \begin{Bmatrix} \bar{\mathbf{F}} - \bar{\mathbf{C}} \dot{\mathbf{p}}_b^* - \bar{\mathbf{K}} \mathbf{p}_b \\ \bar{\mathbf{M}} \dot{\mathbf{p}}_b^* \end{Bmatrix} \quad (2.64)$$

In a manner similar to the spatial finite element method, the time interval for one rotor revolution is discretized into a finite number of time elements. Assuming a constant rotor speed the time integration is reduced to an integration around the azimuth ($\Delta t = \Delta\psi/\Omega$). The response equations are written as the summation of the response over each time element as

$$\sum_{i=1}^{N_t} \int_{\psi_i}^{\psi_{i+1}} \delta \mathbf{y}_i^T \mathbf{Q}_i \mathbf{d}\psi = \mathbf{0} \quad (2.65)$$

where N_t is the number of time elements used. The equations are linearized about the current blade response estimate \mathbf{y}_o using a first order Taylor series expansion

$$\sum_{i=1}^{N_t} \int_{\psi_i}^{\psi_{i+1}} \delta \mathbf{y}_i^T [\mathbf{Q}_i(\mathbf{y}_o) + \mathbf{K}_{ti}(\mathbf{y}_o) \Delta \mathbf{y}] \mathbf{d}\psi = \mathbf{0} \quad (2.66)$$

in Equation 2.66,

$$\mathbf{K}_{ti} = \begin{bmatrix} \frac{\partial \bar{\mathbf{F}}}{\partial \mathbf{p}_b} - \bar{\mathbf{K}} & \frac{\partial \bar{\mathbf{F}}}{\partial \mathbf{p}_b^*} - \bar{\mathbf{C}} \\ \mathbf{0} & \bar{\mathbf{M}} \end{bmatrix}_i \quad (2.67)$$

For the i th time element, the normal mode coordinate \mathbf{p}_b around the azimuth is approximated using temporal shape functions (Lagrange polynomials), H_t , and the temporal discrete displacement vector ξ , as

$$\mathbf{p}_{bi}(\psi) = \mathbf{H}_t(s) \xi \quad (2.68)$$

where s is the local temporal coordinate defined as

$$s = \frac{\psi - \psi_i}{\psi_{i+1} - \psi_i} \quad (2.69)$$

and $\psi_{i+1} - \psi_i$ is the time span of the i th time element. The temporal shape functions, H_t , are dependent upon the level of approximation used to describe the response variation within each time element. Several different choices are available for H_t in Ref. [97].

Equation 2.66 can be rewritten as,

$$\sum_{i=1}^{N_t} \int_{\psi_i}^{\psi_{i+1}} \delta \xi_i^T \mathbf{N}^T (\mathbf{Q}_i + \mathbf{K}_{ti} \mathbf{N} \Delta \xi_i) \mathbf{d}\psi = \mathbf{0} \quad (2.70)$$

where

$$\mathbf{N} = \left\{ \begin{array}{c} \mathbf{H}_t(\psi) \\ \mathbf{H}_t^*(\psi) \end{array} \right\} \quad (2.71)$$

Using standard finite element assembly procedures, the normal mode equations for the blade are rewritten in the form,

$$\mathbf{Q}^G + \mathbf{K}_t^G \Delta \xi^G = 0 \quad (2.72)$$

where

$$\mathbf{Q}^G = \sum_{i=1}^{N_t} \int_{\psi_i}^{\psi_{i+1}} \mathbf{N}^T \mathbf{Q}_i d\psi \quad (2.73)$$

$$\mathbf{K}_t^G = \sum_{i=1}^{N_t} \int_{\psi_i}^{\psi_{i+1}} \mathbf{N}^T \mathbf{K}_{ti} \mathbf{N} d\psi \quad (2.74)$$

$$\Delta \xi^G = \sum_{i=1}^{N_t} \Delta \xi \quad (2.75)$$

Equation 2.72 is solved subject to the boundary condition:

$$\xi(0) = \xi(2\pi) \quad (2.76)$$

$$\xi^*(0) = \xi^*(2\pi) \quad (2.77)$$

Convergence of Coupled Trim

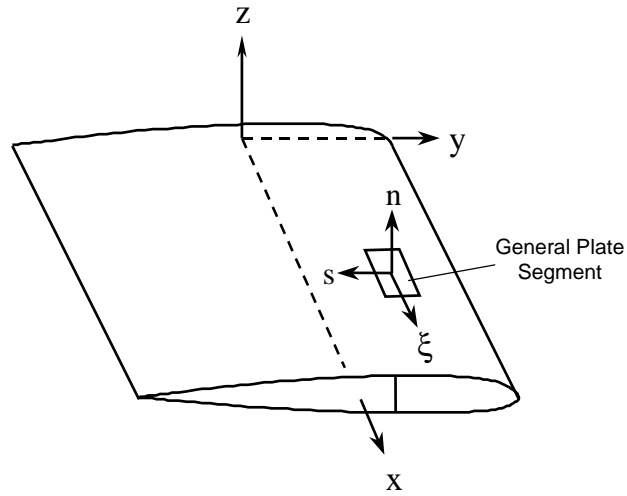
Convergence of the coupled trim solution is achieved when both the blade response equations and the force residuals are numerically satisfied within a specific tolerance. The response convergence is obtained when

$$\frac{\sqrt{\sum_{i=1}^{N_\psi} (q_1 - q_0)^2}}{\sqrt{\sum_{i=1}^{N_\psi} (q_1)^2}} < \epsilon_1^* \quad (2.78)$$

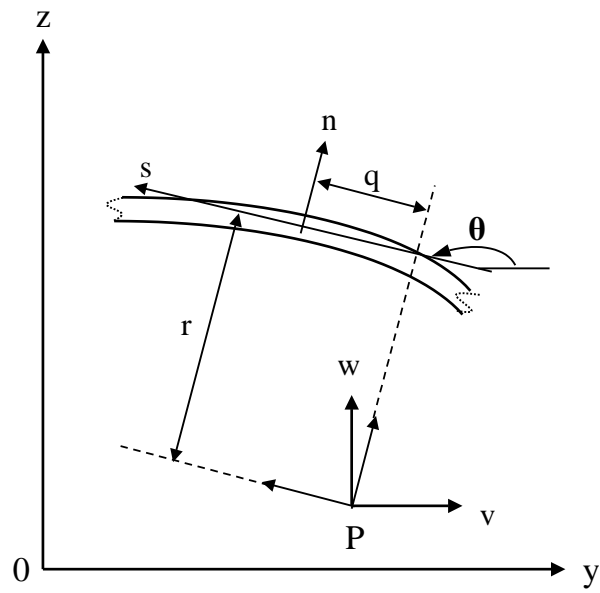
where N_ψ is the number of azimuthal Gaussian integration points; q_0 is the blade tip response for the previous iteration, q_1 is the blade tip response for the current iteration. Similarly, vehicle trim convergence is obtained when

$$\sqrt{\sum_{i=1}^n F_i^2} < \epsilon_2^* \quad (2.79)$$

where F are the residuals of the vehicle forces and moments. n is the total length of the force residual vector. For free-flight trim analysis $n = 6$ is used (the residuals of three forces and three moments); whereas for wind tunnel analysis $n = 3$ (the residuals of vertical force, pitching and rolling moments) is used.



(a)



(b)

Figure 2.1: Coordinate systems of a composite blade

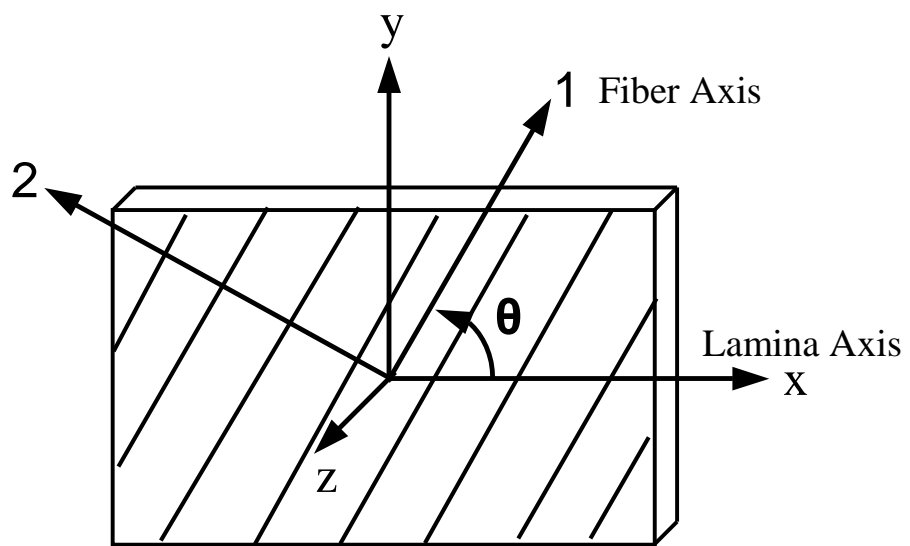


Figure 2.2: Fiber axis and lamina axis of a composite lamina

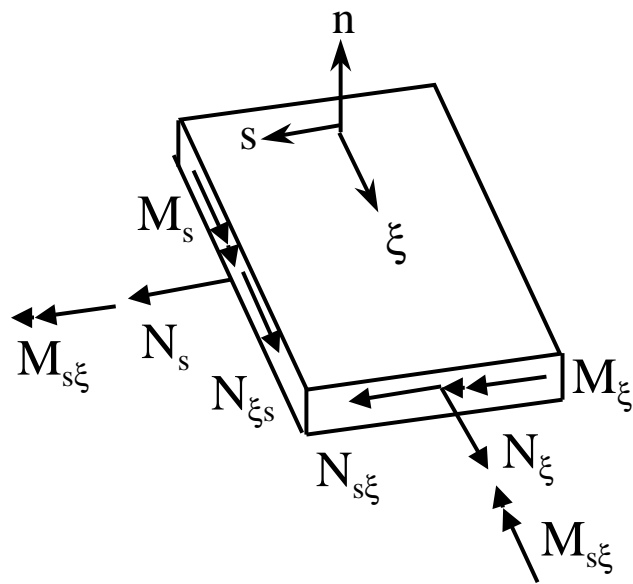


Figure 2.3: Force and moment resultants on a general plate segment

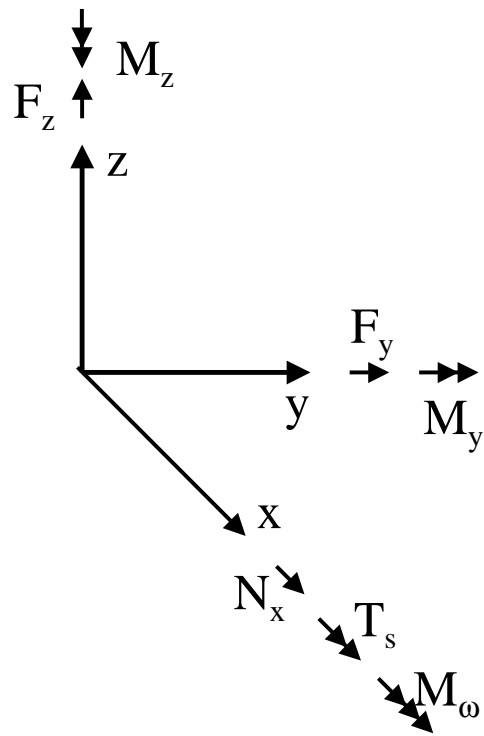


Figure 2.4: Generalized beam forces and moments

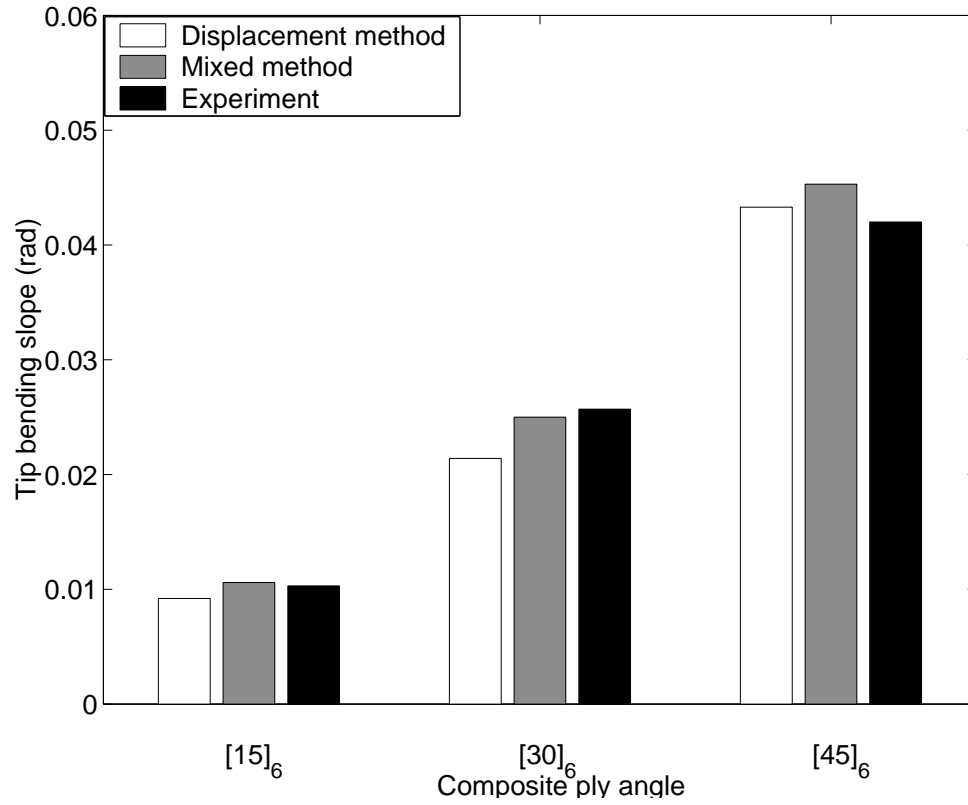


Figure 2.5: Tip bending slope of composite beams with flap-bending/torsion coupling under a unit tip flapwise bending force

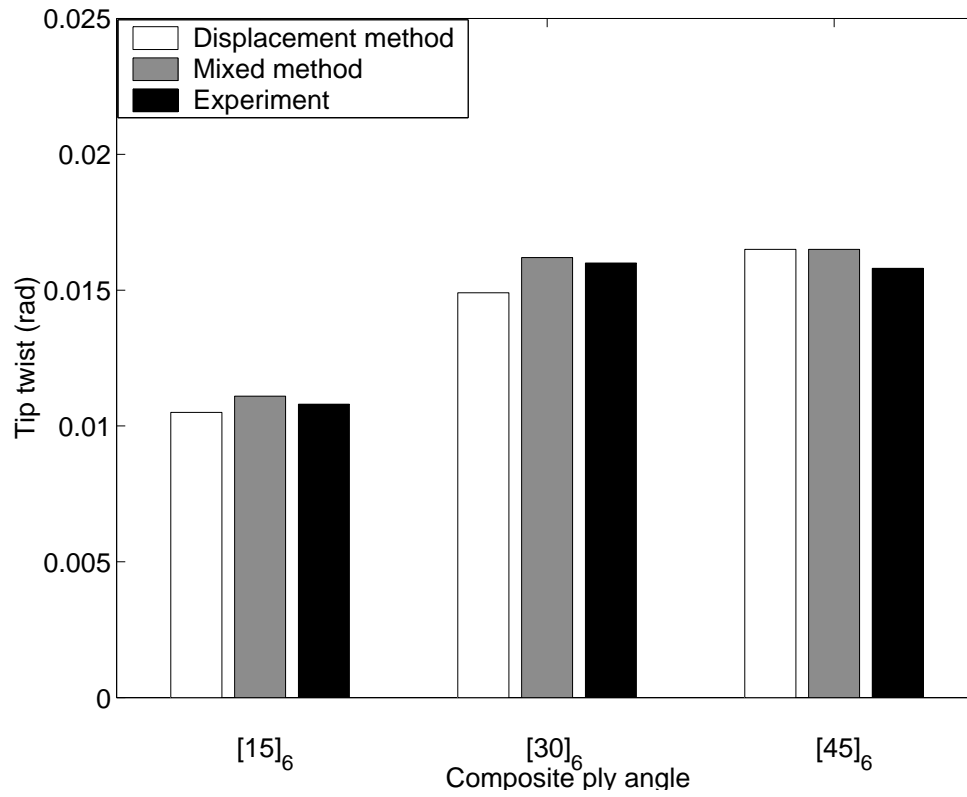


Figure 2.6: Tip twist of composite beams with flap-bending/torsion coupling under a unit tip torque

Chapter 3

Design of Mach Scale Composite

Tailored Rotor

Five sets of Mach scale composite tailored rotors were developed to study the effect of blade flap-bending/torsion couplings on the rotor vibratory hub loads. This chapter discusses the detailed design issues for these composite tailored rotors: design constraints, selection of composite material, design of blade cross section structure, design of blade root insert and leading edge weight, lay-up design of blade composite D-spar.

3.1 General Design Issues

Any new technology may not be easily transferred to the design of a new full scale helicopter rotor without a clear experimental validation. The use of small scale rotor models to achieve this verification is cost effective and also permits a much easier variation of model parameters to conduct a systematic design study.

Generally, there are three types of scaled rotor models: rigid models, Froude scale models and Mach scale models [4]. Rigid models simulate only the aerody-

dynamic profile of the full scale blade and are used to study the basic aerodynamic characteristics under ideal conditions. These models incorporate geometric details and are less expensive to fabricate than dynamically scaled models. Froude scale models are designed to match the centripetal acceleration field of a full scale rotor. If, in addition, the structural and inertial properties are correctly scaled to Froude scale, then the model blades will have the same steady deflection as full scale blades. Such model rotors are typically used for aeroelastic stability testing. In contrast to Froude scale models, Mach scale models are designed to match the tip Mach number of full scale rotors, thereby matching the effect of compressibility on the aerodynamics. Mach scale models, in conjunction with scaled structural and inertial properties are used to study rotor vibratory response, loads, and basic performance.

Small scale rotor models are unable to simultaneously satisfy multiple scaling parameters (such as Mach number, Froude number and Reynolds number, see Table 3.1) in air. However, in the heavy medium (such as Freon), it is possible to simultaneously match both Mach number and Froude number. The NASA Langley Transonic Dynamics Tunnel (TDT) can provide such a Freon test environment [106]. From Table 3.1, it is also seen that the model Reynolds number is lower than that of the full scale rotor by the geometric scale factor, in order to match the Mach number. Bernhard [107] presented a detailed discussion about these rotor scale issues in his dissertation.

The design of a new Mach scale model blade normally includes simulation of both aerodynamic and dynamic characteristics. The aerodynamic design decides blade general sizing, blade planform and airfoil sections [108, 109]. The blade dynamic design determines blade natural frequency placement and ro-

tor aeroelastic properties. A key issue of the dynamic design of the present Mach scale composite tailored blades is to simultaneously achieve large elastic couplings, while minimizing the frequency difference between the coupled and baseline blades. The reason for the latter is that changes in natural frequencies alter the overall dynamic response and can mask the effect of elastic coupling.

At the University of Maryland, several small scale rotor models have been fabricated, and tested in the Glenn L. Martin wind tunnel, such as rotors tested by Bi [110], Chen [111], Koratkar [112] and Roget [113]. Table 3.2 lists the main parameters and testing conditions of these rotor models. The nominal rotor speed of these rotors did not exceed 1900 rpm. In contrast, the present Mach scale composite rotors will be tested at higher rotor speeds (up to 2300 rpm), faster advance ratio (up to 0.38) and higher thrust levels. These target test conditions places significantly more stringent structural integrity design constraints on the rotor design.

3.2 Full Scale Rotor Analysis

Prior to the design and fabrication of Mach scale composite tailored rotors, a comparison study is performed for a full scale articulated rotor and its simulated configuration, in which blade elastic couplings are introduced. This study explores the impact of elastic couplings on the full scale rotor aeroelastic behavior and provides guidelines for the design of Mach scale composite tailored rotors.

3.2.1 Full Scale Rotors

In this study, the full scale rotor is an articulated rotor using the basic parameters of the UH-60 BLACK HAWK rotor (see Table 3.3) as baseline data. Two elastic coupling categories are examined: flap-bending/torsion coupling (FBT) and chordwise-bending/torsion coupling (CBT). The couplings can be positive and negative. Positive flap-bending/torsion coupling is defined as blade flap bending up resulting in blade nose down twist. Positive chordwise-bending/torsion coupling is defined as blade lag bending resulting in blade nose down twist. For each category, three blade coupling configurations are considered. They are: positive coupling along the whole blade span, negative coupling along the whole blade span, and spanwise mixed coupling with positive coupling over the outboard blade span and negative coupling over the inboard blade portion. Based on the ratio of blade coupling stiffness to blade flapwise stiffness in the previous work [104, 101, 105], the basic values of non-dimensional flap-bending/torsion stiffness and chordwise-bending/torsion coupling stiffness used for this study are assumed as 0.31 and 0.62 (normalized with respect to the baseline blade flapwise stiffness), respectively.

The baseline rotor blade does not have any elastic coupling. The coupled derivative rotors include a variety of different coupling configurations, and have the same blade geometry and similar natural frequencies to the baseline blade. UMARC was used to perform aeroelastic analysis of the full scale rotor.

3.2.2 Effect of Couplings on Blade Frequency and Mode Shape

Non-dimensional blade rotating frequencies for all rotor configurations are listed in Table 3.4, where abbreviation FBT and CBT represent flap-bending/torsion coupling and chordwise-bending/torsion coupling, respectively. P, N, and P/N represent positive, negative and mixed positive/negative spanwise coupling distributions. From Table 3.4, it is seen that despite the presence of different elastic couplings, there is very little difference between the natural frequencies of the baseline uncoupled blade and those of coupled blades. The difference is within 1.8% of the baseline frequencies. The small frequency variation with coupling precludes frequency shifts dominating the impact of composite coupling on rotor vibration characteristics.

For the articulated rotor, the first flap mode and the first lag mode are rigid modes. Elastic motion is seen in the second and higher modes. The second flap mode with flap and torsion motion is shown in Figure 3.1 for the baseline rotor and its flap-bending/torsion coupled configurations. It is seen that the elastic flap and torsion motions are structurally coupled. The torsion motion is significantly changed due to the introducing of flap-bending/torsion couplings, while the lag motion and the flap motion are same for all the blade configurations. For example, in Figure 3.1 for the negative flap-bending/torsion coupling case (FBT-N), the ratio of torsion deflection to the flap deflection is 4.4 at the blade tip, comparing with the value of 1.4 for the baseline uncoupled blade. Hence, even a small flap mode tip bending can produce large elastic twist at the tip of the coupled blade and change the twist distribution along the blade, because of the intrinsic structural flap-bending/torsion coupling. This change can significantly

affect blade response and loads.

Therefore, the changes in rotor vibration characteristics between the different coupled rotors are induced by changes in blade elastic response arising from the structural couplings rather than different frequencies.

3.2.3 Effect of Couplings on Vibratory Hub Loads

The 4/rev vibratory hub loads of baseline rotor are compared with those of coupled rotors in Figures 3.2 to 3.5 for two advance ratios ($\mu=0.12$ and 0.3) with $C_T/\sigma = 0.08$ and tip Mach number of 0.65. The forces are normalized with respect to the steady vertical force and the moments are normalized with respect to the steady torque. It is evident that the flap-bending/torsion coupling has a significant effect on 4/rev hub vibratory loads (see Figures 3.2 and 3.3). Compared with the values of the baseline rotor, the negative flap-bending/torsion coupling (FBT-N) decreases 4/rev drag force (F_{xH}^{4P}), 4/rev rolling moment (M_{xH}^{4P}) and 4/rev pitching moment (M_{yH}^{4P}), but increase 4/rev vertical force (F_{zH}^{4P}), 4/rev side force (F_{yH}^{4P}) and 4/rev torque (M_{zH}^{4P}) at the advance ratio μ of 0.12. The positive flap-bending/torsion coupling (FBT-P) decreases 4/rev torque (M_{zH}^{4P}), but increase other five vibratory load components. With the mixed positive/negative flap bending-torsion coupling (FBT-P/N), all 4/rev loads are reduced. The reduction in this case ranges from 9% to 14%, the maximum reduction obtained in the 4/rev pitching moment (M_{yH}^{4P}).

The 4/rev vibratory loads for the advance ratio μ of 0.3, are shown in Figure 3.3. The positive flap-bending/torsion coupling slightly decreases the 4/rev drag force (F_{xH}^{4P}), 4/rev vertical force (F_{zH}^{4P}), but increases the 4/rev side force (F_{yH}^{4P}) and 4/rev rolling moment (M_{xH}^{4P}). Again, the mixed flap-bending/torsion

coupling (FBT-P/N) exhibits an overall reduction of the vibratory loads for this advance ratio. A peak reduction of 23% is achieved in the side force (F_{yH}^{4P}).

Compared with the effect of flap-bending/torsion coupling, the impact of chordwise-bending/torsion couplings on the 4/rev vibratory hub loads is very small. As shown in Figures 3.4 and 3.5, the 4/rev vibratory loads of chordwise-bending/torsion coupled rotors have the same level as those of baseline uncoupled rotor in forward flight for the advance ratios of 0.12 and 0.3, just with slight changes in some cases. Smith and Chopra [74] showed the same effect of chordwise-bending/torsion coupling on a soft-inplane hingeless composite rotor. Hence, the present work will focus on the effect of flap-bending/torsion couplings.

3.3 Parameters of Mach Scale Composite Tailored Rotor

The design of Mach scale composite tailored rotor models was nominally based on the UH-60 BLACK HAWK rotor. Two primary design constraints are imposed by the available hub components and the wind tunnel test section. The Glenn L. Martin wind tunnel has a test section of 11×7.75 feet. The model rotor diameter is typically restricted to half (45% to 55%) of the wind tunnel width to avoid interference effects [114, 110]. This translates to a maximum rotor diameter of 4.95 to 6.05 feet. The existing articulated hub (see Figure 3.6) is a four-bladed, fully articulated rotor system with coincident flap and lead-lag hinges. Figure 3.7 shows a design drawing of the hub arm. It is seen that this hub has a 2.125 inch hinge offset.

Limited by these constraints, the diameter of Mach scale composite tailored rotor was determined to be 6 feet, resulting in a flap hinge offset of 5.9%. This hinge offset is still a typical value for an articulated rotor and close to the 4.7% hinge offset of the UH-60 rotor. The higher hinge offset of the model rotor results in a higher fundamental flap frequency of 1.05/rev than that of the UH-60 rotor (1.04/rev). However, the impact of the first flap frequency on the 4/rev vibratory hub loads is not critical.

The UH-60 BLACK HAWK standard rotor blade has a radius of 322 inches, a nominal chord of 20.76 inches, a rectangular blade planform with a swept tip and non-linear twist. The nominal operating speed is 258 rpm, resulting in a hover tip Mach number of 0.65. The main blade profile is a cambered SC1094R8 airfoil, whereas the outboard profile is an SC1095 airfoil. The Mach scale model rotor blade is nominally based on the UH-60 standard blade. In order to simplify fabrication, the blade design features a rectangular planform without tip sweep, a linear twist of -12 deg and a single airfoil section (SC1095). The Mach scale operating speed is 2300 rpm. It should be noted that the chord was increased to match that chord/radius ratio of the wide chord blade. Prior to this research only symmetric, untwisted rotor blades had been fabricated at the University of Maryland. The asymmetric SC1095 airfoil, with a relatively thin maximum thickness of 9.5%, the twist and the high operating speed present unique challenges in the design of tooling and structure of the model rotor blades. In addition the high operating speed significantly increased the requirements on the hydraulic drive system for the rotor test stand.

The main parameters of Mach scale composite tailored rotor are listed in Table 3.5.

3.4 Structural Design of Mach Scale Composite Tailored Blade

The primary structural design objective is to maintain structural integrity (i.e. provide adequate safety margin) at the maximum rotor speed, advance ratio and thrust test condition. As shown in Figure 3.8, the structure design of the present Mach scale composite tailored rotor blades comprises a composite D-spar (laid up on a foam core mandrel with embedded leading edge weights), an aft foam core, a composite weave skin and a composite blade root insert. The composite spar is the primary structural element of the blade, not only withstanding the blade loads, but also providing the desired elastic couplings. The leading edge weights are used to ensure correct chordwise mass balance for aeroelastic stability. The aft foam core and the blade skin are used to maintain the blade airfoil profile. The blade root insert is a connection to transfer blade loads to the hub. In this section the design process for the different sub-structure elements and the blade as a whole are presented in detail.

3.4.1 Composite Material Selection

Composite materials are made up of two or more distinct materials, usually the reinforcing fiber and the matrix. The fiber provides most of the stiffness and strength, and the matrix binds the fibers together providing load transfer between fibers and between the composite and the external supports.

The selection of the composite material often depends on the manufacturing process and the requirements of the structural performance.

Various manufacturing methods have been developed to build composite

structures and parts, such as wet lay-up, prepreg lay-up, bag molding, and filament winding [116]. They differ in the process to: place the fibers along the desired orientation, impregnate the fibers with the resin, consolidate the impregnated fibers to remove excess resin and air, cure the composite, and extract the composite from the mold.

The simple and common composite manufacturing method is to place the uncured composite material manually into a mold so that the material can be shaped into the final part. To reduce the handling difficulty of resin and fibers, composite prepregs are usually used. A prepreg consists of preimpregnated fibers with resin and cured slightly to increase its bond viscosity [117].

The prepregs are produced by a manufacturing company through a careful control of the resin and fiber ratio, and as such the properties of the prepreg are stable during its shelf life. In a prepreg, the fibers are usually arranged in a unidirectional tape or a woven fabric.

Using the unidirectional tape, the fibers within the composite layers can be easily tailored to an arbitrary orientation to meet the requirements of tailored composite structure. Hence an uni-directional prepreg tape, IM7/8552 graphite/epoxy [118], is selected to fabricate the present Mach scale composite tailored blades. The IM7/8552 graphite/epoxy prepreg tape is an amine-cured, toughened epoxy resin reinforced with unidirectional carbon fibers. Carbon has a significantly higher longitudinal elastic modulus than E-Glass and therefore can generate a considerably stronger bending-torsion coupling.

The IM7/8552 graphite/epoxy prepreg weave is used for the skin of the composite blade. It significantly improved the blade surface finishing quality and structural integrity.

3.4.2 Measurement of Composite Mechanical Properties

Mechanical Properties of Composite Material

Composite material properties depend upon the resin-to-fiber volume ratio, fiber type and resin type. Prediction of the material properties of a composite laminate from the elastic properties of its constituents (fiber and resin) is not very accurate by micromechanics formulation. It is more accurate to characterize composite material properties for initial design studies by performing standard tensile tests on sample coupons of the material.

There are four main mechanical properties for the analysis of composite structures. They are E_1 : the longitudinal tensile modulus in the direction of the fiber orientation (axis 1 in Figure 2.2); E_2 : the tensile modulus transverse to the fiber direction; G_{12} : in plane shear modulus and ν_{12} : major Poisson ratio. From these four parameters, the mechanical properties of composite can be obtained along arbitrary lamina axes (axes x and y in Figure 2.2) using Equations 2.1-2.8.

Material Test

Experimental measurement of the main mechanical properties of the IM7/8552 graphite/epoxy prepreg was carried out by the tensile testing of three sample coupons, using an MTS 810 Materials Test machine. Figure 3.9 shows the test setup. These coupons were fabricated from the IM7/8552 graphite/epoxy prepreg tape with the layups of $[0]_6$, $[90]_6$ and $[\pm 45]_{2s}$, respectively. One of the test coupon is shown in Figure 3.10. During the testing, three coupons were loaded in tension up to 4900 lbf (250 test points), 145 lbf (60 test points) and 100 lbf (30 test points), respectively, before they were damaged. The coupons were instrumented by four strain gages along the longitudinal and lateral di-

reactions (see Figure 3.10). The stains at each test point were measured and averaged. Four mechanical properties of the IM7/8552 graphite/epoxy prepreg can be derived from these measurements.

From the measurement of coupon $[0]_6$:

$$E_1 = \frac{F_1}{\epsilon_1 S} \quad (3.1)$$

From the measurement of coupon $[90]_6$:

$$E_2 = \frac{F_2}{\epsilon_2 S} \quad (3.2)$$

$$\nu_{12} = -\frac{\epsilon_2}{\epsilon_1} \quad (3.3)$$

From the measurement of coupon $[\pm 45]_{2s}$:

$$G_{12} = \frac{F_x}{2S(\epsilon_x - \epsilon_y)} \quad (3.4)$$

where S is the cross-section area of the coupon; F_1 , F_2 and F_x are tensile forces applied to the test coupons along the axes 1, 2 and x (see Figure 2.2), respectively; ϵ_1 , ϵ_2 , ϵ_x and ϵ_y are measured strains along the axes 1, 2, x and y , respectively. The mechanical properties of IM7/8552 prepreg tape obtained from Equation 3.1 to Equation 3.4 are listed in Table 3.6, and compared with those values in the product data sheet [118] and Ref. [107]. It is seen that the measured E_1 and E_2 are close to those values in the data sheet. Note that no values of the shear modulus G_{12} and the major Poisson ratio ν_{12} are provided in the production data sheet [118]. Ref. [107] estimated values of G_{12} and ν_{12} by micromechanics [115]. Both measured and estimated values of ν_{12} fall in an acceptable range. However, the estimated G_{12} of Ref.[107] has an obvious difference from the present measured value. The shear modulus normally depends

upon the resin-to-fiber volume ratio and the property of resin. It is quite challenging to describe the shear behavior of a unidirectional laminate with sufficient accuracy.

The measured material properties of IM7/8552 prepreg tape are used in the current research.

3.4.3 Structural Design of Composite Spar

The composite spar of blade is the primary structural element supporting the blade loads. Furthermore, the suitable orientations of the laminate in the spar are used to obtain the desired elastic flap-bending/torsion couplings. Two spar configurations were considered for the composite blade: one-cell rectangular box spar and two-cell D-spar. Two non-twisted sample blades with NACA0012 profile were fabricated to examine the structural integrity of these spar configurations.

One-Cell Composite Box Spar

It is easy to build a rectangular foam core and layup a one-cell box spar using composite lamina. With a balanced layup in all walls of the spar, there is no elastic coupling. When the top and bottom walls incorporate unbalanced layup, the flap-bending/torsion coupling can be achieved.

The cross section of a sample composite blade with one-cell rectangular box spar is shown in Figure 3.11(a). A mold with NACA0012 profile and 3 inch chord was used to build this blade. To provide the space for the composite box spar, the foam core had to be cut into four pieces. Because of the small thickness of this profile, it was difficult to obtain the desired shapes of these foam pieces.

This resulted in nonuniform pressure forces applied to the top and the bottom surfaces of the spar as the mold was fastened. Thus, it is seen that the cross section of spar does not retain the accurate rectangular shape after curing.

The Mach scale composite blade has an asymmetric SC1095 airfoil with 2.667 inch chord and a -12 deg pretwist. It will be more difficult to prepare the foam core parts with the desired shape and place the one cell box spar in the desired location.

Two-Cell Composite D-Spar

The D-spar is laid up on a foam core mandrel. This mandrel is created in several steps. First, a foam blank was sanded to obtain approximate shape of the airfoil profile. Then, this foam blank was heated up to the forming temperature using a mold. Finally, the foam core mandrel of the D-spar was cut from the cured foam core. Next, by assembling an unbalanced layup on top and bottom walls, the flap-bending/torsion coupling can be obtained. Alternating upper and lower spar layers were interlaced around the leading edge for structural integrity.

It is shown that a two-cell composite D-spar can maintain a good shape (see Figure 3.11(b)) after the curing process. Thus, the composite D-spar configuration is used for the present Mach scale composite tailored blade. The detailed layup design of composite D-spar will be determined later in this Chapter using an iteration process combining the structural analysis and comprehensive aeroelastic analysis.

3.4.4 Design of Composite Blade Root Insert

The blade root insert is the structural load transfer element between the blade and the attachment arm of the articulated hub, as shown in Figures 3.8 and 3.12. The blade loads are transferred from the blade spar, skin and foams to the root insert and finally to the hub.

Two designs of blade root inserts were considered: a pure composite insert (Root Insert A in Figure 3.12) and an aluminum insert (Root Insert B in Figure 3.12). The composite root insert A was fabricated with a $[0]_{42}$ layup of IM7/8552 graphite/epoxy prepreg, as shown in Figure 3.13, with the length of 2.2 inch and width of 0.5334 inch. The aluminum insert B is an aluminum sheet with a thickness of 0.15 inch, encased in IM7/8552 face sheets (with a layup of $[0]_{12}$). Insert A and B have the same overall dimensions.

To examine the strength and the structural integrity of these root inserts, two sample composite blades were fabricated (one each with the different insert) for tensile testing. The testing was carried out by the MTS material testing machine (the test results are shown in Figure 3.14). The sample blades have the same spar layup as those of Mach scale composite blades. The respective inserts were placed in a machined opening in the aft section of the root of the fore foam core section (see Figure 3.12), before wrapping the D-spar and complete assembly of the sample blade section. As such the root insert simply replaces a portion of the foam core mandrel for the D-spar.

The sample blade with aluminum inserts (insert B) was tested up to the tensile force of 4137 lbf, when skin damage was observed in the transition area between the insert and the foam (see Figure 3.15). The cause of the failure may be the high stress concentration in this area. This suggests that more

attention should be paid to this transition area during the fabrication process of a composite blade. The blade with the composite inserts (insert A) was loaded up to 4390 lbf without any visible damage on this blade.

During the tensile test, the first ply failure load of these blade inserts was also recorded. If the first ply failure load was defined as the load at the first acoustic energy release, the measured first ply failure loads were 2500 lbf for the composite insert (insert A) and 1600 lbf for the aluminum insert (insert B). The root centrifugal force at blade grip (radial location 7.5 inch) is calculated to be 1210 lbf for the Mach scale composite blades rotating at the nominal speed of 2300 rpm. It follows that insert A and B have respective first ply failure safety factors of 2.1 and 1.3.

From these measurements, it is shown that the pure composite insert A has a better performance than the aluminum insert B. Therefore, the pure composite root insert is chosen for the present Mach scale composite tailored blades.

3.4.5 Design of Leading-Edge Weight

Leading-edge weights are embedded in the blade to bring the blade cross-section center of gravity to the aerodynamic center (quarter chord). This is required for aeroelastic stability. In order to minimize the size of the leading edge weights, tungsten alloy (class IV, with a density of 18500 kg/m^3) was used to build the weights.

Two leading edge weight configurations were studied. For the first one (see Figure 3.16), tungsten rods (with a length of 2.4 inch and a diameter of 0.124 inch) are directly used as the leading edge weights. These rods are commercially available. Before the tungsten rods were inserted into the slots along the

leading edge of the blade fore foam core, they were covered by two IM7/8552 graphite/epoxy unidirectional prepreg strips. When heated in the mold, these two composite strips cured and bonded the leading edge rods with the foam core and the blade skin, like a retention cage, to keep the leading edge weight from tearing off at large rotating speeds. This is a simple way to prepare leading edge weights for integration into the blade. However, with the rods it is not easy to obtain a high quality leading edge, especially given the narrow asymmetric nose contour of the blade profile.

For the second configuration (see Figure 3.17), leading edge weights with the airfoil profile were designed. These parts were electron discharge machined (EDM) from a tungsten plate. Each fabricated piece has a length of 2.4 inch and a width of 0.124 inch. Six leading edge weights are embedded into each blade with a spanwise gap of 1.4 inch, as shown in Figure 3.8. Compared with the first configuration (tungsten rod with composite cage), this leading edge weight has several advantages: 1) it improves the structural integrity of blade leading edge, 2) it is easy to mill the leading edge slot in the fore foam core using a CNC machine, 3) it is easy to hold the chordwise location of the weight, when fastening the mold, and 4) it reduces the preparation time for wrapping a composite blade. Thus, the tungsten leading edge weight with the airfoil profile is used for the present Mach scale composite tailored blade.

3.5 Layup Design of Composite D-spar

Blade flap-bending/torsion couplings are introduced by using a desired layup and orientation of composite plies in the composite D-spar. An important as-

spect of the composite D-spar design is to simultaneously achieve large elastic couplings, suitable frequency placement, and minimum stiffness difference between the baseline uncoupled blade and the coupled blades. Two sequential analysis tools were used to design the D-spar: the composite cross-section structural tool (required for computing blade section properties, including elastic coupling terms, for a given unbalanced spar layup) and UMARC for the subsequent comprehensive aeroelastic analysis to estimate the impact of elastic coupling on vibration. Figure 3.18 shows the flow chart of iteration design process for composite D-spar. The blade structural properties include axial stiffness (EA), lag stiffness (EI_z), flapwise stiffness (EI_y), torsion stiffness (GJ), flap-bending/torsion coupling stiffness (EFT) and blade mass. There are three check points for the D-spar structural design: 1) minimum stiffness difference between the baseline blade and the coupled blade, 2) validation of the structural analysis (checked by the bench-top test of sample blades), and 3) good structural integrity (checked by the hover rotating test of sample blades). Then, the blade structural properties are used as the input data for UMARC to predict blade frequencies and vibratory hub loads. The objective of UMARC analysis is not only to check the suitable frequency placements, but also to seek the maximum reduction of 4/rev vibratory hub loads with suitable flap-bending/torsion coupling value and distribution.

To study the structural behavior of these composite tailored blades with D-spar, the variation of the structural stiffness with fiber orientation angles in the D-spar was analyzed. Blade cross-section stiffnesses of a baseline blade and a blade with flap-bending/torsion coupling are shown in Figures 3.19-3.21. The layups of these blades are listed in Table 3.7. Note that fiber orientation angle

is defined as positive for the top wall of the D-spar when angled outboard from trailing to leading edge (see Figure 3.22). The same fiber orientation is defined as negative for the bottom wall of the spar. In both blade configurations, the D-spar web is located at 33% chord. It is seen that the structural stiffnesses vary significantly with the spar orientation angle. The difference in torsion stiffness between the baseline uncoupled blade and the coupled blade becomes larger with the increasing of fiber orientation angle, while the flapwise stiffness difference remains small even with a large orientation angle. When the angle is small (below 30°), the torsion stiffness decreases and the flapwise stiffness increases with the decrease of the spar orientation angle, θ . It is also evident in Figure 3.21 that the largest flap-bending/torsion coupling is achieved with a spar fiber angle of around 20° . From these figures, it is seen that for a small scale rotor, there is limited design flexibility to simultaneously meet the primary targets.

Before rotor aeroelastic analysis is performed, several pretwisted sample composite blades were fabricated and tested to evaluate the structural analysis of the composite D-spar. One composite coupled blade has a layup of $[33]_4$ spar, ± 45 skin and ± 33 web (35% chord). A bench-top shaker test (see Chapter 5) was carried out to measure the flapwise natural frequencies of this blade. The measurements are compared with the predicted values, plotted in Figure 5.16. It is seen that the agreement between the analysis and the experimental data is good.

Two sample blades with a layup of $[33]_4$ spar, ± 45 skin and ± 33 web (35% chord) were also selected to form a two-blade rotor. This rotor was successfully rotated up to 2300 rpm on a hover stand to examine the blade structural integrity.

Following the structural analysis of the composite D-spar, comprehensive

aeroelastic analysis (using UMARC) of the composite tailored rotor is performed to determine suitable ply lay-up of composite D-spar and coupling distribution along the blade span. In this design phase, there are two check points: suitable blade frequency placement and minimum 4/rev vibratory hub loads with desired flap-bending/torsion coupling configuration.

After the iteration design process, five flap-bending/torsion coupling configurations of Mach scale composite rotor are finally determined, see Figure 3.23. Positive flap-bending/torsion coupling of blade is defined as flap up bending resulting in a nose down twist. The first blade is a baseline blade with no coupling, the second and third blades exhibit spanwise uniform flap-bending/torsion coupling only (with the positive coupling designated FBT-P and the negative coupling designated FBT-N), and the last two blades feature spanwise segmented flap-bending/torsion couplings (designated FBT-P/N and FBT-P/0/N respectively, also referred to as mixed coupling rotors). Specifically, FBT-P/N incorporates a spanwise segmented coupling that is positive outboard and negative inboard; and FBT-P/0/N has a spanwise segmented coupling that is positive outboard, uncoupled in the midspan, and negative inboard. All these coupled blades have same value of coupling. The lay-up of these Mach scale composite tailored blades is tabulated in Table 3.8. The blade stiffness properties are listed in Table 3.9.

The fan plots of the Mach scale composite rotors are shown in Figure 3.24 and the natural frequencies at nominal rotor operating speed 2300 rpm are listed in Table 3.10. It is evident that the effect of the desired flap-bending/torsion coupling on the frequency placement is very small. The largest frequency difference between the mixed coupled (FBT-P/N) blade and the baseline blade is

2.5% in the torsion frequency. The relatively small frequency variation with coupling precludes frequency shifts dominating the impact of composite coupling on vibration characteristics. Figure 3.25 shows the mode shapes for the baseline and coupled rotor blades. The effect of the coupling into the torsion response and the effect of spanwise segmentation are clearly noticeable.

The predicted non-dimensional 4/rev vibratory hub loads for these model rotors are presented in Figure 3.26 and Figure 3.27, for advance ratios μ of 0.12 and 0.33, respectively. The rotor speed is 2300 rpm and thrust level C_T/σ is 0.08. The maximum vibratory load reduction is achieved with the mixed flap-bending/torsion coupled rotors. For both advance ratios, the mixed positive/negative couplings reduce all 4/rev hub loads, compared with the uncoupled baseline rotor. For example, for the spanwise triple-segmented coupling blade (FBT-P/0/N), the 4/rev vertical shear force is reduced by 10% at the advance ratio of 0.33; for the spanwise dual-segmented coupling blade (FBT-P/N), the 4/rev rolling moment is reduced by 25% and the head moment by 22% at the advance ratio of 0.33. Detailed percentage reductions of 4/rev vibratory hub loads of the mixed flap-bending/torsion coupled rotors with respect to the baseline rotor are listed in Table 3.11.

Table 3.1: Scaling parameters of small scale rotor

Ratio of model/full scale	Mach scale	Froude scale
Length parameter	S	S
Rotor radius	S	S
Rotor speed	$1/S$	$1/S^{\frac{1}{2}}$
Mach number	1	$S^{\frac{1}{2}}$
Froude number	$1/S$	1
Reynolds number	S	$S^{\frac{2}{3}}$

Table 3.2: Three previous model tests in the Glenn L. Martin Wind Tunnel

	Ref. [110]	Ref. [111]	Ref. [112]
Hub	articulated	bearingless	bearingless
Rotor diameter (ft)	5.4	6.0	5.0
Solidity	0.098	0.1061	0.1273
Rotor speed (rpm)	1860	875	1800
Tip Mach No.	0.5	0.25	0.45
Max. advance ratio, μ	0.25	0.33	0.3
Max. wind speed (mph)	89	62	96
Max. C_T/σ	0.085	0.012	0.047

Table 3.3: Basic parameters of the UH-60 BLACK HAWK rotor

Rotor diameter (feet)	53.67
Number of blades	4
Solidity	0.0826
Speed (rpm)	258
Hover tip Mach number	0.65
Blade airfoil	SC1095/SC1094R8
Blade chord (inch)	20.76
Twist	non-linear
Hinge offset	4.7%

Table 3.4: Non-dimensional blade natural frequencies of a full scale baseline articulated rotor and its simulated composite coupled derivatives (FBT: flap-bending/torsion coupling, CBT: chordwise-bending/torsion coupling, P: positive, N: negative, P/N: positive/negative)

Mode	Baseline	FBT-P	FBT-N	FBT-P/N	CBT-P	CBT-N	CBT-P/N
Lag 1	0.271	0.271	0.271	0.271	0.271	0.271	0.271
Flap 1	1.036	1.036	1.036	1.036	1.036	1.036	1.036
Flap 2	2.747	2.741	2.722	2.729	2.747	2.747	2.747
Flap 3	4.516	4.507	4.499	4.520	4.565	4.536	4.520
Torsion 1	4.229	4.195	4.261	4.150	4.170	4.182	4.197

Table 3.5: Parameters of Mach scale composite rotor

Rotor diameter (feet)	6
Number of blades	4
Solidity	0.0943
Lock number	5.93
Mass (slug/ft)	0.0047
Inertia, mk_{m1}^2 , mk_{m2}^2	0.0000046, 0.00045
Speed (rpm)	2300
Hover tip Mach number	0.65
Blade airfoil	SC1095
Blade chord (inch)	2.667
Twist (deg)	-12
Hinge offset	5.9%

Table 3.6: Mechanical properties of IM7/8552 graphite/epoxy unidirectional prepreg tape

	Measurement	Ref. [118]	Ref. [107]
0° tensile modulus (E_1), <i>GPa</i>	169.6	164.1	164.1
90° tensile modulus (E_2), <i>GPa</i>	10.3	11.7	11.7
in plane shear modulus (G_{12}), <i>GPa</i>	8.3	NA	11.0
Poisson ratio (ν_{12})	0.34	NA	0.31
cured ply thickness, <i>inch</i>	0.0069	0.007	0.007
area weight, <i>kg/m²</i>	0.2891(after curing)	0.2946	0.2946

Table 3.7: Layup of composite blade with two-cell D-spar

Skin	$[\pm 45]$ weave
Baseline spar	top: $[\mp \theta]_s$; bottom: $[\pm \theta]_s$
Coupled spar	top: $[\theta]_4$; bottom: $[-\theta]_4$
Web	$[\pm \theta]$

Table 3.8: Skin, spar and web layups of Mach scale composite blades

Skin layup	$[\pm 45]$ weave
Baseline spar	top: $[\pm \theta_m]_s$; bottom: $[\mp \theta_m]_s$
Positive flap-bending/torsion coupled spar	top: $[\theta_n]$; bottom: $[-\theta_n]$
Negative flap-bending/torsion coupled spar	top: $[-\theta_n]$; bottom: $[\theta_n]$
Web	$[\pm \theta_p]$
Web location	33% chord
Composite material	<i>IM7/8552</i> graphite/epoxy

Table 3.9: Normalized cross-section stiffness of Mach scale composite tailored blade, with respect to baseline flap stiffness

Blade	Flap stiffness	Torsion stiffness	Coupling stiffness
baseline	1.	0.838	0
flap-bending/torsion coupling	0.964	0.829	0.291

Table 3.10: Non-dimensional natural frequencies of Mach scale composite tailored at 2300 rpm

	Baseline	FBT-P/N	FBT-P/0/N	FBT-N	FBT-P
Lag 1	0.327	0.327	0.327	0.327	0.327
Flap 1	1.052	1.052	1.052	1.052	1.052
Flap 2	2.673	2.642	2.652	2.640	2.640
Flap 3	4.852	4.801	4.925	4.730	4.730
Torsion 1	4.630	4.511	4.445	4.607	4.607

Table 3.11: Predicted reduction (percentage) of 4/rev vibratory hub loads of composite rotor with mixed flap-bending/torsion couplings ($C_T/\sigma = 0.08$; μ : advance ratio; F_{xH}^{4P} : 4/rev drag force, F_{yH}^{4P} : 4/rev side force, F_{zH}^{4P} : 4/rev vertical force, M_{xH}^{4P} : 4/rev rolling moment, M_{yH}^{4P} : 4/rev pitching moment, M_{zH}^{4P} : 4/rev torque, F_{iH}^{4P} : $(F_{xH}^{4P^2} + F_{yH}^{4P^2})^{0.5}$, M_{hH}^{4P} : $(M_{xH}^{4P^2} + M_{yH}^{4P^2})^{0.5}$)

Spanwise dual-segmented coupling (FBT-P/N)								
μ	F_{xH}^{4P}	F_{yH}^{4P}	F_{zH}^{4P}	M_{xH}^{4P}	M_{yH}^{4P}	M_{zH}^{4P}	F_{iH}^{4P}	M_{hH}^{4P}
0.12	10	17	3	18	22	6	18	21
0.33	27	8	8	25	12	10	20	22
Spanwise triple-segmented coupling (FBT-P/0/N)								
μ	F_{xH}^{4P}	F_{yH}^{4P}	F_{zH}^{4P}	M_{xH}^{4P}	M_{yH}^{4P}	M_{zH}^{4P}	F_{iH}^{4P}	M_{hH}^{4P}
0.12	4	18	8	23	16	12	16	20
0.33	32	11	10	16	20	14	24	17

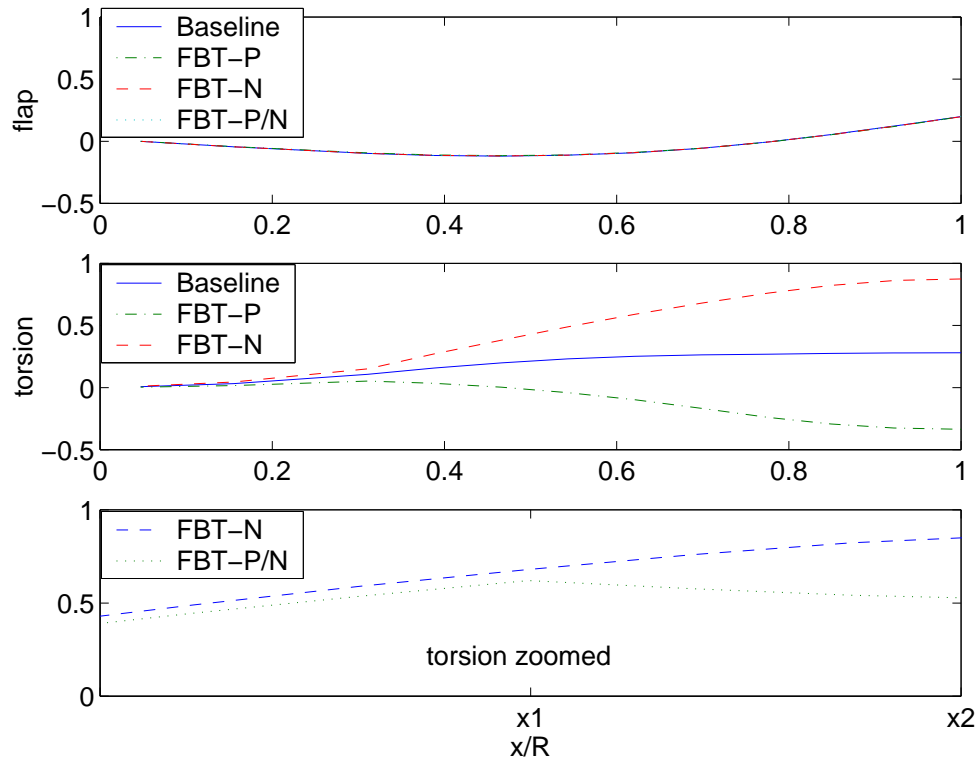


Figure 3.1: The second flap mode shape of full scale articulated rotors (FBT: flap-bending/torsion coupling, P: positive, N: negative, P/N: positive/negative)

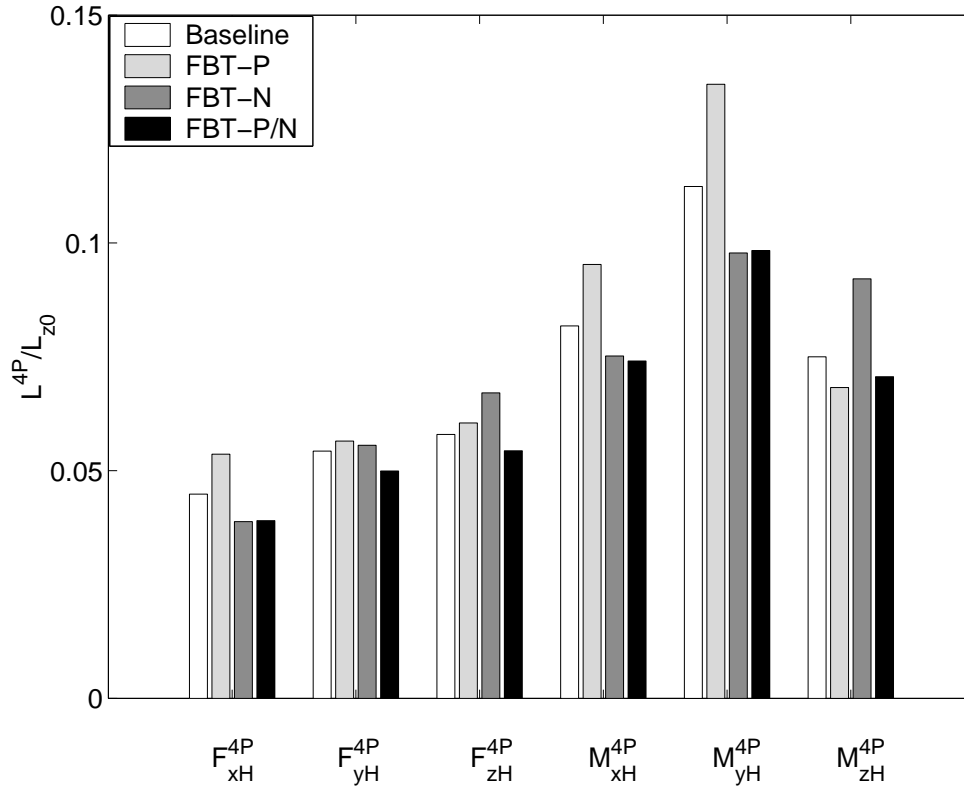


Figure 3.2: 4/rev vibratory hub loads of a full scale baseline rotor and its simulated derivatives with flap-bending/torsion coupling ($\mu = 0.12, C_T/\sigma = 0.08$; F_{yH}^{4P} : 4/rev side force, F_{zH}^{4P} : 4/rev vertical force, M_{xH}^{4P} : 4/rev rolling moment, M_{yH}^{4P} : 4/rev pitching moment, M_{zH}^{4P} : 4/rev torque)

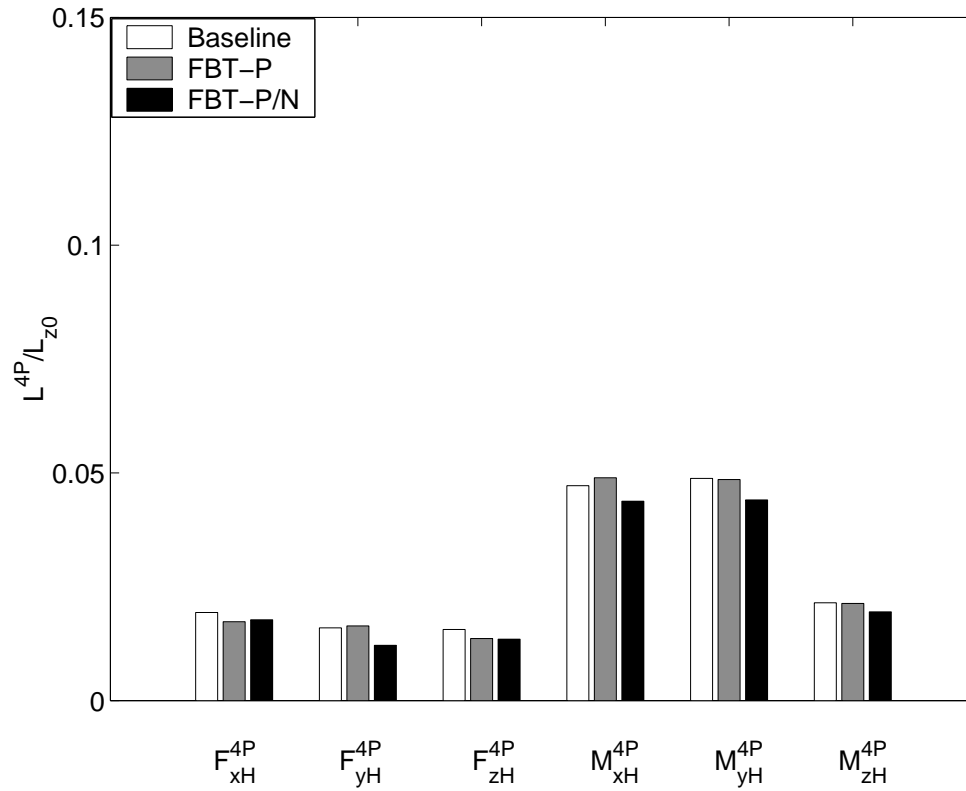


Figure 3.3: 4/rev vibratory hub loads of a full scale baseline rotor and its simulated derivatives with flap-bending/torsion coupling ($\mu = 0.3, C_T/\sigma = 0.08$)

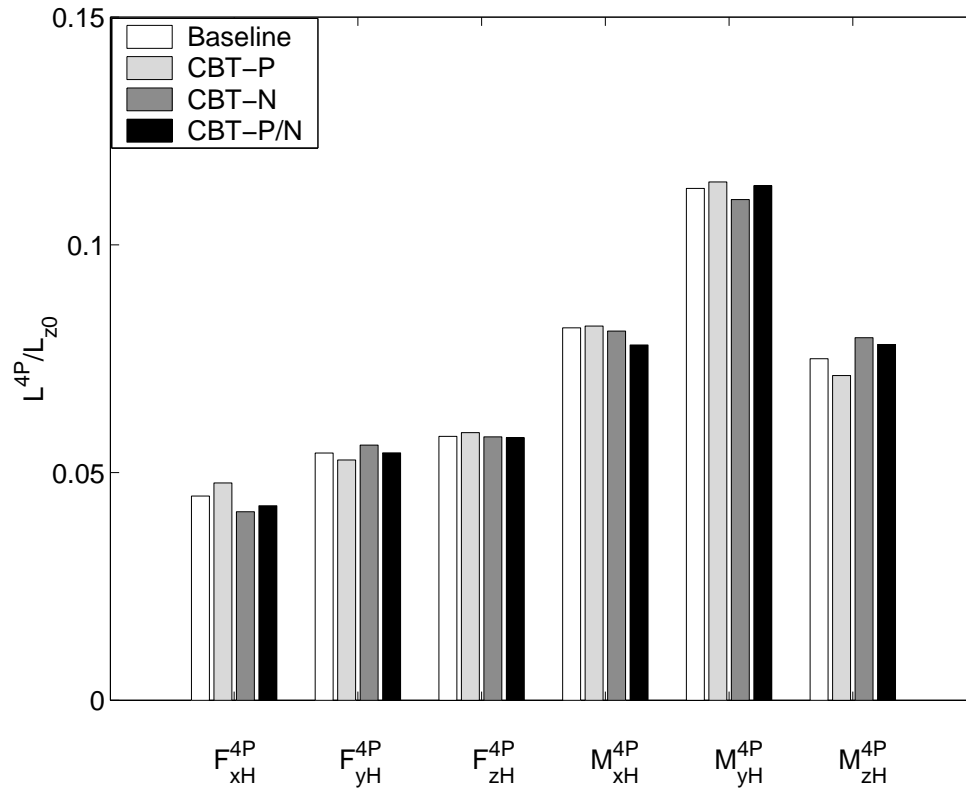


Figure 3.4: 4/rev vibratory hub loads of a full scale baseline rotor and its simulated derivatives with chordwise-bending/torsion coupling ($\mu = 0.12, C_T/\sigma = 0.08$)

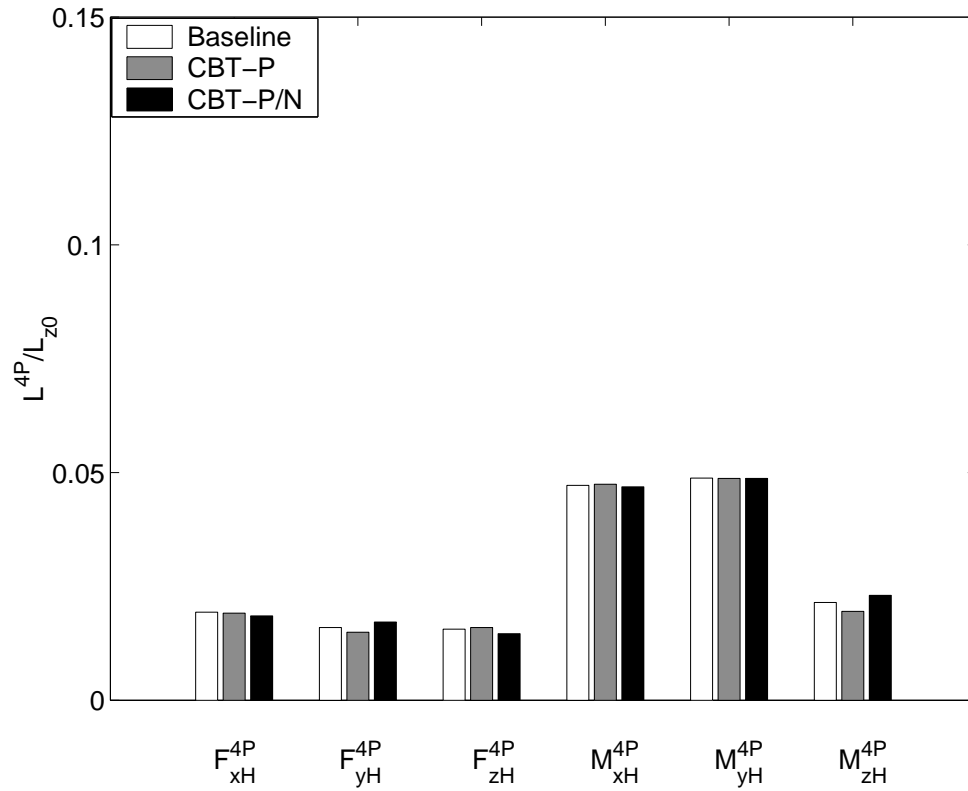


Figure 3.5: 4/rev vibratory hub loads of a full scale baseline rotor and its simulated derivatives with chordwise-bending/torsion coupling ($\mu = 0.3, C_T/\sigma = 0.08$)

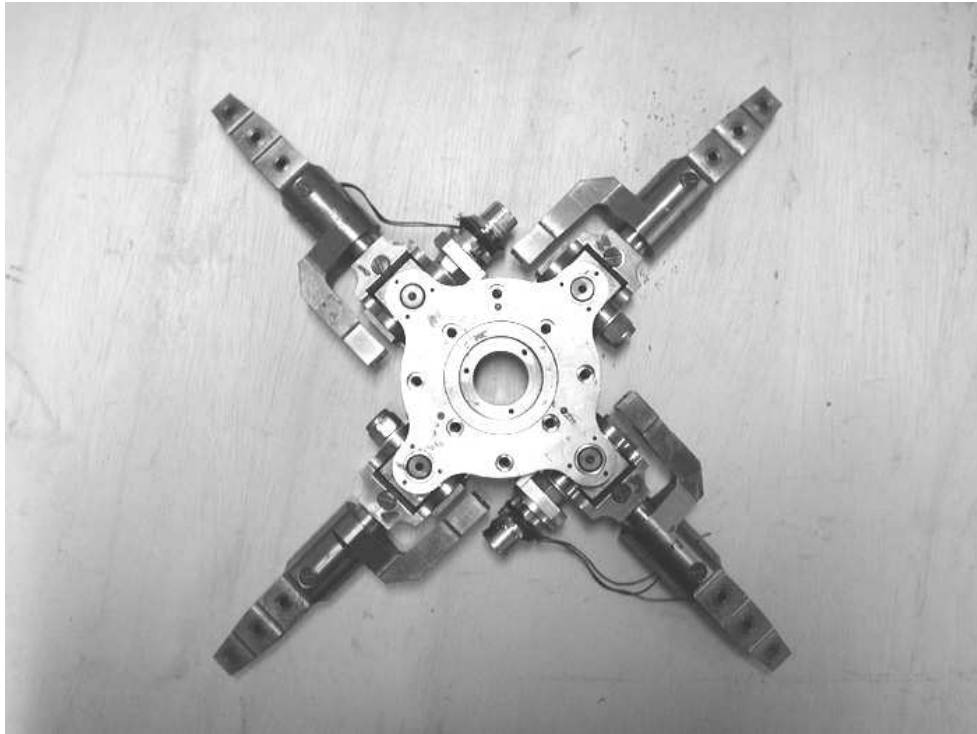


Figure 3.6: Articulated rotor hub

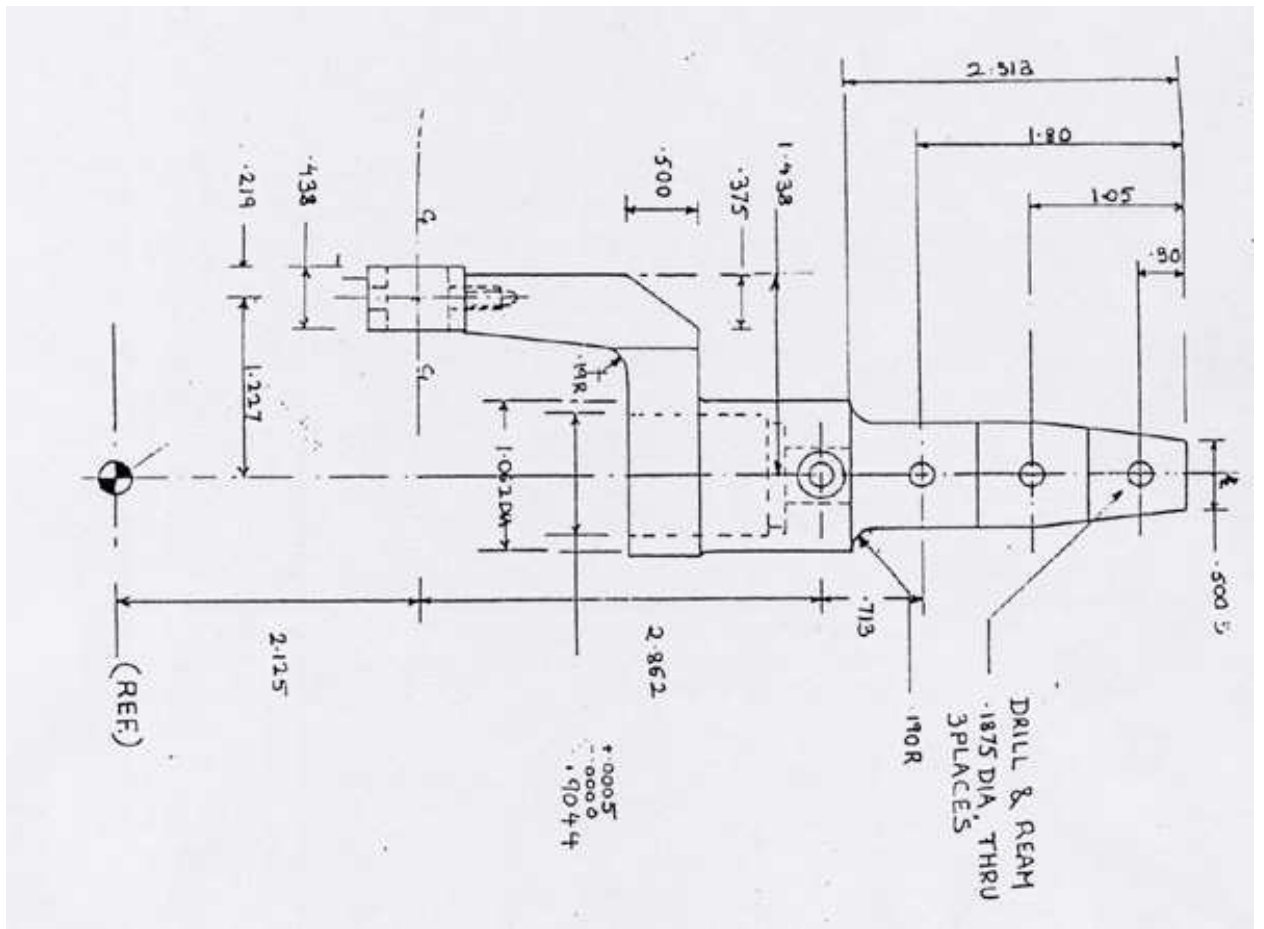
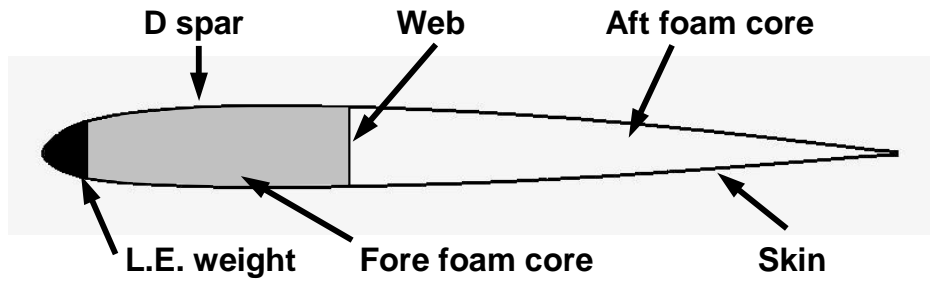
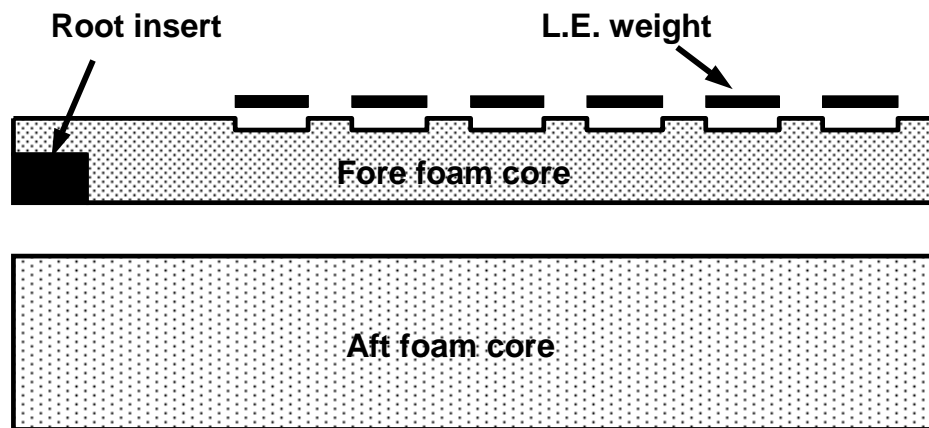


Figure 3.7: Design drawing of an articulated hub arm



a) Chordwise structure



b) Spanwise structure

Figure 3.8: Structure of Mach scale composite tailored blade

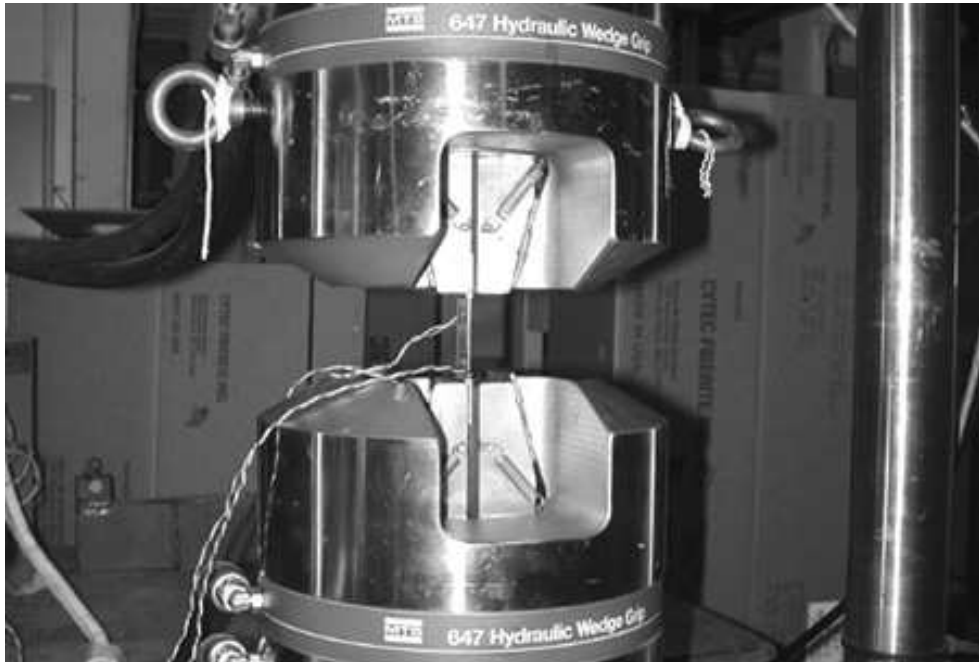


Figure 3.9: Material test of IM7/8552 prepreg

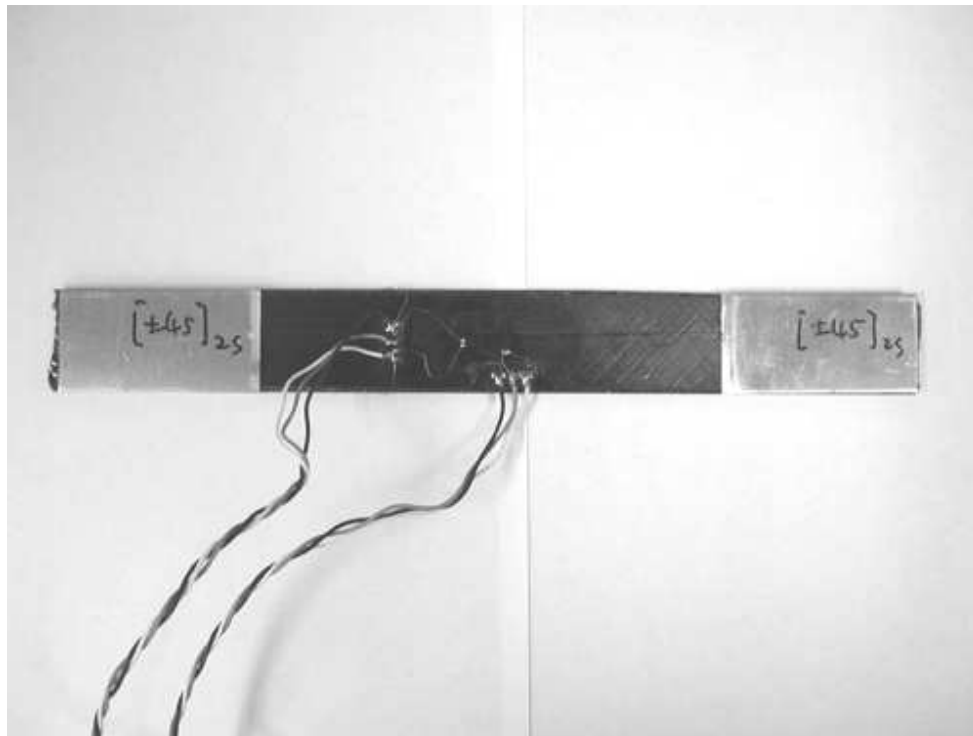


Figure 3.10: IM7/8552 test coupon with the layup of $[\pm 45]_{2s}$

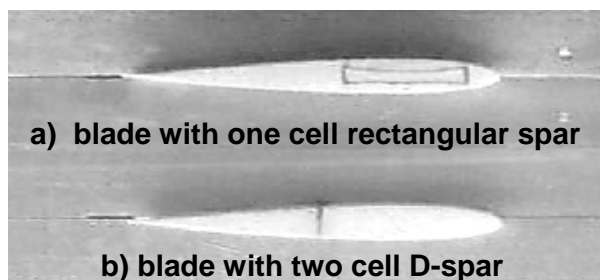
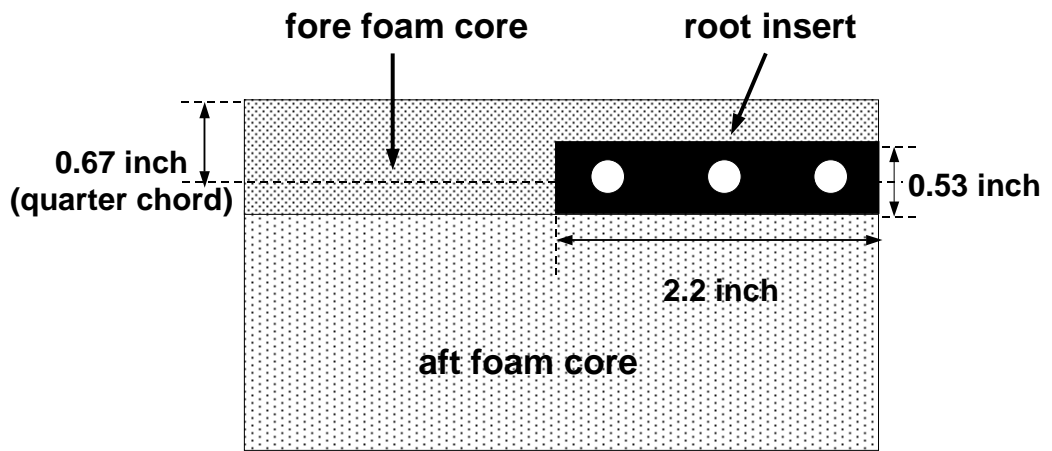
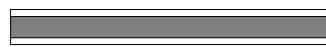


Figure 3.11: Composite blade cross-sections with one-cell box spar and two-cell D-spar



Root insert A



Root insert B

Figure 3.12: Blade root insert details

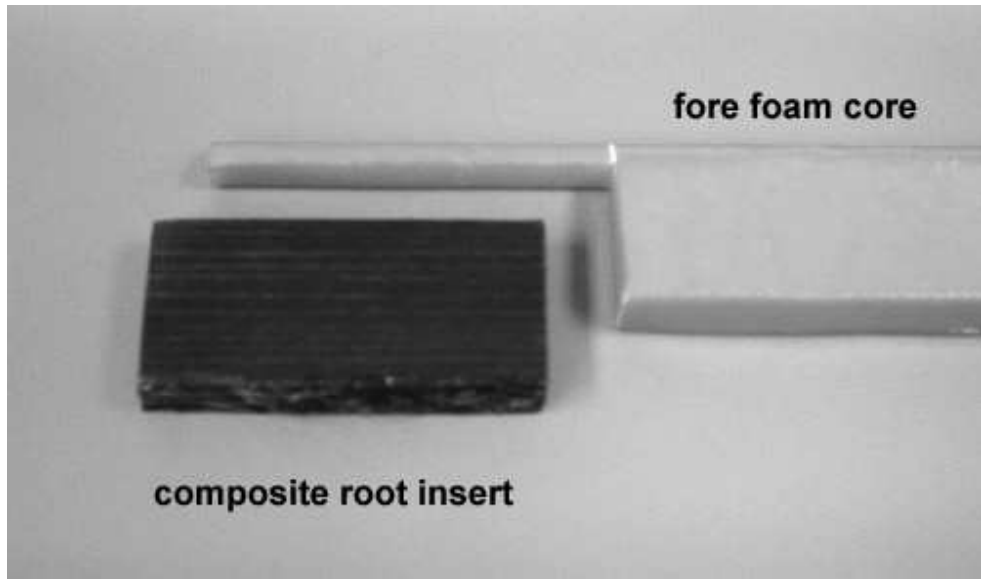


Figure 3.13: Composite root insert

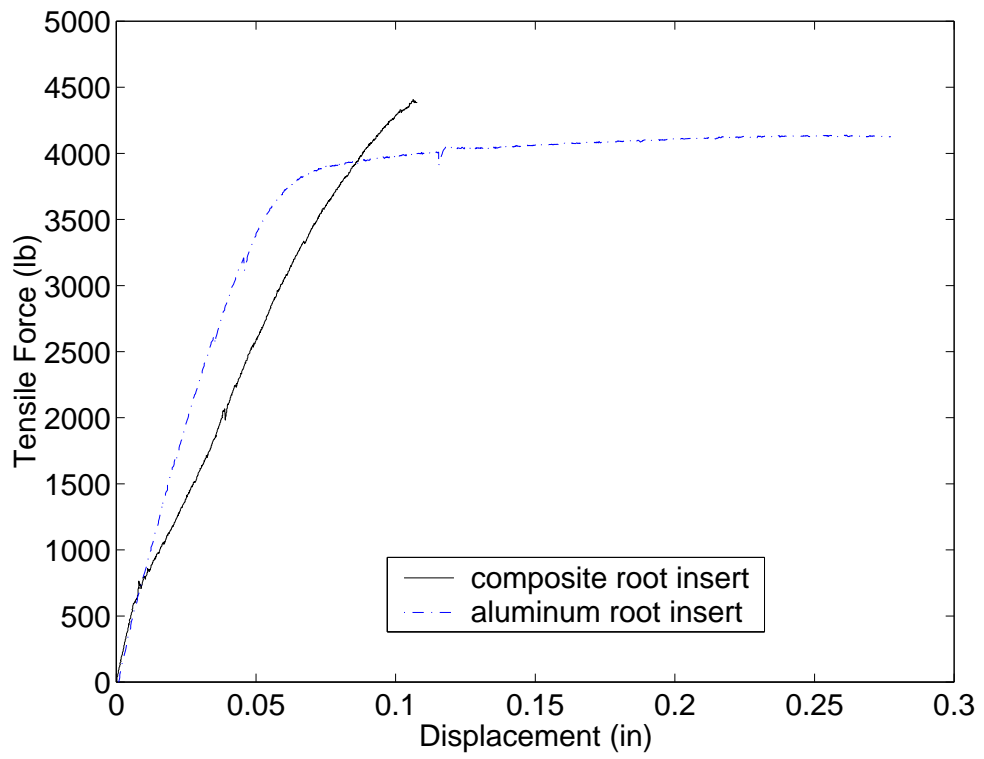


Figure 3.14: Tensile test results of blade root inserts

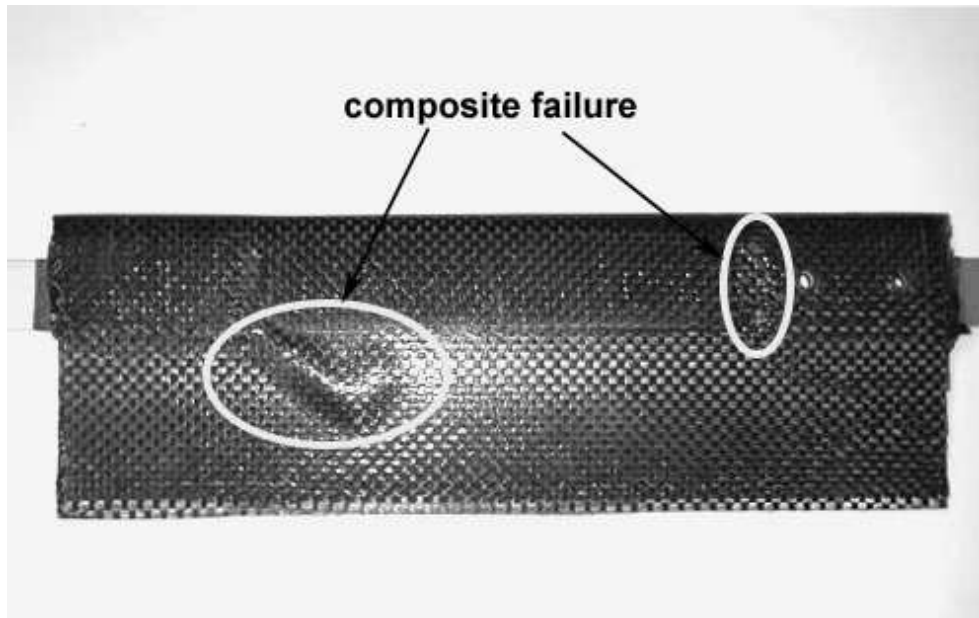


Figure 3.15: Failure of a composite blade with aluminum root insert

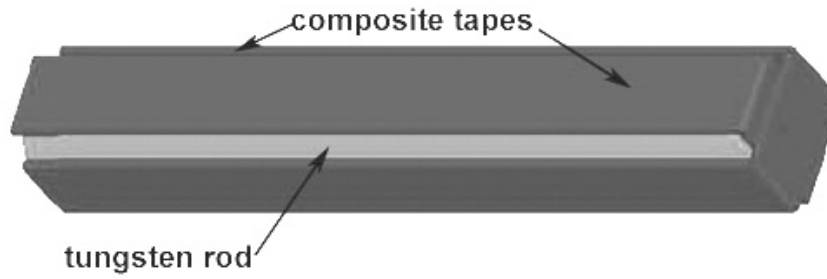


Figure 3.16: Tungsten rod with composite cage



Figure 3.17: Tungsten leading edge weight with airfoil profile

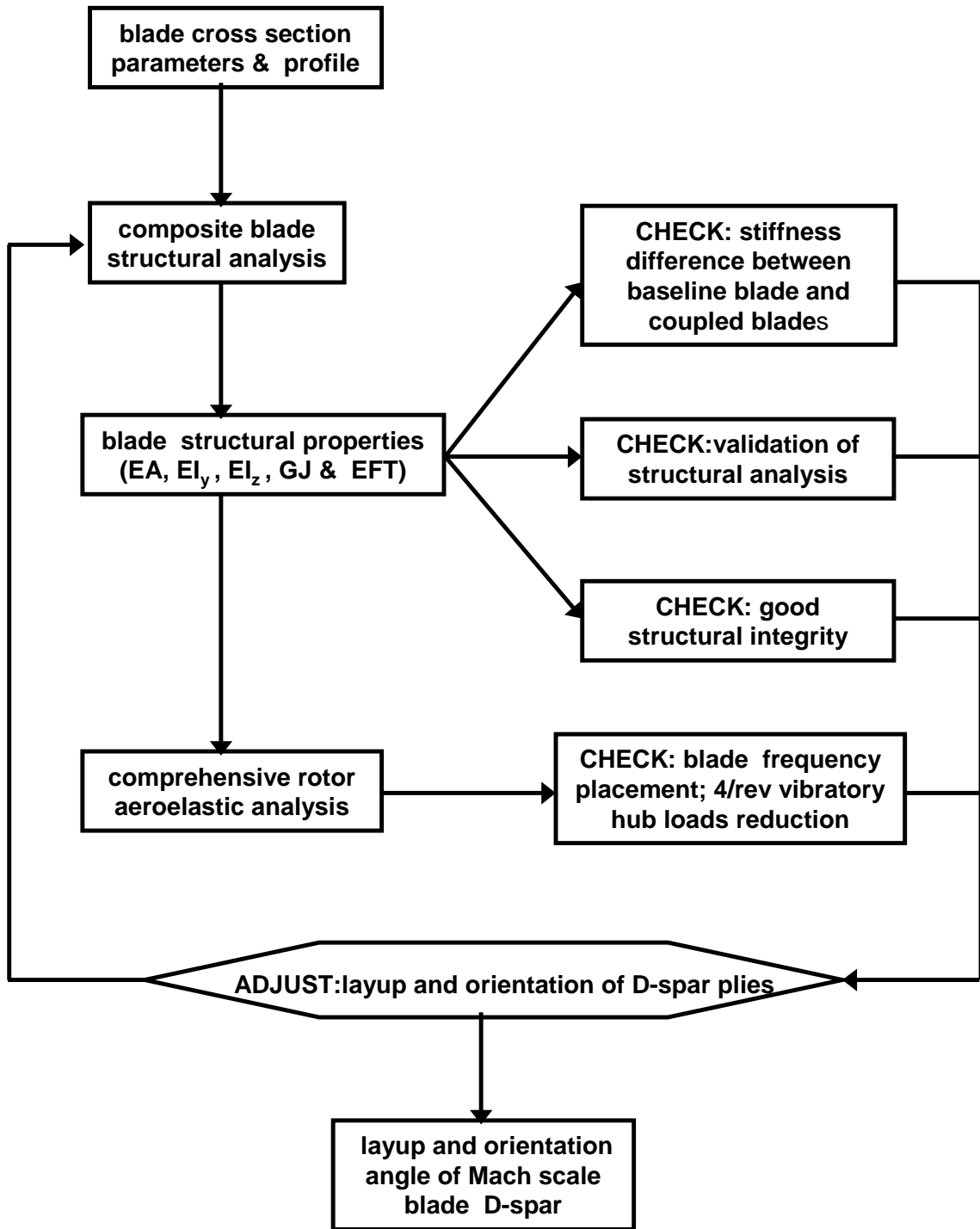


Figure 3.18: Design flow chart of composite D-spar

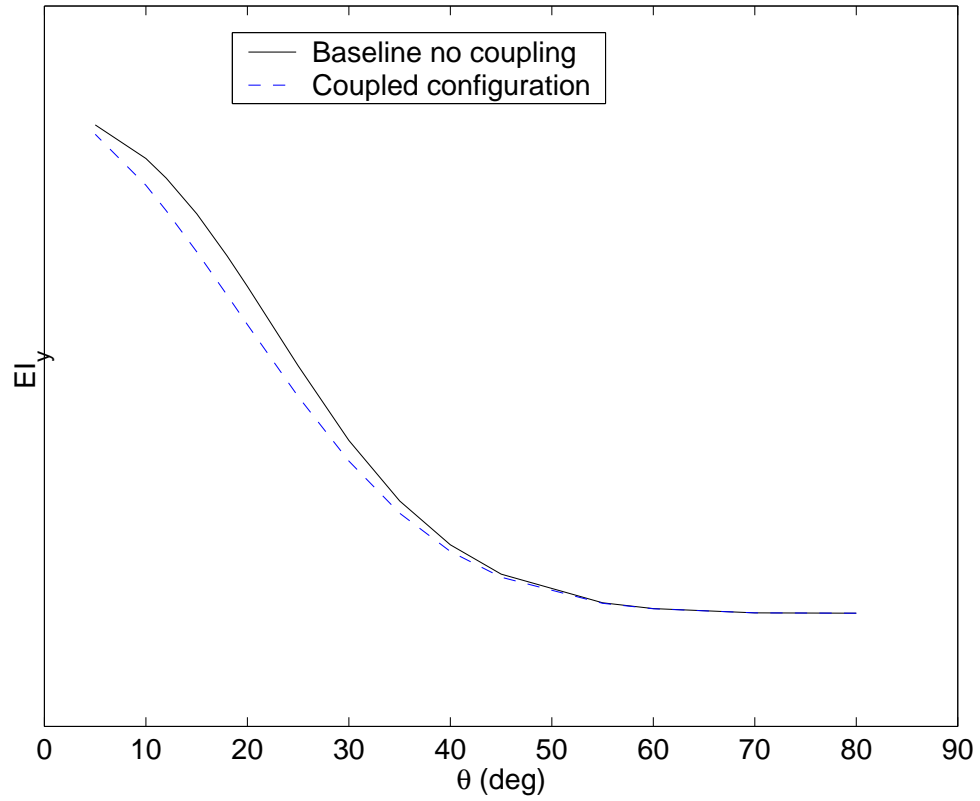


Figure 3.19: Flapwise stiffness (EI_y) of composite tailored blade versus fiber orientation angle of the D-spar

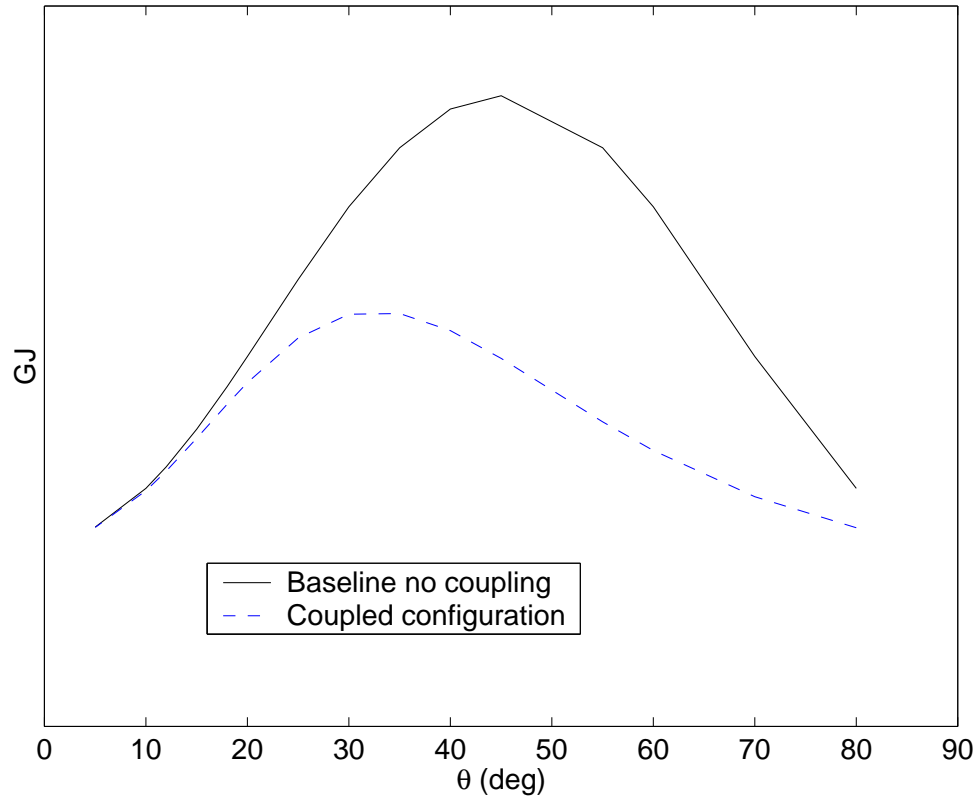


Figure 3.20: Torsion stiffness (GJ) of composite tailored blade versus fiber orientation angle of the D-spar

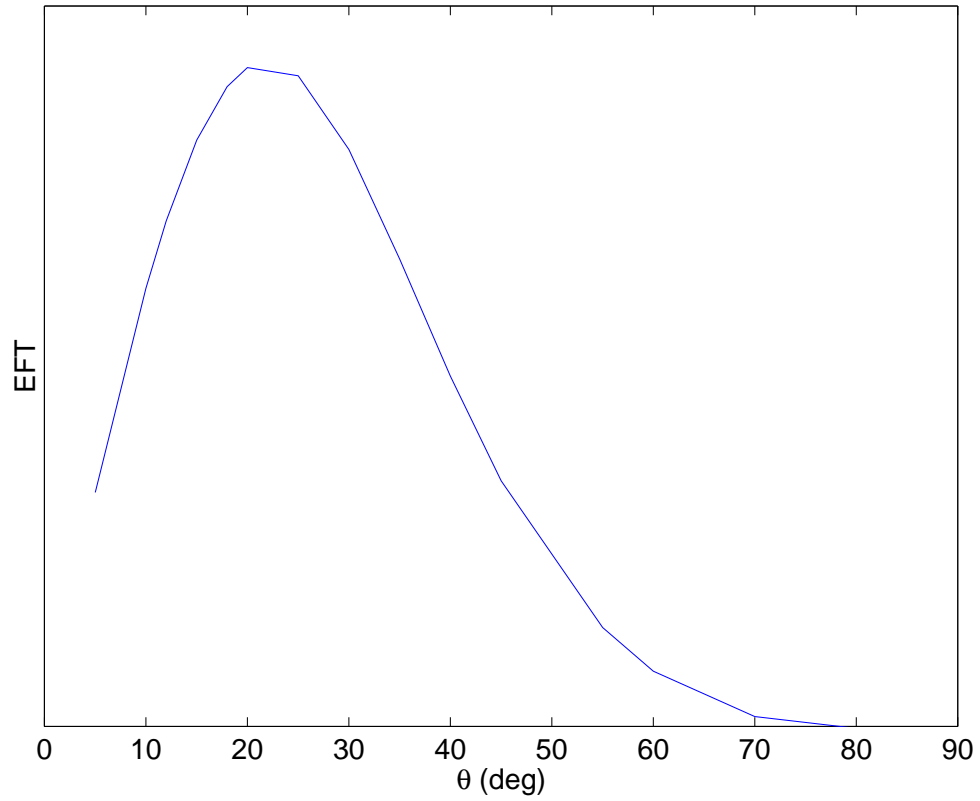


Figure 3.21: Flap-bending/torsion coupling stiffness (EFT) of composite tailored blade versus fiber orientation angle of the D-spar

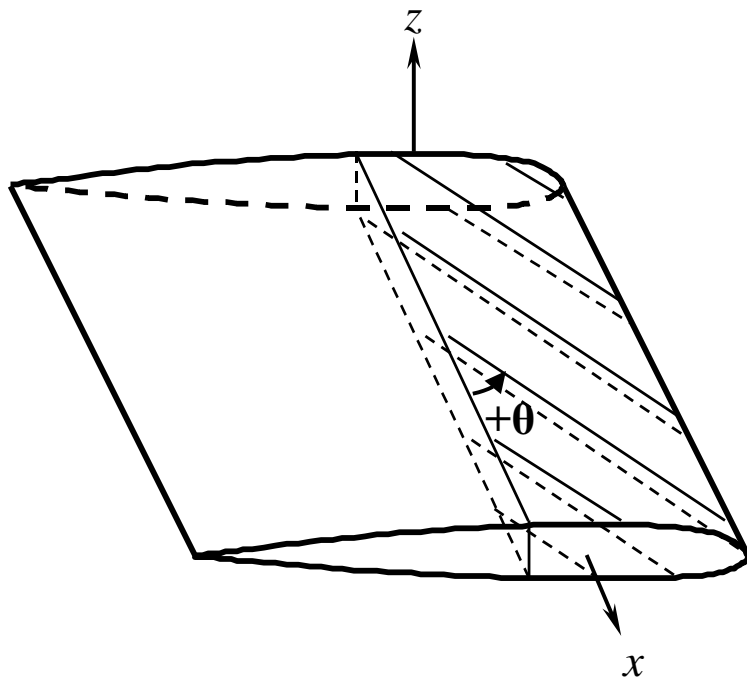


Figure 3.22: Definition of fiber orientation angle

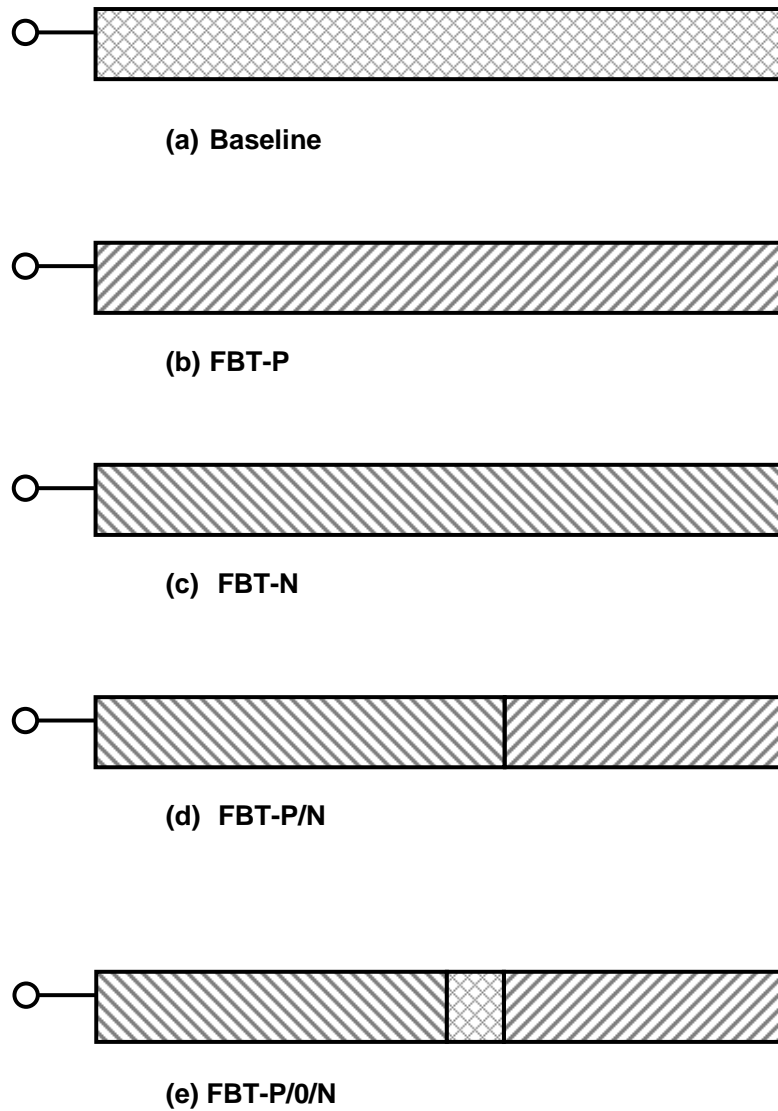


Figure 3.23: Lay-up of different composite tailored blade configurations (top view of D-spar). FBT:flap-bending/torsion coupling; P: positive coupling; N: negative coupling; 0: no coupling; (a) baseline uncoupled blade; (b) FBT-P uniform positive coupling; (c) FBT-N uniform negative coupling; (d) FBT-P/N spanwise segmented coupling (positive outboard and negative inboard); (e) FBT-P/0/N spanwise segmented coupling (positive outboard, uncoupled midspan, negative inboard)

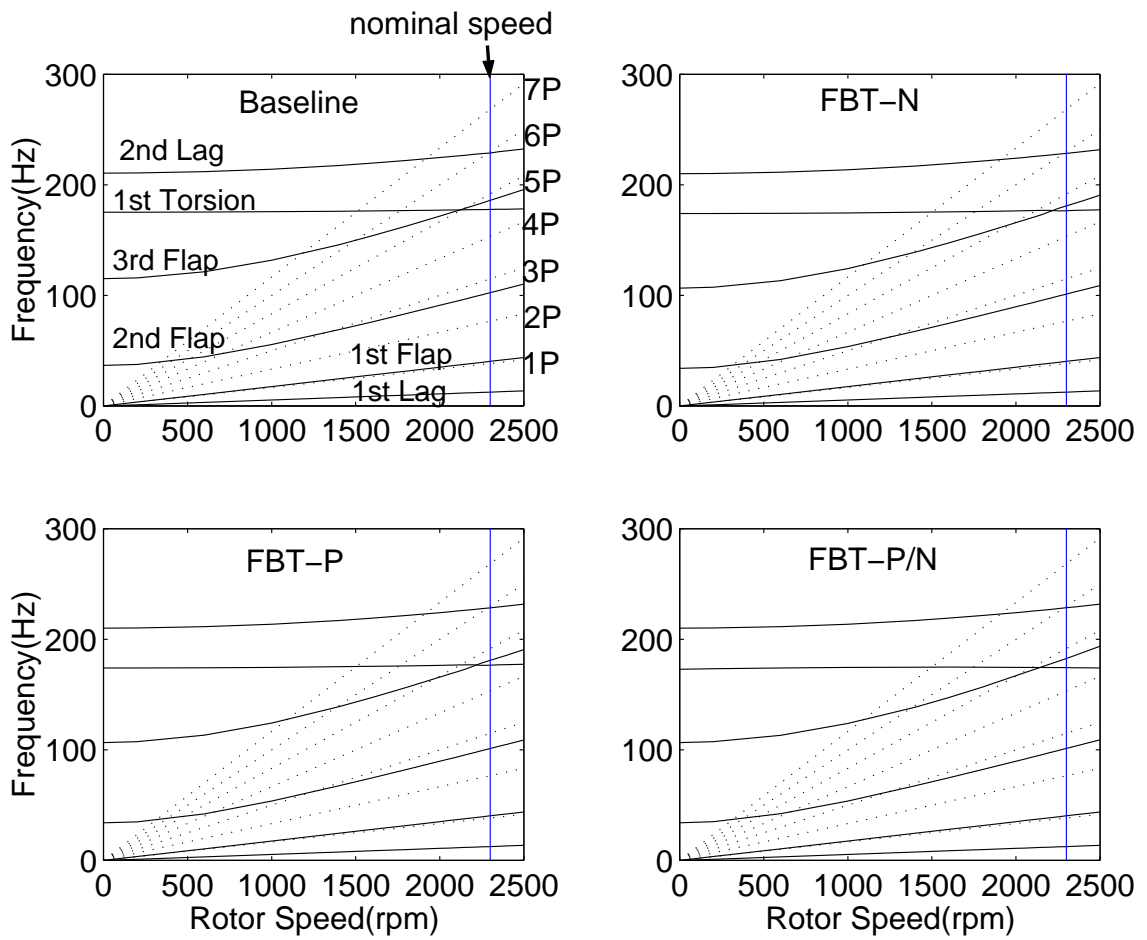


Figure 3.24: Fan plots of Mach scale composite tailored rotors

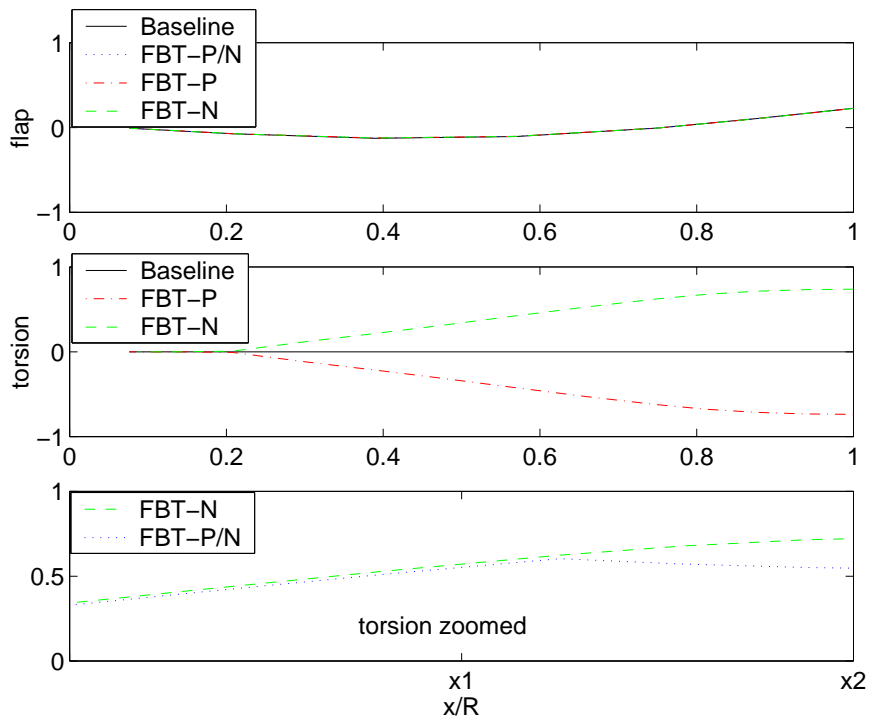


Figure 3.25: The second flap mode shape of composite tailored blades

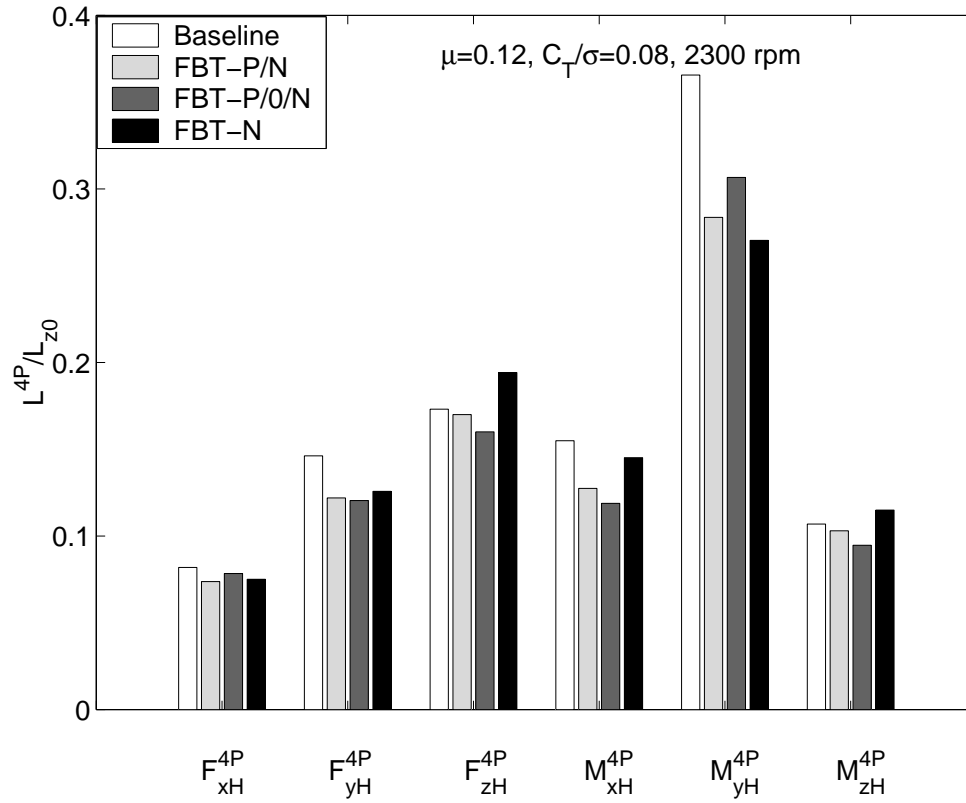


Figure 3.26: Predicted 4/rev vibratory hub loads of Mach scale composite tailored rotors ($\mu = 0.12, C_T/\sigma = 0.08$)

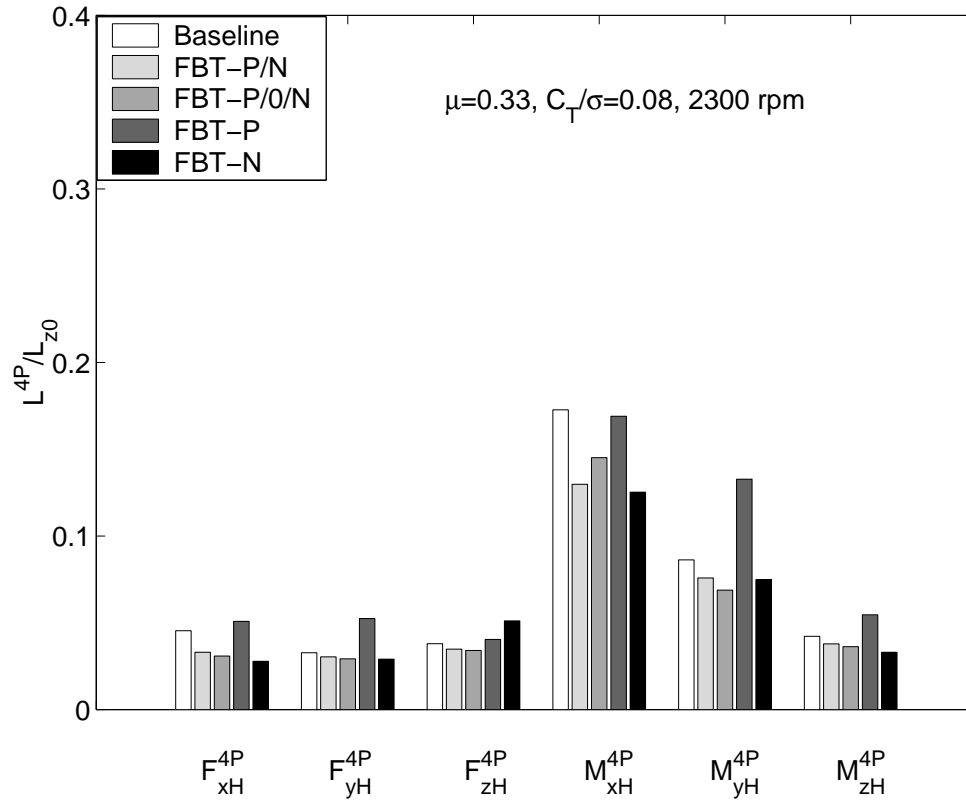


Figure 3.27: Predicted 4/rev vibratory hub loads of Mach scale composite tailored rotors ($\mu = 0.33, C_T/\sigma = 0.08$)

Chapter 4

Fabrication of Mach Scale Composite Tailored Rotor

Five sets of Mach scale composite tailored rotors were fabricated at the Smart Structures Laboratory of the Alfred Gessow Rotorcraft Center in the University of Maryland. They were designated as Baseline, FBT-P, FBT-N, FBT-P/N and FBT-P/0/N, respectively, see Figure 3.23. To fabricate these blades, a new twisted blade mold was designed and manufactured. In this chapter, the detailed fabrication processes of Mach scale composite tailored blades are presented.

4.1 Design of New Twisted Blade Mold

This blade mold was designed for the fabrication of the composite blade which has a SC1095 profile, a rectangular planform, a linear twist of -12° , a chord of 2.667 inch and a length of 30.6 inch. The mold consists of two parts (the top half and the bottom half), which are split along the middle plane of the blade cross-section.

The mold internal profile was designed using Matlab, using the desired di-

mensions of blade cross section. The chord of the mold exceeds the design chord of the blade to facilitate resin out-flow and trimming of a high quality trailing edge of the cured blade, with a small groove to show final trim line, as shown in Figure 4.1. The groove has a length of 0.43 inch and maintains a constant thickness of 0.02 inch from 98% chord onward. This is required to obtain a good bond between the upper and lower skins at the trailing edge. Also, the wider chord leaves a space for the final trimming of the cured blade.

The mold profile was then input into I-deas, which is an integrated package of mechanical engineering CAE/CAD/CAM software tools [119]. Using I-deas, the two dimensional cross section profile (see Figure 4.1) is extruded into a length of 31 inch in conjunction with a -12° linear twist, to form the internal part of the mold. The length of 31 inch is larger than the blade desired length (30.6 inch) with a margin of 0.4 inch. This margin provides space for the resin flow from the blade during the cure cycle, and space for trimming the blade tip and root. The quarter chord line of the mold is placed horizontally.

The next step is to design the external shape of the mold. The mold has a rectangular planform with a width of 5.1 inch and a length of 33 inch, as shown in Figure 4.2. To facilitate machining by a three-axis CNC milling machine, the mold was designed to be split between two halves that follow the leading edge vertical tangency. That enables a vertical end mill to machine the overhang at any point along the leading edge of the mold cross-section. The twisted mating surfaces were designed as short as possible to save the machining time. Four dowel pins and 16 small pins were provided to align the two halves of the mold, especially during the closing of the mold. Finally, the CAD design of the mold was exported to IGS files, and then these files were transferred to the CNC

machine. The fabricated mold is shown in Figure 4.3, which was manufactured out of 6061-T651 aluminum alloy by FlightFab, Inc. [120] Following a similar process, four pairs of blade root grips with internal airfoil profile (see Figure 4.4) and a pair of blade clamps (also with internal airfoil profile) were designed and fabricated.

A mold clamping fixture was designed to fasten the mold. With a flat aluminum base, eight aluminum beams and sixteen bolts (see Figure 4.5), loads are uniformly applied to the mold to compress the composite blade.

4.2 Fabrication Process

The components of the composite blade are shown in Figure 4.6. The blade structure consists of an IM7/8552 graphite/epoxy D-spar laid up on a foam core mandrel with embedded leading edge weights, an aft cell foam core, an IM7/8552 graphite/epoxy weave skin and a composite blade root insert. There are six main steps to fabricate a composite tailored blade. These are: a) forming the rigid foam core, b) assembly of leading edge weights and root insert, c) tailoring of composite prepreg, d) layup of the spar, e) assembly of complete rotor blade and curing in the oven, and f) final blade finishing. The detailed fabrication process steps of the D-spar layup are listed in Appendix C.

4.2.1 Preparation of Foam Core

The foam cores not only act as a layup mandrel for the composite D-spar, but also maintain the airfoil profile of the blade. They are made from Rohacell IG foams [121].

To form a foam core, a rectangular Rohacell foam blank is sanded into an approximate SC1095 airfoil shape using a template and a sanding spindle (see Figure 4.7). The slightly oversized (about 10%) foam is sanded again using sanding paper to obtain better profile shape to fit into the mold. Then it is placed in the twisted mold, heated to $350^{\circ}F$ ($177^{\circ}C$) forming temperature in an oven (Despatch series 1000), and formed to the desired profile by means of compression provided by fastening the mold.

The cured foam cores are cut into a fore cell (with a width of 33% chord) and an aft cell (with a width of 67% chord). A special tool is built (see Figure 4.8) to obtain high cutting quality for the twisted foam. The flexible twisted foam is bonded to a non-twisted flat base using a double-side tape. The flat base has a profile for the top half of SC1095 airfoil. A knife is held by a fixture which can move along both spanwise and chordwise directions. This tool can ensure that the cutting surface of the twisted foam is perpendicular to the middle plane of the airfoil.

For these Mach scale composite blades, the fore foam core is made from Rohacell IG-71 foam, whereas the aft foam core is made from Rohacell IG-31. The higher density IG-71 is selected for the fore foam core, because it acts as a layup mandrel for the composite D-spar and provides improved support for the leading edge weights bonded inside the leading edge curvature of the spar. Furthermore, the aft section IG-31 foam core has half the density of IG-71 foam core, which helps with blade section chordwise c.g. control.

To provide a space for the root insert, a small foam piece with the size of 2.2×0.5334 inch is cut from the root of the fore foam core. Six leading edge weight slots are also precisely milled into the leading edge of the foam core by

a CNC machine. Figure 4.9 shows the milling of the leading edge slots. An aluminum L-beam and five binder clips are used to hold the foam core.

4.2.2 Preparation of Blade Layup

In preparation for the composite layup of the D-spar, the unidirectional IM7/8552 graphite/epoxy prepreg tape (with the width of 12 inch) is tailored into the composite lamina with a desired fiber orientation angle. The fiber orientation angle used in defining the layups is positive toward the leading edge for the top wall of the spar (see Figure 3.22). The same orientation is defined as negative for the bottom wall of the spar. Figure 4.10 shows the detailed tailoring process. The tailoring of the composite is carried out on a cutting table. Before the tailoring, the table was cleaned with acetone and then was covered by a ply of release film (Wrightlon 4600 Blue [122]). Composite properties may be degraded if the prepreg is contaminated by dust.

A cutting template is used to accurately and repeatedly cut the unidirectional prepreg tape. The fiber direction is marked on the backing paper of the composite sheet (Figure 4.10(b)). The marker is used as a reference during the wrapping of composite D-spar. After the final trimming (Figure 4.10(c)), the unidirectional prepreg tape (Figure 4.10(a)) is tailored into a composite lamina with the desired fiber orientation angle θ (Figure 4.10(d)). A composite lamina with the fiber orientation angle of $-\theta$ can be tailored by the similar approach. The tailored composite sheets should also be put into a clean envelope bag, and placed flat in the refrigerator at a temperature of $0^{\circ}F$ ($-18^{\circ}C$). This process prevents moisture contamination and fiber breakage.

Pre-layup actions also include the fabrication of the root insert and the lead-

ing edge weights. The composite root insert (described in Chapter 3) is assembled from forty two plies of unidirectional IM7/8552 prepreg strip with a length of 2.2 inches and a width of 0.5334 inches. To build the root insert, these composite strips are stacked one by one with two edges against the inner corner of a L-shaped aluminum block. That ensures a uniform length and width of the insert during the fabrication process. The tungsten leading edge weights are wire cut from a tungsten plate (class IV), using electrical discharge machining (EDM) to obtain the airfoil profile. Before the leading edge weights are inserted into the foam slots, they are cleaned with acetone.

Another step in the layup preparation is the assembly of the root insert, the leading edge weights, and the fore foam core. Firstly, the root insert and the leading edge weights are wrapped with one ply of film adhesive (Cytec FM300 [123]). Then, they are inserted into the root slot and the leading edge slots of the foam, respectively. Finally, the foam, comprising the root insert and the leading edge weights, is wrapped using one ply of film adhesive to form a mandrel for composite D-spar wrapping, see the upper part of Figure 4.11.

4.2.3 Layup of Composite D-spar

There are five sets of composite D-spar to be fabricated, see Figure 3.23. They have different layup configurations and spanwise flap-bending/torsion coupling distributions. As shown in Table 3.8, each D-spar consists of multiple layers of composite. For the baseline D-spar without coupling, these composite layers have a balanced layup. The symmetric layup with unbalance in the top and bottom walls of the D-spar is used for the coupled blade. For the positive coupled D-spar (FBT-P), the top spar layers have the same fiber orientation angle of θ , while the

negative coupled D-spar (FBT-N) have the same fiber orientation angle of $-\theta$ at the top. At the bottom of the spar, the composite layers have the orientation angles with the opposite sign. To layup the D-spar with the mixed coupling, two composite strips with the opposite orientation angles have to be used along the span of the layup to obtain the desired spanwise segmented coupling in the same layer. Figure 4.12 shows a spanwise layup detail of a D-spar with mixed positive/negative coupling (FBT-P/N). In the transition region of the composite layers, there is a one inch overlap between the composite strips with the opposite fiber orientation angles to improve the local structural integrity of the blade.

Before the wrapping of the composite D-spar, several working drafts are drawn to show the orientation angle of each layer and to indicate the detailed wrapping steps. Following these drafts, firstly, the composite strip with a desired width is cut from the tailored composite lamina, which is shown in Figure 4.10(d), for each spar layer. Then, this strip is placed at the desired location on the surface of the foam mandrel. A hot gun and a rubber roller are used to compress the composite strip to the mandrel. After wrapping the top strip and bottom strip for the same layer, a shrink tape (PTFE stretch tape) is used to make spar wrapping more compact. Figure 4.13 shows a composite D-spar compressed by the shrink tape and a fabricated D-spar. Alternating top and bottom spar layers are interlaced around the leading edge of composite D-spar for structural integrity.

Finally, the D-spar is mated with the aft foam core and wrapped with one ply of ± 45 IM7/8552 graphite/epoxy weave skin as the blade skin.

4.2.4 Blade Curing and Finishing

The assembled uncured blade is wrapped in a ply of release film and placed into the lower half of the mold, which has already been treated with release agent (Frekote NC-700). Figure 4.14 shows an uncured sample blade in the mold. The blade is restrained by two strips of high temperature tape to prevent it from dislodging during closing and fastening of the mold. Then, the assembly of composite blade is cured in the closed mold in the oven. The temperature of the composite blade is measured by a thermocouple, which is attached to the mold surface. According to the data sheet of 8552 epoxy [118], the cure cycle of the composite blade begins with room temperature and includes two steps: holding the mold temperature at $225^{\circ}F$ ($107^{\circ}C$) for 30 minutes and finally holding the temperature at $350^{\circ}F$ ($177^{\circ}C$) for 120 minutes before the oven is turned off.

After the mold has cooled down to the room temperature, the blade is removed from the mold. The epoxy bead at the leading edge is removed using fine files and sand paper in order to obtain an aerodynamically clean leading edge. Thereafter, the blade is trimmed to the exact length (30.6 inch) and chord (2.667 inch) by a small CNC machine, see Figures 4.15 and 4.16. An airfoil shaped clamp is used to hold the blade during the trimming.

The final fabrication step for the composite blade is to drill the bolt hole pattern for the blade grips into the blade root insert. The blade root is clamped in an airfoil shaped clamp that also serves a drill guide for the blade root grip bolt pattern. A milling machine is used locate the origin of the blade clamp and drill guide and then drill the blade grip bolt pattern. There are three holes with the desired diameter (0.1875 inch, see Figure 3.7) and spanwise locations (30.3 inch, 29.55 inch and 28.8 inch to the blade tip, respectively, see Figure 3.7)

passing through the fixture. Thus, this fixture is also used as the template of the drilling. After setting the original point of the tool, the drilling work is carried out using the CNC machine. A brad-point drill bit is used to avoid delamination, fuzz and fray of the composite.

Five sets of composite tailored rotor blades were fabricated, including the baseline blades and the coupled blades with different flap-bending/torsion couplings (FBT-P, FBT-N, FBT-P/N and FBT-P/0/N, respectively). Figure 4.17 shows a fabricated Mach scale composite tailored blade with linear pretwist. Six blades were fabricated for each of the baseline and uniform coupled rotors (FBT-N and FBT-P), and seven blades were fabricated for each of the two mixed-coupling rotors (FBT-P/N and FBT-P/0/N). The extra blades were fabricated to a) permit selection of closest match blades for 4-bladed rotor wind tunnel testing, b) provide spare blades in the event of unforeseen damage, and c) provide specimens for destructive characterization. The average mass of the 32 blades that were fabricated is 176.9 gm, with a maximum mass difference of 1.2%. The static and dynamic characterization of the blades is detailed in Chapter 5.

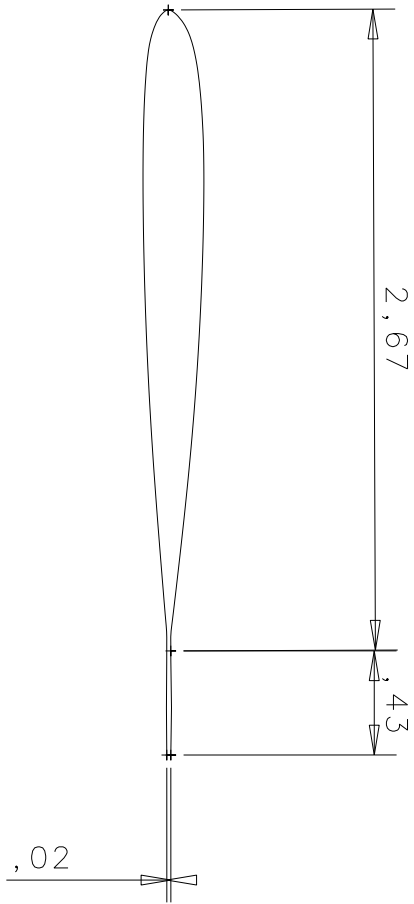


Figure 4.1: Internal cross-section profile of the blade mold

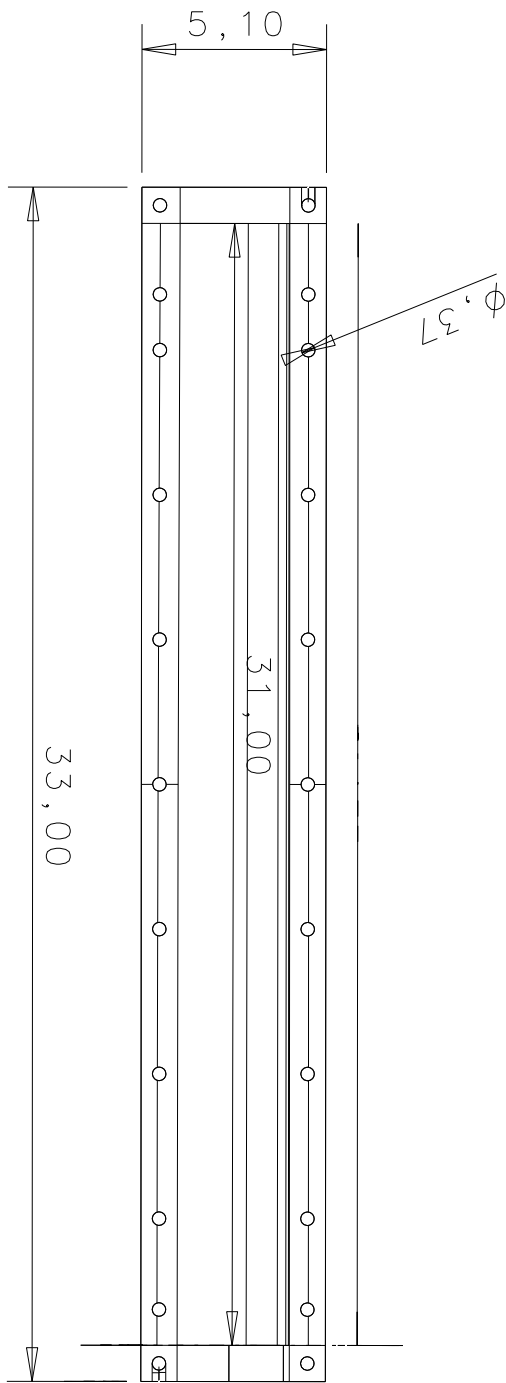


Figure 4.2: Dimensions of the blade mold

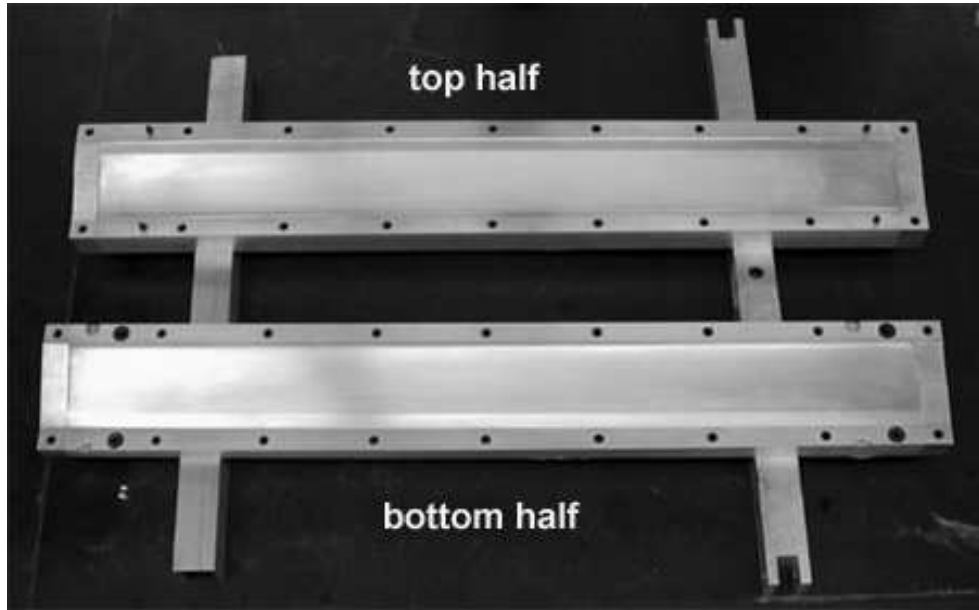


Figure 4.3: New twisted blade mold

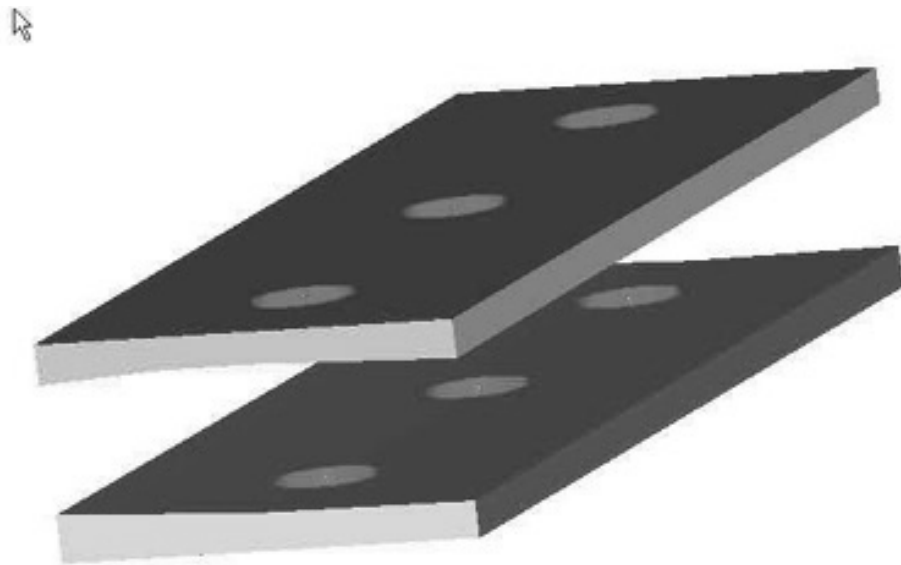


Figure 4.4: Blade-hub connecting grip

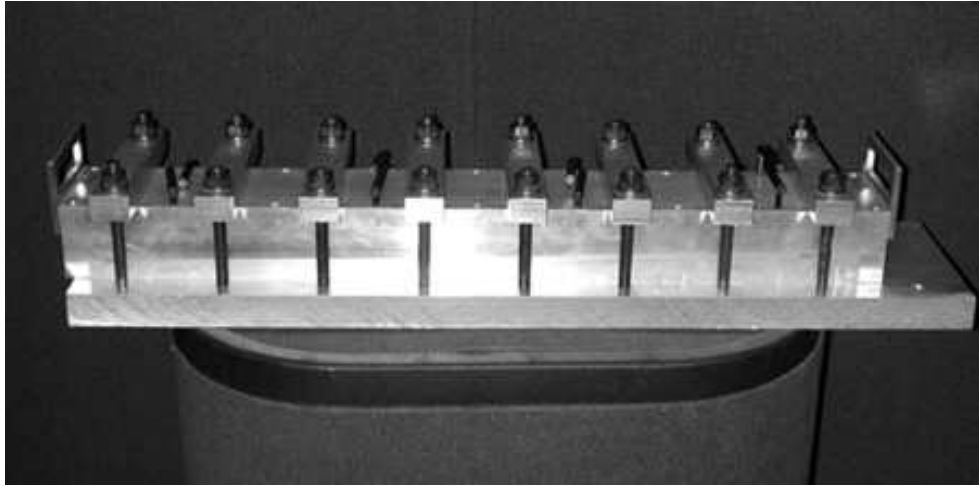
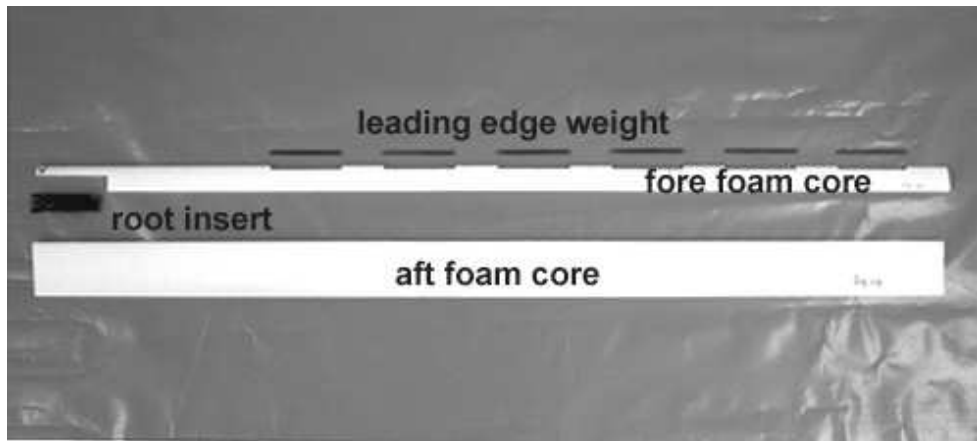
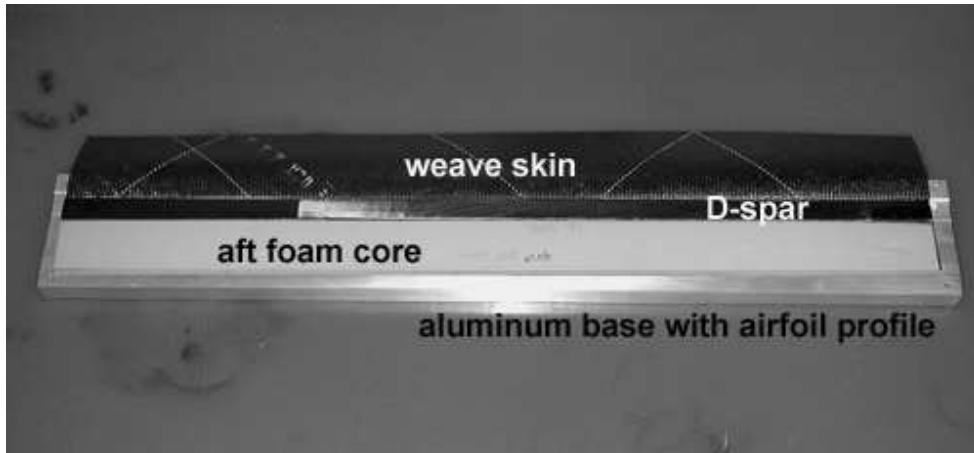


Figure 4.5: Fastening the mold



(a)



(b)

Figure 4.6: Components of Mach scale composite tailored blade

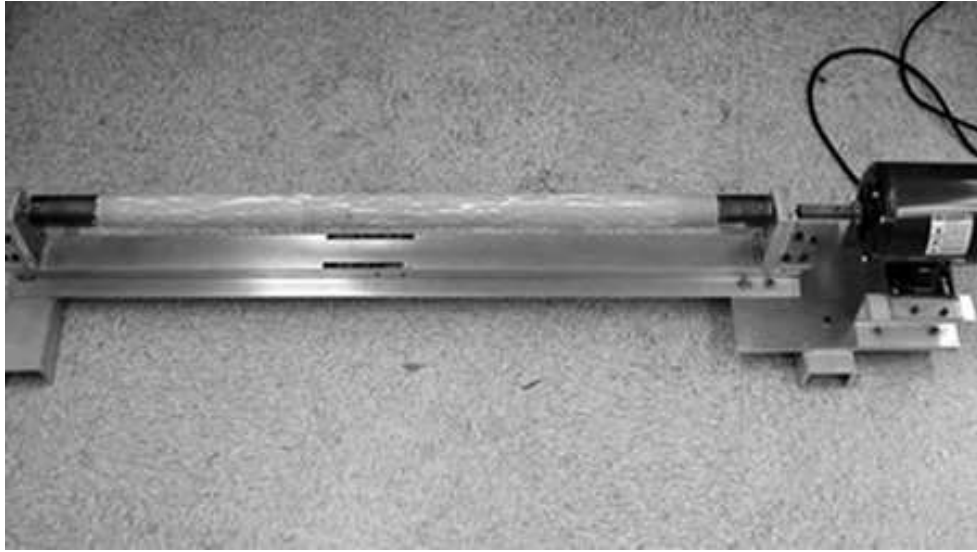


Figure 4.7: Foam sanding machine

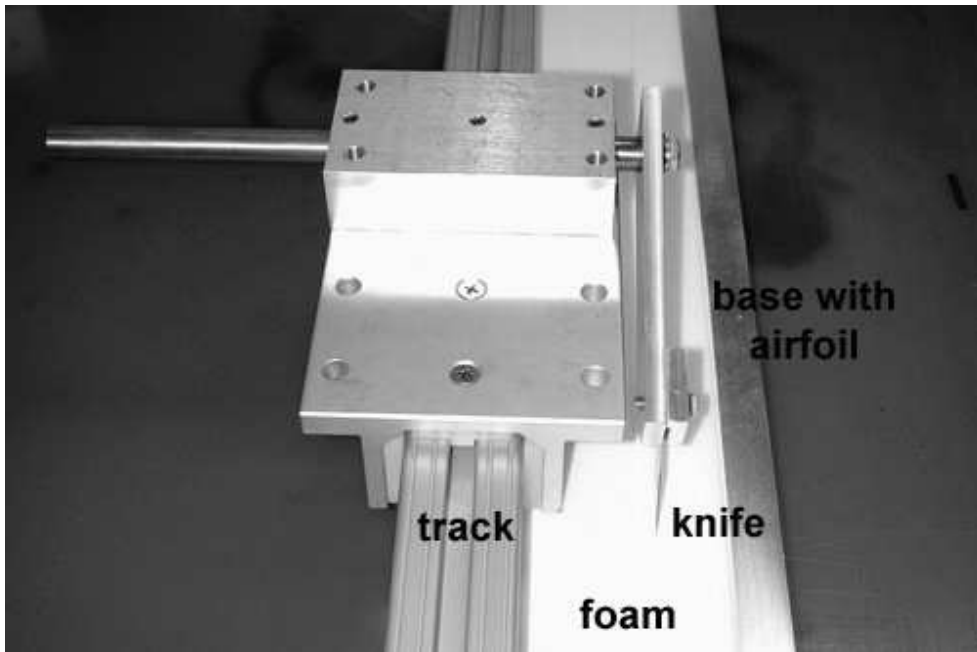


Figure 4.8: Cutting the foam core



Figure 4.9: Milling leading edge slots in the fore foam core

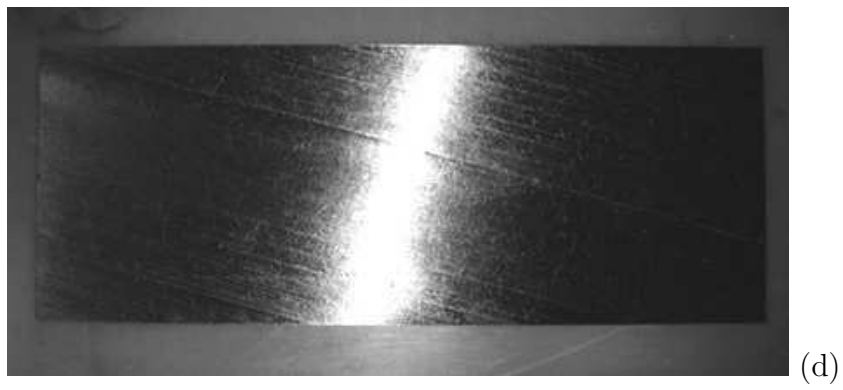
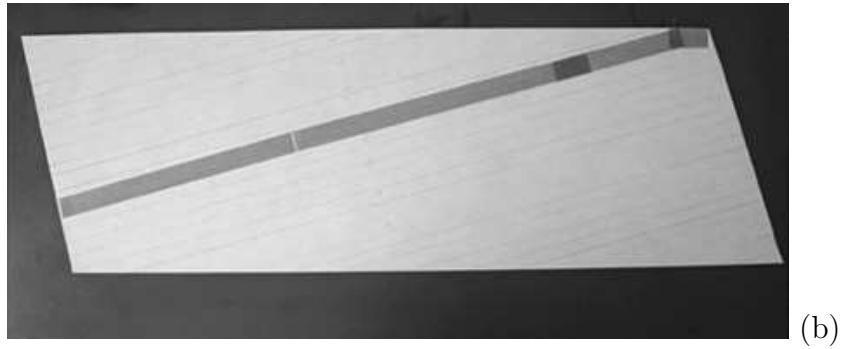
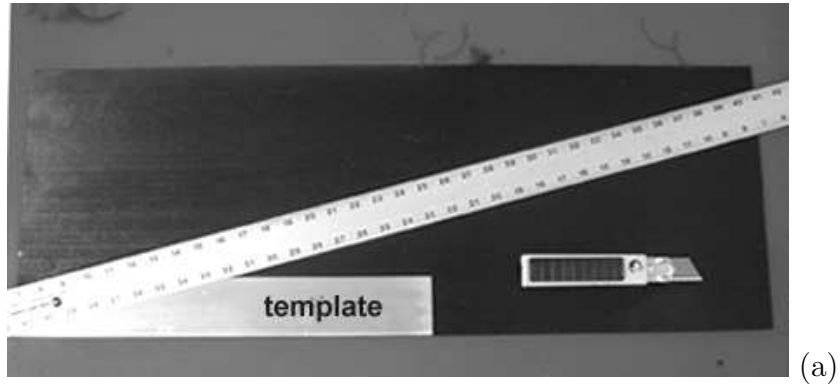


Figure 4.10: Tailoring composite lamina

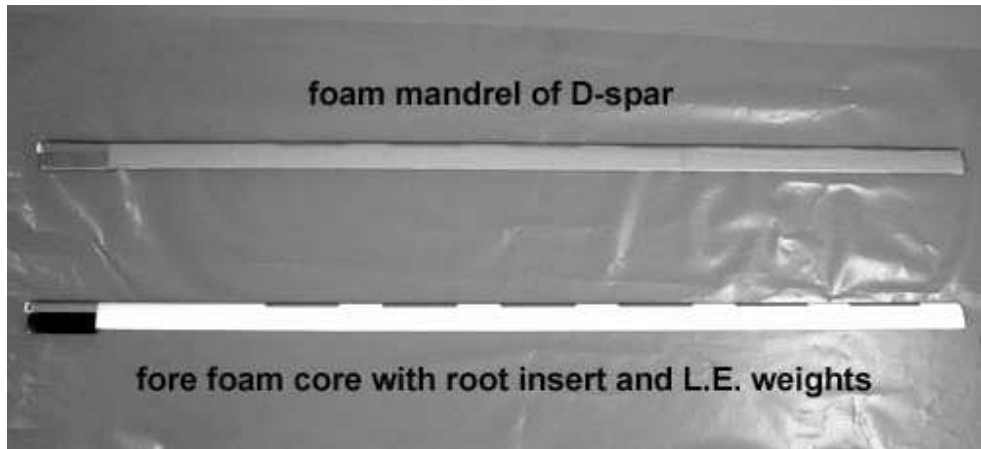


Figure 4.11: Foam mandrel of composite D-spar

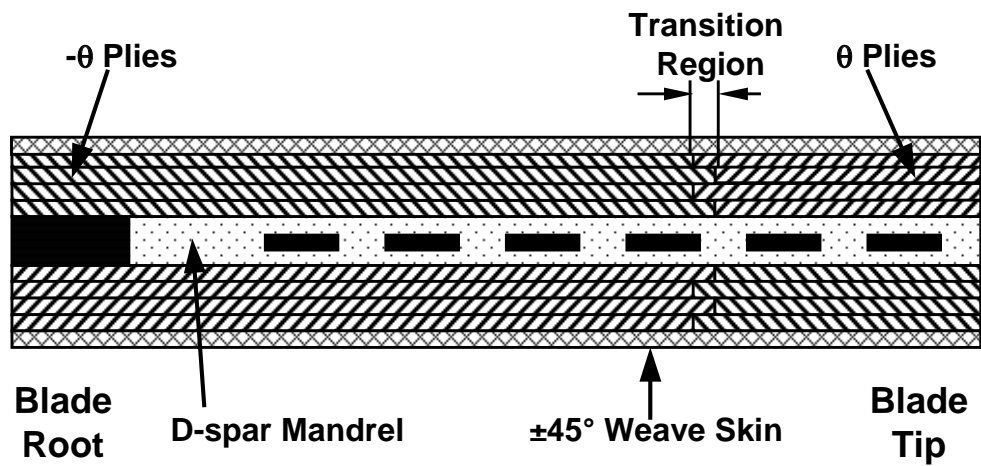


Figure 4.12: Layup of mixed coupling blade (FBT-P/N)

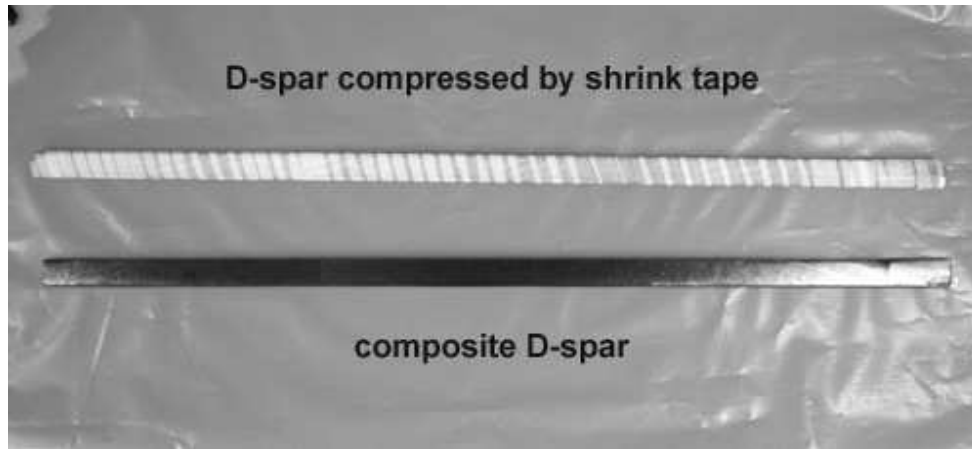


Figure 4.13: Composite tailored D-spar

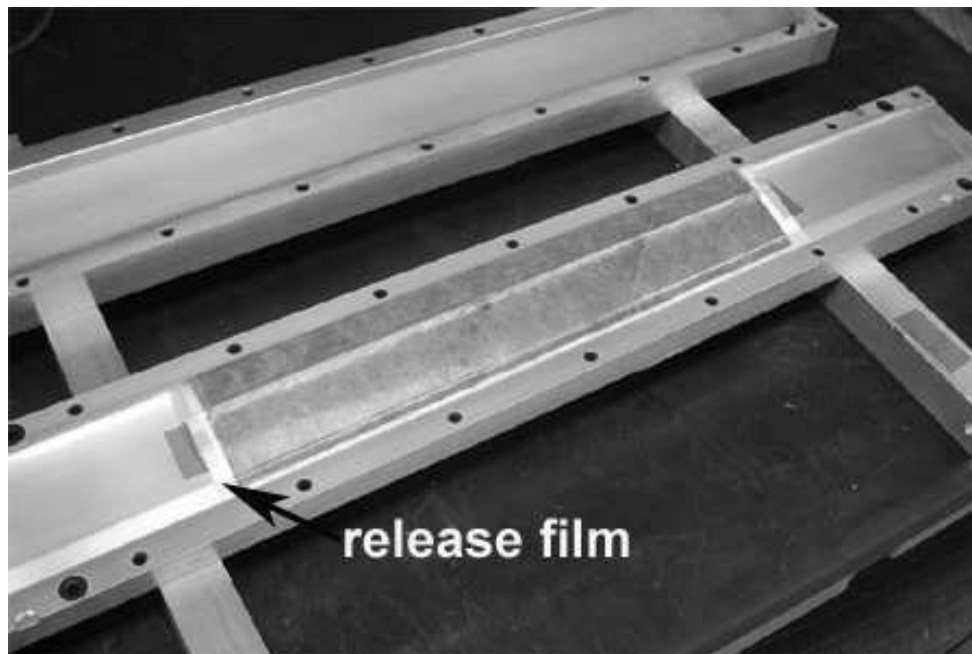


Figure 4.14: Final assembly of composite blade in the mold

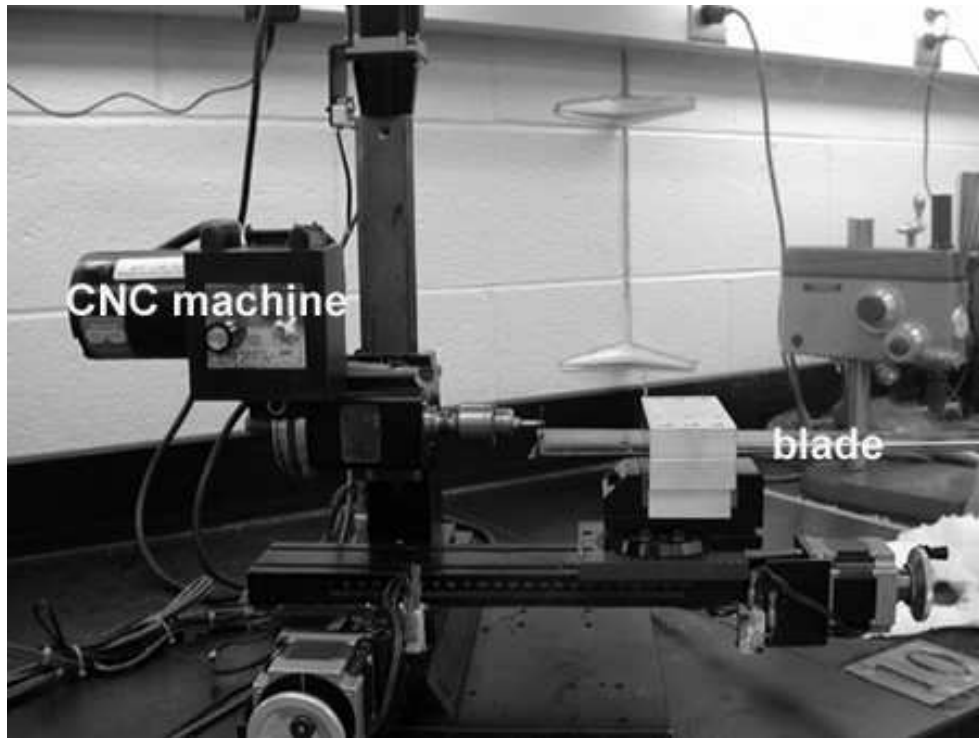


Figure 4.15: Trimming of the blade tip using CNC machine

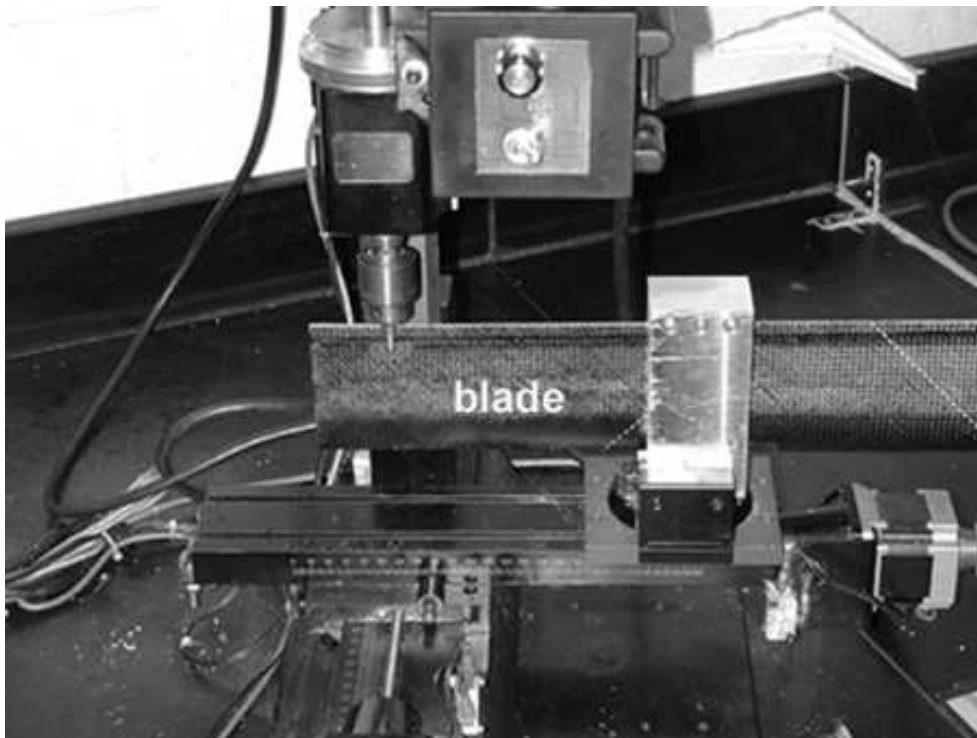


Figure 4.16: Trimming of the blade trailing edge using CNC machine

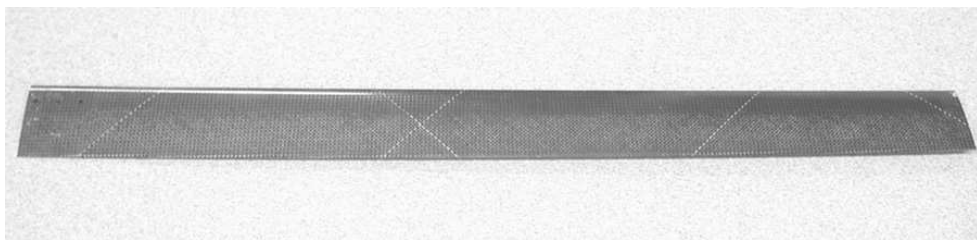


Figure 4.17: Mach scale composite tailored blade with linear pretwist

Chapter 5

Experimental Examination of Blade Structural Properties

Prior to the spin test of the fabricated Mach scale composite tailored rotors, a series of bench-top static tests, bench-top shaker tests and non-rotating dynamic tests were performed to examine the blade structural properties. The bench-top static test was also used to select four blades with closest matching properties for each rotor set.

This chapter describes the detailed testing procedures and the experimental equipment used for these tests, and presents the experimental data.

5.1 Bench-top Static Test

5.1.1 Test Setup

The bench-top static test setup consists of a test stand (see Figure 5.1) and a laser optic system to measure blade deflections (see Figure 5.2). The blade root is clamped in an airfoil shaped blade clamp that in turn is restrained between

two steel plates of the test stand. Bending force and torque are applied to the blade using dead weight loading, by means of a suitable arrangement of pulleys, loading lines and an airfoil shaped clamp, as shown in Figure 5.1.

A laser optical system and a mirror are used to measure blade bending slope and twist. The mirror is bonded on the blade and the light beam is reflected from the mirror onto a vertical record board, which is covered with a graph paper. When a bending force or a torque is applied to the blade, the light spot moves away from the original position. Both the original and the deflected light spot are recorded. The blade bending slope and the twist are determined from the amount that the light spot is moved. Vertical distance relative to the original position represents the bending deflection, while horizontal distance represents torsional deflection. Figure 5.3 shows the optical geometry to measure the blade bending slope (w'_f) under a tip bending force. In general the displacement angle is small (i.e. small angle approximation is valid). The distance (L) between the blade and recording board controls the measurement resolution, and for the present tests was set at 35 feet. Using the measured vertical deflection and the known distance, the bending slope is given by the equation

$$w'_f = \frac{\Delta l}{2L} \quad (5.1)$$

The analysis is similar for a torsional displacement of the blade tip, however in this case the deflection of the light spot in the recording board is in the horizontal direction.

5.1.2 Test Results

Each fabricated Mach scale composite tailored blade was tested using this test stand. For the blade bending deflection data, measurements were taken at three load levels and in both directions (flap up and flap down), except for the baseline blades. For the blade torsion response data, measurements were taken at five load levels and also in both directions (nose up and nose down).

Figures 5.4- 5.13 show the experimental data for all five sets of composite tailored blades as well as the values predicted by analysis. The analysis values of blade deflections are calculated by the force-displace relations of a cantilevered composite blade with flap-bending/torsion coupling, as

$$\begin{Bmatrix} M \\ T \end{Bmatrix} = \begin{bmatrix} EI_y & EFT \\ EFT & GJ \end{bmatrix} \begin{Bmatrix} w'' \\ \phi'_x \end{Bmatrix} \quad (5.2)$$

where EI_y , GJ and EFT are blade flapwise bending stiffness, torsional stiffness and flap-bending/torsion coupling stiffness, respectively. These structural properties were predicted using the mixed method of composite blade structural analysis. w is blade flapwise bending deflection and ϕ_x is blade torsional deflection. M and T are blade applied bending and torsion loads respectively.

For a cantilevered blade under a tip flapwise bending force, Equation 5.2 has the form of

$$\begin{aligned} P(l-x) &= EI_y w_f'' + EFT \phi_f' \\ 0 &= EFT w_f'' + GJ \phi_f' \end{aligned} \quad (5.3)$$

where P is the applied tip bending force, l is the spanwise location of the applied force, and x is the spanwise location of a measure point. From Equation 5.2, the blade bending slope (w'_f) and bending-induced twist (ϕ_f) can be obtained as

$$\begin{aligned} w'_f &= \frac{GJ}{2(EI_y GJ - EFT^2)} P(2lx - x^2) \\ \phi_f &= \frac{EFT}{2(EI_y GJ - EFT^2)} P(2lx - x^2) \end{aligned} \quad (5.4)$$

Using a same procedure, the blade twist (ϕ_t) and torsion-induced bending slope (w'_t) of a cantilevered blade subjected to a tip torque can be obtained from Equation 5.2 as

$$\begin{aligned} w'_t &= \frac{EFT}{EFT^2 - EI_y GJ} Tx \\ \phi_t &= \frac{EI_y}{EI_y GJ - EFT^2} Tx \end{aligned} \quad (5.5)$$

where T is the applied tip torque.

From Figures 5.4- 5.13, it is seen that the predictions correlate well with the measurements. Six blades were fabricated for each of the baseline and uniform coupled rotors (FBT-N and FBT-P), and seven blades were fabricated for each of the two mixed-coupling rotors (FBT-P/N and FBT-P/0/N). Based on the experimental data the four best matched blades were selected for each rotor configuration. It is seen that the test data for the selected four blades of each rotor exhibit good repeatability.

In Figures 5.4 and 5.9, it is seen that the baseline blades do not exhibit the tip induced twist under tip force and the tip induced slope under tip torque. This confirms that the baseline blade has no flap-bending/torsion coupling.

In Figures 5.6 and 5.7, the coupled blades with uniform negative flap-bending/torsion coupling (FBT-N) and the coupled blades with uniform positive coupling (FBT-P) show the same blade bending slopes, because they have same flapwise bending stiffness. However, the induced tip twists for these two blade configurations have the opposite sign. Similar behavior can be observed in Figures 5.11 and 5.12, when torsional loads are applied to these blades. This means that the only difference between the FBT-N coupled blade and the FBT-P coupled blade is the sign of the flap-bending/torsion coupling stiffnesses.

Figures 5.5 and 5.8 show the tip induced twist of two mixed flap-bending/torsion coupling blades (FBT-P/N and FBT-P/0/N) has the same sign as that of the negative coupled blade (see Figure 5.6). Under the tip loads, these two blades exhibit the overall effect of the negative flap-bending/torsion coupling, because most of the blade span has negative coupling for these two mixed coupling configurations (see layup configurations of composite tailored blade in Figure 3.23).

5.2 Bench-top Shaker Test

The structural analysis of the composite tailored blades was further validated by the bench-top shaker testing of the sample blades.

The dynamic test stand is set up on an optical table (Newport Corporation RS-3000), as shown in Figure 5.14. An air compressor serves as the air source to isolate legs of this table. The isolation system floats the table and totally

isolates it from disturbances of floor.

The composite blade is cantilevered using an airfoil shaped clamp that itself is clamped in a dual vice assembly. Two T-shape frames are used to suspend a shaker and to hold a laser sensor. The location of the shaker and the laser sensor can be adjusted along the frames.

The blade is excited by an electromagnetic shaker (LDS 4 lb), which is suspended using eight rubber strings from the T-shape frame. The output force from shaker is applied to the blade through a load cell and a rigid rod. The rod is bonded perpendicularly to the surface of the blade using M-bond. The load cell measures the force input to the blade. A laser sensor (Schaevitz DistanceStar) is used to measure the blade vibratory response.

A SigLab data acquisition and signal processing system is used to provide control algorithm and acquire test data. A sine sweep signal is applied to the shaker with the load cell feedback to maintain the constant force magnitude for the whole frequency spectra. The input voltage of the load cell is set before the excitation. Through a power amplifier, the output voltage to shaker is adjusted automatically by the feedback control algorithm integrated in the SigLab system.

The excitation point is located at 3 inch from the root of the cantilevered blade and a 600 mv input voltage is used for the load cell. Two sample blades were tested to validate the blade structural analysis, before the final fabrication of five sets of Mach scale composite blades. These sample blades were fabricated using the same processes and materials described in Chapter 4. One blade was built using a NACA0012 mold, with a layup of $[35]_4$ spar, ± 45 skin and $\pm 35_s$ web (35% chord). Another blade (as shown in Figure 5.14) has the same profile and dimensions as those of Mach scale composite blades, but with a layup of $[33]_4$

spar, ± 45 skin and ± 33 web (35% chord). The tip vibration response of these blades was measured. The measured and predicted flapwise natural frequencies are compared for each of the two sample blades (with cantilevered boundary condition) in Figures 5.15 and 5.16, respectively. It is seen that the predictions correlate well with the experimental data. The difference between the analysis and the measured values is less than 2%.

5.3 Non-rotating Dynamic Test

Non-rotating vibration testing was performed to measure the fundamental torsion frequency of composite tailored blades, when mounted on the rotor test stand. This is the Mach scaled rotor stand of the University of Maryland (the details about this stand will be presented in Chapter 6), which was used for the wind tunnel test of the Mach scale composite tailored blades.

Because the swashplate of this rotor test stand is controlled by three low bandwidth electric motors, it can not provide the high frequency excitation to the blade. To conduct this vibration test, one normal pitch link of the articulated hub was replaced with a piezoelectric actuator, as shown in Figure 5.17. This P-845.20/LVPZT Translator from Physik Instrumente (PI) can generate $30\mu m$ nominal stroke. The amplifier used to drive the actuator is a LVPZT-Amplifier.

The SigLab system was used to perform swept sine test from 50 Hz to 300 Hz, with 2 volt input voltage to the amplifier. The frequency response of the blade was measured from torsion strain gauges bonded at the root of the blade (30%R). Five blades were tested, including the baseline blades and four coupled blade with different spanwise coupling configurations (FBT-P/N, FBT-P, FBT-N and

FBT-P/0/N respectively). The measured frequency responses of these blades are shown in Figure 5.18. It is seen that the magnitude apexes of frequency response is 186 Hz, 188.5 Hz, 186 Hz, 188 Hz and 187.5 Hz for these blades respectively. They are identified as the first non-rotating torsion frequency for these composite blades with hub connection. The predicted frequency is 177 Hz, corresponding to an under-prediction of 5%. However, the difference of measured non-rotating torsion frequencies is within 1% between these composite tailored blades. It is evident that the effect of the flap-bending/torsion coupling on the frequency is very small.

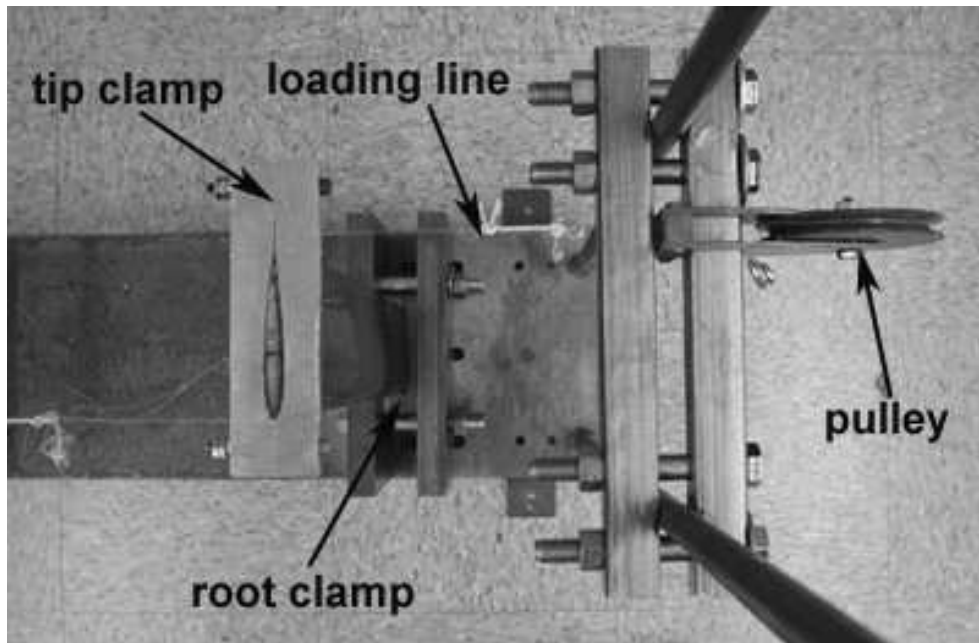


Figure 5.1: Bench-top static test stand

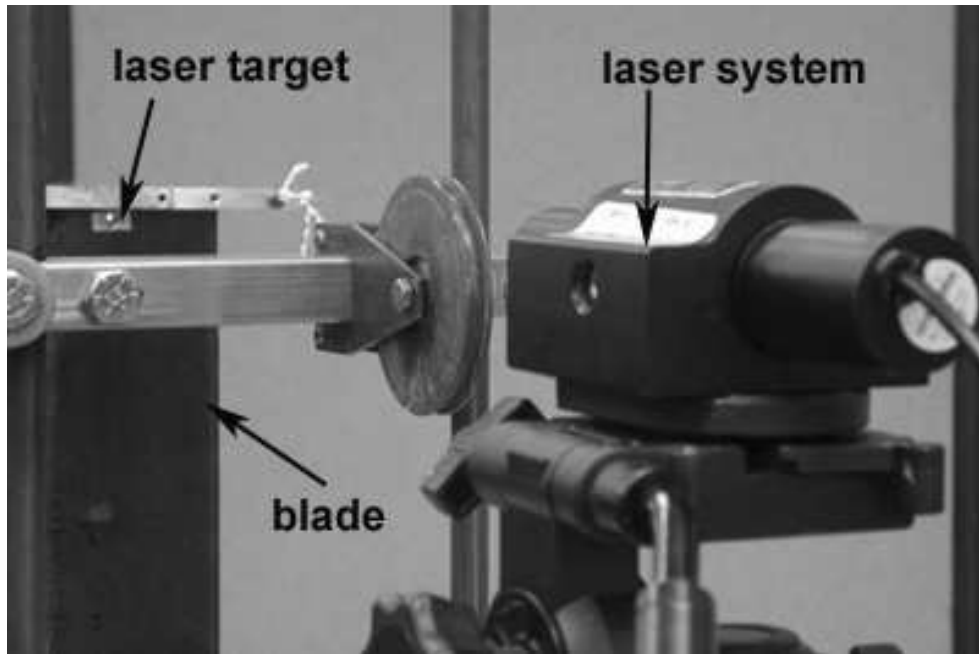
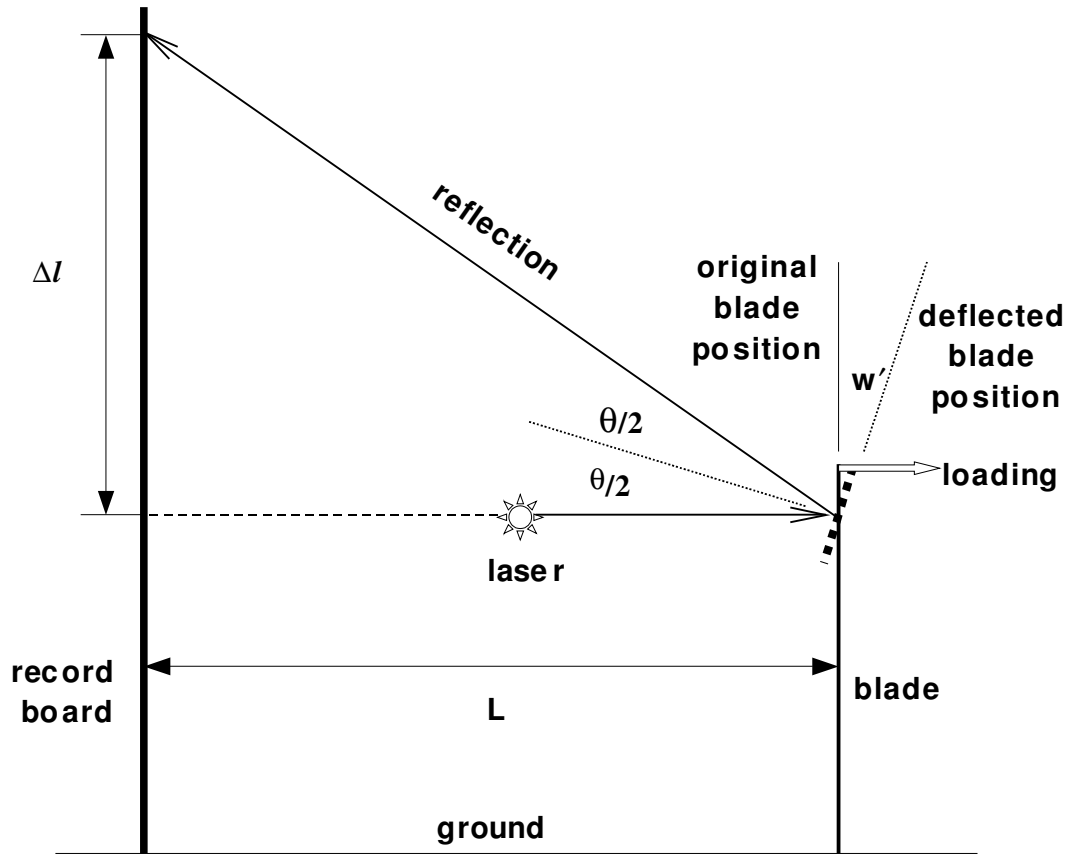


Figure 5.2: Measurement system for blade static deflection



$$\theta = \tan^{-1}(\Delta l / L)$$

blade bending slope: $w' = \theta/2$

Figure 5.3: Optical geometry to measure blade slope

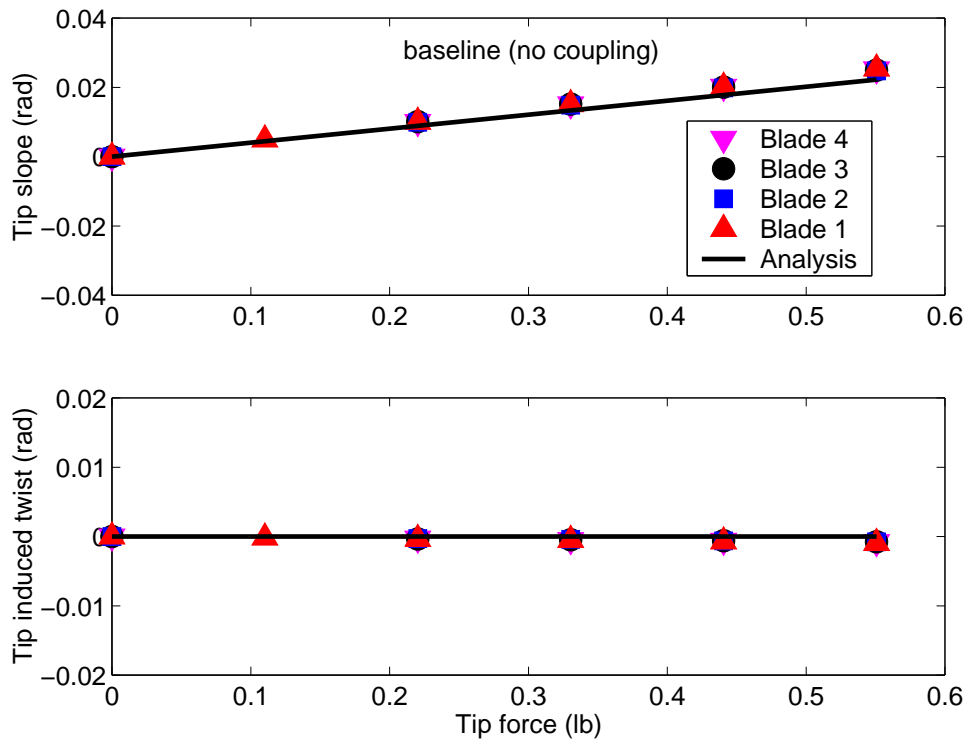


Figure 5.4: Tip response of baseline composite blades under tip flapwise bending force

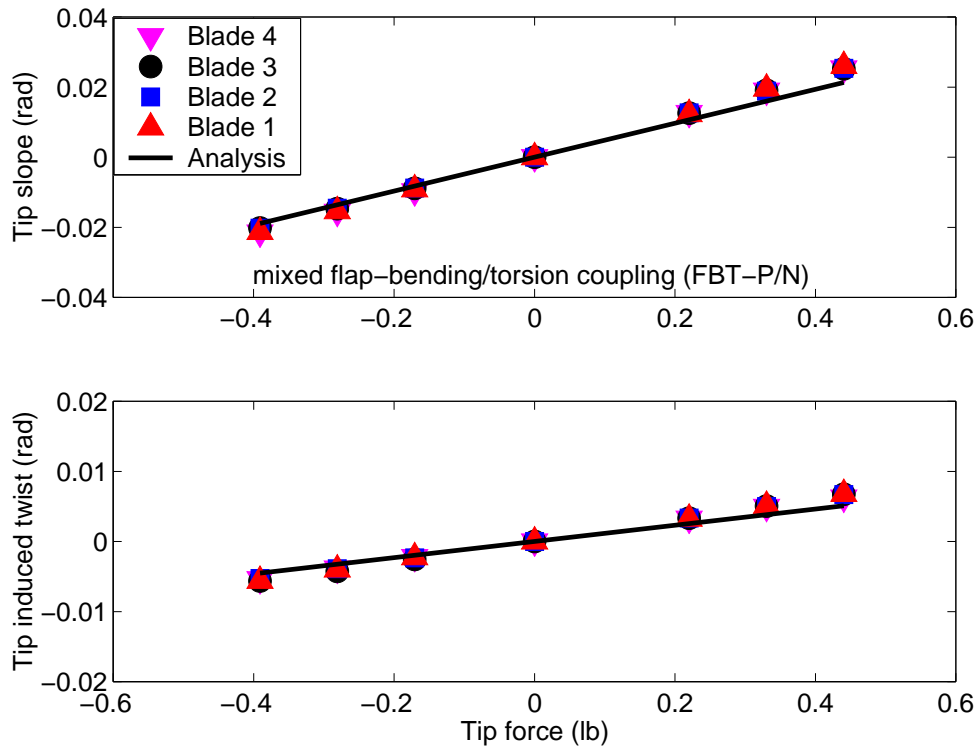


Figure 5.5: Tip response of composite blades with mixed flap-bending/torsion coupling (FBT-P/N) under tip flapwise bending force

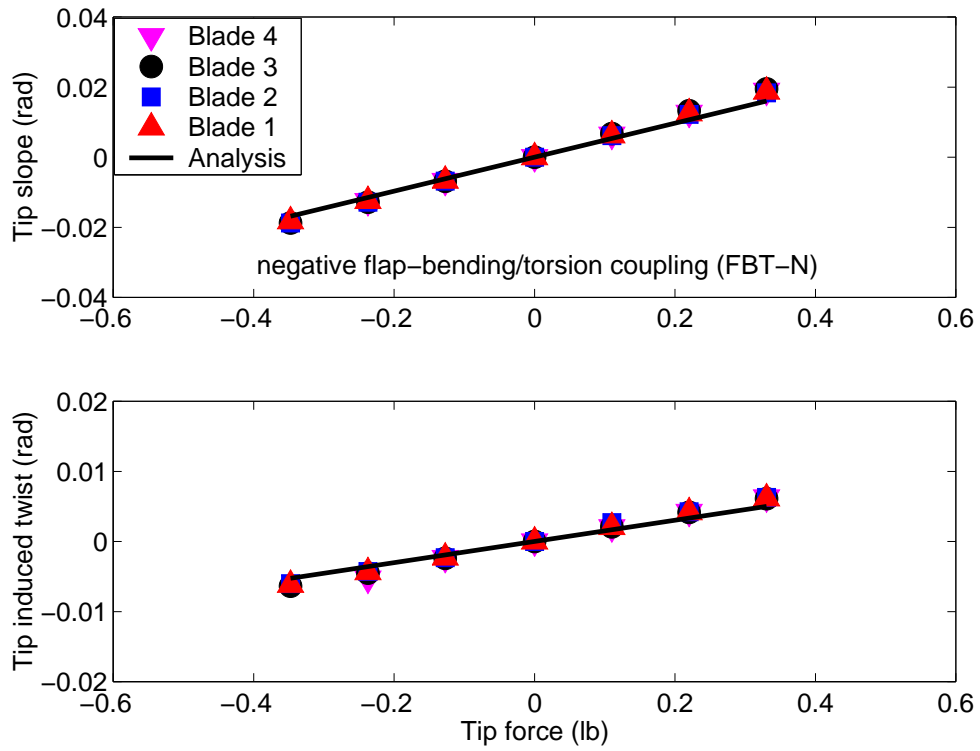


Figure 5.6: Tip response of composite blades with negative flap-bending/torsion coupling (FBT-N) under tip flapwise bending force

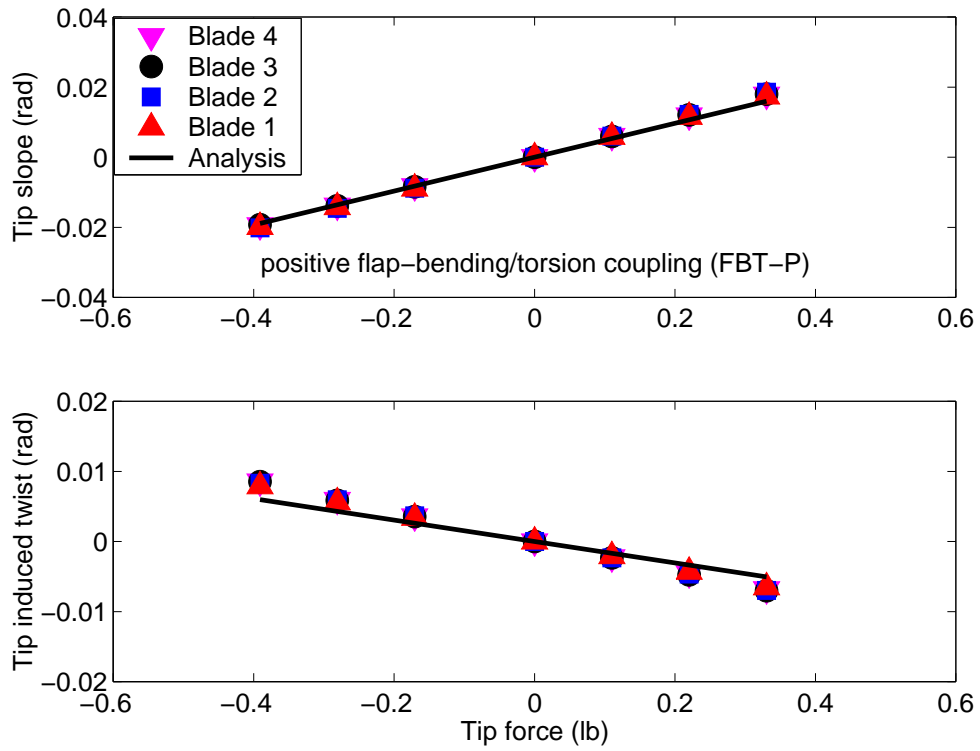


Figure 5.7: Tip response of composite blades with positive flap-bending/torsion coupling (FBT-P) under tip flapwise bending force

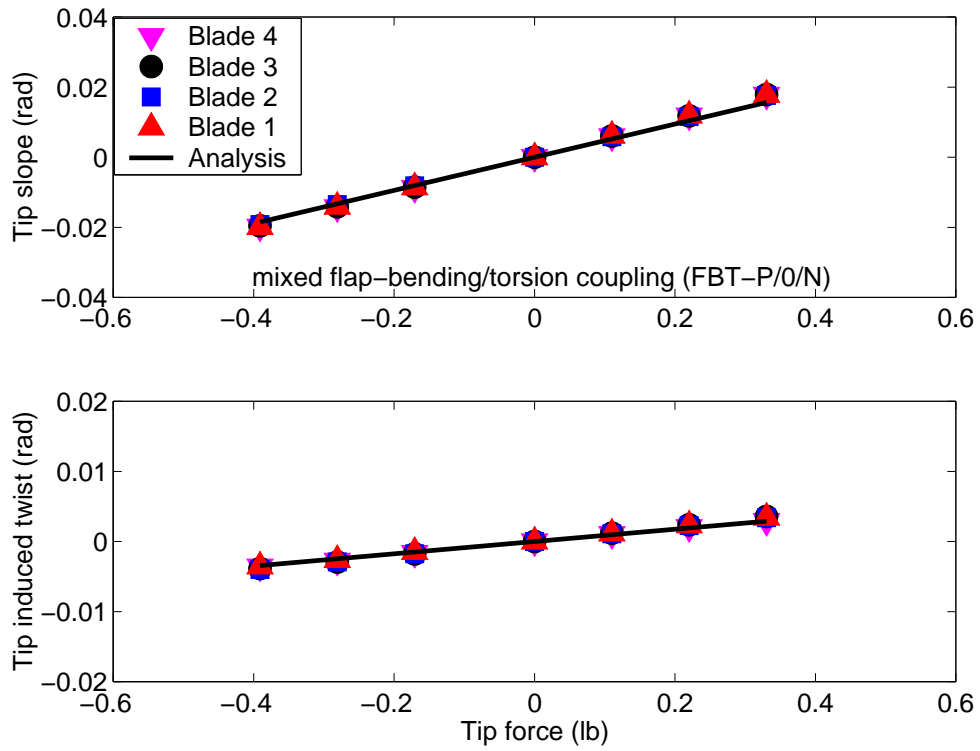


Figure 5.8: Tip response of composite blades with mixed flap-bending/torsion coupling (FBT-P/0/N) under tip flapwise bending force

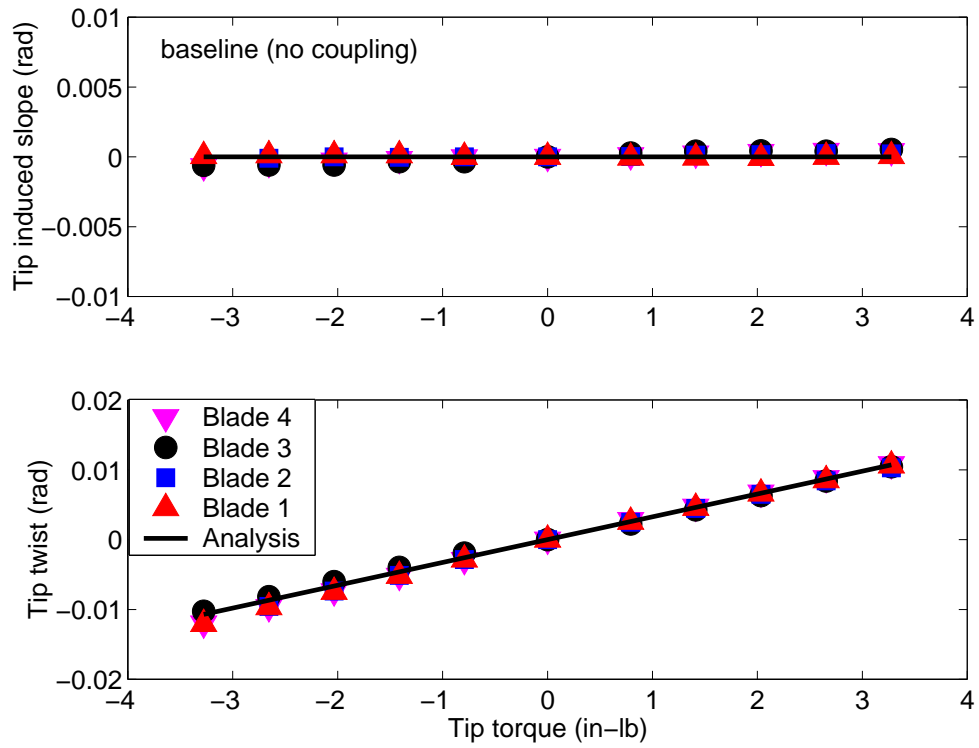


Figure 5.9: Tip response of baseline composite blades under tip torque

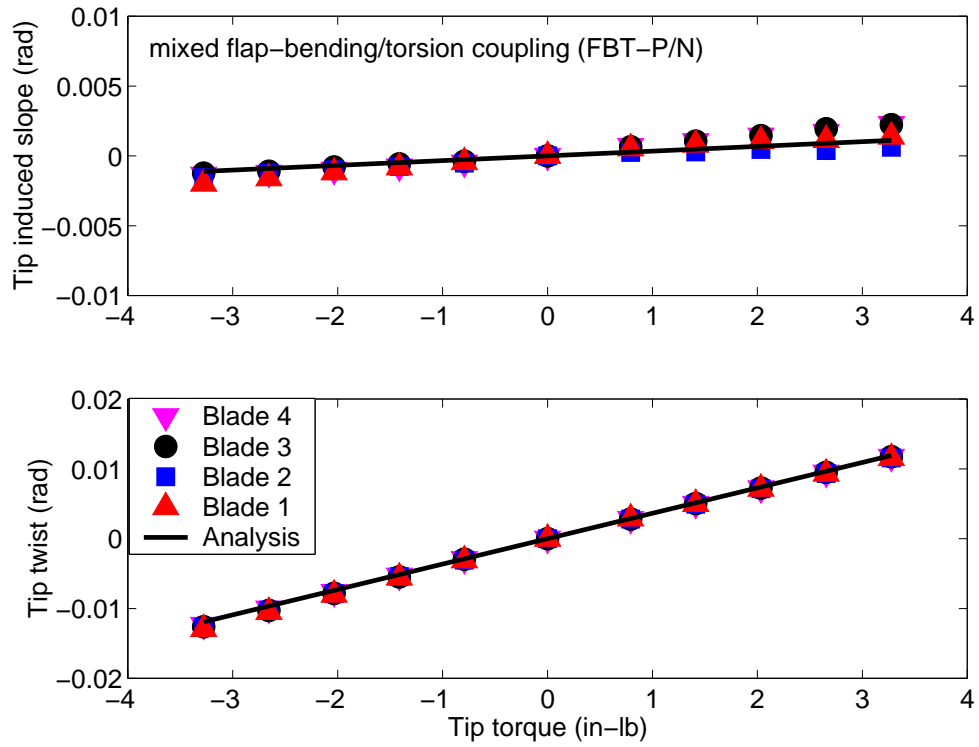


Figure 5.10: Tip response of composite blades with mixed flap-bending/torsion coupling (FBT-P/N) under tip torque

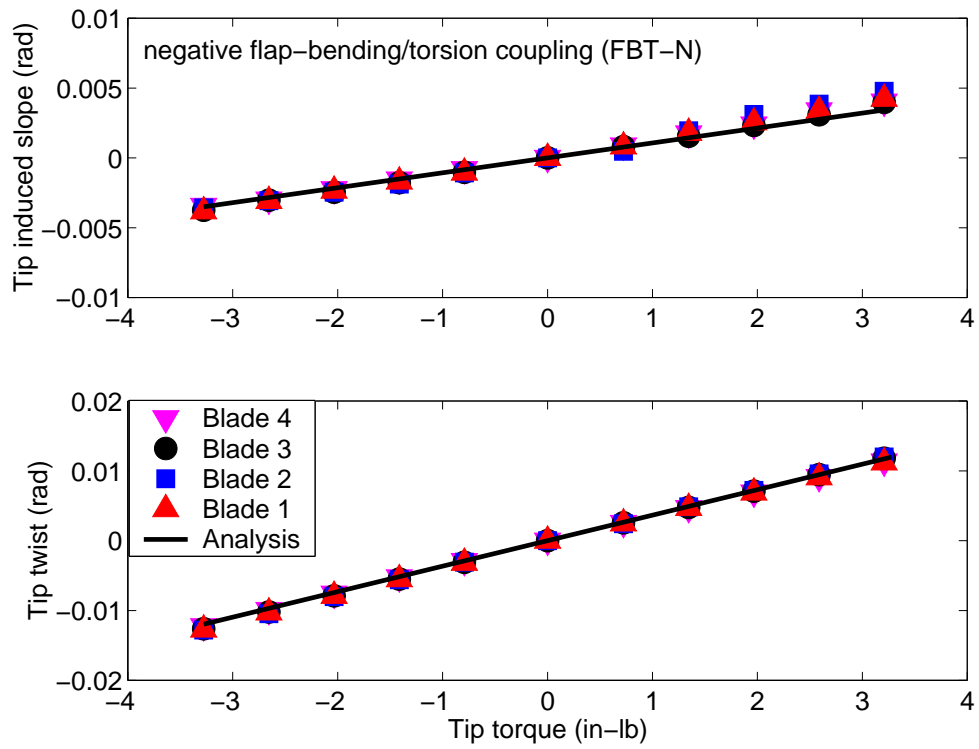


Figure 5.11: Tip response of composite blades with negative flap-bending/torsion coupling (FBT-N) under tip torque

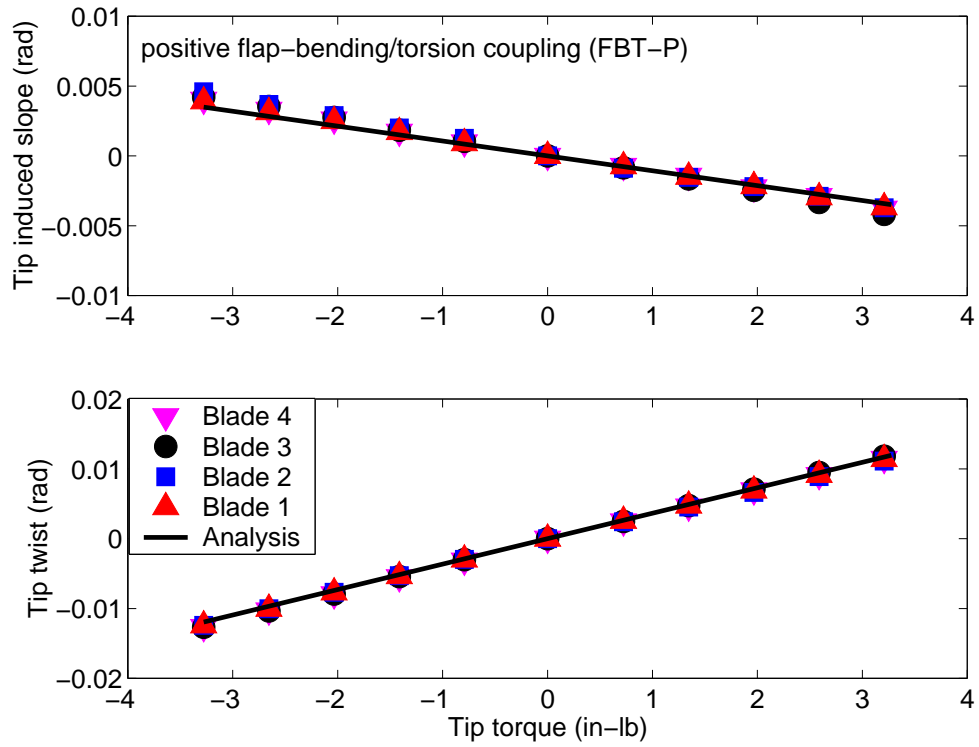


Figure 5.12: Tip response of composite blades with positive flap-bending/torsion coupling (FBT-P) under tip torque

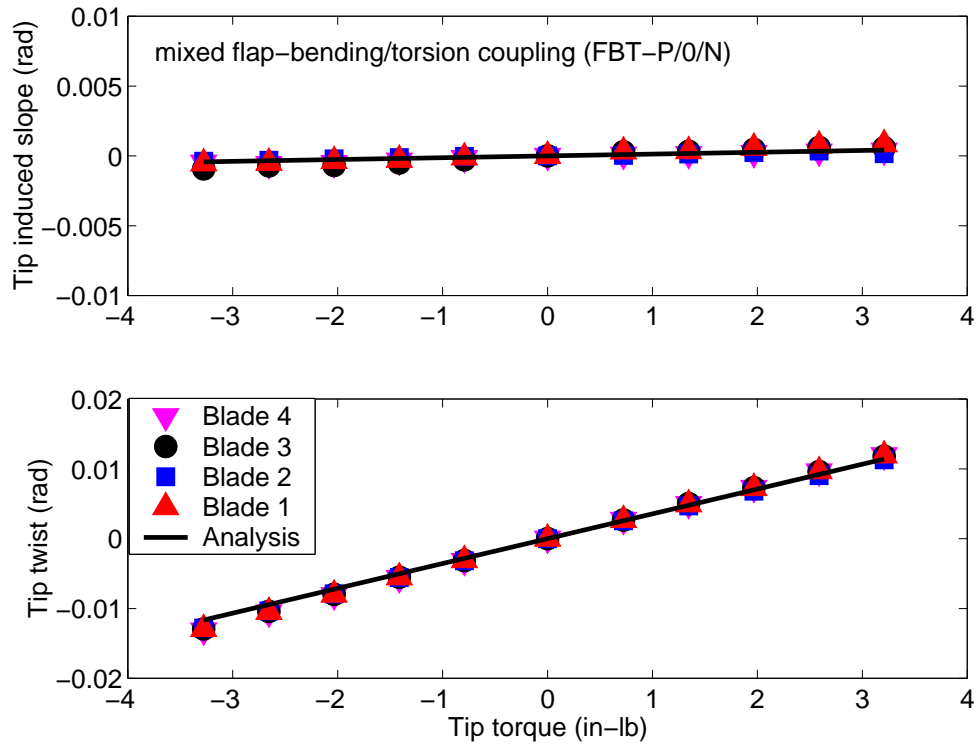


Figure 5.13: Tip response of composite blades with mixed flap-bending/torsion coupling (FBT-P/0/N) under tip torque

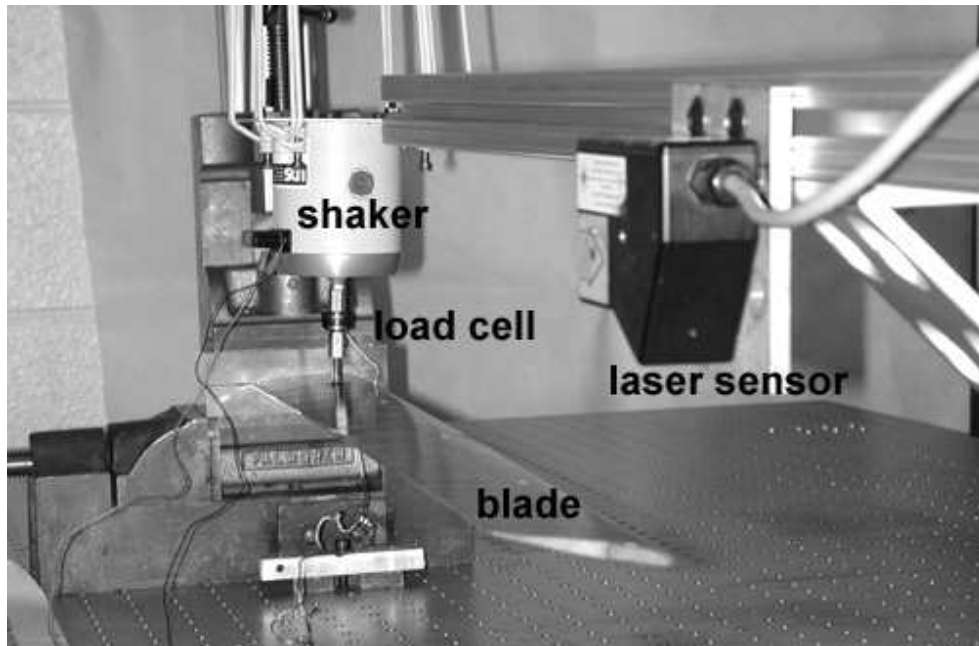


Figure 5.14: Bench-top shaker test of a cantilevered composite tailored blade

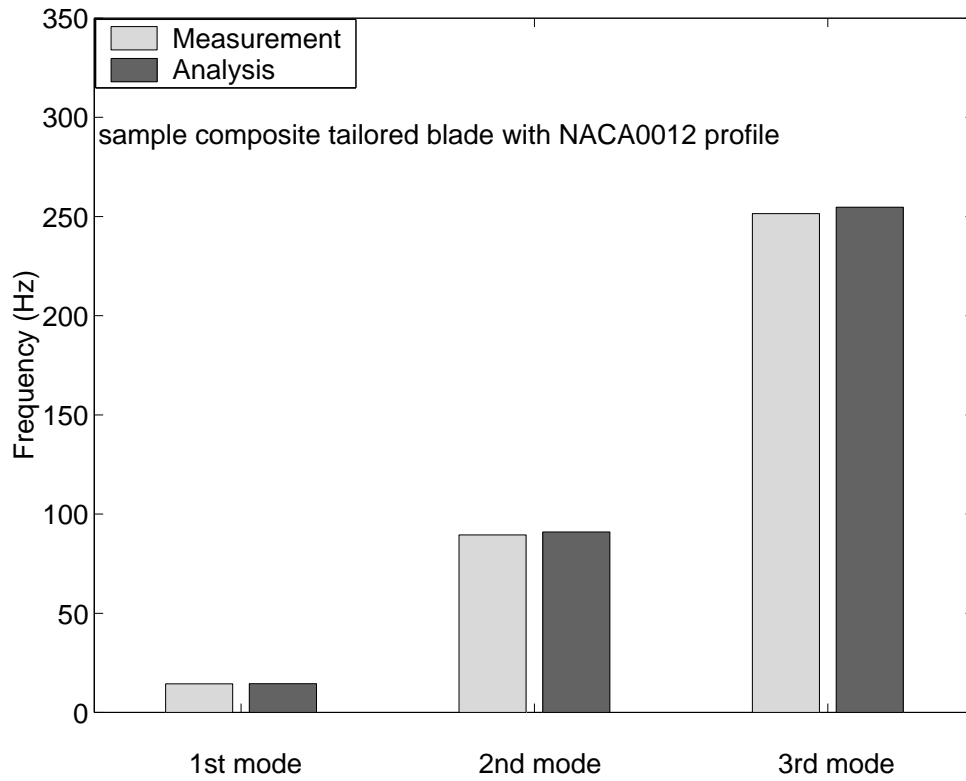


Figure 5.15: Flapwise natural frequencies of a cantilevered composite tailored blade: NACA0012 profile; spar layup: $[35]_4$; skin layup: ± 45 ; web: $\pm 35_s$ (35%chord)

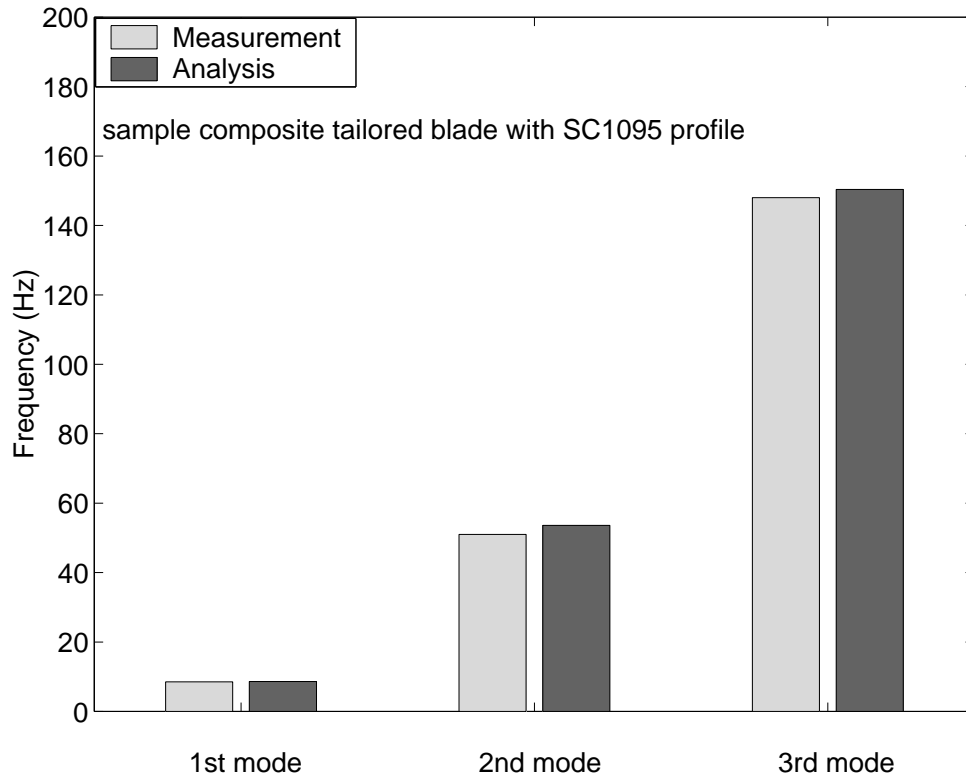


Figure 5.16: Flapwise natural frequencies of a cantilevered composite tailored blade: SC1095 profile; spar layup: $[33]_4$; skin layup: ± 45 ; web: ± 33 (35%chord)

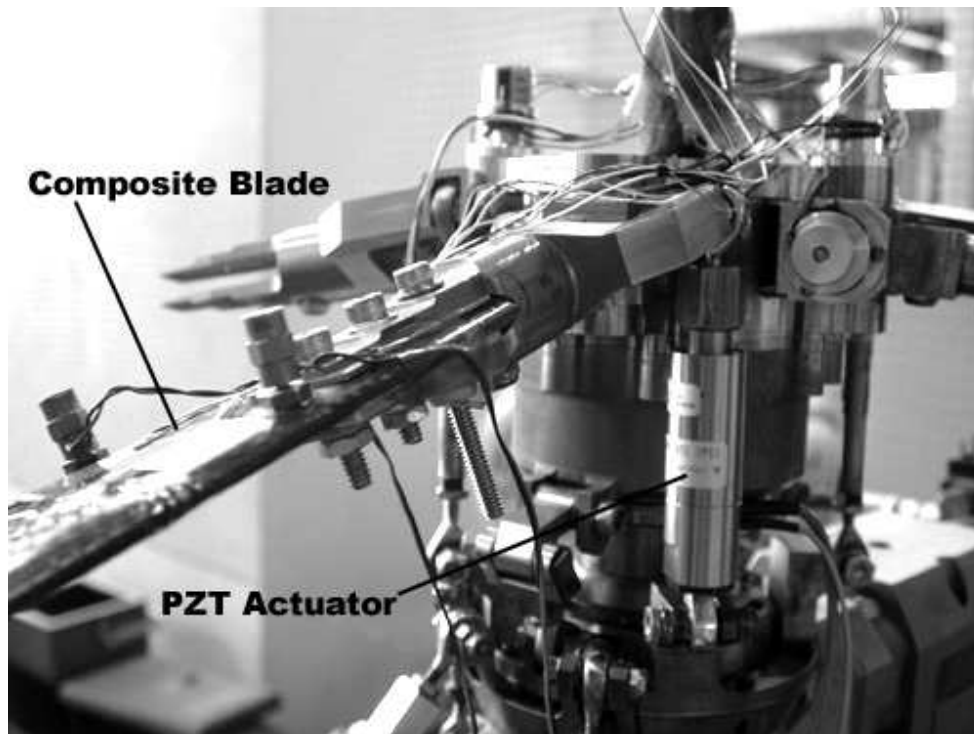


Figure 5.17: Non-rotating dynamic test of composite tailored blade using piezo-electric actuator

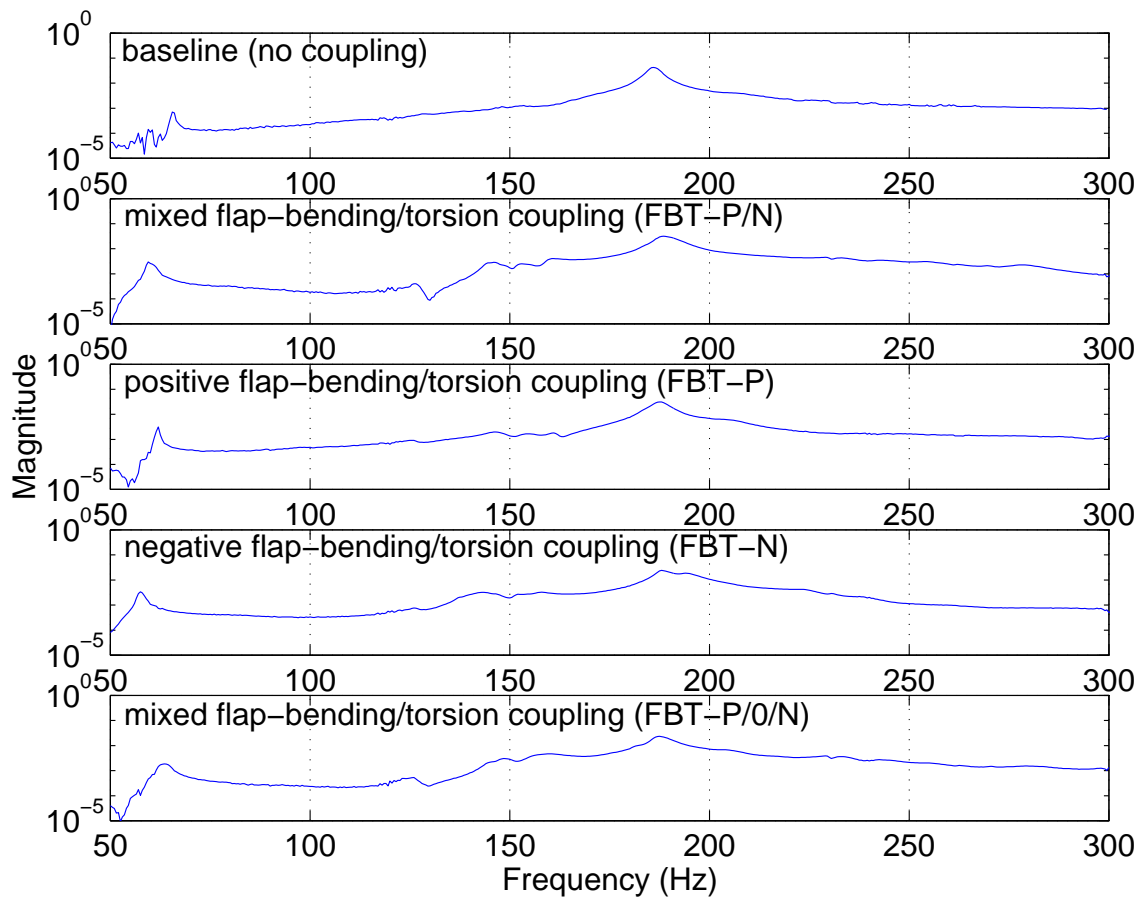


Figure 5.18: Frequency response of non-rotating composite tailored blades

Chapter 6

Wind Tunnel Test Results and Discussion

All five sets of Mach scale composite tailored rotors were tested at different advance ratios and thrust levels in the Glenn L. Martin Wind Tunnel at the University of Maryland. This chapter describes in detail the wind tunnel testing process, the results and the data quality.

6.1 Test Facilities

6.1.1 Rotor Test Stand

The rotor test stand (see Figure 6.1) of the Alfred Gessow Rotorcraft Center is driven by a Mannesmann-Rexroth 75 hp (55.9 kw) hydraulic motor and a Vickers hydraulic pump. This hydraulic pump is powered by an electric motor. As mentioned in Chapter 3, the previous rotor model tests using this stand never reached the rotor speed of 2000 rpm. To test the present Mach scale composite tailored rotors at a rotor speed of 2300 rpm, the electric motor of the

pump system was upgraded from 50 hp (37.3 kw) to 75 hp (55.9 kw). A 2:1 reduction belt and pulley arrangement is incorporated to transfer torque from the hydraulic motor spindle to the main rotor shaft. The test stand can be configured to support either a bearingless or an articulated hub. For the present tests, a fully articulated hub (see Figure 3.6) was installed.

The swashplate of this test stand is controlled by three low bandwidth electric motors. Three LVDT sensors are used to read rotor collective pitch and cyclic pitch angles in degrees. The swashplate allows the rotor collective pitch and cyclic pitch angles to be varied during the test.

A six-component fixed frame balance is used to measure hub forces and moments. A quadratic non-linear calibration relates the six signals to the three forces and three moments. Rotor torque is measured by a torque disk (as shown in Figure 6.2), instrumented with four full-bridge strain gages. The torque disk is integrated into the rotor shaft.

Data transfer between the rotating frame and the fixed frame is via a 64-wire slip-ring that is mated to the shaft below the drive pulley. The data acquisition system consists of an acquisition software developed using LabView, and a National Instruments board (PCI-6071E) with 32 differential input channels running on a Pentium III 600 MHz processor.

Two adjacent flap hinges of the articulated hub are instrumented with Hall effect sensors. These sensors are used to measure the root flap angle of two blades. The outputs of the sensors are displayed in the form of a Lissajous figure on an oscilloscope, as shown in Figure 6.3. This figure is used to trim the rotor during the wind tunnel test.

Two of the four blades in each rotor set are instrumented with three full-

bridge flap and three full-bridge torsion gauges respectively at 30%, 50% and 75% blade radius along the quarter chord of the blade. These strain gauges are calibrated using the bench-top test setup depicted in Figures 5.1 and 5.2.

Two accelerometers are mounted on the body of the stand in longitudinal and lateral directions. They are used to monitor the vibration of the rotor stand.

6.1.2 Wind Tunnel

The Glenn L. Martin Wind Tunnel is a closed circuit tunnel with a rectangular (11 ft \times 7.75 ft) test section. The air speed in the test section ranges from 2 mph to 230 mph.

In the wind tunnel, the rotor stand assembly is installed on a tiltable platform, which can adjust the rotor shaft angle. As shown in Figure 6.1, a composite fuselage model is mounted below the plane of the rotor to provide an aerodynamically smooth shape to the stand assembly. An aluminum shield is also mounted to the post below the fuselage to protect the slip ring from exposure to the airflow.

For the present tests, an accumulator (see Figure 6.4) is installed upstream of the pressure input to the hydraulic motor, to make the hydraulic pressure more stable.

6.2 Test Procedure

Prior to the testing in the wind tunnel, hover testing of all five sets of Mach scale composite tailored rotors was carried out on the test stand to verify blade structural integrity and to perform functional check-outs of the test system and

instrumentation. The rotors were tested at speeds up to 2300 rpm.

Once the rotor system was installed in the wind tunnel, impulse tests were conducted to determine the natural frequencies of the rotor stand. The frequency response was measured by the fixed frame accelerometers. The first stand frequency was identified to be 8.2 Hz. During the test, the rotor was operated to quickly pass through the critical resonance area.

Before starting the wind tunnel, the rotor shaft angle was set and then hover tests at 1000 rpm, 1500 rpm and 1800 rpm were performed to check stand vibration and rotor tracking. The rotor tracking was monitored by a wall-mounted in-plane video camera and a strobe light. Pitch link adjustments can be used to bring all blades into track. Once the desired rotor speed was established, the wind speed was increased to the required advance ratio. Table 6.1 lists the wind tunnel test matrix that was used for all the five rotors.

The rotor was trimmed for the particular combination of rotor speed, wind speed, shaft angle, and thrust level by adjusting the longitudinal and lateral cyclic pitch angles to obtain the minimal size of the Lissajous figure (Figure 6.3). The rotor trim minimized the blade first harmonic flapping amplitudes of two flap angle signals. This implied that the tip path plane was perpendicular to the rotor shaft axis. To make the test data comparable, each of the five rotors was trimmed to the same normal force (from the measurement of fixed frame balance) for a given test condition.

Upon completion of the test, the wind speed was gradually reduced to zero. After the wind tunnel speed was brought down to below 5 mph, the rotor speed was gradually reduced to zero.

6.3 Results and Discussion

6.3.1 Overview of Test Data Quality

Multiple measurements were taken at each wind tunnel test condition. For every combination of rotor speed and advance ratio, the measurements were repeated twice for each normal force trim setting in a sequence of low, high, low, high normal force. The test results are averaged for the repeated data points.

With the rotor trimmed for each target test condition, the data were normally recorded for 6 seconds at 4000 samples/sec. One second of recording time contributed one data block. Figures 6.5 to 6.9 present an overview of vibration measurements at the rotor speed of 2300 rpm, for all the five composite rotor configurations. The data are shown for all advance ratios and the higher of the two thrust levels of the test matrix in Table 6.1. The data for each test condition, comprising two 6 second records, were broken into 12 measurement blocks. For each block the 4/rev component of each of the six fixed frame balance channels (raw voltage) was computed. In these figures, the minimum, the maximum and the mean of the all measurement blocks are respectively represented by the lower bar, the upper bar and center dot. The first column of data represents the values for baseline uncoupled rotor, and the other four columns are the values of coupled FBT-P/N, FBT-P, FBT-N and FBT-P/0/N rotors, respectively.

It is evident that minimum-maximum data spread is generally small for most test conditions at advance ratios of 0.1 to 0.3 (Figures 6.5 to 6.7). However, the data exhibit large scatter for the highest advance ratios 0.35 and 0.38 (wind speed: 172 mph and 187 mph, respectively) at the rotor speed of 2300 rpm (see Figures 6.8 and 6.9). Furthermore, for these tests the minimum-maximum

spreads for the respective different rotors are sufficiently large that they overlap for most of cases, for example, the 4/rev side force (F_{yH}^{4P}) measurement (see Figure 6.8(a)) and 4/rev vertical force (F_{zH}^{4P}) measurement (Figure 6.9(b)). Consequently meaningful comparison between different rotor configurations is not possible at these two highest advance ratios, 0.35 and 0.38.

The larger data scatter at the high advance ratios may be related to the difficulty in trimming the rotors at those test conditions. In addition to inherently high vibration levels that complicate rotor trimming, it may be necessary to further investigate the impact of test stand dynamics (beyond the fundamental natural frequency), test section flow quality, rotor speed stability and other possible contributors to trim problems.

6.3.2 Rotor Vibratory Hub Loads

This section presents measured vibratory hub loads of all five sets of composite rotors for a variety of test conditions.

In Figures 6.10 to 6.12, the measured 4/rev vibratory hub loads of the four composite coupled rotors are compared with those of the baseline uncoupled rotor at the nominal rotor speed of 2300 rpm, for the higher of the two test matrix thrust levels at each advance ratio of 0.1, 0.2 and 0.3. For these cases, C_T/σ is 0.094, 0.093 and 0.078, respectively. The 4/rev vibratory hub forces, including drag force (F_{xH}^{4P}), side force (F_{yH}^{4P}) and normal force (F_{zH}^{4P}) are normalized with the baseline rotor steady normal force in the given test condition. Similarly, the 4/rev vibratory hub moments, including rolling moment (M_{xH}^{4P}), pitching moment (M_{yH}^{4P}) and torque (M_{zH}^{4P}) are normalized with the baseline rotor steady torque for that test condition. It is evident that the highest vibratory hub loads

are encountered in the transition flight region (advance ratio 0.1), followed by the vibration levels at the advance ratio of 0.3. In Figure 6.10, the rolling moment data is unavailable for the baseline rotor for this test condition, because of the loss of a slip ring channel. The normalized 4/rev hub loads demonstrate notable differences between the baseline uncoupled rotor and the composite coupled rotors. This reflects the impact of the composite flap-bending/torsion couplings on the rotor vibratory loads.

Compared to the baseline rotor, all four composite rotors with flap-bending/torsion couplings show a reduction of the 4/rev vertical force (F_{zH}^{4P}), except for the negative coupled rotor (FBT-N) at the advance ratio of 0.3. However, in some cases other vibration components are increased. The reduction varies with coupling configurations and flight conditions.

The composite coupled rotor with the spanwise dual-segmented flap-bending/torsion coupling (FBT-P/N) reduced all three 4/rev vibratory hub forces, 4/rev pitching moment (M_{yH}^{4P}), and 4/rev rolling moment (M_{xH}^{4P}) for test conditions with advance ratios of 0.1 to 0.3. For example, the 4/rev vertical force (F_{zH}^{4P}) is reduced by 9%, 34% and 15% at advance ratios 0.1, 0.2 and 0.3, respectively. The corresponding reductions in the in-plane hub force ($F_{iH}^{4P}: (F_{xH}^{4P^2} + F_{yH}^{4P^2})^{0.5}$) are 14%, 27% and 3%. Data of 4/rev rolling moment (M_{xH}^{4P}) at advance ratio 0.1 is not available and the reductions at advance ratio 0.2 is 13% and at advance ratio 0.3 is 14%. The 4/rev pitching moment (M_{yH}^{4P}) shows the largest percentage reduction compared to the other vibration components for the FBT-P/N rotor. Reductions in the 4/rev pitching moment at all three advance ratios are 46%, 40% and 28%, respectively. It should be noted that typically the vibratory rolling moment dominates the pitching moment and hence contributes more sig-

nificantly to the combined rotor head moment ($M_{hH}^{4P} \cdot (M_{xH}^{4P^2} + M_{yH}^{4P^2})^{0.5}$). The 4/rev vibratory rotor head moment reduction is 15% and 14%, respectively at the advance ratios of 0.2 and 0.3. The spanwise dual-segmented flap-bending/torsion coupled rotor (FBT-P/N) is the optimized design with minimum vibration from the present research. It successfully demonstrates the overall reduction of 4/rev vibratory hub loads.

The composite coupled rotor with spanwise triple-segmented coupling (FBT-P/0/N) achieves higher reduction in the vibratory vertical force (30%) and pitching moment (50%) than the spanwise dual-segmented coupled rotor (FBT-P/N) at advance ratio of 0.1, but lower reduction of the 4/rev in-plane hub force (5%). For both segmented rotor configurations (FBT-P/N and FBT-P/0/N) higher vibration reduction was typically achieved at low advance ratio 0.1 than at 0.3.

The negative coupled composite rotor (FBT-N) reduces the 4/rev drag force (F_{xH}^{4P}) and the 4/rev pitching moment (M_{yH}^{4P}) for the test conditions with advance ratios of 0.1 to 0.3. The 4/rev drag force is reduced by 10%, 26% and 20% at advance ratios 0.1, 0.2 and 0.3, respectively. Reductions in pitching moment at all three advance ratios are 20%, 42% and 55%. The positive coupled composite rotor (FBT-P) exhibits the highest reduction (33%) of the 4/rev vertical force at the low advance ratio of 0.1. However, it increases the other vibration components in most cases at the rotor speed of 2300 rpm.

For all four coupled rotors, the 4/rev vibratory torque increases for most test conditions, compared with those values of the baseline rotor. For example, the FBT-P/N rotor has an increase in the 4/rev vibratory torque at the rotor speed of 2300 rpm and advance ratios of 0.1, 0.2 and 0.3 of 33%, 12% and 32%, respectively. For reference it should be noted that for those three test conditions

the ratio of vibratory to steady torque (for the FBT-P/N rotor) respectively is 13%, 4% and 5%. It is not expected that such an increase in the 4/rev vibratory torque will significantly impact transmission fatigue design of helicopter.

In Figure 6.13, the predicted 4/rev vibratory hub loads of the four composite coupled rotors are compared with those of the baseline rotor at the rotor speed of 2300 rpm and the advance ratio of 0.3. Comparing with the test data (see Figure 6.12), it is seen that the predictions are lower than the measurements. It is not unusual that the analysis underpredicts the rotor vibration level. Several secondary contributors such as the test stand dynamics, and the test section flow quality may affect the measurement of the rotor vibration level. However, for the most components of the vibratory load, the predictions show the same trend of vibration variations as the measurements for the composite coupled rotors.

The vibratory loads of all five sets of composite tailored rotor were also measured at the rotor speed of 2000 rpm. In Figures 6.14 to 6.16, the average measured 4/rev vibratory hub loads of the four composite coupled rotors are compared with those of the baseline uncoupled rotor at this rotor speed, for the higher thrust level at each advance ratio of 0.1, 0.2 and 0.3. For these test conditions, the rotor thrust level C_T/σ is 0.094, 0.09 and 0.071, respectively. The minimum-maximum data spread for these cases is presented in Appendix D. In comparing these 2000 rpm data and 2300 rpm data (Figures 6.10 to 6.12), it should be noted that the cross-over of third blade flap bending frequency and first torsion frequency is near 2150 rpm (see Figure 3.24) and hence rotor dynamics at 2000 and 2300 rpm are different.

Similar to the results at the nominal speed of 2300 rpm, all four composite coupled rotors exhibit a reduction of the 4/rev vertical force (F_{zH}^{4P}), compared

to the baseline rotor. At a rotor speed of 2000 rpm, the positive coupled rotor (FBT-P) generally achieves larger F_{zH}^{4P} reductions than the other coupled rotors. The 4/rev vertical force of FBT-P rotor is reduced by 30%, 55% and 39% at advance ratios 0.1, 0.2 and 0.3, respectively. At this rotor speed, the highest F_{zH}^{4P} reduction is 58% achieved by the negative coupled rotor (FBT-N) at advance ratio of $\mu = 0.2$.

The mixed coupled composite rotor with spanwise dual-segmented flap-bending/-torsion coupling (FBT-P/N) still reduces all three 4/rev vibratory hub forces, 4/rev pitching moment and 4/rev rolling moment for test conditions with advance ratios of 0.1 to 0.3, at the rotor speed of 2000 rpm. For example, the 4/rev vertical force is reduced by 19%, 37% and 21% at advance ratios 0.1, 0.2 and 0.3, respectively. The reductions of 4/rev in-plane hub force (F_{iH}^{4P}) are 9%, 24% and 12%. Reductions in 4/rev rolling moment (M_{xH}^{4P}) at advance ratio 0.2 is 41% and at advance ratio 0.3 is 30%. The reductions of 4/rev pitching moment (M_{yH}^{4P}) at all three advance ratios are 13%, 11% and 14%. The mixed coupled composite rotor with spanwise triple-segmented flap-bending/torsion coupling (FBT-P/0/N) shows more 4/rev vertical force (F_{zH}^{4P}) reduction than the FBT-P/N rotor, with reduction of 30%, 50% and 25% at advance ratios 0.1, 0.2 and 0.3, respectively. But it does not show overall superior performance in the reduction of other 4/rev vibration components.

When considering the in-plane vibratory 4/rev hub force (F_{iH}^{4P}) of the positive coupled rotor (FBT-P), it is interesting to note that FBT-P rotor obtains high reduction in the 4/rev in-plane force (F_{iH}^{4P}) for all three advance ratios at 2000 rpm, but increases it for all advance ratios at 2300 rpm. That is most likely attributable to the different frequency placement at 2000 rpm and 2300 rpm.

To evaluate the impact of different thrust levels on the effectiveness of the flap-bending/torsion coupling on rotor vibratory loads, results for the lower of the two test matrix thrust levels for each advance ratio are shown in Figures 6.17 to 6.19 (for a rotor speed of 2300 rpm). In these cases, C_T/σ is 0.077, 0.075 and 0.061 at advance ratios of 0.1, 0.2 and 0.3, respectively.

As shown in these plots, all four composite coupled rotors reduce the 4/rev vertical force (F_{zH}^{4P}), compared to the baseline rotor. The reduction of F_{zH}^{4P} is highest at the advance ratio of 0.2 for all coupled rotors. Reductions in 4/rev vertical force for four coupled rotors at this advance ratio are 32% (FBT-P/N), 28% (FBT-P), 33% (FBT-N) and 34% (FBT-P/0/N), respectively.

The spanwise dual-segmented coupled rotor (FBT-P/N) still reduces all three vibratory hub forces and the pitching and rolling moment for test conditions with advance ratios of 0.1 to 0.3. For example, the 4/rev drag force is reduced by 27%, 27% and 7% at advance ratios 0.1, 0.2 and 0.3, respectively. The reductions of in-plane hub force (F_{iH}^{4P}) are 22%, 19% and 1%. Reductions in pitching moment (M_{yH}^{4P}) at all three advance ratios are 58%, 35% and 13%.

Comparing Figures 6.17- 6.19 with Figures 6.10- 6.12, it is evident that the variations of 4/rev vibratory hub loads between each coupled rotor and the baseline rotor for the lower of the two test matrix thrust levels exhibit the similar trend and percentage changes as those for the highest thrust level. The test results for the lower thrust level at the rotor speed of 2000 rpm are presented in Appendix D.

From the measurement of wind tunnel tests, it is shown that the compos-

ite tailored flap-bending/torsion couplings have significant effects on the 4/rev vibratory hub loads. The test results demonstrate that, with a suitable tailoring of flap-bending/torsion coupling in the blade structure (such as the mixed coupled spanwise dual-segmented flap-bending/torsion coupling: FBT-P/N from the current research), it is possible to significantly reduce rotor 4/rev vibratory hub forces, pitching moment and rolling moment, for a variety of flight conditions.

6.3.3 Blade Oscillatory Flap Bending Moment

The oscillatory flap bending moment of the composite blades were also measured during the test using full-bridge flap strain gages along the blade span.

Figure 6.20(a) shows a 0.2 second time domain window of the blade oscillatory flap bending moment for the baseline blade and the blade with spanwise dual-segmented coupling (FBT-P/N) at an advance ratio of 0.3 and rotor speed of 2000 rpm. Figure 6.20(b) shows the corresponding frequency spectrum. The measurements were taken at three spanwise locations: 30%, 50% and 75% radius. From Figure 6.20, it is seen that the amplitudes of 3/rev (100Hz) and 5/rev (167Hz) oscillatory flap bending moment of the mixed coupling blade are lower than those of the baseline blade. The percentage reductions are: 13% and 71%, respectively, for 3/rev and 5/rev at the blade root location (30% radius); 8% and 16%, respectively, for 3/rev and 5/rev at the blade mid span (50% radius); and 59% for 5/rev at the blade outboard location (75% radius). This reduction of the 3/rev and 5/rev blade flap bending loads is a key driver in reducing the 4/rev rotor hub loads. The flap bending mode shape plotted in Figures 3.25 depicts the coupling of blade flap and torsion. Due to the coupling, the change

of blade flap bending moment induces the change of blade elastic twist. The vibration change possibly occurs as a result of the changes in the amplitude and phasing of the torsion response, and the energy transfer between the flap and torsion motions. Thus, with proper tailoring of the blade flap-bending/torsion coupling (in terms of coupling strength and spanwise distribution), the rotor blade dynamic response can be influenced to reduce vibratory hub loads.

In Figure 6.20, it is also seen that both blades have higher bending moments at the mid span (50% radius) than at 30% and 75% span. More test results of oscillatory flap bending moments are shown in Figures 6.21 to 6.23 at advance ratios of 0.1, 0.2 and 0.3 with the rotor speed of 2300 rpm. In these figures, the test results of four composite coupled blades are compared to those of baseline blade at the mid span (50% radius). The results are presented in both time domain and frequency domain. At the advance ratio of 0.1, the data of the composite blade with the mixed coupling (FBT-P/N) are not available due to an improper functioning of the corresponding channel of the slip-ring. Figures 6.21(b) to 6.23(b) shows that the amplitudes of 3/rev oscillatory flap bending moment of three coupled blades (FBT-P/N, FBT-N, and FBT-P/0/N) are significantly lower than those of baseline blade at all three advance ratios. The percentage reductions are: 58% for FBT-N blade and 57% for FBT-P/0/N blade at the advance ratio of 0.1; 62% by FBT-P/N blade, 48% by FBT-N and 51% by FBT-P/0/N at the advance ratio of 0.2, and 41% by FBT-P/N blade, 8% by FBT-N and 40% by FBT-P/0/N at the advance ratio of 0.3.

6.4 Feasibility Study of Full Scale Composite Tailored Rotor

The wind tunnel test results shown in previous sections have demonstrated the feasibility of using composite tailored flap-bending/torsion coupling in rotor blades to reduce 4/rev rotor vibratory hub loads. These Mach scale composite coupled rotors use the same rotor hub system, retain the same blade profile, planform and weight as the baseline uncoupled rotor. The only difference between the composite coupled rotors and the baseline rotor is the composite layup of their D-spars. The analysis in section 3.2 also showed that the simulated composite coupled blade of the UH-60 BLACK HAWK rotor has potential benefits in vibration reduction. This section discusses the feasibility of the development of full scale composite coupled rotor with low vibration for the UH-60 BLACK HAWK rotor.

Composite spars are widely used in the design of full scale blades as primary load path carriers. It is envisioned that the spar layup can be modified to introduce beneficial structural couplings, while retaining the primary spar functions to carry blade loads and contribute to blade frequency placement. For the purpose of this full-scale feasibility assessment, the blade structure will be similar to the Mach scale blade structure, comprising a graphite/epoxy D-spar, foam cores and graphite/epoxy weave skin. Actual full scale design studies will have to further address fabrication, quality assurance and maintainability and reliability requirements.

For this feasibility study, the key issue is to design the full scale composite tailored blade with the same dynamic properties as the baseline uncoupled UH-

60 BLACK HAWK blade. For this purpose, the blade non-dimensional flapwise stiffness, chordwise stiffness, torsion stiffness and axial stiffness of the UH-60 rotor are used as design targets for full scale composite coupled blades. In the meantime, the flap-bending/torsion coupling is also checked to obtain a desired value. Using the design tools and design process for composite tailored blade developed in Chapter 2 and Chapter 3, the layups of the composite D-spar and the composite skin are obtained for the full scale composite tailored blades, as shown in Table 6.2. The full scale composite blades have a structure with a graphite/epoxy IM7/8552 composite D-spar. The graphite/epoxy IM7/8552 weave is used to build blade skin. The uncoupled baseline composite blade has a balanced D-spar layup, while the composite coupled blade has an unbalanced D-spar layup. With these layup design, the full scale composite tailored blades have same non-dimensional flapwise stiffness and torsion stiffness as the UH-60 BLACK HAWK blade (see Table 6.3). The axial stiffness and chordwise stiffness of the full scale composite coupled rotor are also very close to the values of the UH-60 BLACK HAWK rotor. Their natural frequencies are almost same, as shown in Table 6.4.

For these full scale composite coupled blades, the non-dimensional flap-bending/torsion coupling stiffness is 0.31 (normalized with respect to the blade flapwise stiffness), which is the same value used for the analysis of simulated coupling configurations of the UH-60 BLACK HAWK rotor (see section 3.2). In this analysis, a simulated configuration of the UH-60 blade with spanwise dual-segmented flap-bending/torsion coupling (FBT-P/N) reduced the overall 4/rev vibratory hub loads, compared to the baseline UH-60 uncoupled rotor. Thus, with the same mixed spanwise coupling distribution, the full scale composite

coupled blade with the composite layup developed in this feasibility study can obtain the same benefits of vibration reduction (see section 3.2) for the UH-60 rotor.

Table 6.1: Test matrix for wind tunnel test of Mach scale composite rotors

Rotor speed (rpm)	Shaft angle (deg)	Advance ratio	C_T/σ
2000	4	0.1	0.077
2000	4	0.1	0.094
2300	4	0.1	0.077
2300	4	0.1	0.094
2000	4	0.2	0.072
2000	4	0.2	0.090
2300	4	0.2	0.075
2300	4	0.2	0.093
2000	4	0.3	0.060
2000	4	0.3	0.071
2300	4	0.3	0.061
2300	4	0.3	0.078
2300	8	0.35	0.033
2300	8	0.35	0.052
2300	8	0.38	0.024
2300	8	0.38	0.042

Table 6.2: Skin, spar and web layups of full scale composite tailored rotors

Skin layup	$[\pm 45]_4$ weave
Uncoupled spar layup	$[0_3 / \pm \theta_A / \pm \theta_B / \pm \theta_{C,2} / \pm \theta_D]_s$
Coupled spar layup	$[0_3 / \theta_{A,2} / \theta_{B,2} / \theta_{C,4} / \theta_{D,2}]_s$
Web layup	$[0_3 / \pm \theta_A / \pm \theta_B / \pm \theta_{C,2} / \pm \theta_D]_s$
Web location	34% chord
Material	IM7/8552

Table 6.3: Normalized stiffness of the UH-60 blade and the full scale composite coupled blade, with respect to the UH-60 flapwise stiffness (EI_y : flapwise stiffness, EI_z : chordwise stiffness, GJ : torsion stiffness, EFT : flap-bending/torsion coupled stiffness)

Blade	EI_y	EI_z	GJ	EFT
UH-60 rotor	1.	29.	0.99	0.
Full scale composite coupled rotor	1.	30.	0.99	0.31

Table 6.4: Natural frequency comparison of the UH-60 blade and the full scale composite coupled blade

Blade	Lag 1	Flap 1	Flap 2	Flap 3	Torsion 1
UH-60 rotor	0.271	1.036	2.747	4.516	4.229
Full scale composite coupled rotor	0.271	1.036	2.730	4.440	4.226

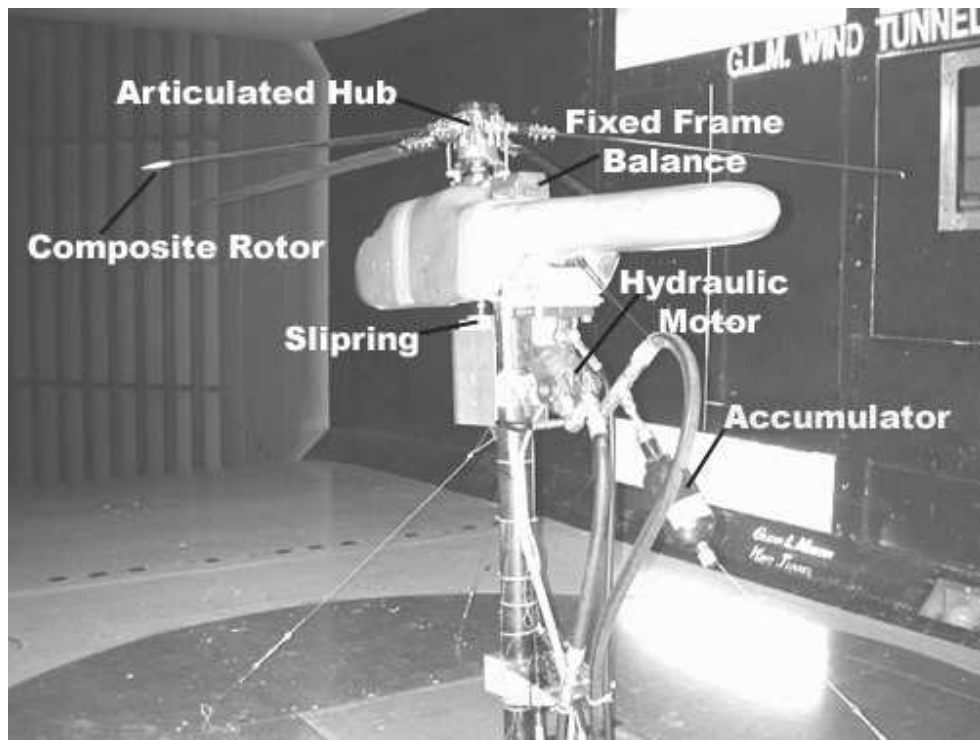


Figure 6.1: Rotor test stand in the Glenn L. Martin Wind Tunnel

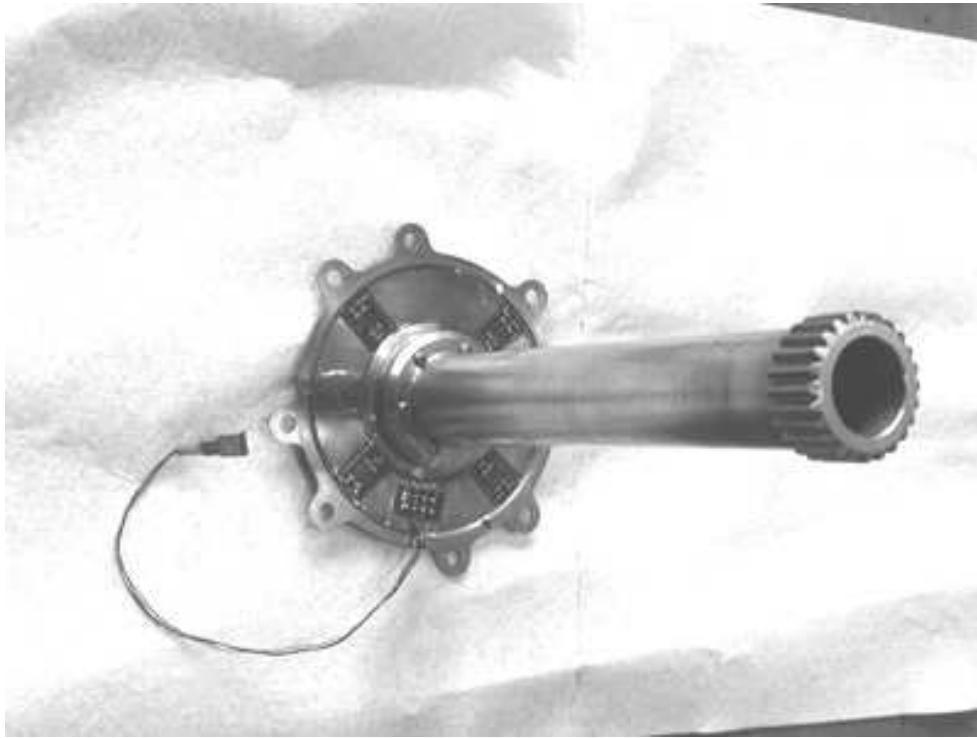


Figure 6.2: Rotor torque disk

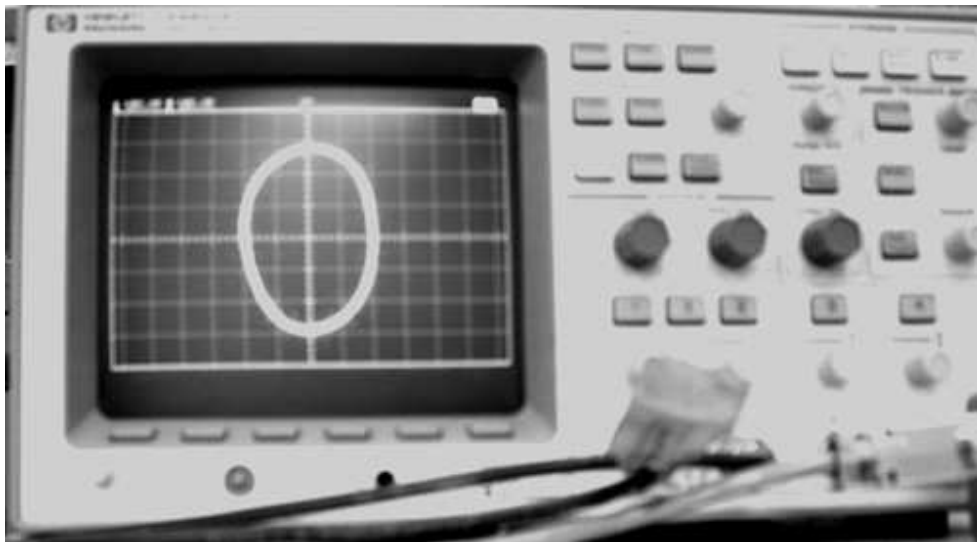


Figure 6.3: Lissajous figure of two flap angle signals

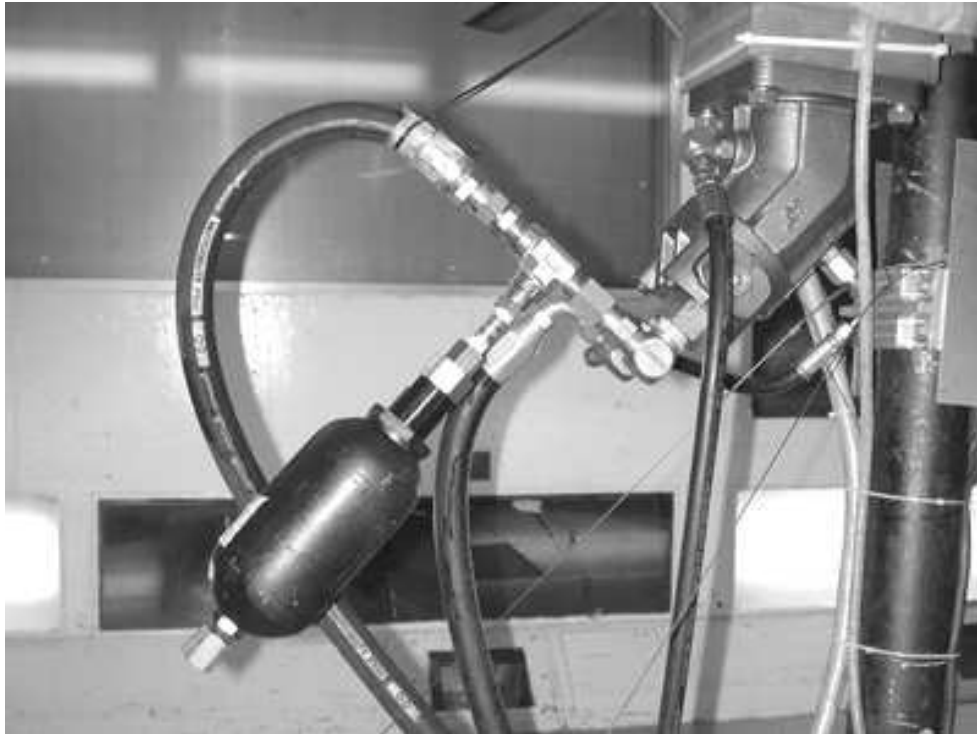
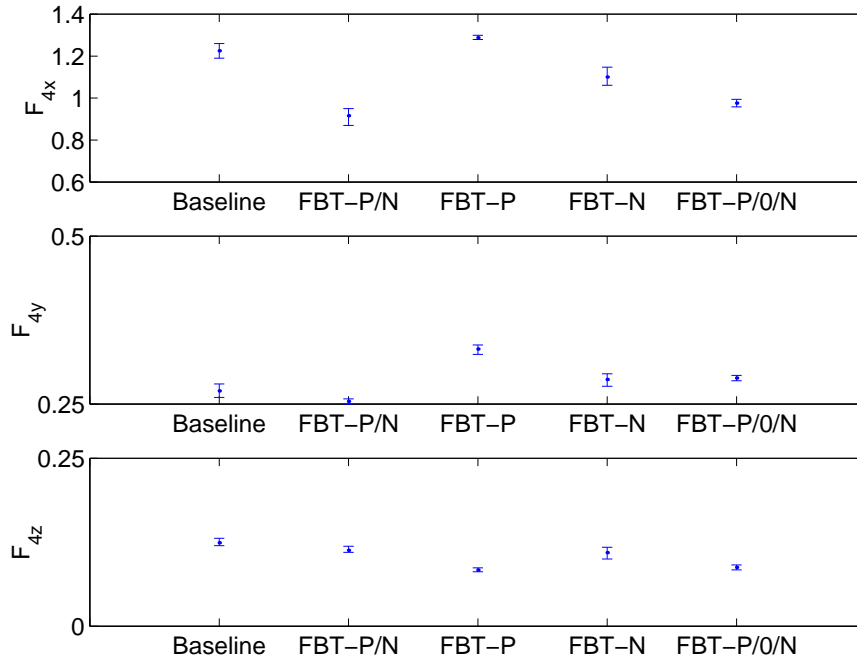
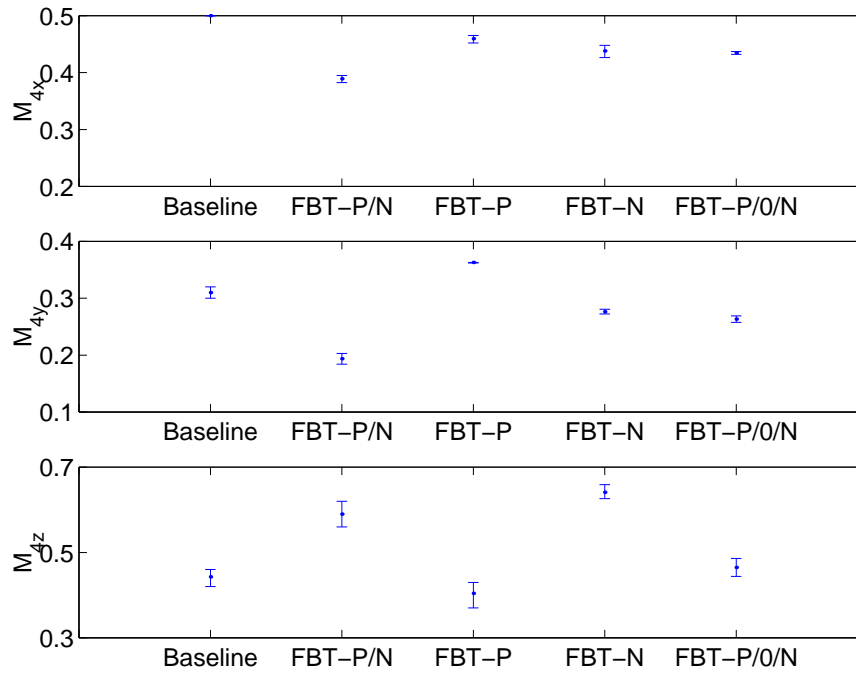


Figure 6.4: Accumulator connected to the hydraulic motor

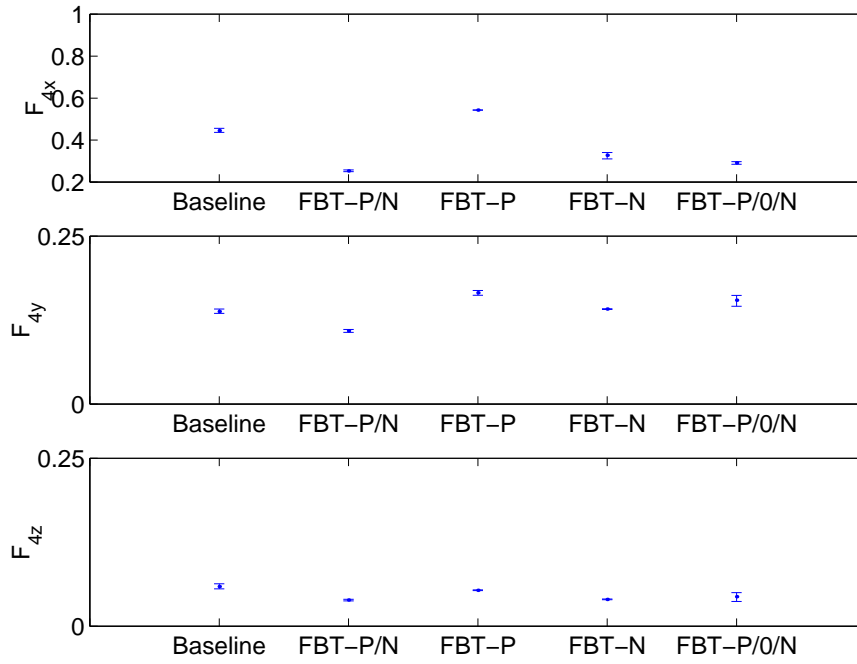


(a) 4/rev vibratory forces

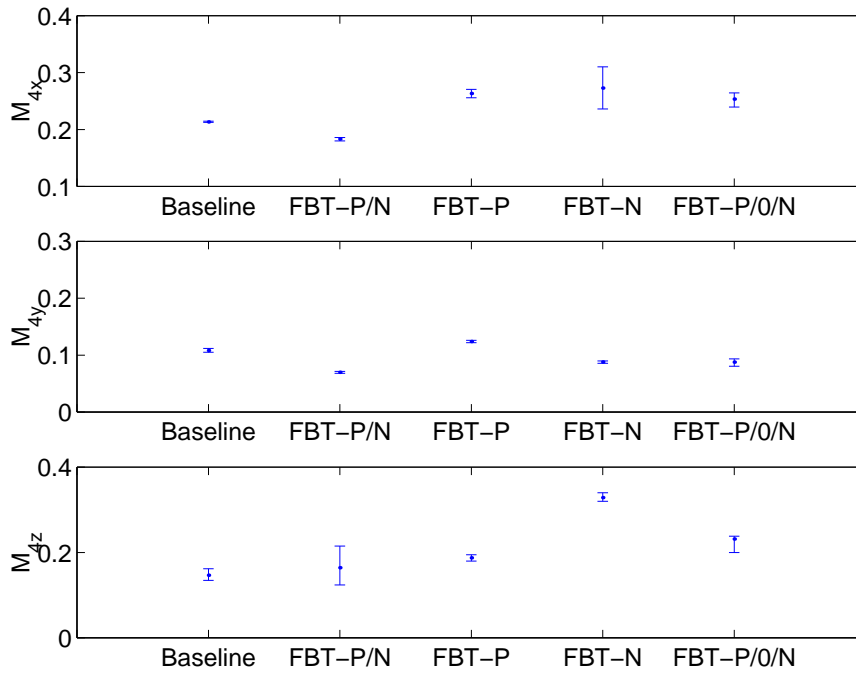


(b) 4/rev vibratory moments

Figure 6.5: The average, minimum and maximum values of the measured 4/rev vibration at $\mu = 0.1$, $C_T/\sigma = 0.094$, 2300 rpm

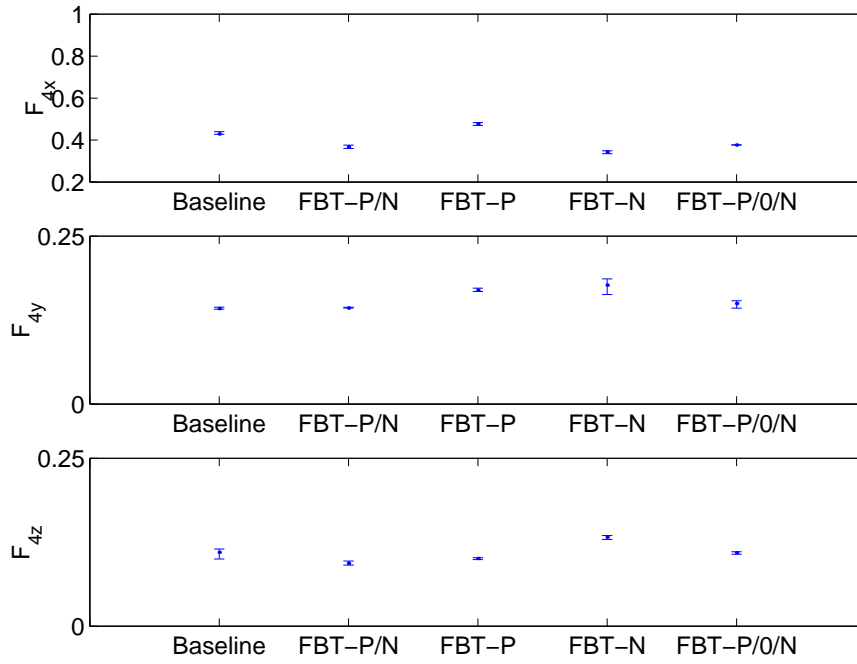


(a) 4/rev vibratory forces

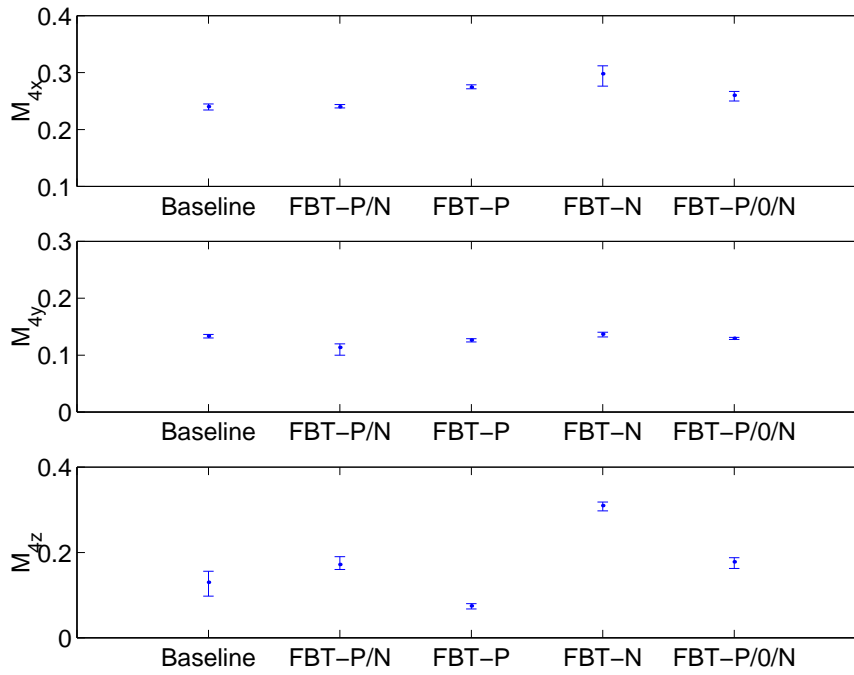


(b) 4/rev vibratory moments

Figure 6.6: The average, minimum and maximum values of the measured 4/rev vibration at $\mu = 0.2$, $C_T/\sigma = 0.093$, 2300 rpm

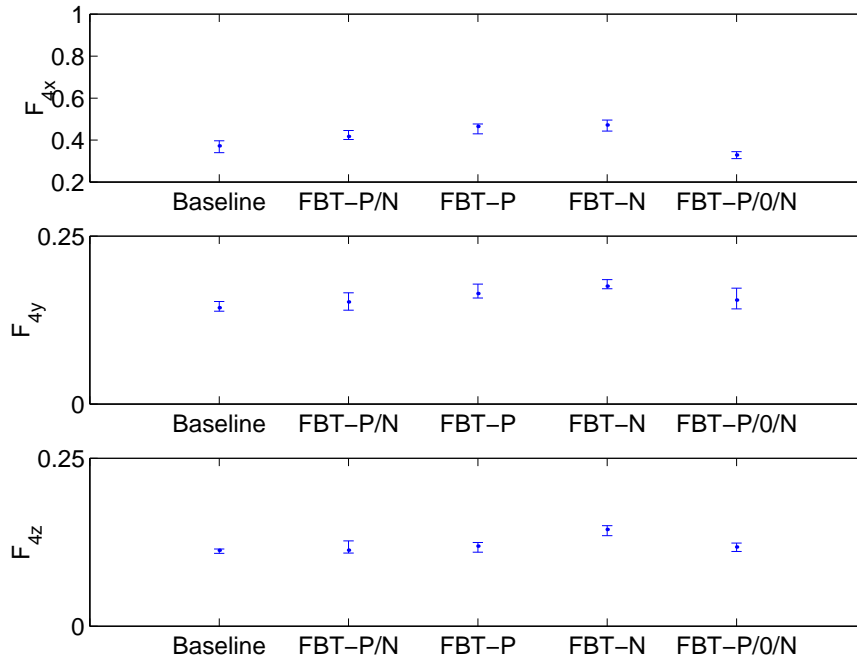


(a) 4/rev vibratory forces

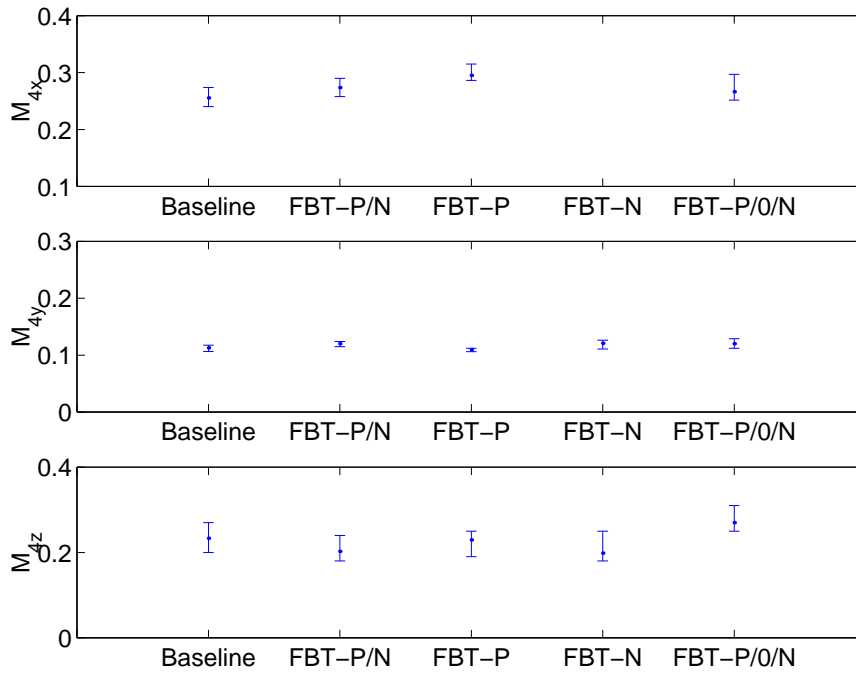


(b) 4/rev vibratory moments

Figure 6.7: The average, minimum and maximum values of the measured 4/rev vibration at $\mu = 0.3$, $C_T/\sigma = 0.078$, 2300 rpm

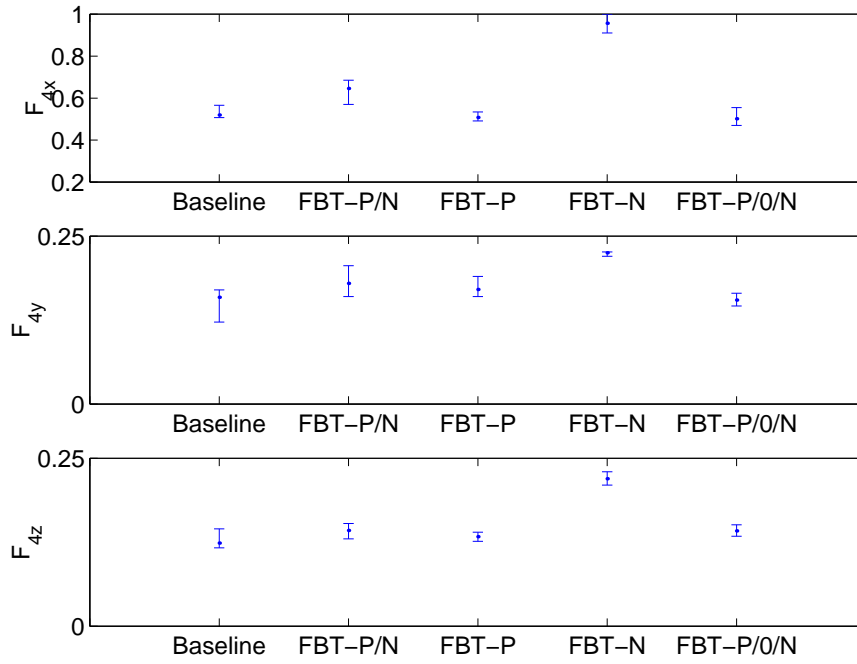


(a) 4/rev vibratory forces

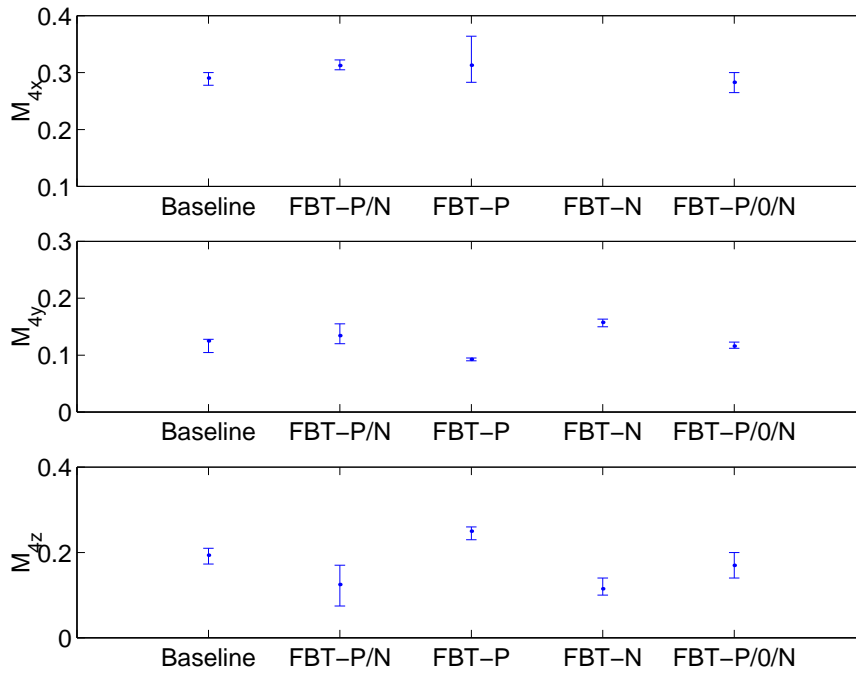


(b) 4/rev vibratory moments

Figure 6.8: The average, minimum and maximum values of the measured 4/rev vibration at $\mu = 0.35$, $C_T/\sigma = 0.052$, 2300 rpm



(a) 4/rev vibratory forces



(b) 4/rev vibratory moments

Figure 6.9: The average, minimum and maximum values of the measured 4/rev vibration at $\mu = 0.38$, $C_T/\sigma = 0.042$, 2300 rpm

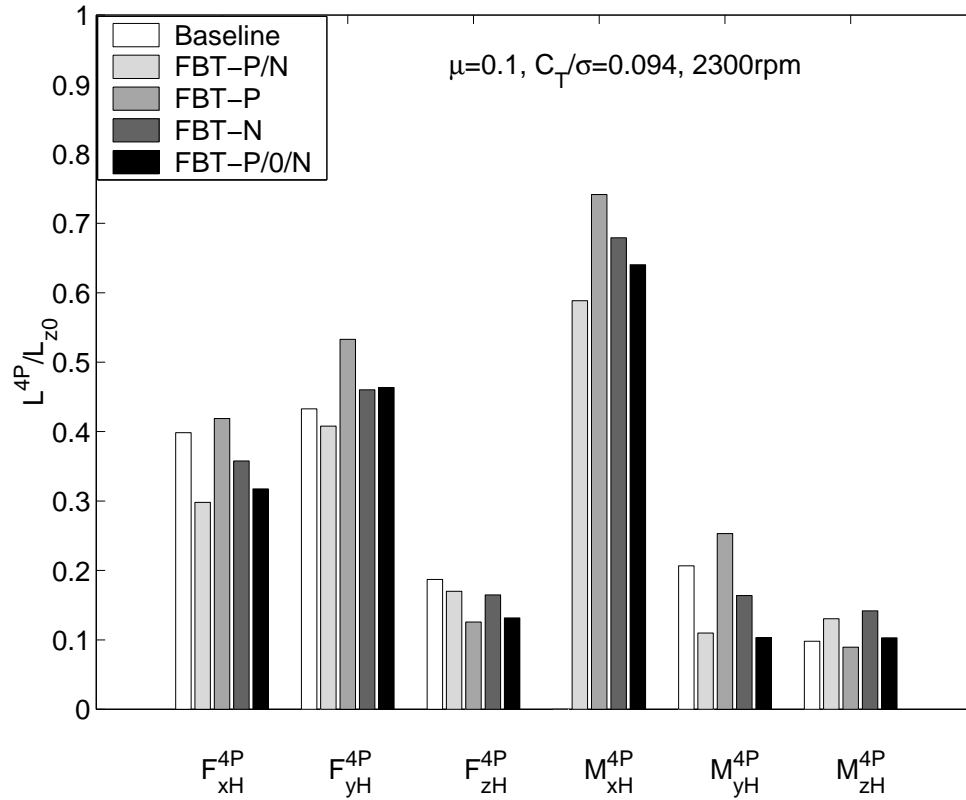


Figure 6.10: Non-dimensional measured 4/rev vibratory hub loads at $\mu = 0.1, C_T/\sigma = 0.094, 2300 \text{ rpm}$ (F_{xH}^{4P} : 4/rev drag force, F_{yH}^{4P} : 4/rev side force, F_{zH}^{4P} : 4/rev vertical force, M_{xH}^{4P} : 4/rev rolling moment, M_{yH}^{4P} : 4/rev pitching moment, M_{zH}^{4P} : 4/rev torque)

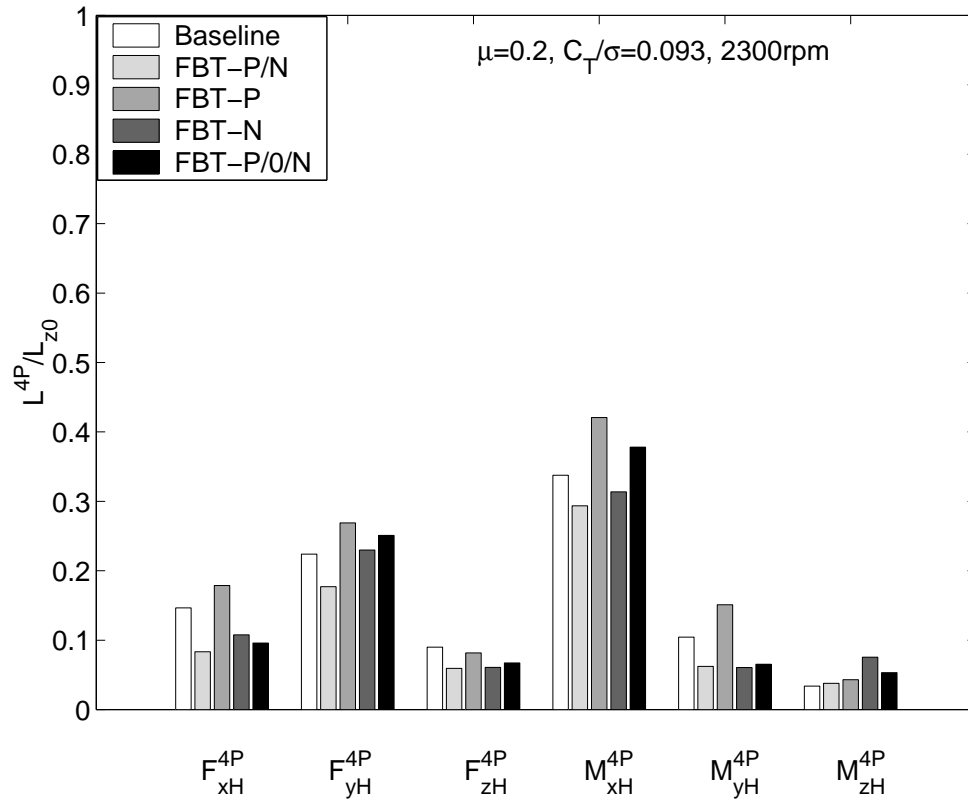


Figure 6.11: Non-dimensional measured 4/rev vibratory hub loads at $\mu = 0.2, C_T/\sigma = 0.093, 2300 \text{ rpm}$

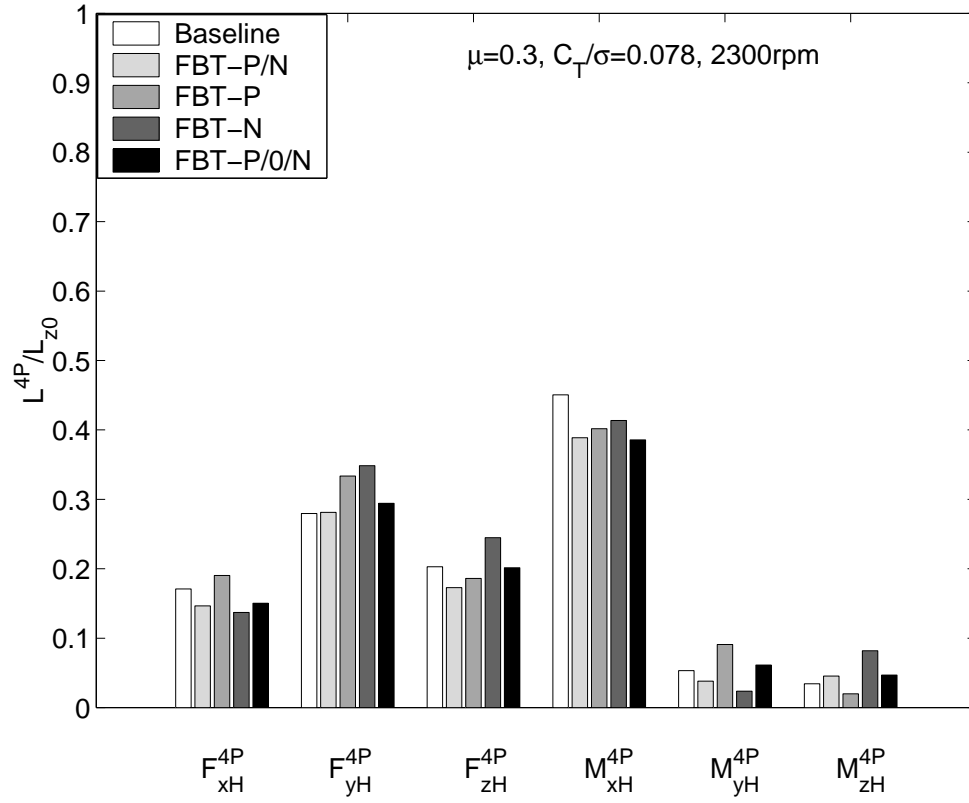


Figure 6.12: Non-dimensional measured 4/rev vibratory hub loads at $\mu = 0.3, C_T/\sigma = 0.078, 2300 \text{ rpm}$

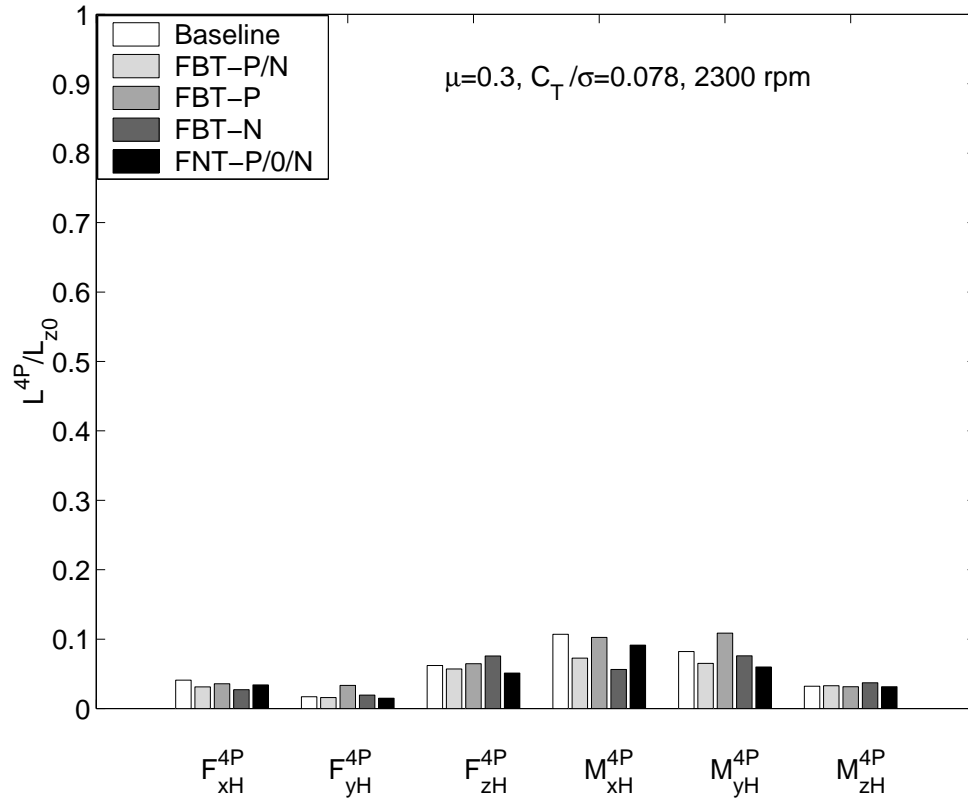


Figure 6.13: Predicted 4/rev vibratory hub loads at $\mu = 0.3, C_T/\sigma = 0.078, 2300$ rpm

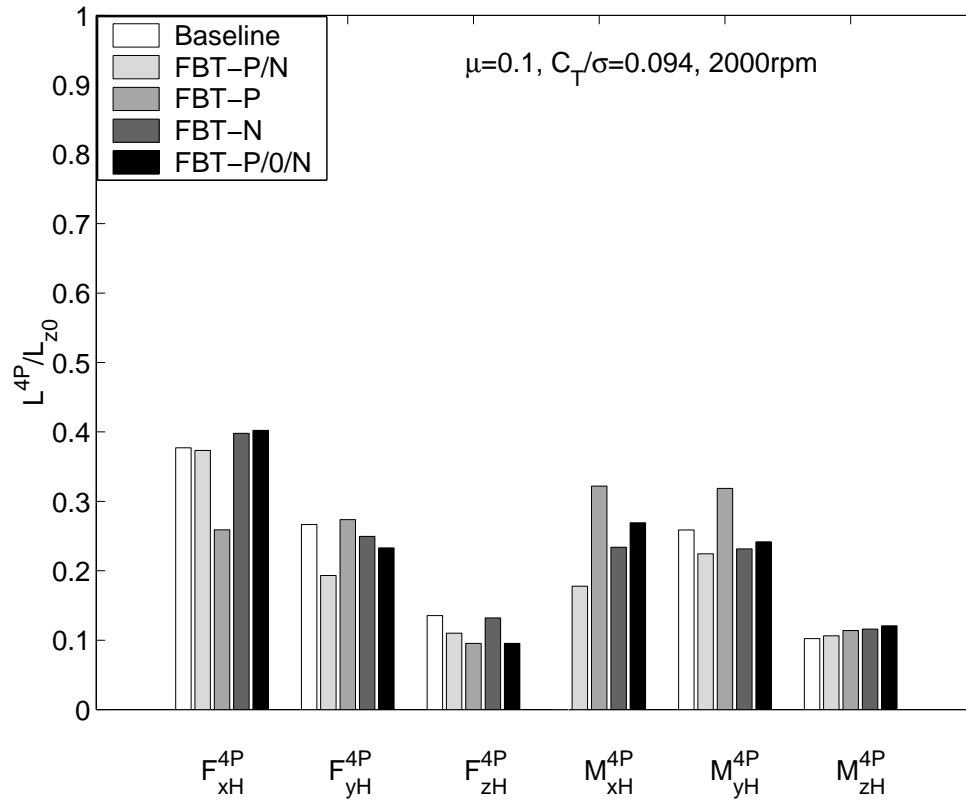


Figure 6.14: Non-dimensional measured 4/rev vibratory hub loads at $\mu = 0.1, C_T/\sigma = 0.094, 2000 \text{ rpm}$

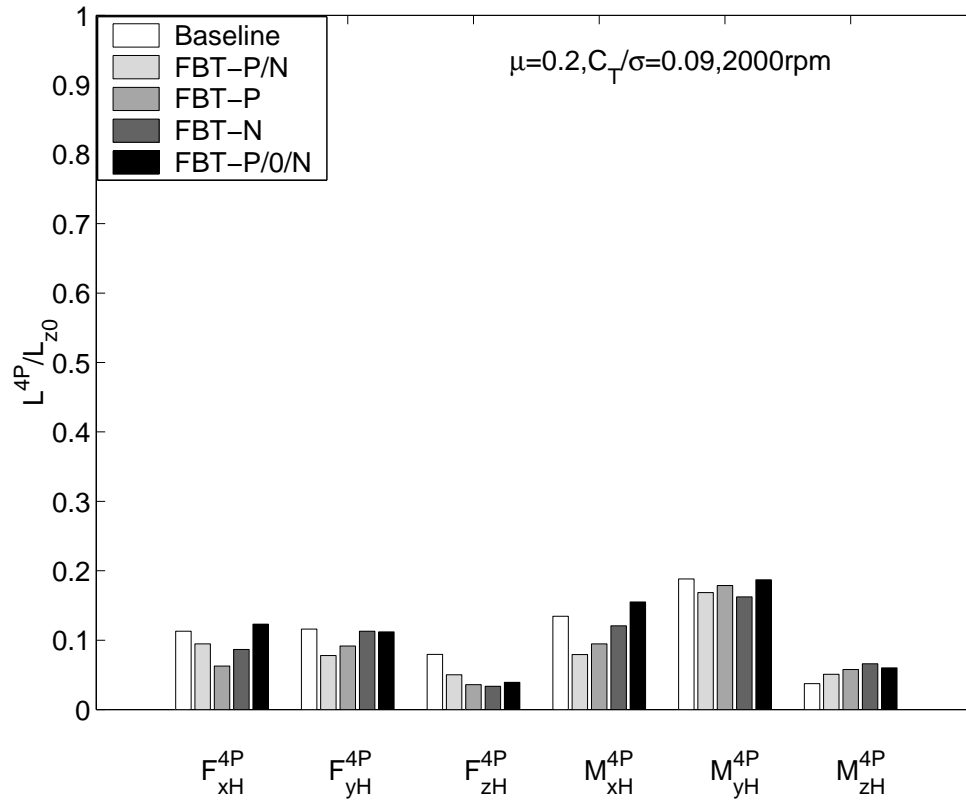


Figure 6.15: Non-dimensional measured 4/rev vibratory hub loads at $\mu = 0.2, C_T/\sigma = 0.090, 2000 \text{ rpm}$

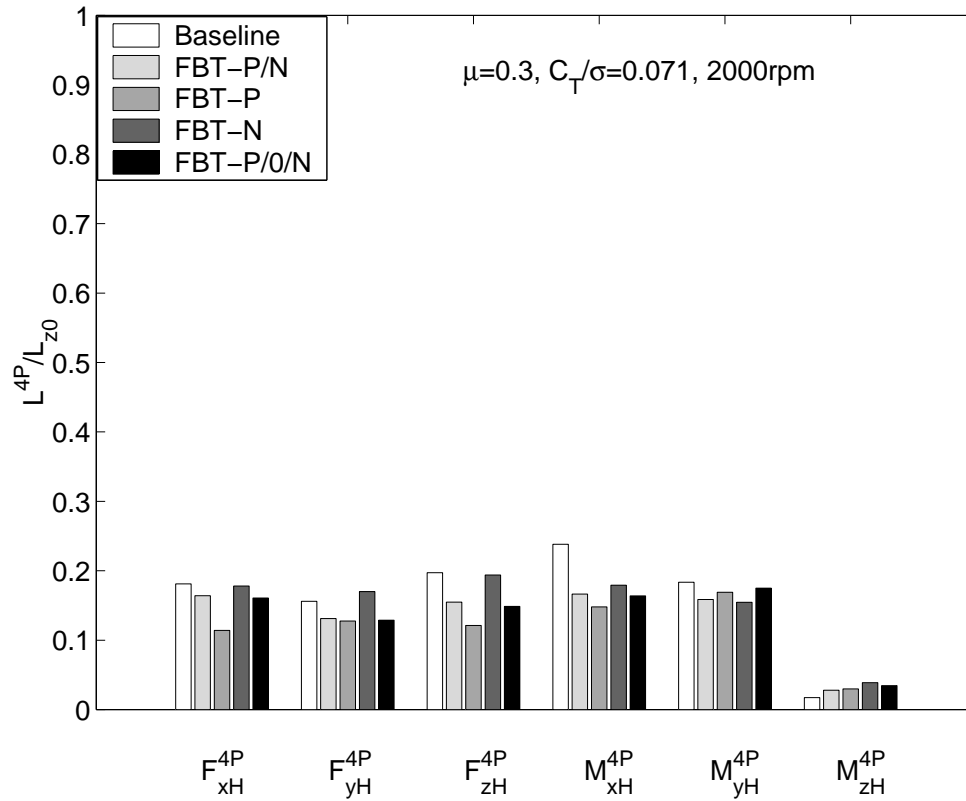


Figure 6.16: Non-dimensional measured 4/rev vibratory hub loads at $\mu = 0.3, C_T/\sigma = 0.071, 2000 \text{ rpm}$

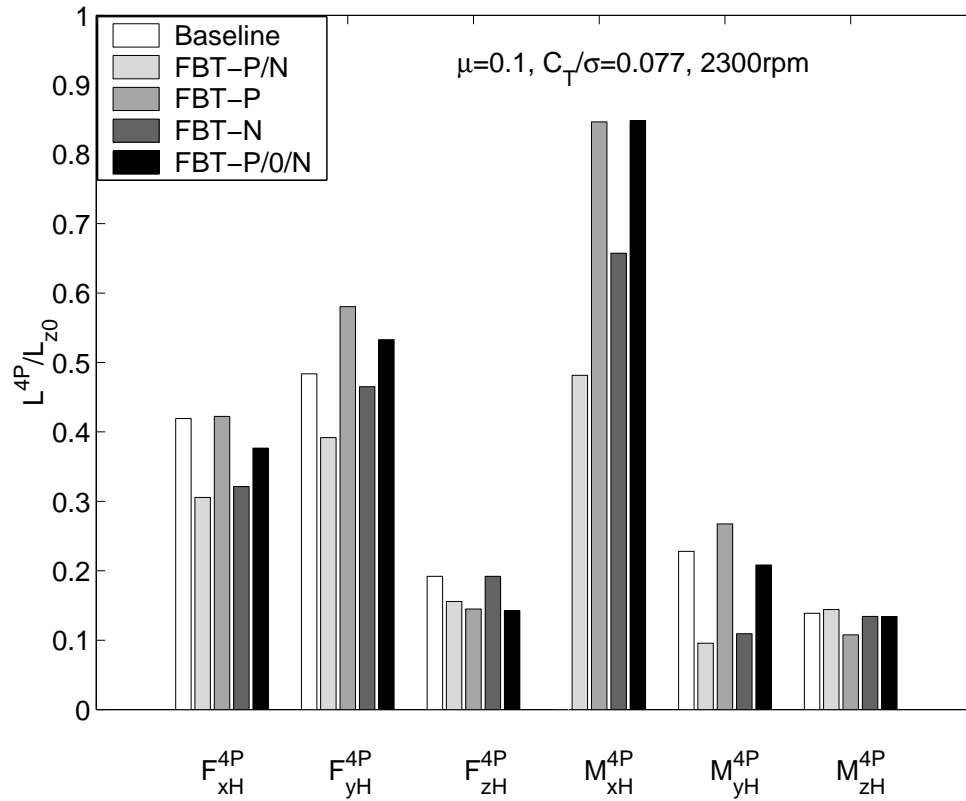


Figure 6.17: Non-dimensional measured 4/rev vibratory hub loads at $\mu = 0.1, C_T/\sigma = 0.077, 2300 \text{ rpm}$

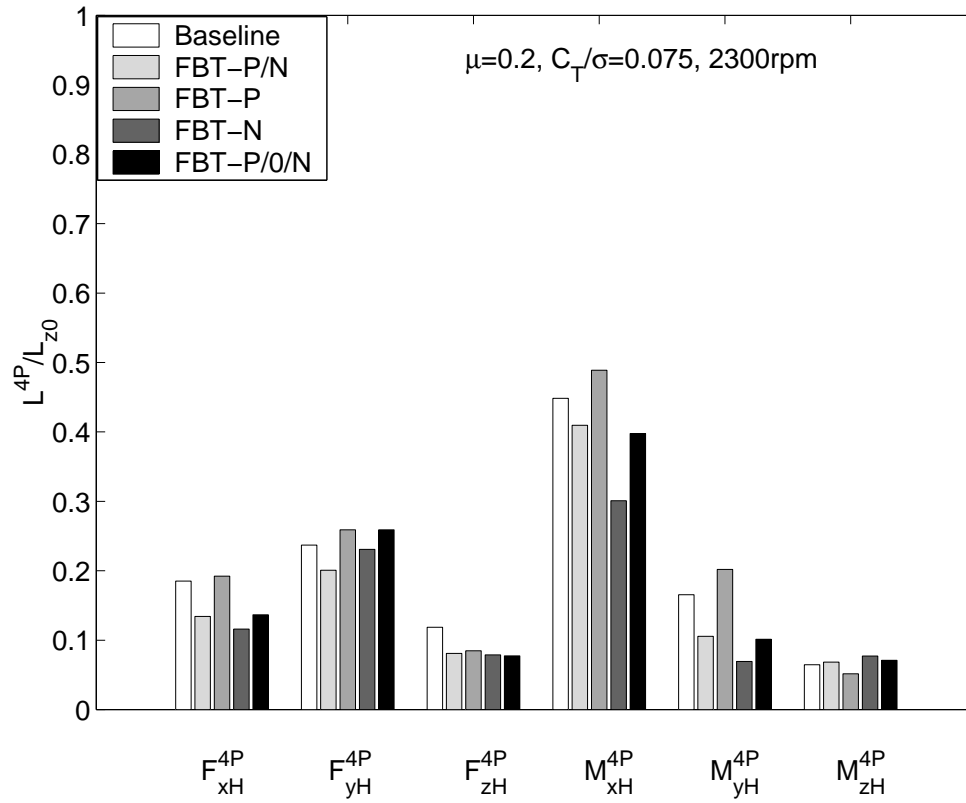


Figure 6.18: Non-dimensional measured 4/rev vibratory hub loads at $\mu = 0.2, C_T/\sigma = 0.075, 2300 \text{ rpm}$

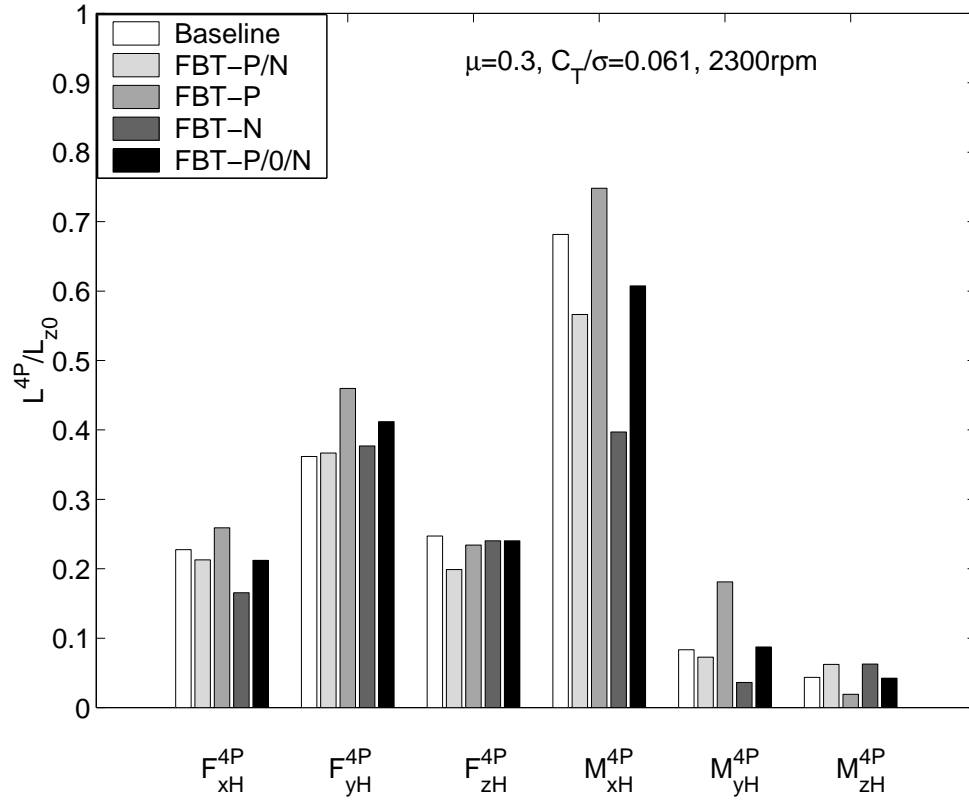


Figure 6.19: Non-dimensional measured 4/rev vibratory hub loads at $\mu = 0.3, C_T/\sigma = 0.061, 2300 \text{ rpm}$

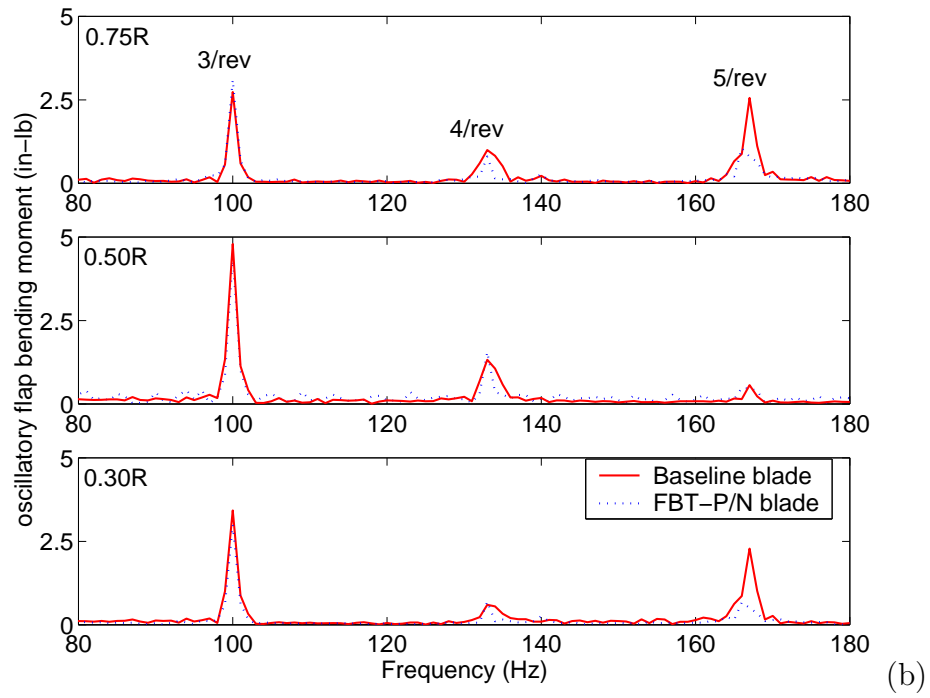
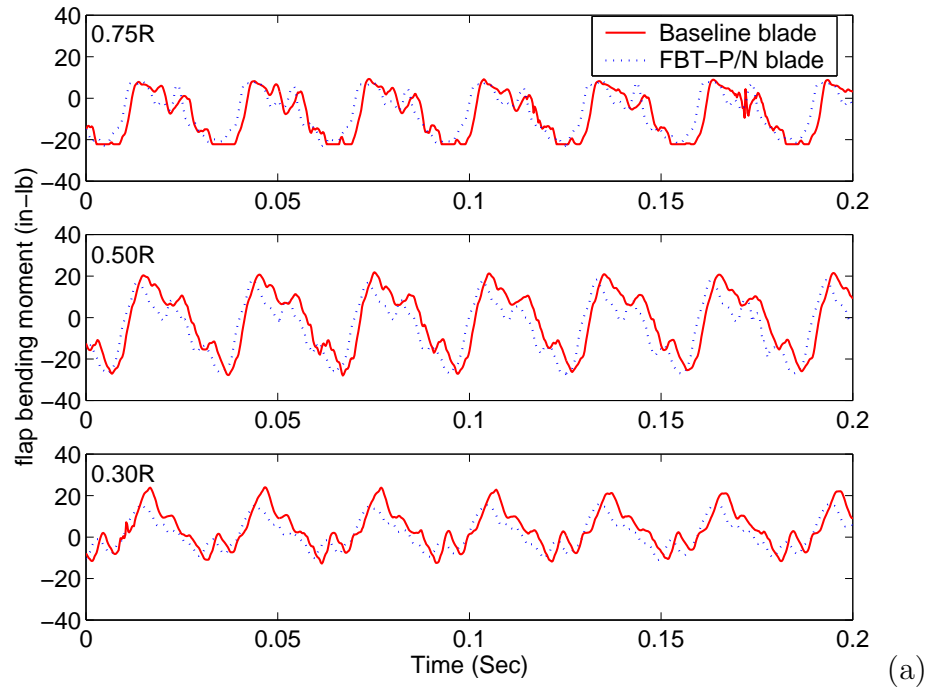


Figure 6.20: Blade oscillatory flap bending moment at $\mu = 0.3$, 2000 rpm

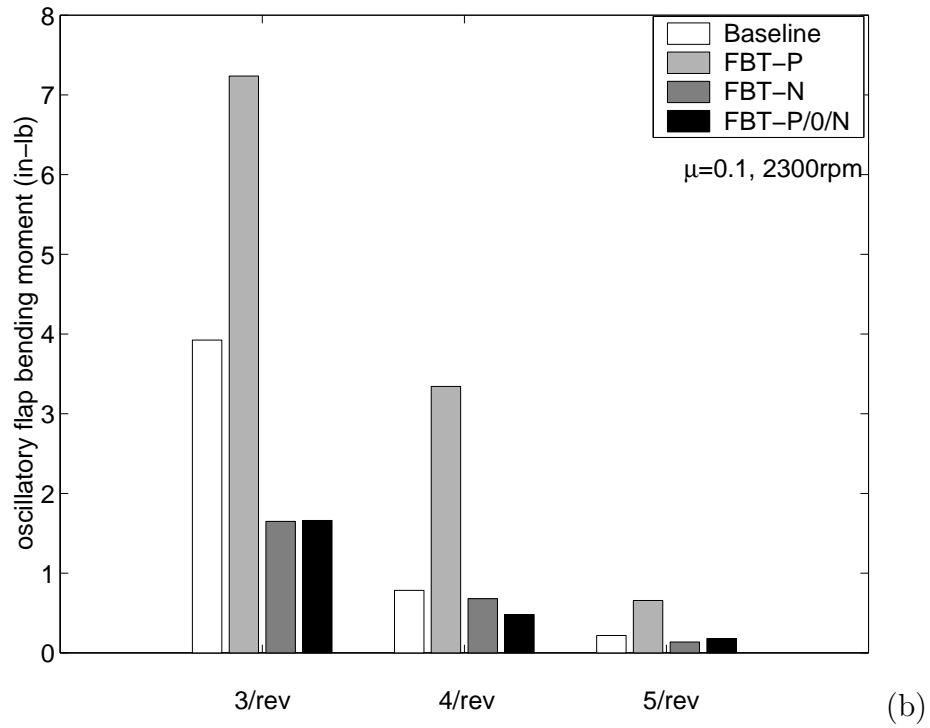
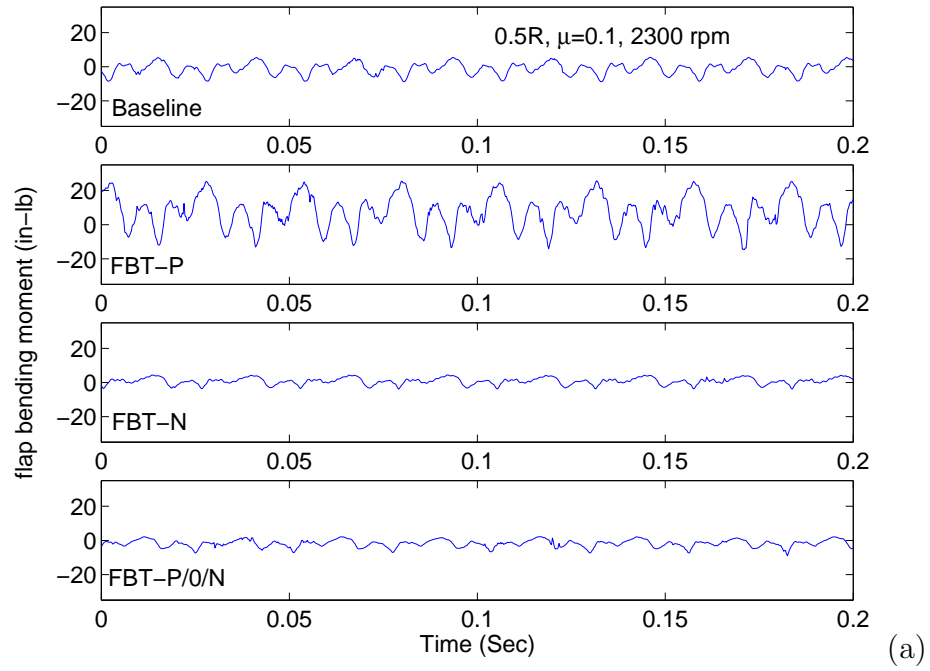


Figure 6.21: Blade oscillatory flap bending moment at $\mu = 0.1$, 2300 rpm

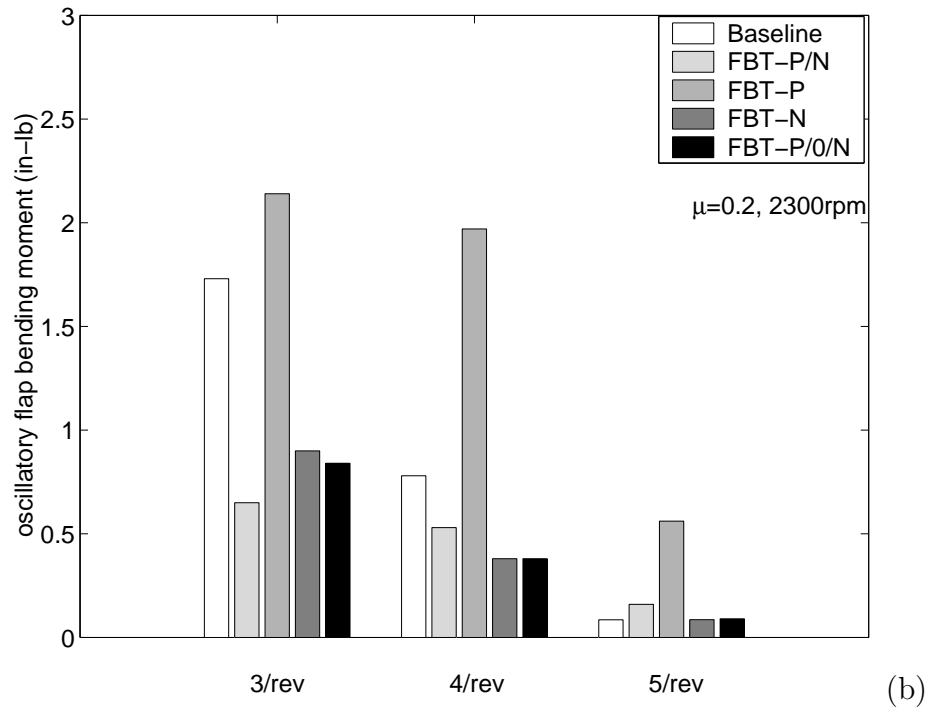
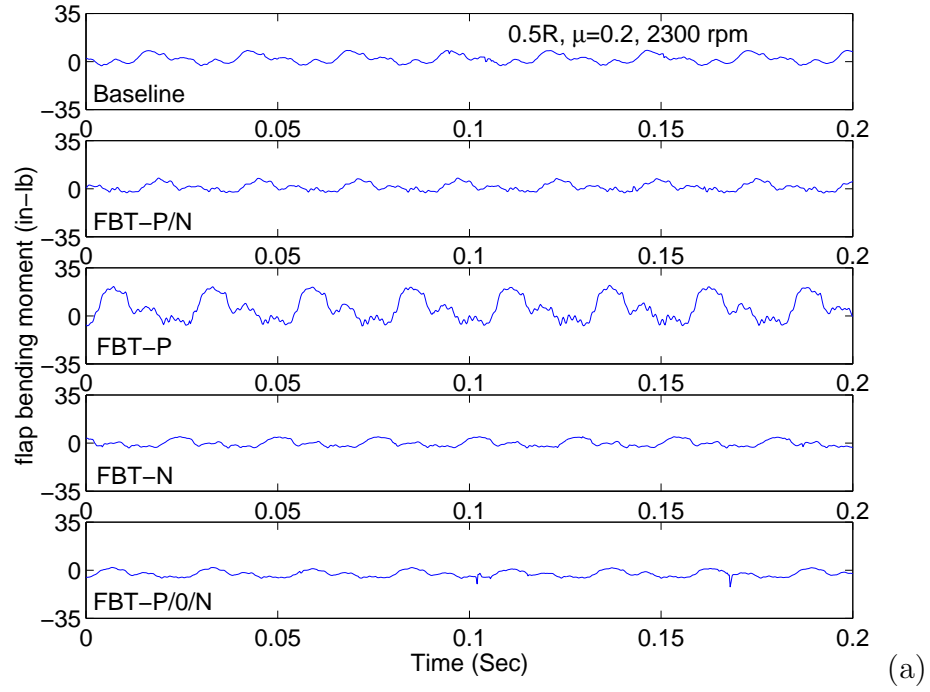


Figure 6.22: Blade oscillatory flap bending moment at $\mu = 0.2$, 2300 rpm

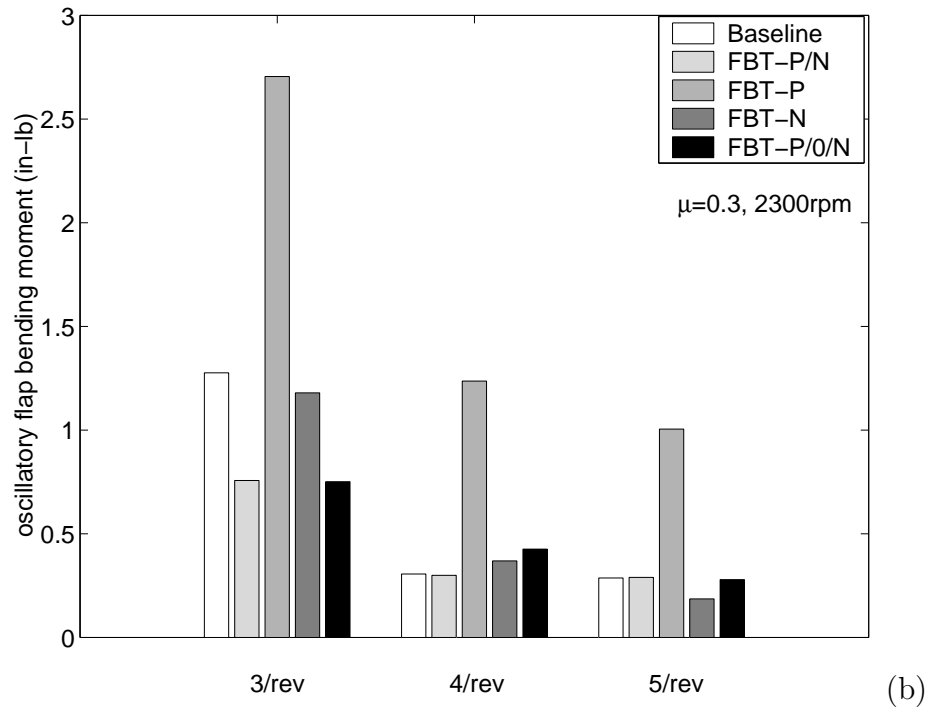
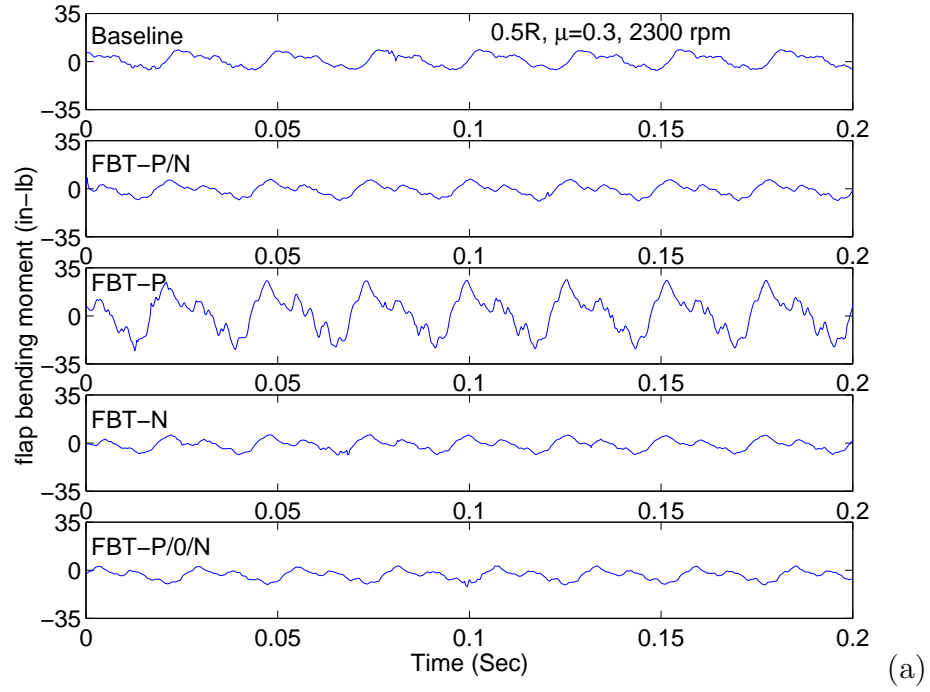


Figure 6.23: Blade oscillatory flap bending moment at $\mu = 0.3$, 2300 rpm

Chapter 7

Summaries and Conclusions

This dissertation describes the development of Mach scale composite tailored rotors with flap-bending/torsion couplings for vibration reduction. The research include the analysis, design, fabrication, bench-top testing, hover testing and wind tunnel testing of these composite rotors. The following sections outline the key summaries and conclusions of the present research.

7.1 Composite Rotor Analysis

The aeroelastic analysis of composite rotor included the calculation of composite blade cross-section properties and the analysis of composite rotor aeroelastic behavior. The structural model used in the present research was derived from the mixed force and displacement method. In the model, the composite laminate analysis was based on classical lamination theory. The displacement formulation was used to obtain direct strain components, whereas the shear related terms were obtained from the equations of equilibrium of the blade general shell segment. The formulation for the blade extensional stiffness, bending stiffness, torsion stiffness, and coupling stiffnesses were derived from the strain energy

of the blade. The analysis using this structural model showed good correlation with the test data.

Rotor aeroelastic analysis was carried out using a modified version of UMARC, which can include the analysis of composite coupled blade. In UMARC, the rotor-fuselage equations were formulated using Hamilton's principle and were discretized using finite elements in space and time. The effect of composite materials is introduced through the strain energy variation. The rotor blade was discretized in the spatial domain using 15 degree of freedom beam finite elements. The aerodynamic analysis included a free wake model. Rotor hub loads were calculated using the force summation method. The vehicle trim and blade response solutions were calculated as one coupled solution. The blade response was calculated using finite elements in time after the nonlinear equations in space were transformed into normal mode equations.

These composite rotor analytical tools were also used to design a full scale composite coupled blade with flap-bending/torsion coupling (composite D-spar layup: $[0_3/\theta_{A,2}/\theta_{B,2}/\theta_{C,4}/\theta_{D,2}]_s$) for the UH-60 rotor.

7.2 Mach Scale Composite Tailored Blade Design

Prior to the design of the Mach scale composite tailored rotor, a study was performed for a full scale baseline articulated rotor and its simulated composite coupled derivatives to explore the impact of elastic couplings on the full scale rotor aeroelastic behavior and to provide guidelines for the design of Mach scale composite blades. It was seen that there is very little difference between the

natural frequencies of the baseline uncoupled blade and those of coupled blades. It was found that the flap-bending/torsion couplings had significant effect on the 4/rev vibratory hub loads of these full scale rotors. Compared with the effect of flap-bending/torsion coupling, the impact of chordwise-bending/torsion couplings on the 4/rev vibratory hub loads was negligible.

The design of the present Mach scale rotor was constrained by an existing articulated rotor hub, the test section dimensions of the Glenn L. Martin Wind Tunnel, and the basic parameters of the UH-60 rotor. A nominal speed of 2300 rpm was set for the composite tailored rotor to achieve the same tip Mach number of 0.65 as the UH-60 rotor.

The structure of Mach scale composite tailored blade consisted of a composite spar with embedded leading edge weights, an aft cell foam core, a composite skin and a root insert. After a series of comparison analyses and tests, a two-cell composite D-spar, a novel composite root insert and leading-edge weights with airfoil profile were developed for the structure of the present Mach scale composite blade. The composite D-spar was built out of the IM7/8552 graphite/epoxy prepreg. Material testing was carried out to obtain the mechanical properties of the IM7/8552 prepreg. These measurements were used for the design of the Mach scale composite blade.

The layup and orientation of composite D-spar, and spanwise coupling distributions were determined using an iterative process combining composite blade cross-section structural analysis and comprehensive rotor aeroelastic analysis. A balanced D-spar layup was used for the Mach scale baseline uncoupled rotor blade, while an unbalanced D-spar layup was used for the Mach scale composite blade with flap-bending/torsion couplings. It was found that spanwise segmented

couplings (positive coupling along outboard of blade and negative coupling along inboard of blade) can provide superior benefits in vibration reduction, compared to uniform spanwise couplings.

7.3 Mach Scale Composite Tailored Blade Fabrication

A new fabrication process was developed to manufacture Mach scale composite tailored rotor blades using a matched-die molding technique. This process included: forming the foam core mandrel, tailoring the composite lamina, layup of the composite D-spar, co-curing of composite blade, and final trimming of the cured blade. Using this process, high quality Mach scale composite tailored rotors were successfully fabricated with identical structural properties, good blade structural integrity, and good correlation between measured and predicted blade properties. To perform comparison studies, five sets of rotors with different coupling configurations were fabricated, including an uncoupled baseline rotor, two rotors with spanwise uniform flap-bending/torsion couplings, and two rotors with spanwise segmented flap-bending/torsion couplings.

For the blade fabrication, a new blade mold was designed and manufactured.

7.4 Bench-top Tests

Prior to hover testing of the fabricated Mach scale composite tailored rotors, a series of bench-top static tests, bench-top shaker tests, and non-rotating dynamic tests were performed to examine the blade structural properties and

validate the blade structural analysis. For the bench-top static tests, the blade was subjected to a tip bending force and tip torque in a test stand. The blade tip bending slope and twist were measured using a laser optic system. The bench-top dynamic tests were conducted (using an electromagnetic shaker) to identify the blade flapwise cantilever natural frequencies. Non-rotating tests were performed on the hover stand (with a piezoelectric actuator temporarily replacing the pitch link) to measure the fundamental non-rotating torsion frequency of the blade (as installed on the rotor hub).

The measured data from the different bench-top tests showed good repeatability, and had good correlation with the predicted values. These data were also used to select four blades with closest structural properties for each rotor set.

7.5 Wind Tunnel Tests

All the five sets of Mach scale composite tailored rotors were tested at rotor speeds up to 2300 rpm (tip Mach number 0.65), advance ratios up to 0.38 (wind speed 187 mph) and for different thrust levels in the Glenn L. Martin Wind Tunnel at the University of Maryland.

The flap-bending/torsion couplings have been demonstrated to have a notable effect on the rotor vibratory hub loads. All the four coupled rotors reduced the 4/rev normal force for advance ratios up to 0.3. In terms of overall reduction of 4/rev normal force, in-plane hub force and rotor head moment, the spanwise dual-segmented rotor with outboard positive and inboard negative coupling (FBT-P/N) performed the best. In the highest vibration condition of 0.1 advance ratio (at 2300 rpm), the 4/rev vertical force was reduced by 9%, the

4/rev in-plane force by 14% and the 4/rev pitching moment by 46% for FBT-P/N rotor; in comparison the peak reductions in vibratory loads of the other coupled rotors were: 33% for the 4/rev normal force (FBT-P), and 50% for the 4/rev pitching moment (FBT-P/0/N). At the advance ratio of 0.3 the FBT-P/N delivered the best vibration reduction of all the rotors, achieving 15% for the 4/rev vertical force, 3% for the 4/rev in-plane force and 14% for the 4/rev head moment. The reductions in vibratory hub loads are due to the experimentally observed reductions in blade oscillatory 3/rev and 5/rev flap bending moments.

Compared to the baseline blade, the spanwise segmented flap-bending/torsion coupling (FBT-P/N) significantly changed the blade oscillatory flap bending moment. At an advance ratio 0.3 and rotor speed of 2000 rpm, the amplitudes of 3/rev and 5/rev oscillatory flap bending moments for the spanwise dual-segmented coupling blade (FBT-P/N) are lower than those for the baseline blade (at three blade spanwise locations: 30%, 50% and 70% radius). The reduction was as large as 71% for 5/rev component at 30% radius.

This is the first time that the notable effect of structural couplings on rotor vibration characteristics has been systematically evaluated experimentally and analytically. This is also the first time that it has been experimentally demonstrated that a suitably designed structural coupling (in terms of coupling strength and spanwise distribution) can significantly reduce the three vibratory rotor hub forces, and the vibratory pitching and rolling moments.

7.6 Recommendations for Future Work

The current research experimentally demonstrated the effect of the composite flap-bending/torsion couplings on the rotor vibration reduction. This section lists some topics that may help future research to obtain more benefits from the composite blade tailored couplings.

1. During the design process, an optimization study may be developed using fiber orientation angle as design variable to tailor the coupling value and spanwise coupling distribution to minimize vibratory hub loads and improve rotor performance. It may be important to carry out a formal design optimization to minimize vibration for a typical articulated rotor.
2. The current research of the composite tailored blades with uniform planform may be extended to the composite coupled blades with advanced geometry, including: variable sweep, anhedral, planform taper and advanced airfoils. Optimization of structural coupling and advanced geometry features may yield larger vibration reductions.
3. The present study focused on a typical articulated rotor. It is shown analytically that vibration reduction benefits can be obtained by including composite couplings in a hingeless rotor. It will be valuable to demonstrate the vibration reduction potential of structural couplings on a Mach scale hingeless rotor.
4. Taking the advantages of smart structure technology, the composite coupled rotor may include smart actuators, such as a composite rotor with flap-bending/torsion coupling and with an active trailing edge flap. Com-

bining smart structures with composite tailored coupling may yield substantially improved rotor design.

5. The current research is focused on the investigation of the effect of composite couplings on the vibratory hub loads. The further research may be focused on the impact of the composite couplings on the rotor performance.
6. The ultimate goal is to demonstrate the feasibility of structural coupling induced vibration reduction on a full scale rotor in the wind tunnel and then in flight test.

Appendix A

Composite Blade Section Properties (Displacement Method)

$$K_{11} = \int_s A_{11} ds \quad (\text{A.1})$$

$$K_{12} = \int_s (zA_{11} + B_{11} \cos \theta) ds \quad (\text{A.2})$$

$$K_{13} = \int_s (yA_{11} - B_{11} \sin \theta) ds \quad (\text{A.3})$$

$$K_{14} = - \int_s (\varphi A_{11} + qB_{11}) ds \quad (\text{A.4})$$

$$K_{15} = \int_s (rA_{16} - 2B_{16}) ds \quad (\text{A.5})$$

$$K_{16} = \int_s A_{16} \cos \theta ds \quad (\text{A.6})$$

$$K_{17} = \int_s A_{16} \sin \theta ds \quad (\text{A.7})$$

$$K_{18} = \int_s B_{11} \sin \theta ds \quad (\text{A.8})$$

$$K_{19} = - \int_s B_{11} \cos \theta ds \quad (\text{A.9})$$

$$K_{22} = \int_s (A_{11}z^2 + 2B_{11}z \cos \theta + D_{11} \cos^2 \theta) ds \quad (\text{A.10})$$

$$K_{23} = \int_s (A_{11}yz + B_{11}y \cos \theta - B_{11}z \sin \theta - D_{11} \cos \theta \sin \theta) ds \quad (\text{A.11})$$

$$K_{24} = - \int_s (\varphi z A_{11} + qz B_{11} + \varphi B_{11} \cos \theta + D_{11} q \cos \theta) ds \quad (\text{A.12})$$

$$K_{25} = \int_s (r A_{16} - 2B_{16}z + r B_{16} \cos \theta - 2D_{16} \cos \theta) ds \quad (\text{A.13})$$

$$K_{26} = \int_s (A_{16}z \cos \theta + B_{16} \cos^2 \theta) ds \quad (\text{A.14})$$

$$K_{27} = \int_s (A_{16}z \sin \theta + B_{16} \cos \theta \sin \theta) ds \quad (\text{A.15})$$

$$K_{28} = \int_s (B_{11}z \sin \theta + D_{11} \cos \theta \sin \theta) ds \quad (\text{A.16})$$

$$K_{29} = \int_s (B_{11}z \cos \theta + D_{11} \cos^2 \theta) ds \quad (\text{A.17})$$

$$K_{33} = \int_s (A_{11}y^2 - 2B_{11}y \sin \theta + D_{11} \sin^2 \theta) ds \quad (\text{A.18})$$

$$K_{34} = \int_s (-\varphi y A_{11} - B_{11} q y + D_{11} q \sin \theta + B_{11} \varphi \sin \theta) ds \quad (\text{A.19})$$

$$K_{35} = \int_s (r y A_{16} - 2B_{16}y + 2D_{16} \sin \theta - r B_{16} \sin \theta) ds \quad (\text{A.20})$$

$$K_{36} = \int_s (A_{16}y \cos \theta - B_{16} \cos \theta \sin \theta) ds \quad (\text{A.21})$$

$$K_{37} = \int_s (A_{16}y \sin \theta - B_{16} \sin^2 \theta) ds \quad (\text{A.22})$$

$$K_{38} = \int_s (B_{11}y \sin \theta - D_{11} \sin^2 \theta) ds \quad (\text{A.23})$$

$$K_{39} = - \int_s (B_{11}y \cos \theta + D_{11}) \cos \theta \sin \theta ds \quad (\text{A.24})$$

$$K_{44} = \int_s (A_{11}\phi^2 + 2B_{11}q\phi + D_{11}q^2) ds \quad (\text{A.25})$$

$$K_{45} = \int_s (-r\varphi A_{16} - qr B_{16} + 2D_{16}q + 2\varphi B_{16}) ds \quad (\text{A.26})$$

$$K_{46} = - \int_s (\varphi A_{16} + q B_{16}) \cos \theta ds \quad (\text{A.27})$$

$$K_{47} = - \int_s (\varphi A_{16} + q B_{16}) \sin \theta ds \quad (\text{A.28})$$

$$K_{48} = - \int_s (B_{11}\varphi + D_{11}q) \sin \theta ds \quad (\text{A.29})$$

$$K_{49} = \int_s (B_{11}\varphi + D_{11}q) \cos \theta ds \quad (\text{A.30})$$

$$K_{55} = \int_s (r^2 A_{66} - 4r B_{66} + 4D_{66}) ds \quad (\text{A.31})$$

$$K_{56} = \int_s (r A_{66} - 2B_{66}) \cos \theta ds \quad (\text{A.32})$$

$$K_{57} = \int_s (r A_{66} - 2B_{66}) \sin \theta ds \quad (\text{A.33})$$

$$K_{58} = \int_s (r B_{16} - 2r D_{16}) \sin \theta ds \quad (\text{A.34})$$

$$K_{59} = \int_s (-r B_{16} + 2D_{16}) \cos \theta ds \quad (\text{A.35})$$

$$K_{66} = \int_s A_{66} \cos^2 \theta ds \quad (\text{A.36})$$

$$K_{67} = \int_s A_{66} \cos \theta \sin \theta ds \quad (\text{A.37})$$

$$K_{68} = \int_s B_{16} \cos \theta \sin \theta ds \quad (\text{A.38})$$

$$K_{69} = - \int_s B_{16} \cos^2 \theta ds \quad (\text{A.39})$$

$$K_{77} = \int_s A_{66} \sin^2 \theta ds \quad (\text{A.40})$$

$$K_{78} = \int_s B_{16} \sin^2 \theta ds \quad (\text{A.41})$$

$$K_{79} = - \int_s B_{16} \cos \theta \sin \theta ds \quad (\text{A.42})$$

$$K_{88} = \int_s D_{11} \sin^2 \theta ds \quad (\text{A.43})$$

$$K_{89} = - \int_s D_{11} \cos \theta \sin \theta ds \quad (\text{A.44})$$

$$K_{99} = \int_s D_{11} \cos^2 \theta ds \quad (\text{A.45})$$

Appendix B

Composite Blade Section Properties (Mixed Method)

$$K_{11} = \int_s (A'_{11} - \frac{A'^2_{16}}{A'_{66}}) ds + \int_s \frac{1}{A'_{66}} C_u^2 ds \quad (\text{B.1})$$

$$K_{12} = \int_s (A'_{11} - \frac{A'^2_{16}}{A'_{66}}) z ds + \int_s \frac{1}{A'_{66}} C_u C_{\phi_y} ds \quad (\text{B.2})$$

$$K_{13} = \int_s (A'_{11} - \frac{A'^2_{16}}{A'_{66}}) y ds + \int_s \frac{1}{A'_{66}} C_u C_{\phi_z} ds \quad (\text{B.3})$$

$$K_{14} = \int_s \frac{1}{A'_{66}} C_u C_{\phi_x} ds \quad (\text{B.4})$$

$$K_{22} = \int_s (A'_{11} - \frac{A'^2_{16}}{A'_{66}}) z^2 ds + \int_s \frac{1}{A'_{66}} C_{\phi_y}^2 ds \quad (\text{B.5})$$

$$K_{23} = \int_s (A'_{11} - \frac{A'^2_{16}}{A'_{66}}) z^2 ds + \int_s \frac{1}{A'_{66}} C_{\phi_y} C_{\phi_z} ds \quad (\text{B.6})$$

$$K_{24} = \int_s \frac{1}{A'_{66}} C_{\phi_y} C_{\phi_x} ds \quad (\text{B.7})$$

$$K_{33} = \int_s (A'_{11} - \frac{A'^2_{16}}{A'_{66}}) y^2 ds + \int_s \frac{1}{A'_{66}} C_{\phi_z}^2 ds \quad (\text{B.8})$$

$$K_{34} = \int_s \frac{1}{A'_{66}} C_{\phi_z} C_{\phi_x} ds \quad (\text{B.9})$$

$$K_{44} = \int_s C_{\phi_x}^2 ds \quad (\text{B.10})$$

where C_u , C_{ϕ_x} , C_{ϕ_y} and C_{ϕ_z} are calculated for each cell of blade cross-section.

$$C_u = \frac{\int_s \frac{A'_{16}}{A'_{66}} ds}{\int_s \frac{1}{A'_{66}} ds} \quad (\text{B.11})$$

$$C_{\phi_y} = \frac{\int_s \frac{A'_{16}}{A'_{66}} z ds}{\int_s \frac{1}{A'_{66}} ds} \quad (\text{B.12})$$

$$C_{\phi_z} = \frac{\int_s \frac{A'_{16}}{A'_{66}} y ds}{\int_s \frac{1}{A'_{66}} ds} \quad (\text{B.13})$$

$$C_{\phi_x} = \frac{\int_s r ds}{\int_s \frac{1}{A'_{66}} ds} \quad (\text{B.14})$$

Appendix C

Process of Blade Composite D-Spar Wrapping

The process includes composite lamina tailoring, foam core mandrel cutting, and D-spar wrapping.

C.1 Tailoring Unidirectional Prepreg

1. Take composite material and adhesive film out of refrigerator (warm up 20 minutes before using).
2. Clean cutting table using acetone.
3. Clean knife, template, and roller using acetone.
4. Lay a ply of release film on the cutting table.
5. Draw drafts to show the cutting process in details, including desired length and orientation angle.
6. Cut unidirectional prepreg roll into composite sheet with desired length.

7. Use a permanent marker to mark the fiber orientation on the backing paper of the composite sheet.
8. Use a template (or a large adjustable protractor-triangle and a long steel ruler) to tailor the composite sheet and obtain composite lamina with the desired orientation angle.
10. Place the composite lamina flatly in a clean bag.

C.2 Making Foam Core Mandrel

1. Make markers on the top and bottom surfaces of foam core.
2. Mark the web location on the surface of foam core.
3. Cut the foam core using special tools to obtain good cutting surface, which should be perpendicular to the middle plane of the airfoil.
4. Use a mask tape to measure the perimeter of the leading edge part.
5. Cut adhesive film with the desired width.
6. Wrap the leading edge foam using the adhesive film (a heat gun may be helpful) to obtain the foam mandrel.
6. Place the leading edge foam mandrel in a clean bag.

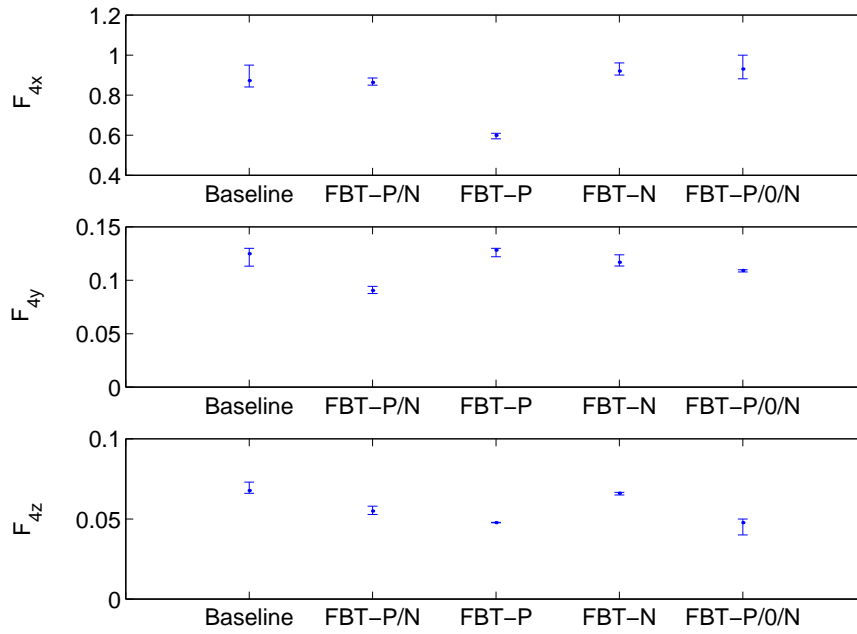
C.3 Wrapping Composite D-Spar

1. Draw a draft to show the layup of D-spar, note the length and the orientation angle for each layer, and indicate the wrapping order.

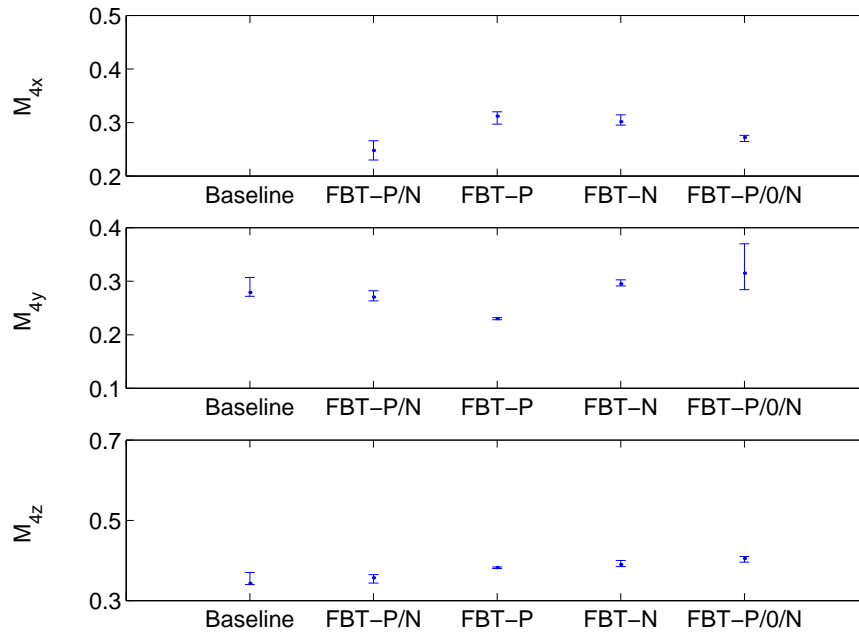
2. Make a check list for the wrapping of each layer.
3. Make markers on the top and bottom surfaces of foam core mandrel.
4. Use a mask tape to measure the perimeter of the leading edge foam mandrel.
5. Cut a strip with the desired width from the tailored composite lamina.
6. Place the composite strip in the desired side of the foam core mandrel, and use a roller to make the strip and the mandrel stick together.
7. Mark the layer number and orientation angle on the backing paper of the strip, and check out this layer in the checking list.
8. Use a shrink tape to compress the wrapping.
9. After the wrapping, place the composite D-spar in a clean bag.
10. Store the D-spar in the refrigerator at a temperature of $0^{\circ}F$.

Appendix D

Additional Wind Tunnel Test Data

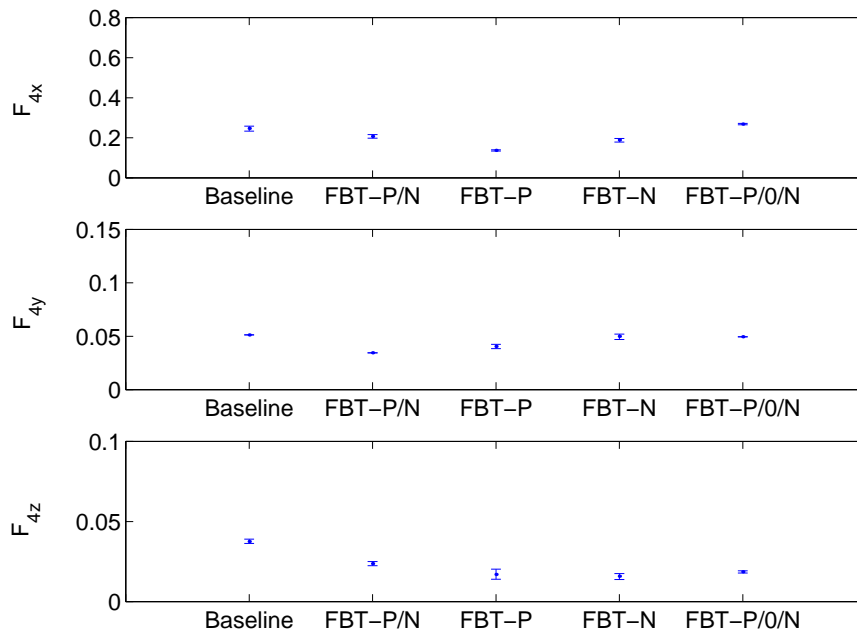


(a) 4/rev vibratory forces

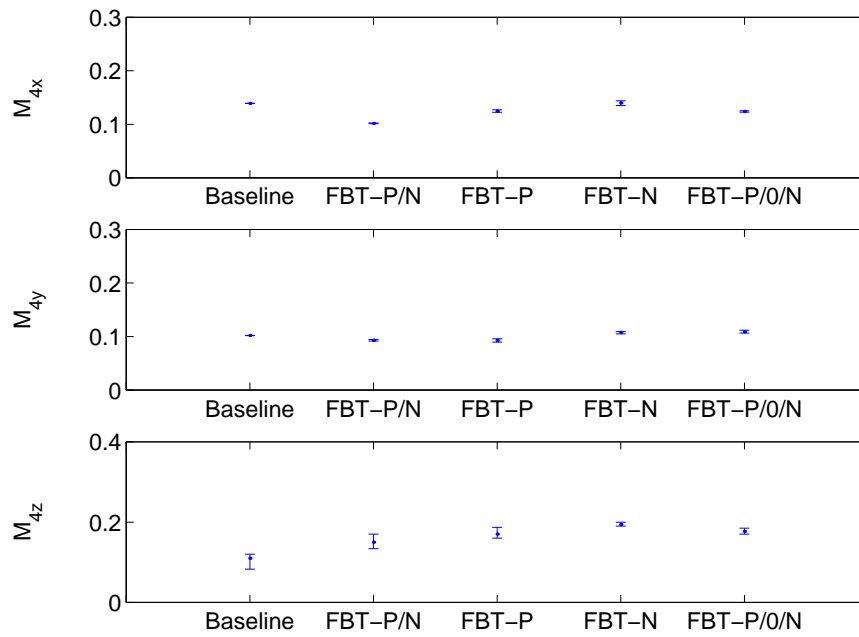


(b) 4/rev vibratory moments

Figure D.1: The average, minimum and maximum values of the measured 4/rev vibration at $\mu = 0.1$, $C_T/\sigma = 0.094$, 2000 rpm

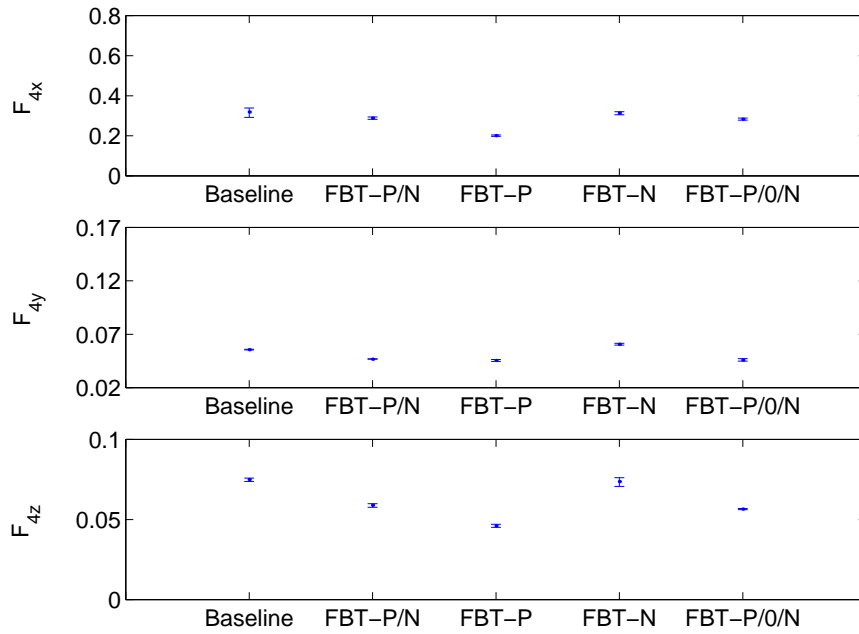


(a) 4/rev vibratory forces

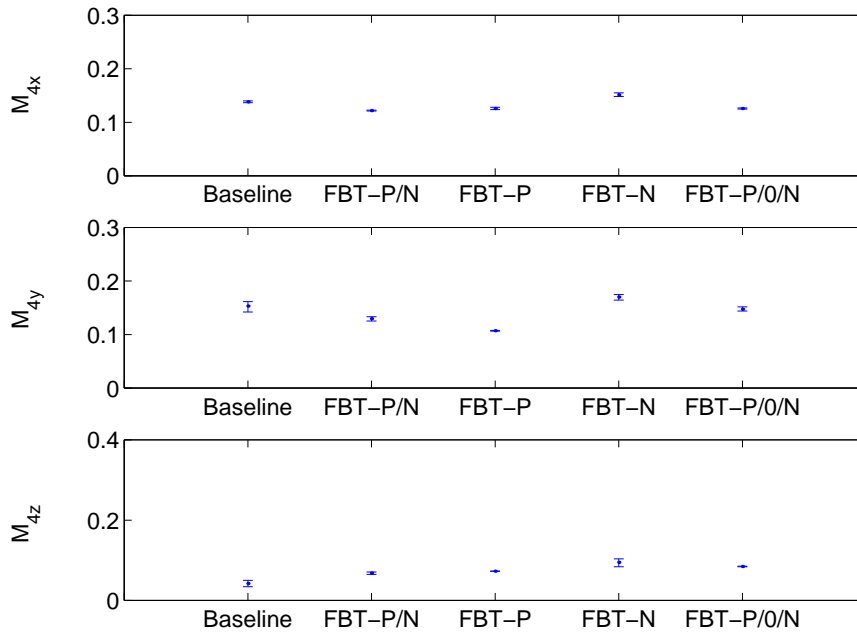


(b) 4/rev vibratory moments

Figure D.2: The average, minimum and maximum values of the measured 4/rev vibration at $\mu = 0.2$, $C_T/\sigma = 0.090$, 2000 rpm



(a) 4/rev vibratory forces



(b) 4/rev vibratory moments

Figure D.3: The average, minimum and maximum values of the measured 4/rev vibration at $\mu = 0.3$, $C_T/\sigma = 0.071$, 2000 rpm

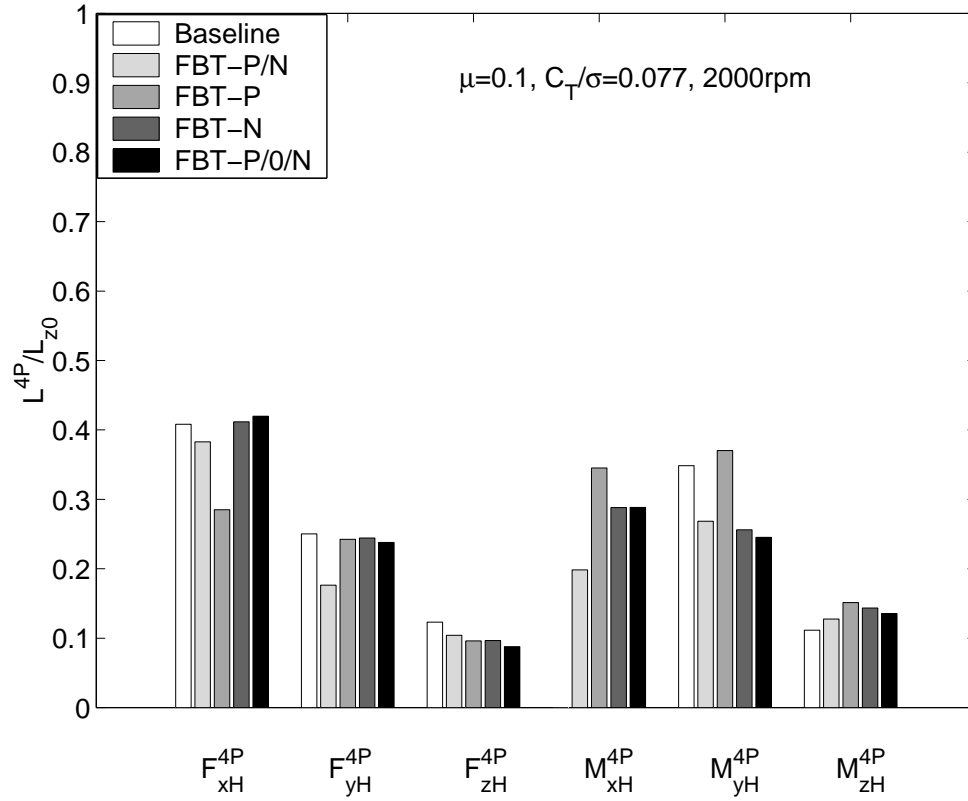


Figure D.4: Non-dimensional measured 4/rev vibratory hub loads at $\mu = 0.1, C_T/\sigma = 0.077, 2000 \text{ rpm}$

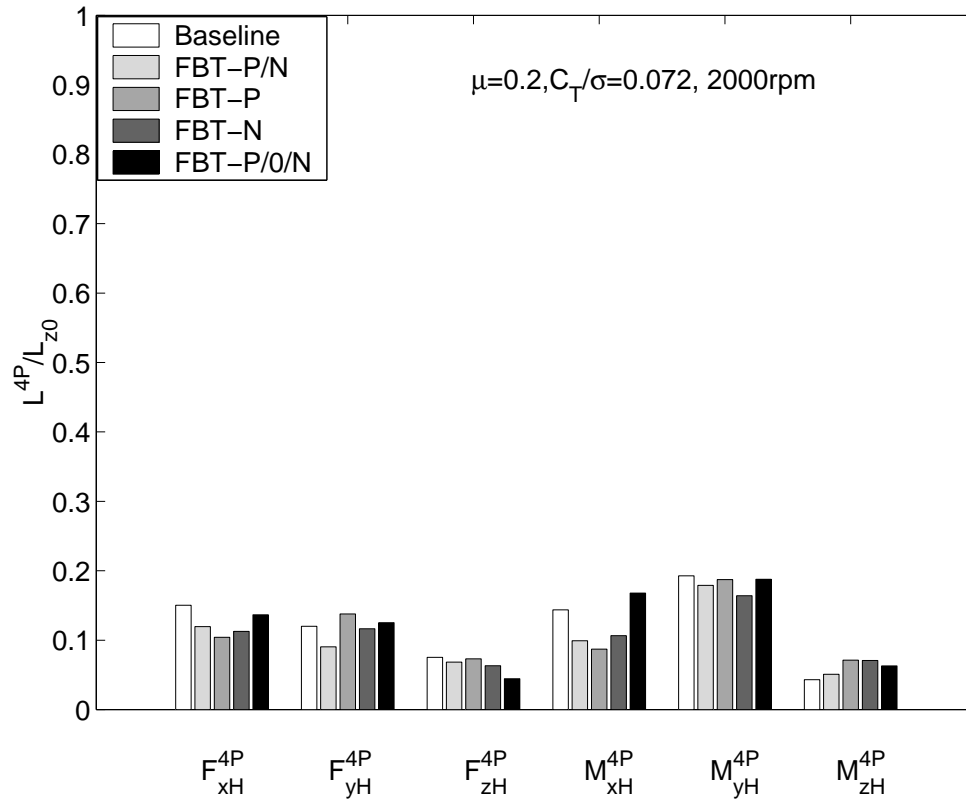


Figure D.5: Non-dimensional measured 4/rev vibratory hub loads at $\mu = 0.2, C_T/\sigma = 0.072, 2000 \text{ rpm}$

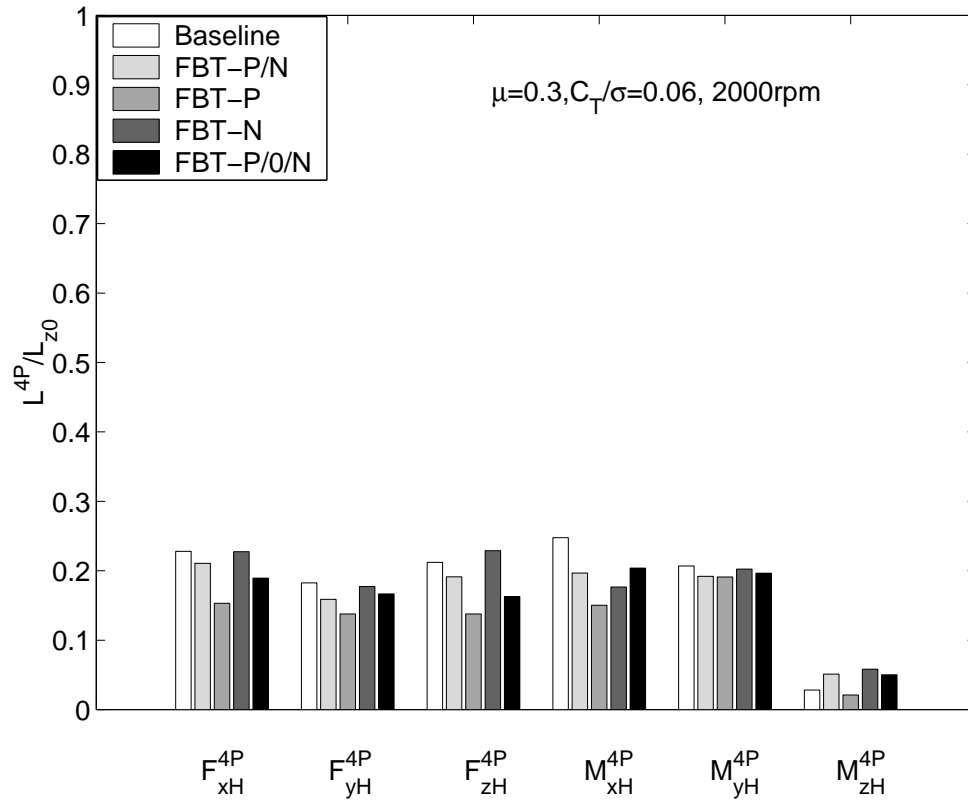


Figure D.6: Non-dimensional measured 4/rev vibratory hub loads at $\mu = 0.3, C_T/\sigma = 0.060, 2000 \text{ rpm}$

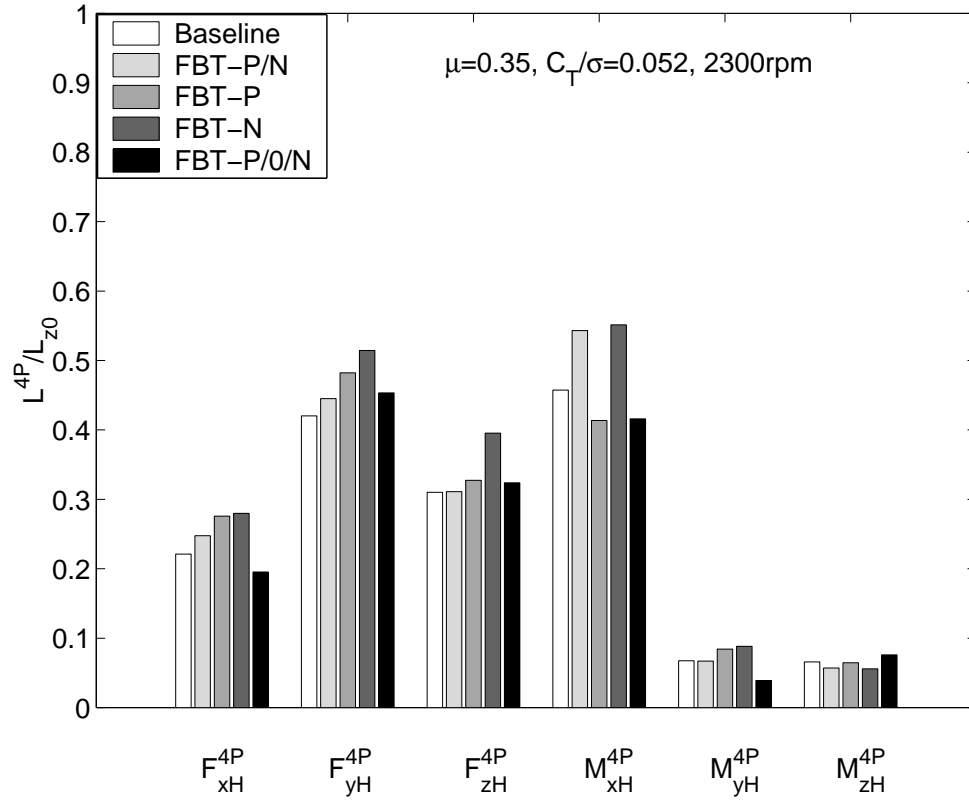


Figure D.7: Non-dimensional measured 4/rev vibratory hub loads at $\mu = 0.35, C_T/\sigma = 0.052, 2300 \text{ rpm}$

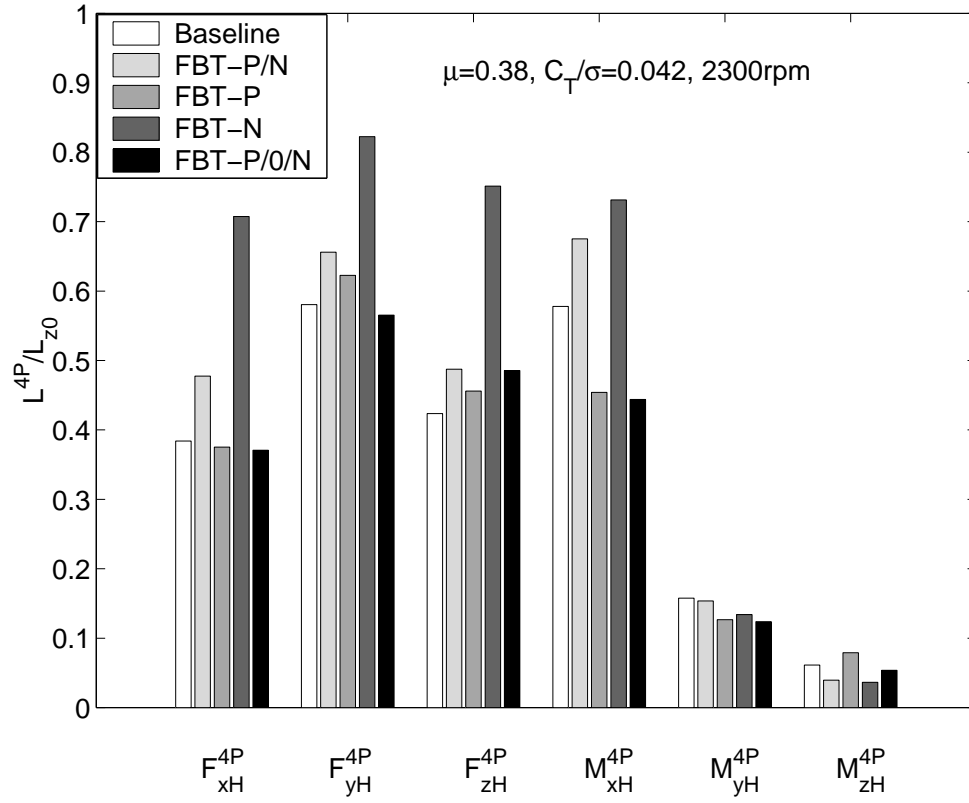


Figure D.8: Non-dimensional measured 4/rev vibratory hub loads at $\mu = 0.38, C_T/\sigma = 0.042, 2300 \text{ rpm}$

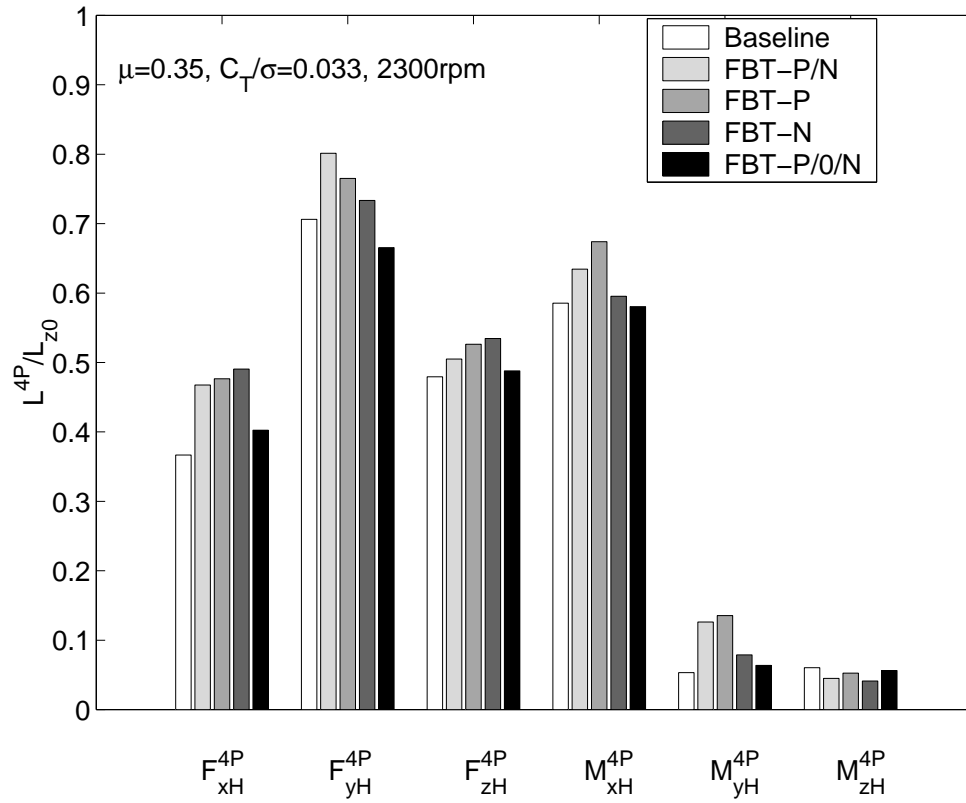


Figure D.9: Non-dimensional measured 4/rev vibratory hub loads at $\mu = 0.35, C_T/\sigma = 0.033, 2300 \text{ rpm}$

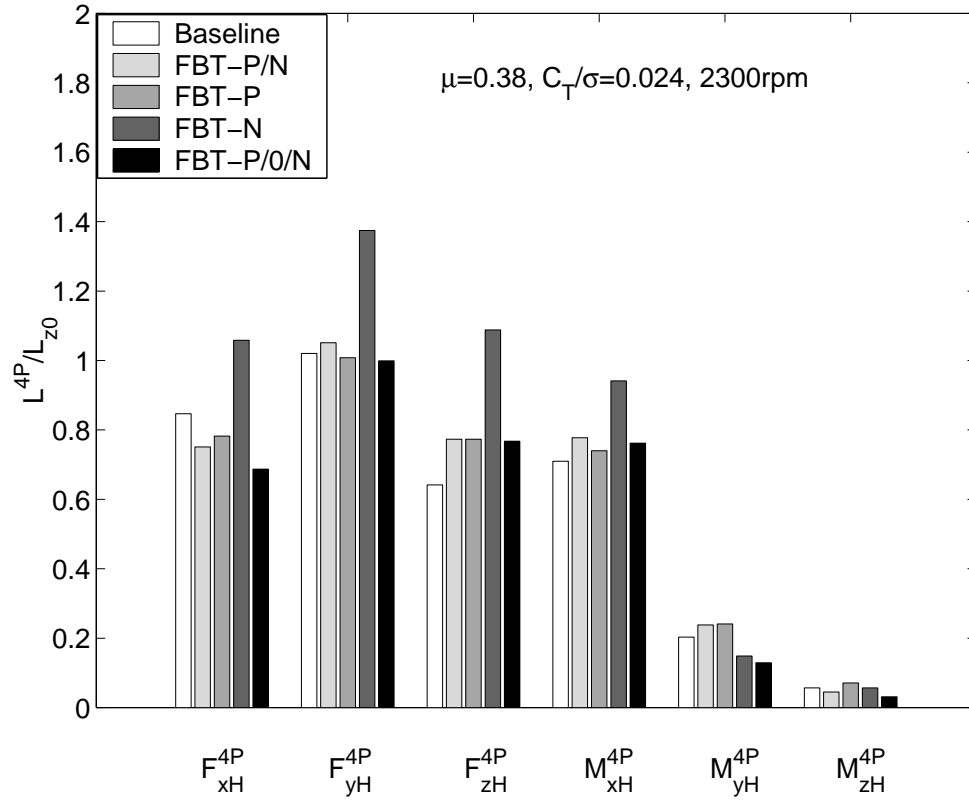


Figure D.10: Non-dimensional measured 4/rev vibratory hub loads at $\mu = 0.38, C_T/\sigma = 0.024, 2300 \text{ rpm}$

BIBLIOGRAPHY

- [1] Foye, R. L., “ Evolution of the Application of Composite Materials to Helicopter,” *Journal of the American Helicopter Society*, Vol.26, No.4, October 1981, pp. 5-15.
- [2] D’Ambra, F., “The Impact of New Materials on the Development of Rotary Wing Aircraft,” *Journal of the American Helicopter Society*, Vol.26, No.4, October 1981, pp. 16-23.
- [3] Varanay, S., and Ozier, M., “Advanced Composite Application for Structures and Housing,” *Proceedings of the American Helicopter Society 60th Annual Forum*, Baltimore, MD, June 7-10, 2004.
- [4] Chopra, I., *Helicopter Dynamics (Printed Note)*, Department of Aerospace Engineering, University of Maryland, 2000.
- [5] Zhang, X., *Helicopter Dynamic Design*, Aviation Industry Press, Beijing, December 1993.
- [6] Loewy, R. G., “ Helicopter Vibrations: A Technological Perspective,” *Journal of the American Helicopter Society*, Vol.29, No.4, October 1984, pp. 4-30.

- [7] Viswanathan, S. P. and Myers, A. W., “Reduction of Helicopter Vibrations through Control of Hub-Impedance,” *Journal of the American Helicopter Society*, Vol.25, No.4, October 1980, pp. 3-12.
- [8] Chopra, I., “Status of Application of Smart Structure Technology to Rotorcraft Systems,” *Journal of the American Helicopter Society*, Vol.45, No.4, October 2000, pp. 228-252.
- [9] Hooper, E., “Rotor Isolation/Vibration Absorption,” *Top Technology Achievements in the History of Vertical Flight*, the American Helicopter Society, 1994.
- [10] Hamouda, M. H., and Pierce, G. A., “Helicopter Vibration Suppression Using Simple Pendulum Absorbers on the Rotor Blade,” *Journal of the American Helicopter Society*, Vol.29, No.3, October 1984, pp. 19-29.
- [11] Yang, M., Chopra, I., and Haas, D. J., “Vibration Prediction for Rotor System with Faults Using Coupled Rotor-Fuselage Model,” *Journal of Aircraft*, Vol.41, No.2, March-April 2004, pp. 348-358.
- [12] Schuett, E., “Application of Passive Rotor Isolation for alleviation of Rotor Induced Vibration,” *Journal of the American Helicopter Society*, Vol.14, No.2, April 1969, pp. 34-48.
- [13] Desjardins, R. A., and Hooper, W. E., “Antiresonant Rotor Isolation for Vibration Reduction,” *Journal of the American Helicopter Society*, Vol.25, No.3, July 1980, pp. 46-55.
- [14] Staple, A. E., “An Evaluation of Active Control of Structural Response As a Means of Reduction Helicopter Vibration,” *Proceedings of the 15th Euro-*

pean Rotorcraft Forum, Paper No.51, Amsterdam, Netherlands, September 1989.

- [15] Welsh, W. A., von Hardenberg, P. C., von Hardenberg, P. W., and Staple, A. E., "Test and Evaluation of Fuselage Vibration Utilizing Active Control of Structural Response (ACSR) Optimized to ADS-27," *Proceedings of the American Helicopter Society 46th Annual Forum*, Washington, DC, May 21-23, 1990, pp.21-37.
- [16] Welsh, W. A., Fredrickson, C., Rauch, C., and Lyndon, I., "Flight test of an Active Vibration Control System on the UH-60 BLACK HAWK Helicopter," *Proceedings of the American Helicopter Society 51st Annual Forum*, Fort Worth, TX, May 9-11, 1995, pp. 393-402.
- [17] Smith, M. R., Pascal, R. J., van Schoor, M. C., Masters, B. P., Blaurock, C., Prechtel, E. F., Rodgers, J. P., and Fridmann, D. S., "Dynamically Tailored Airframe Structures Program," *Proceedings of the American Helicopter Society 57th Annual Forum*, Washington, DC, May 9-11, 2001.
- [18] Taylor, R. B., "Helicopter Vibration Reduction by Rotor Blade Modal Shaping," *Proceedings of the American Helicopter Society 38th Annual Forum*, Anaheim, CA, May 9-11, 1982, pp. 90-101.
- [19] Balckwell, R. H., "Blade Design for Reduced Helicopter Vibration," *Journal of the American Helicopter Society*, Vol.28, No.3, July 1983, pp. 33-41.
- [20] Weller, W. H., and Davis, M. W., "Experimental Verification of Helicopter Blade Designs Optimized for Minimum Vibration," *Proceedings of*

the American Helicopter Society 44th Annual Forum, Washington, DC, June 16-18, 1988, pp.263-279.

- [21] Pritchard, J. I., and Adelman, H. M., "Optimal Placement of Tuning Masses for Vibration Reduction in Helicopter Rotor Blades" *AIAA Journal*, Vol.28, No. 2, Feb. 1990, pp. 309-315.
- [22] Balckwell, R. H., and Merkley, D. J., "The Aeroelastically Conformable Rotor Concept," *Journal of the American Helicopter Society*, Vol.24, No.3, July 1979, pp. 37-44.
- [23] Balckwell, R. H., Murrill, R. J., Yeager, W. T. Jr, and Mirick, P. H., "Wind Tunnel Evaluation of Aeroelastically Conformable Rotors," *Journal of the American Helicopter Society*, Vol.26, No.2, April 1981, pp. 31-39.
- [24] Shaw, J., and Albion, N., "Active Control of Helicopter Rotorfor Vibration Reduction," *Journal of the American Helicopter Society*, Vol.26, No.3, July 1981, pp. 32-39.
- [25] Chopra, I., and McCloud, J. L., " A Numerical Simulation Study of Open-Loop, Closed-Loop and Adaptive Multicycle Control Systems," *Journal of the American Helicopter Society*, Vol.28, No.1, January 1983, pp. 63-77.
- [26] Nguyen, K., and Chopra, I., "Application of High Harmonic Control to Rotors Operating at High Speed and Thrust," *Journal of the American Helicopter Society*, Vol.35, No.3, July 1990, pp. 78-89.
- [27] Wood, E. R., Powers, R. W., Cline, C.H., and Hammond, C.E., "On Developing and Flight Testing a Higher Harmonic Flight Control System," *Journal of the American Helicopter Society*, Vol.30, No.1, January 1985, pp.3-20.

- [28] Shaw, J., Albion, N., Hanker, E. J., and Teal, R. S., “Higher Harmonic Flight Control: Wind Tunnel Demonstration of Fully Effective Vibration Hub Force Suppression,” *Journal of the American Helicopter Society*, Vol.34, No.1, January 1989, pp.14-25.
- [29] Ham, N. D., “Helicopter Individual Blade Control and Its Applications,” *Proceedings of the American Helicopter Society 39th Annual Forum*, St. Louis, MO, May 9-11, 1983, pp. 613-623.
- [30] Jacklin, S. A., Nguyen, K., Blaas, A., and Richter, P., “Full-Scale Wind Tunnel Test of a Helicopter Individual Blade Control System,” *Proceedings of the American Helicopter Society 50th Annual Forum*, Washington, DC, May 11-13, 1994, pp.579-596.
- [31] Jacklin, S. A., Haber, A., de Simone, G., Norman, T. R., Kitaplioglu, C., and Shinoda, P., “Full-Scale Wind Tunnel Test of an Individual Blade Control System for a UH-60 Helicopter,” *Proceedings of the American Helicopter Society 58th Annual Forum*, Montreal, Canada, June 11-13, 2002.
- [32] Fuerst, D., Kessler, C., Auspitzer, T., Hausberg, A., Mueller, M., and Witte, H., “Closed Loop IBC-System and Flight Test Results on the CH-53G Helicopter,” *Proceedings of the American Helicopter Society 60th Annual Forum*, Baltimore, MD, June 7-10, 2004.
- [33] Chopra, I., “Review of State of Art of Smart Structures and Integrated Systems,” *AIAA Journal*, Vol.40, No.11, November 2002, pp. 2145-2187.

- [34] Milgram, J., Chopra, I., and Straub, F., “Rotors with Trailing Edge Flaps: Analysis and Comparison with Experimental Data,” *Journal of the American Helicopter Society*, Vol.43, No.4, October 1998, pp.319-332.
- [35] Lee, T., and Chopra, I., “Development and Validation of a Refined Piezostack-Actuated Trailing-Edge Flap Actuator for a Helicopter Rotor,” *Proceedings of SPIE’s North American Symposium on Smart Structures and Materials*, Paper No.3668-03, Newport Beach, CA, March 1-4, 1999.
- [36] Bernhard, A. P., and Chopra, I., “Trailing Edge Flap Activated by a Piezo-Induced Bending-Torsion Coupled Beam,” *Journal of the American Helicopter Society*, Vol.44, No.1, January 2002, pp.3-15.
- [37] Koratkar, H. A., and Chopra, I., “Wind Tunnel Testing of a Smart Rotor Model with Trailing-Edge Flaps,” *Journal of the American Helicopter Society*, Vol.47, No.4, October 2002, pp.263-272.
- [38] Shen, J., and Chopra, I., “Aeroelastic Modeling of Trailing-Edge Flaps with Smart Material Actuators,” *Proceedings of the 41st AIAA/ASME/ASCE/AHS Structures, Structural Dynamics, and Material Conference*, AIAA Paper 2000-1622, Atlanta, GA, April 3-6, 2000.
- [39] Straub, F. K., Kennedy, D. K., Domzalski, D.B., Hassan, A. A., Ngo, H., Anand, V., and Birchette, T., “Smart Material-Actuated Rotor Technology - SMART,” *Journal of Intelligent Material System and Structures*, Vol.15, No.4, April 2004, pp.249-260.

- [40] Chen, P. C., and Chopra, I., "Wind Tunnel Test of a Smart Rotor with Individual Blade Twist Control," *Journal of Intelligent Material System and Structures*, Vol.8, No.5, May 1997, pp.414-425.
- [41] Bernhard, A. P., and Chopra, I., "Hover test of a Mach-scale rotor-model with active blade tips," *Journal of the American Helicopter Society*, Vol.47, No.4, October 2002, pp.273-284.
- [42] Bernhard, A. P., and Chopra, I., "Hover test of Mach-scale active-twist rotor using piezo-bending-torsion actuators," *Journal of Aircraft*, Vol.39, No.4, July-August 2002, pp.678-688.
- [43] Shin, S. J., "Integral Twist Actuation of Helicopter Rotor Blades for Vibration Reduction," *Ph.D. Dissertation*, Department of Aeronautics and Astronautics, Massachusetts Institute of Technology, 2001.
- [44] Cesnik, C.E.S., Shin, S. J., Wilkie, W. K., Wilbur, M. L., and Mirick, P. H., "Modeling, Design, and Testing of the NASA/ARMY/MIT Active Twist Rotor Prototype Blade," *Proceedings of the American Helicopter Society 55th Annual Forum*, Montreal, Canada, May 25-27, 1999.
- [45] Wilbur, M. L., Yeager, W. T. Jr., and Sekula, M. K., "Further Examination of the Vibratory Loads Reduction Results from the NASA/ARMY/MIT Active Twist Rotor Test," *Proceedings of the American Helicopter Society 58th Annual Forum*, Montreal, Canada, June 11-13, 2002.
- [46] Bernhard, A. P., and Wong, J., "Sikorsky Active Rotor Control Evaluation of NASA/ARMY/MIT Active Twist Rotor," *Proceedings of the American Helicopter Society 59th Annual Forum*, Phoenix, AZ, May 6-8, 2003.

- [47] Ford, T., "New Shape in the Sky," *Aircraft Engineering*, Vol.57, No.9, September 1985, pp.2-5.
- [48] Ganguli, R., and Chopra, I., "Aeroelastic Optimization of a Helicopter Rotor with Two-Cell Composite Blades," *AIAA Journal*, Vol.34, No.4, April 1996, pp. 835-841.
- [49] Ganguli, R., and Chopra, I., "Aeroelastic Optimization of a Helicopter Rotor to Reduce Vibration and Dynamic Stresses," *Journal of Aircraft*, Vol.33, No.4, July-August 1996, pp. 808-815.
- [50] Ganguli, R., and Chopra, I., "Aeroelastic Optimization of an Advanced Geometry Composite Helicopter Rotor," *Proceedings of the American Helicopter Society 51st Annual Forum*, Fort Worth, TX, May 9-11, 1995.
- [51] Yuan, K. A., and Friedmann, P. P., "Structural Optimization for Vibratory Loads Reduction of Composite Helicopter Rotor Blades with Advanced Geometry Tips," *Journal of the American Helicopter Society*, Vol.43, No.3, July 1998, pp. 246-256.
- [52] Floros, M. W., and Smith, E. C., "Elastically Tailored Rotor Blades for Stall Alleviation and Vibration Reduction," *Proceedings of the American Helicopter Society Aeromechanics Specialists' Meeting*, Atlanta, Georgia, Nov. 13-14, 2000.
- [53] Floros, M. W., "Elastically Tailored Composite Rotor Blades for Stall Alleviation and Vibration Reduction," *Ph.D. Dissertation*, Department of Aerospace Engineering, Pennsylvania State University, 2000.

- [54] Jung, S. N., Nagaraj, V. T., and Chopra, I. , “Assessment of Composite Rotor Blade Modeling Techniques,” *Journal of the American Helicopter Society*, Vol.44, No.3, July 1999, pp.188-205.
- [55] Hodges, D. H., “Review of Composite Rotor Blade Modeling”, *AIAA Journal*, Vol.28, No.3, March 1990, pp. 561-565.
- [56] Friedmann, P. P. and Hodges, D. H., “Rotary Wing Aeroelasticity - A Historical Perspective,” *Journal of Aircraft*, Vol.40, No.6, November-December 2003, pp.1019-1046.
- [57] Mansfield, E.H., and Sobey, A. J., “The Fibre Composite Helicopter Blade; Part 1: Stiffness Properties, Part 2: Prospects for Aeroelastic Tailoring,” *Aeronautical Quarterly*, Vol.30, No.2, May 1979, pp.413-449.
- [58] Rehfield, L. W., “Design Analysis Methodology for Composite Rotor Blades,” *Proceedings of the 7th DoD/NASA Conference on Fibrous Composites in Structural Design*, Denver, CO, June 17-20, 1985.
- [59] Rehfield, L. W., Atilgan, A. R., and Hodges, D. H., “Nonclassical Behavior of Thin-Walled Composite Beams with Closed Cross Sections,” *Journal of the American Helicopter Society*, Vol.35, No.2, April 1990, pp.42-51.
- [60] Bauchau, O. A., “Beam Theory for Anisotropic Materials,” *Journal of Applied Mechanics*, Vol.52, No.2, June 1985, pp.416-422.
- [61] Hong, C. H., and Chopra, I., “Aeroelastic Stability Analysis of a Composite Rotor Blade,” *Journal of the American Helicopter Society*, Vol.30, No.2, April 1985, pp.57-67.

- [62] Smith, E.C. and Chopra, I., "Formulation and Evaluation of an Analytical Model for Composite Box-Beams," *Journal of the American Helicopter Society*, Vol. 36, No. 3, July 1991, pp.23-35
- [63] Chandra, R., Stemple, A. D., and Chopra, I., "Thin-Walled Composite Beams under Bending Torsional, and Extensional Loads," *Journal of Aircraft*, Vol.27, No.7, July 1990, pp.619-626.
- [64] Chandra, R., and Chopra, I., "Experimental and Theoretical Analysis of Composite I-Beams with Elastic Couplings," *AIAA Journal*, Vol.29, No.12, December 1991, pp.2197-2206.
- [65] Chandra, R., and Chopra, I., "Structural Response of Composite Beams and Blades with Elastic Couplings," *Composites Engineering*, Vol.2, Nos 5-7, 1992, pp.347-374.
- [66] Jung, S. N., Nagaraj V. T., and Chopra, I. , "Refined Structural Model for Thin and Thick- Walled Composite Rotor Blades," *AIAA Journal*, Vol.40, No.1, January 2002, pp. 105-116.
- [67] Giavotto, V., Borri, M., Mantegazza, P., Ghiringhelli, G., Carmaschi, V., Maffioli, G. C., and Mussi, F., "Anisotropic Beam Theory and Applications," *Computers and Structures*, Vol.16, No.1-4, 1983, pp.403-413.
- [68] Bauchau, O. A., and Hong, C. H., "Finite Element Approach to Rotor Blade Modeling," *Journal of the American Helicopter Society*, Vol.32, No.1, January 1987, pp.60-67.

- [69] Stemple, A. D., and Lee, S. W., "Finite-Element Model for Composite Beams with Arbitrary Cross-Sectional Warping," *AIAA Journal*, Vol.26, No.12, December 1988, pp.1512-1520.
- [70] Kosmatka, J. B., and Friedmann, P. P., "Vibration Analysis of Composite Turbopropellers Using a Nonlinear Beam-Type Finite Element Approach," *AIAA Journal*, Vol.27, No.11, November 1989, pp.1606-1614.
- [71] Atilgan, A. R., and Hodges, D. H., "A Geometrically Nonlinear Analysis for Nonhomogeneous, Anisotropic Beams," *Proceedings of the 30th AIAA/ASME/ASCE/AHS Structures, Structural Dynamics, and Material Conference*, AIAA Paper 89-1264, Mobile, AL, April 3-5, 1989.
- [72] Cesnik, C.E.S., and Hodges, D. H., "VABS: A New Concept for Composite Rotor Blade Cross-Sectional Modeling," *Journal of the American Helicopter Society*, Vol.42, No.1, January 1997, pp.27-38.
- [73] Panda, B., and Chopra, I., "Dynamics of Composite Rotor Blades in Forward Flight," *Vertica*, Vol.11, No.1/2, January 1987, pp.187-209
- [74] Smith, E. C., and Chopra, I., "Aeroelastic Response, Loads and Stability of a Composite Rotor in Forward Flight," *AIAA Journal*, Vol.31, No.7, July 1993, pp. 1265-1274.
- [75] Smith, E.C., and Chopra, I., "Air and Ground Resonance of Helicopters with Elastically Tailored Composite Rotor Blades," *Journal of the American Helicopter Society*, Vol.38, No.4, October 1993, pp.50-61.
- [76] Yuan, K., Friedmann, P. P., and Venkatesan, C., "Aeroelastic Behavior of Composite Rotor Blades with Swept Tips," *Proceedings of the American*

Helicopter Society 48th Annual Forum, Washington, DC, June 3-5, 1992, pp.1039-1059.

- [77] Yuan, K., Friedmann, P. P., and Venkatesan, C., "Aeroelastic Stability Response and Loads of Swept Tip Composite Rotor Blades in Forward Flight," *Proceedings of the 35th AIAA/ AHS/ ASME/ ASCE/ ASC Structures, Structural Dynamics, and Materials Conference*, Hilton Head, SC, AIAA Paper No.94-1309, April 18-20, 1994.
- [78] Fulton, M. V., and Hodges, D. H., "Aeroelastic Stability of Composite Hingeless Rotor Blades in Hover-Part I: Theory," *Mathematical and Computer Modeling*, Vol.18, No.3/4, 1993, pp.1-17.
- [79] Fulton, M. V., and Hodges, D. H., "Aeroelastic Stability of Composite Hingeless Rotor Blades in Hover-Part II:Results," *Mathematical and Computer Modeling*, Vol.18, No.3/4, 1993, pp.19-35.
- [80] Nixon, M. W., "Aeroelastic Response and Stability of Tiltrotors with Elastically-Coupled Composite Rotor Blades," *Ph.D. Dissertation*, Department of Aerospace Engineering, University of Maryland, 1993.
- [81] Nixon, M. W., Piatak, D. J., Corso, L. M., and Popelka, D. A., "Aeroelastic Tailoring for Stability Augmentation and Performance Enhancements of Tiltrotor Aircraft," *Journal of the American Helicopter Society*, Vol.45, No.4, October 2000, pp. 270-279.
- [82] Tracy, A. L., and Chopra, I., "Aeroelastic Analysis of a Composite Bearingless Rotor in Forward Flight Using an Improved Warping Model," *Journal of the American Helicopter Society*, Vol.40, No.3, July 1995, pp. 80-91.

- [83] Datta, A., and Chopra, I., "Validation and Understanding of UH-60A Vibratory Loads in Steady Level Flight", *Journal of the American Helicopter Society*, Vol.49, No.3, July 2004, pp. 271-287.
- [84] Chandra, R., and Chopra, I., "Experimental-Theoretical Investigation of the Vibration Characteristics of Rotating Composite Box Beams," *Journal of Aircraft*, Vol.29, No.4, July-Aug. 1992, pp.657-664.
- [85] Chandra, R., and Chopra, I., "Analytical-Experimental Investigation of Free-Vibration Characteristics of Rotating Composite I-Beams," *Journal of Aircraft*, Vol.30, No.6, Nov-Dec. 1993, pp.927-934.
- [86] Nixon, M. W., "Extension-Twist Coupling of Composite Circular Tubes with Application to Tilt Rotor Blade Design," *Proceedings of the 28th AIAA/ASME/ASCE/AHS Structures, Structural Dynamics, and Material Conference*, AIAA paper No. 87-0772, Monterey, CA, April 6-8, 1987, pp. 295-303.
- [87] Lake, R. C., Izadpanah, A. P., and Baucom, R. M., "Dynamic Testing and Analysis of Extension-Twist-Coupled Composite Tubular Spars," *Proceedings of the Tenth International Modal Analysis Conference*, San Diego, CA, February 3-7, 1992.
- [88] Lake, R. C., Izadpanah, A. P., and Baucom, R. M., "Experimental and Analytical Investigation of Dynamic Characteristics of Extension-Twist-Coupled Composite Tubular Spars," NASA TP-3225, ARL-TR-30, January 1993.

- [89] Weiser, E.S., and Baucom, R. M., "Molding of Complex Composite Parts Utilizing Modified Silicone Rubber Tooling," *Journal of Advanced Materials*, Vol.26, No.1, October 1994, pp.2-8.
- [90] Minguet, P., and Dugundji, J., "Experiments and Analysis for Composite Blades Under Large Deflections. Part I-Static Behavior," *AIAA Journal*, Vol. 28, No.9, September 1990, pp. 1573-1580.
- [91] Minguet, P., and Dugundji, J., "Experiments and Analysis for Composite Blades Under Large Deflections. Part II-Dynamic Behavior," *AIAA Journal*, Vol. 28, No.9, September 1990, pp. 1581-1588.
- [92] Bauchau, O. A., Coffenberry, B. S., and Rehfield, L. W., "Composite Box-Beam Analysis Theory and Experiments," *Journal of Reinforced Plastics and Composite*, Vol.6, No.1, January 1987, pp.25-35.
- [93] Rand, O., "Experimental Investigation of Periodically Excited Rotating Composite Rotor Blades," *Journal of Aircraft*, Vol.28, No.12, December 1991, pp. 876-883.
- [94] Epps, J., and Chandra, R., "Natural Frequencies of Rotating Composite Beams with Tip Sweep," *Journal of the American Helicopter Society*, Vol.41, No.1, January 1996, pp. 29-36.
- [95] Done, G.T.S., "Rotorcraft Dynamics and Aeroelasticity Research in the U.K.," *Proceedings of the sixth International Workshop on Dynamics and Aeroelastic Stability Modelling of Rotorcraft Systems*, Los Angeles, CA, Nov.8-10, 1995.

- [96] Tracy, A.L., and Chopra, I., "Aeroelastic Stability Investigation of a Composite Hingeless Rotor in Hover," *Journal of Aircraft*, Vol.35, No.5, September-October 1998, pp. 791-797.
- [97] Bir, G., Chopra, I., et al., "University of Maryland Advanced Rotorcraft Code (UMARC) Theory Manual," UM-AERO Report 94-18, August 1992.
- [98] Vlasov, V. Z., "Thin-Walled Elastic Beams," Translated from Russian, National Science Foundation and Department of Commerce, USA, 1961.
- [99] Gjelsvik, A., *The Theory of Thin Walled Bars*, John Wiley & Sons, Inc., New York, 1981.
- [100] Nagaraj, V. T., Technical Note, 2002.
- [101] Tracy, A. L., "Aeromechanical Stability Investigation of Elastically Coupled Composite Helicopter Rotors," *Ph.D. Dissertation*, Department of Aerospace Engineering, University of Maryland, 1996.
- [102] Jones, R. M., *Mechanics of Composite Materials*, Hemisphere Publishing Corporation, New York, NY, 1999 (2nd ed.).
- [103] Hyer, M. W., *Stress Analysis of Fiber-Reinforced Composite Materials*, McGraw-Hill Companies, Inc., Boston, MA, 1998.
- [104] Ganguli, R., "Aeroelastic Optimization of Advanced Geometry and Composite Helicopter Rotors," *Ph.D. Dissertation*, Department of Aerospace Engineering, University of Maryland, 1994.
- [105] Smith, E. C., "Aeroelastic Response and Aeromechanical Stability of Helicopters with Elastically Coupled Composite Helicopter Rotor Blades," *Ph.D.*

- Dissertation*, Department of Aerospace Engineering, University of Maryland, 1992.
- [106] Singleton, J. D., and Yeager, W. T. Jr., “Important scaling parameters for testing model-scale helicopter rotors,” *Proceedings of the 20th AIAA, Advanced Measurement and Ground Testing Technology Conference*, Albuquerque, NM, June 15-18, 1998.
- [107] Bernhard, A. P. F., “Smart Helicopter Rotor with Active Blade Tips,” *Ph.D. Dissertation*, Department of Aerospace Engineering, University of Maryland, 2000.
- [108] Leishman, J. G., *Principles of Helicopter Aerodynamics*, Cambridge University Press, Cambridge, United Kingdom, 2000.
- [109] Seddon, J., and Newman, S., *Basic Helicopter Aerodynamics*, American Institute of Aeronautics and Astronautics, Inc., Reston, VA, 2001.
- [110] Bi, N. P., “Contributions to the Experimental Investigation of Rotor/Body Aerodynamic Interactions,” *Ph.D. Dissertation*, Department of Aerospace Engineering, University of Maryland, 1991.
- [111] Chen, P. C., “Development of A Smart Rotor with Induced-strain Actuation of Blade Twist,” *Ph.D. Dissertation*, Department of Aerospace Engineering, University of Maryland, 1996.
- [112] Koratkar, N., “Smart Helicopter Rotor with Piezoelectric Bender Actuated Trailing-Edge Flaps,” *Ph.D. Dissertation*, Department of Aerospace Engineering, University of Maryland, 2000.

- [113] Roget, B., and Chopra, I., "Development and Testing of an Individual Blade Control Algorithm for Vibration Reduction of a Dissimilar Rotor," *Proceedings of the American Helicopter Society 60th Annual Forum*, Baltimore, MD, June 7-10, 2004.
- [114] Heyson, H. H., "Rapid Estimation of Wind-Tunnel Correction with Application to Wind-Tunnel and Model Design," NASA TD D-6416, 1971.
- [115] Technical Communication with Bernhard, A.P.F., 2001-2004.
- [116] Barbero, E. J., *Introduction to Composite Materials Design*, Taylor & Francis, Philadelphia, PA, 1999.
- [117] Strong, A. B., *Fundamentals of Composite Manufacturing: Materials, Methods, and Applications*, Society of Manufacturing Engineers, Dearborn, MI, 1989.
- [118] Hexcel Composites, *8552 Epoxy Matrix Product Data*, www.hexcel.com, 2001.
- [119] Structural Dynamics Research Corporation. *I-deas Master Series*, 1999.
- [120] FlightFab, Inc., www.flightfab.com, 2001.
- [121] Northern Fiber Glass Sales, Inc. *Properties of Rohacell IG*, www.nfgsales.com/rohacell_IG.htm, 1998.
- [122] Airtech Advanced Materials Group, *Airtech Catalog*, www.airtechintl.com, 2001.
- [123] Cytec Engineered Materials, *FM 300 High Shear Strength Modified Epoxy Adhesive*, www.cytec.com/business/EngineeredMaterials, 1998.